DOCTORAL DISSERTATION

Constraining Black Hole Growth Across Cosmic Time – The Faintest Active Galactic Nuclei

SANJA JONIĆ

LEIBNIZ-INSTITUT FÜR ASTROPHYSIK POTSDAM (AIP)

zur Erlangung des akademischen Grades
doctor rerum naturalium (Dr. rer. nat.)
in der Wissenschaftsdisziplin Astrophysik

eingereicht an der
Universität Potsdam
Mathematisch-Naturwissenschaftliche Fakultät
Institut für Physik und Astronomie

October 21, 2020

Betreuer: Prof. Dr. Lutz Wisotzki, Dr. Jakob C. Walcher

1. Gutachter: Prof. Dr. Lutz Wisotzki
Leibniz-Institute for Astrophysics Potsdam (AIP)

2. Gutachter: Prof. Dr. Philipp Richter
University of Potsdam

3. Gutachter: Prof. Dr. Amy Reines
Montana State University

Published online on the
Publication Server of the University of Potsdam:
https://doi.org/10.25932/publishup-50975
https://nbn-resolving.org/urn:nbn:de:kobv:517-opus4-509753

Contents

ABSTRACT

Active Galactic Nuclei (AGN) are considered to be the main powering source of active galaxies, where central Super Massive Black Holes (SMBHs), with masses between 10^6 and 10^9 $M_\odot$ gravitationally pull the surrounding material via accretion. AGN phenomenon expands over a very wide range of luminosities, from the most luminous high-redshift quasars (QSOs), to the local Low-Luminosity AGN (LLAGN), with significantly weaker luminosities. While "typical" luminous AGNs distinguish themselves by their characteristical blue featureless continuum, the Broad Emission Lines (BELs) with Full Widths at Half Maximum (FWHM) in order of few thousands km s^1, arising from the so-called Broad Line Region (BLR), and strong radio and/or X-ray emission, detection of LLAGNs on the other hand is quite challenging due to their extremely weak emission lines, and absence of the power-law continuum. In order to fully understand AGN evolution and their duty-cycles across cosmic history, we need a proper knowledge of AGN phenomenon at all luminosities and redshifts, as well as perspectives from different wavelength bands.

In this thesis I present a search for AGN signatures in central spectra of 542 local ($0.005 < z < 0.03$) galaxies from the Calar Alto Legacy Integral Field Area (CALIFA) survey. The adopted aperture of $3'' \times 3''$ corresponds to central $\sim 100 - 500$ pc for the redshift range of CALIFA. Using the standard emission-line ratio diagnostic diagrams, we initially classified all CALIFA emission-line galaxies (526) into star-forming, LINER-like, Seyfert 2 and intermediates. We further detected signatures of the broad Hα component in 89 spectra from the sample, of which more than 60% are present in the central spectra of LINER-like galaxies. These BELs are very weak, with luminosities in range $10^{38} - 10^{41}$ erg s^{-1}, but with FWHMs between 1000 km s^{-1} and 6000 km s^{-1}, comparable to those of luminous high-z AGN. This result implies that type 1 AGN are in fact quite frequent in the local Universe. We also identified additional 29 Seyfert 2 galaxies using the emission-line ratio diagnostic diagrams.

Using the $M_{BH} - \sigma_*$ correlation, we estimated black hole masses of 55 type 1 AGN from CALIFA, a sample for which we had estimates of bulge stellar velocity dispersions σ_*. We compared these masses to the ones that we estimated from the virial method and found large discrepancies. We analyzed the validity of both methods for black hole mass estimation of local LLAGN, and concluded that most likely virial scaling relations can no longer be applied as a valid M_{BH} estimator in such low-luminosity regime. These black holes accrete at very low rate, having Eddington ratios in range $4.1 \times 10^{-5} - 2.4 \times 10^{-3}$. Detection of BELs with such low luminosities and at such low Eddington rates implies that these LLAGN are still able to form the BLR, although with probably modified structure of the central engine.

In order to obtain full picture of black hole growth across cosmic time, it is essential that we study them in different stages of their activity. For that purpose, we estimated the broad AGN Luminosity Function (AGNLF) of our entire type 1 AGN sample using the $1/V_{max}$ method. The shape of AGNLF indicates an apparent flattening below luminosities $L_{H\alpha} \sim 10^{39}$ erg s^{-1}. Correspondingly we estimated active Black Hole Mass Function (BHMF) and Eddington Ration Distribution Function (ERDF) for a sub-sample of type 1 AGN for which we have M_{BH} and λ estimates. The flattening is also present in both BHMF and ERDF, around $\log(M_{BH}) \sim 7.7$ and $\log(\lambda) < 3$, respectively. We estimated the fraction of active SMBHs in CALIFA by comparing our active BHMF to the one of the local quiescent SMBHs. The shape of

the active fraction which decreases with increasing M_{BH}, as well as the flattening of AGNLF, BHMF and ERDF is consistent with scenario of AGN cosmic downsizing.

To complete AGN census in the CALIFA galaxy sample, it is necessary to search for them in various wavelength bands. For the purpose of completing the census we performed cross-correlations between all 542 CALIFA galaxies and multiwavelength surveys, *Swift* – BAT 105 month catalogue (in hard 15 - 195 keV X-ray band), and NRAO VLA Sky Survey (NVSS, in 1.4 GHz radio domain). This added 1 new AGN candidate in X-ray, and 7 in radio wavelength band to our local LLAGN count.

It is possible to detect AGN emission signatures within 10 – 20 kpc outside of the central galactic regions. This may happen when the central AGN has recently switched off and the photoionized material is spread across the galaxy within the light-travel-time, or the photoionized material is blown away from the nucleus by outflows. In order to detect these extended AGN regions we constructed spatially resolved emission-line ratio diagnostic diagrams of all emission-line galaxies from the CALIFA, and found 1 new object that was previously not identified as AGN.

Obtaining the complete AGN census in CALIFA, with five different AGN types, showed that LLAGN contribute a significant fraction of 24% of the emission-line galaxies in the CALIFA sample. This result implies that AGN are quite common in the local Universe, and although being in very low activity stage, they contribute to large fraction of all local SMBHs. Within this thesis we approached the upper limit of AGN fraction in the local Universe and gained some deeper understanding of the LLAGN phenomenon.

CHAPTER 1

Intoduction

1.1 Active Galactic Nuclei

1.1.1 AGN phenomenology

Active Galactic Nucleus (AGN) constitute an important phase in life cycle of galaxies. They expand over a wide range of luminosities, from the most luminous quasars (QSOs) with $L_B = 10^{11} - 10^{14}\ L_\odot$ to those of significantly lower luminosities widely present in our local Universe. It is still not entirely known to what extent of low luminosites AGN phenomenon persists, due to inability of surveys to reach the low-luminosity end and resolve the central source. In order to fully understand the processes of galaxy formation and evolution, we need a proper knowledge and understanding of the AGN phenomenon at all luminosities and redshifts.

The most common type of AGN are Seyfert galaxies with significantly lower luminosities ($L_B = 10^8 - 10^{11}\ L_\odot$) than those of QSOs. The fundamental difference between Seyferts and quasars is in the amount of radiation emitted by the central compact source. Being the most luminous class of AGN, QSO emission outshines the one of the host galaxy, therefore they can be seen at the great distances as a point-like sources. The optical spectra of QSOs and Seyferts are quite similar, with characteristical strong high-ionization emission lines, and can be categorized into two distinctive classes – type 1 and type 2. Type 1 objects have very Broad Emission Lines (BELs) present in their spectra, that may be detected in both permitted (HI,HeI,HII,MgII) and forbidden ([OIII],[NII],[SII]) broad emission lines. These BELs have Full Widths at Half Maximum (FWHMs) around $1 - 10$ km s^{-1}. Seyfert 2 galaxies, on the other side, do not have BELs present in their spectra. However, Narrow Emission Lines (NELs) of both type 1 and type 2 AGN are still quite broad (FWHM $\sim$ 500 km s^{-1}) comparing to the ones from the quiescent galaxies. There are interemediate types between Seyferts 1 and Seyferts 2 galaxies, depending on the strength ratio of broad and narrow emission lines, labeled as Seyfert type 1.5, 1.8, and 1.9 subclasses. Seyferts reside mainly in the spiral galaxies of types Sb and SBb, while QSOs are mostly located in giant ellipticals (Osterbrock and Pogge, 1985). This is due to the observed correlation that the more luminous AGN hosting the most massive SuperMassive Black Holes (SMBHs) are residing in the most massive galaxies.

Radio galaxies are elliptical galaxies harbouring an AGN in their centers. Similar to Seyferts, they can be divided in two subclasses – with and without BELs: Broad-Line Radio Galaxies (BLRGs) and Narrow-Line Radio Galaxies (NLRGs), respectively. Some of the strongest radio sources are associated with QSOs and are typically located in elliptical galaxies. Seyfert galaxies are typically quiet in radio

domain, since they are mainly located in spirals. Radio galaxies often show a presence of radio lobes or jets, that are emitted from the nucleus and may be the size of the entire galaxy in visible spectrum. These lobes and jets may be one-sided, or two-sided, as seen in some weaker radio sources (Osterbrock and Ferland, 2006). Radio galaxies can also be distinguished according to their radio morphologies into two classes – FR I and FR II, according to Fanaroff-Riley classification, where FR I objects have stronger radio emission in the center, decreasing towards the outer regions, while in case of FR II objects the situation is reversed.

AGN are known to be very optically variable sources, on time scales from years to days. One of the subclasses of QSOs are characterised by their extreme optical variability, and are called Optically Violently Variables (OVV). Their spectra varies on the time scale of few days. Another rapidly variable class of AGN are objects known as BL Lac that, unlike OVV, do not show a presence of strong emission and absorption lines. Their spectral variations are mainly matifested in continuum variations. BL Lac and OVV together are called blazars, and they also show relatively high polarization of the optical light and are known to be strong radio emitters.

Some AGN even show a strong emission in infrared wavelengths, being classified as ultraluminous infrared galaxies (ULIRGs). They are often considered as type 2 QSOs, since the most likely scenario is that the dust around nucleus absorbs and re-radiates the light from the QSO.

1.1.2 Unified model and spectral energy distribution of AGN

AGN have very broad Spectral Energy Distribution (SED), from the γ- and X-rays, over the UV and optical radiation, to the IR and radio wavelengths. The AGN continuum spectrum increases towards the UV wavelengths up to the $\lambda \sim 1000$ Å, and as a first approximation, its shape can be described by the power-law of the form $F_\nu \propto \nu^{-\alpha}$, where α is the spectral index $0 \lesssim \alpha \lesssim 2$, and it usually increases with increasing frequency. The realistic picture is more complex than the power law with the constant spectral index. Broad emission lines of HI, HeI, HeII, and FeII seen in QSOs contribute to the specific spectral feature in the $2000 - 4000$ Å wavelength region, called the "big blue bump" (Shields, 1978; Malkan and Sargent, 1982). The blue bump consists of many unresolved FeII and Balmer Hydrogen lines, creating a pseudo-continuum, and is thermal in origin, originating from the optically thick accretion disk. Although free-free emission might also be responsible for the observed feature. Another characteristical AGN spectral feature occurs around 1 μm, probably as a consequence of emission from the warm dust grains, and is called the "red bump".

The standard AGN model indicates a presence of the rotating SMBH located in its center, that is surrounded by accretion disks of gravitationally pulled material. The powering source of AGN is considered to be conversion of gravitational potential energy into radiation in the accretion disk, that generates strong X-ray emission on the innermost disk orbit, followed by UV and optical continuum.

The accretion disk is surrounded by the, so-called, Broad Line Region (BLR), which is the source of formation of the BELs. The BLR most probably has a clumpy structure, consisting of partially ionized gas clouds, rather than being homogeneous. Continuum radiation photoionizes the gas, producing the BELs. BELs represent velocity of the gas that is driven by the Doppler motion around the central source, indicating a strong gravitational field in the center. Strong emission lines of FeII that are often present in the BLR, indicate temperatures of $\sim 10^4$ K, while semi-forbidden CIII] emission lines indicate number density of $\sim 10^9$ cm^{-3}. The size of the BLR is

relatively small, with the radius of $R \approx 0.07$ pc. The BLR and detection of its BELs is essential for estimating the masses of the central SMBHs, which we will describe in more detail in Section 1.2.2.

The BLR is most likely surrounded by large, optically thick torus of gas and dust. Outside of the torus is the Narrow Line Region (NLR), where NELs are formed. The NLR has significantly larger dimensions than the BLR, typically on the scale of ~ 100 pc. The presence of forbidden emission lines in the NLR indicates an electron density of only $\sim 10^4$ cm^{-3}, while the temperature estimates are around $\sim 10^4$ K, comparable to the BLR. Also, similar to the BLR, the NLR probably consist of gas clouds, although they probably have rather cone-shaped than spherical distribution. The NLR orientation axis overlaps with the radio axis in sources where the extended radio jets have been detected. The distribution of the clouds in the NLR may be driven by radiation pressure and accretion disk wind.

According to the unified AGN model, the observed difference between different types of AGN is mainly due to different orientation angle of the source relative to the line-of sight. An important parameters to study and understand the physics of AGN are the mass and the accretion rate of the central SMBH. The structure of the central engine will be described in more detail in Section 1.2.1.

1.1.3 The physical nature of LINERs

It is found that AGN account for around $10\% - 20\%$ of the galaxies in the local Universe, although with significantly lower levels of activity than the Seyferts (Ho, Filippenko, and Sargent, 1993). A very common class of objects in the local Universe are the, so-called Low-Ionization Nuclear Emission-Line Regions (LINERs), postulated by Heckman (1980b), may contribute to the one-third of all spiral galaxies. LINERs distinguish themselves by the stronger low-ionization narrow emission lines of [OI], [SII], and [NII] than what is found in HII regions and star-forming galaxies. Due to certain similarities in their spectra, and the fact that the BELs are detected in the spectra of some LINERs, it is debated that LINERs account for the majority of faint AGN present in the local Universe (Ferland and Netzer, 1983; Halpern and Steiner, 1983; Ho et al., 1997; Ho, Filippenko, and Sargent, 1993; Ho, Filippenko, and Sargent, 2003),

The common way to separate LINERs from star-forming galaxies, is the strength of their [OIII]/Hβ emission-line flux ratio, as an indicator of ionization level. Baldwin, Phillips, and Terlevich (1981) postulated a method that consists of empirical diagnostic diagrams using strengths of two optical emission line ratios ([OI]/Hα, [SII]/Hα, [NII]/Hα and [OIII]/Hβ) to distinguish between HII regions, Seyfert 2 galaxies, and LINERs. These diagrams are latter revised and improved by Osterbrock and Ferland (2006) and Veilleux and Osterbrock (1987), but are commonly called "the BPT diagrams", for the original authors' initials. Using a combination of modern stellar population synthesis, photoionization, and shock models, Kewley et al. (2001) calculated the first theoretical classification scheme to distinguish between the HII regions on one side, and Seyferts and LINERs on another. They established the, so-called, "maximum starburst line", above which the ionization by star formation is theoretically no longer possible. Kauffmann et al. (2003) made an empirical division between these objects by shifting the Kewley's theoretical line to agree with observations. Kewley et al. (2006) also imposed a purely empirical division line between Seyfert 2 galaxies and LINERs but this separation is often not clearly visible in different survey samples, and has no physical meaning. On Figure 1.1 we show different diagnostic diagrams for SDSS DR7 galaxies, with darker shades indicating

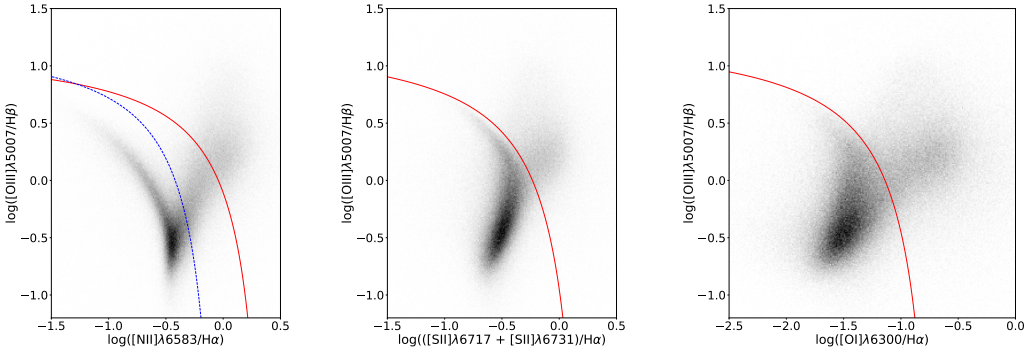

FIGURE 1.1: Diagnostic diagrams of emission line ratios, with the [OIII]/Hβ ratio on the y axis on all three diagrams, and three different lower ionization ratios on the x axis – from left to right: [NII]/Hα, [SII]/Hα, [OI]/Hα. The underlying grey-shaded regions show the distributions of SDSS DR7 galaxies, with darker shades indicating higher object densities. The red solid lines represent the theoretical "maximum-starburst lines" derived by Kewley et al. (2001), and the blue dashed line in the left panel is the empirical demarcation curve established by Kauffmann et al. (2003).

higher object densities. It is important to note that these spectra do not target central regions of galaxies precisely, due to SDSS having fixed aperture sizes.

Although they are often considered to contribute to the low-luminosity end of AGN class, the exact excitation mechanism of LINERs is still an unanswered question. Beside AGN photoionization, few other alternate scenarios for LINER excitation mechanism are proposed, of which a very popular one is collisional ionization by fast shocks (Burbidge, Burbidge, and Sandage, 1963; Osterbrock, 1971; Koski and Osterbrock, 1976; Heckman, 1980b; Dopita and Sutherland, 1995; Lípari et al., 2004). Additional mechanisms include excitation by the cooling flows (Heckman et al., 1981; Fabian et al., 1986; Heckman et al., 1989), by the hot, old, luminous, metal-rich evolved stars (HOLMES) (Alonso-Herrero et al., 2000; Taniguchi, Shioya, and Murayama, 2000), or by the post asymptotic giant branch (pAGB) stars (Kehrig et al., 2012; Singh et al., 2013; Papaderos et al., 2013). Here I will only briefly describe these possible mechanisms, while a concise review of excitation mechanisms of LINERs and analysis of each scenario in greater detail is given by Filippenko (2003) and Ho (2008).

Some early studies (Burbidge, Burbidge, and Sandage, 1963; Osterbrock, 1971; Koski and Osterbrock, 1976; Heckman, 1980b; Dopita and Sutherland, 1995) suggested that the emission-line ratios typical for LINERs can be produced by shock-heated gas, considering the spectral similarity of LINERs and supernova remnants (Koski and Osterbrock, 1976; Fosbury et al., 1978; Heckman, 1980b). Baldwin, Phillips, and Terlevich (1981) as well defined LINER region of standard diagnostic diagrams as the region populated by shock-heated galaxies. Dopita and Sutherland (1995) and Dopita and Sutherland (1996) implied that gas velocities produced by shock can in fact be quite large ($200 - 500$ km s^{-1}), which would result in emission-line ratios observed in LINERs. Most emission lines in LINERs have lower gas velocities ($\sim 100 - 200$ km s^{-1}) which are too slow to produce such shocks. Also, in order for shocks to produce the observed amount of emission in the nucleus, they have to be repeated frequently which is highly unlikely (Filippenko, 2003). It is possible that shocks are dominant in some nuclear regions, but shocks alone cannot explain

the excitation mechanism of LINERs. Shock excitation may be important in galaxies that have large scale outflows and in galaxy mergers (Bremer et al., 2013; Veilleux and Rupke, 2002; Lípari et al., 2004; Monreal-Ibero et al., 2010).

LINER-like emission is also detected outside of the nuclear regions, in extended spectra of some galaxies. These objects, named LIERs considering their non-nuclear emission, show the presence of low ionization emission lines in the regions 10 – 20 kpc from the nucleus, and are often detected in early-type galaxies (Sarzi et al., 2006; Sarzi et al., 2010; Singh et al., 2013). Development of Integral Field Spectroscopy (IFS) enabled us to gain better understanding of these regions and their connection to the nuclear low ionization emission. Among most known studies in this field are works conducted by Heckman et al. (1981), McCarthy et al. (1987), Cracco et al. (2011), Keel et al. (2012), Keel et al. (2015), Obied et al. (2016), Belfiore et al. (2016), Wylezalek (2017), and Hviding et al. (2018)

Very luminous, massive pAGB stars might generate temperatures high enough to produce such emission line strengths typical for LINER-like objects. However, this model may explain extended emission in LIER galaxies (Binette et al., 1994; Taniguchi, Shioya, and Murayama, 2000; Stasińska et al., 2008; Fernandes et al., 2011), mostly in early type galaxies where hot old massive stars become dominant source of ionization (Belfiore et al., 2016), but it is not sufficient to describe nuclear LINER-like emission that is the main interest of this thesis.

Hot, old, luminous, metal-rich evolved stars such as Wolf-Rayet or O-stars with higher temperatures can also produce high energy photons. HOLMES have similar continuum power law shape to the one usually present in LINERs and Seyfert 2 galaxies, and are proposed as ionization mechanism of LINERs by some authors (Alonso-Herrero et al., 2000; Taniguchi, Shioya, and Murayama, 2000). However, (Leitherer, Gruenwald, and Schmutz, 1992) showed that this is a simplified model of Wolf-Rayet stars, while more realistic model would not be able to generate such high-energy photons required for the emission-line ratios detected in LINERs.

Cooling accretion flows (Heckman et al., 1981; Fabian et al., 1986; Heckman et al., 1989) is also proposed as one of the possible excitation mechanism of LINERs, as LINER-like spectra is similar to that of extended gas in elliptical galaxies. These cooling flows are mostly found in massive galaxies and clusters, and are not sufficient to explain the frequency of LINER-like galaxies in the Universe.

As we can see, there are few possibilities that could produce LINER-like emission, of which some mechanisms are probably more important for extended and others for nuclear emission-line regions. Accretion onto the central SMBH by AGN might be the dominant mechanism responsible for nuclear LINER-like emission. Ho et al. (1997) detected broad Hα lines, typical for AGN, in 20% of LINERs defined by the emission-line diagnostic diagrams, using the Palomar survey. This number sets the lower limit for LINERs that are actually considered to be genuine AGN. Multiwavelength studies (González-Martín et al., 2006; González-Martín et al., 2009; González-Martín et al., 2014; Dudik, Satyapal, and Marcu, 2009; Younes et al., 2011; Asmus et al., 2011; Mason et al., 2012; Maoz et al., 2005; Hernández-García et al., 2013; Hernández-García et al., 2014) also confirmed that $75 - 90\%$ of LINERs show AGN signature. The most likely scenario is that the LINERs are a heterogeneous class of objects, of which the most dominant and common excitation mechanisms are accretion onto the central SMBH in its low-activity stage, and contribution by fast shocks. Since the topic of this thesis are AGN, we will be focusing on the fraction of LINERs that we confirmed to be ionized by gas accretion onto the SMBH.

1.1.4 Low-luminosity AGN

As we already mentioned in Section 1.1.2, luminous AGN distinguish themselves as point-like sources with a power law spectrum in the optical and UV domain, described by $F_\nu \propto \nu^{-\alpha}$, with $\alpha \approx 0.5$ (Vanden Berk et al., 2001). At UV wavelengths, the luminous AGN continuum indicates a presence of the big blue bump. In spectra of Low-Luminosity AGN (LLAGN), however, the power law continuum and the big blue bump are evidently absent, as these sources are extremely faint. Even though LLAGN are inhabitants of the local Universe, they are target of many observational challenges due to their very weak emission, and therefore are still not properly understood. Whether they are just scaled-down version of genuine luminous AGN or a have a totally different underlying physical mechanism is still an open question. Very concise review of LLAGN is given by Ho (2008).

Luminous type 1 AGN are easily noticed by the presence of BELs in their optical spectra. If these BELs are detected in the spectra of LLAGN, it will help us understand the underlying physics of these objects, and subsequently find a link to genuine luminous type 1 AGN. In order to detect such weak BELs, AGN surveys must be of sufficient spectral resolution (Ho, 2008), since broad Hα luminosities of these objects are lower even than those of Seyferts ($L_{\mathrm{H}\alpha} < 10^{42}$ erg s^{-1}). Compared to the luminous AGN spectrum, where broad component is responsible for the majority of the total Hα flux density, in LLAGN the broad Hα line is rather weak, consisting of $\sim 50\%$ of the total Hα density, on average, which we analyzed within this thesis.

Since LLAGN have significantly low luminosities, their emission is often highly diluted by the host galaxies' stellar light. Therefore, in order for their proper detection, the stellar contamination must be precisely accounted and subtracted. On the other hand, if broad-line LLAGN are indeed detected, they might be extremely useful for the study of the coevolution of the central SMBHs and their host galaxies, as the AGN light wouldn't dominate the spectra in this case, and the host galaxy properties could be measured with high precision.

Previous work conducted by Ho, Filippenko Sargent (Ho, Filippenko, and Sargent, 1997a; Ho et al., 1997; Ho, Filippenko, and Sargent, 1997b; Ho, Filippenko, and Sargent, 2003) , consists of monitoring the central regions of around 400 nearby galaxies from the Palomar survey (Filippenko and Sargent, 1985; Ho, Filippenko, and Sargent, 1995) in order to search for the LLAGN in the local Universe. They found weak broad Hα emission line ($L_{\mathrm{H}\alpha} \sim 10^{40}$ erg s^{-1}) present in around 20% of AGN in their sample. Their research is performed with the long-slit spectra of moderate resolution. In order to improve the sensitivity to probe even weaker emission lines, better image quality is required.

Eun, Woo, and Bae (2017) searched for broad Hα line in the local ($z < 0.1$) SDSS galaxies, and found significantly lower fraction of type 1 LLAGN in the local Universe – only 3% of galaxies originally categorized as Seyfert 2 type. Presumably this difference is partly caused by the strong dilution effects in more distant galaxies when using a SDSS's 3″ aperture diameter.

In the scenario proposed by Nicastro (2000), which we will discuss in greater detail in Section 1.2.1, the BLR is formed by disk outflows, produced at the transition radius between accretion disk regions dominated by gas and radiation pressure. This radius shrinks with decreasing AGN luminosity, and after a certain point the BLR is expected to disappear. The standard optically thick and geometrically thin accretion disk then transforms into a 3-component structure. Such accretion disk models are considered explain the phenomenon of LLAGN. The dust torus and BLR are expected to disappear for such low-luminosity objects. Yet, in our work, we showed

that the shift from standard accretion disk into 3-component structure occurs rather smoothly, therefore the BLR can still be detected with surveys of sufficient sensitivity and depth.

1.2 Supermassive black holes as central powering source of AGN

1.2.1 Structure of the central engine

As it is already mentioned, the primary ionization source of AGN is the accretion of the surrounding material onto the central SMBH, with masses in range 10^6 $M_\odot$ to 10^9 $M_\odot$ (Kormendy and Richstone, 1995). The highest fraction of AGN energy is produced in the inner regions of the accretion disk, close to the Schwarzschild radius. The gravitational potential energy is converted into kinetic energy through processes of energy dissipation into heat and radiation. The luminosity emitted by the nucleus then can be presented as:

$$L = \eta \dot{M} c^2 \tag{1.1}$$

where $\dot{M}$ is the accretion rate, η is the efficiency of the process, and c is the speed of light. The efficiency of the accretion process represents the fraction of the mass that does not fall onto the central SMBH, but is converted into energy of the AGN, and depends on the radius at which the emission process occurs (Osterbrock and Ferland, 2006). The efficiency has values in range $0.0572 < \eta < 0.423$, where the lower limit represents the efficiency of the non-rotating Schwarzschild black hole, while the maximum efficiency is produced by the fast-rotating Kerr black hole (Novikov and Thorne, 1973).

In order for the material to fall onto the SMBH, the radiation force must be weaker than the gravitational force. The maximum luminosity that a central source of mass M_{BH} can achieve while maintaining balance between the gravitational force and radiation pressure is given by the Eddington luminosity:

$$L_{Edd} = \frac{4\pi G c m_p}{\sigma_T} M_{BH} = 1.3 \times 10^{38} \frac{M_{BH}}{M_\odot} \text{ erg s}^{-1} \tag{1.2}$$

where G is the gravitational constant, m_p – the proton mass, and σ_T is the cross section for Thompson scattering. Eddington limit, or Eddington luminosity, can be applied only on objects with spherical symmetry, otherwise the limit might be surpassed. From the Eddington luminoisty L_{Edd} we can derive the maximum possible accretion rate $\dot{M}_{Edd}$ for the source of mass M_{BH}, given by $\dot{M}_{Edd} = L_{Edd}/(\eta c^2)$. This critical rate, corresponding to L_{Edd} can also be easily exceeded by non-spherically symmetric models.

A widely used parameter to describe AGN accretion rate is its Eddington ratio, defined as:

$$\lambda = \frac{L_{bol}}{L_{Edd}} \tag{1.3}$$

with L_{bol} being the bolometric luminosity of AGN. Since AGN emit in broad spectral range, it is impossible to estimate L_{bol} directly from their SEDs, rather, the certain correction factor is applied, and different wavelength bands or even emission lines can be used as a proxy for L_{bol}. Eddington ratio and accretion rate indicate at which

accretion stage a certain AGN is residing, providing information about the structure of the accretion disk. There is a range of up to three order of magnitudes in Eddington ratios for given SMBH mass M_{BH} (Woo and Urry, 2002).

Accretion disk structure depends on the variety of parameters, such as the accretion rate, strength of the magnetic field, or presence of the jets. At low accretion rates ($\dot{M}_{BH}/\dot{M}_{Edd} \lesssim 1$) and high opacities, the accretion disk is considered to be thin, and optically thick at all radii (Shakura and Sunyaev, 1973), corresponding to the radiativelly efficient ($\eta \approx 0.1$) accretion flows (Blandford, 1985; Begelman, 1985). Broad emission lines are then present in the spectrum, therefore the central source is considered to belong to type 1 AGN. According to the scenario proposed by Nicastro (2000), the BLR is produced by the accretion disk wind, formed at the critical radius in the transition region between gas and radiation pressure dominated disk.

At high accretion rates ($\dot{M}_{BH}/\dot{M}_{Edd} >> 1$), the upward flows are trapped by the accreting material, and the optically thick and geometrically thin accretion disk then transforms into 3-component structure: an inner optically thick disk, a truncated outer geometrically thin disc, and a jet or an outflow. The inner region of the accretion disk (Shakura and Sunyaev, 1976; Esin, McClintock, and Narayan, 1997; Ruan et al., 2019) expands and forms a optically thin quasi-spherical structure, corresponding to the Radiatively Inefficient Accretion Flow (RIAF, Quataert (2003)) that is advection dominated (Narayan and Yi, 1994). Due to very low densities of RIAFs, energy dissipation is much faster than the radiative cooling of the disk.

According to Nicastro (2000) this transition occurs at Eddington ratios $\lambda \approx 10^{-3}$. The transition region between gas and radiation pressure dominated disk region then shrinks, and the critical radius becomes smaller than the innermost stable orbit, therefore the BLR can no longer be formed within this structure, and BELs cannot be seen in the spectrum. Such accretion disk models are considered to be present in case of LLAGN. SMBHs with Eddington ratios below 10^{-3} were therefore considered to be inactive. A schematic representation of the difference between "classical" optically thick and geometrically think radiatively efficient accretion disk and a 3-component structure is shown on Figure 1.2.

The existence of the outer truncated thin disk might possibly explain the SED of LLAGN (Lawrence, 2005). The big blue bump, characteristical for luminous AGN, is evidently absent from the spectra of their low-luminosity counterparts. Instead, there is a peak in the mid-IR part of the LLAGN spectra, forming the so-called big red bump (Lawrence et al., 1985; Willner et al., 1985; Chen and Halpern, 1989; Willner et al., 2004; Bendo et al., 2006; Gu et al., 2007). These changes result in SED of LLAGN to appear steep in the optical and UV parts, lacking the typical power-law feature. This shift from blue to the red bump may be explained by the cool thermal outer disk emission (Lawrence, 2005).

For very low accretion rates ($\dot{M}_{BH}/\dot{M}_{edd}$) of optically thin truncated disk, it is possible for a stable, two-temperature structure to form because of the inability of the inner regions of the disk to cool efficiently (Peterson et al., 2004). This structure is known as the ionized torus and is suspected to play the major role in forming of the radio jets. The magnetic filed of the central source is then trapped in the ionized torus, rapidly rotating within it, and as a consequence collimating the outflow of charged particles, which create a jet-like structure. The jets or outflows can be confirmed by looking at the images from radio observations. LLAGN are considered to be more radio loud than typical broad-line AGN (Trump et al., 2011), which might serve as another aspect in favor of modified accretion disk structure of LLAGN.

In Chapter 3 we showed that BELs can still be detected in LLAGN, indicating that the transition from high-λ geometrically thin and optically thick accretion disks

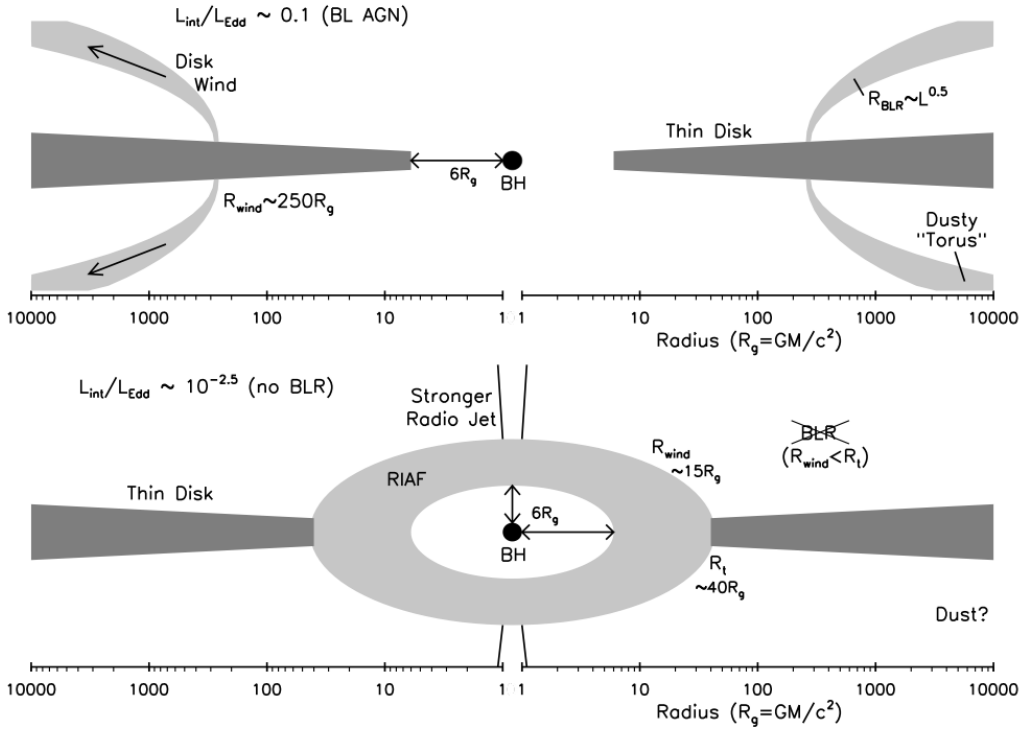

FIGURE 1.2: Difference between optically thick and geometrically thin radiatively efficient accretion disk of AGN accreting at high Eddington ratio (up) and the 3-component structure of LLAGN, consisting of a RIAF, a truncated outer geometrically thin disc, and a jet or an outflow. Image credit: Trump et al. (2011).

to the low-λ 3-component structure, happens rather smoothly, and is not fixed to the value of $\lambda \approx 10^{-3}$. The reason behind such low luminosities of LLAGN may be the combination of both obscuration as well as low accretion rates.

1.2.2 SMBH mass estimation methods

Direct dynamical SMBH measurements

It is a well known fact that SMBH in the centers of galaxies cannot be observed directly, rather only through the effects that they have on the surrounding material. In order for SMBH to be detected, its sphere of influence has to be properly resolved. The sphere of influence represents the radius at which the central SMBH still affects the dynamics of the surrounding stars, given by:

$$R_{inf} = \frac{G_{M_{BH}}}{\sigma_*} = 10.8 \text{ pc } (\frac{M_{BH}}{10^8\ M_\odot})(\frac{\sigma_*}{200 \text{ km s}^{-1}}) \tag{1.4}$$

where σ_* is the stellar velocity dispersion of the stars in the central bulge (Peebles, 1972). Within this radius, the accreting material performs Keplerian motion around the central SMBH. The gravity of the central SMBH no longer has an influence on the surrounding gas and stars beyond this radius R_{inf} (Ferrarese and Ford, 2005). Therefore with spatial resolution smaller than the sphere of influence, the effect of SMBH on the surrounding material can no longer be resolved. This sets a space resolution limit of the telescopes in order to directly measure black hole masses in the centers of galaxies.

The black hole mass of the SgrA*, located in the center of our own Milky Way galaxy is by far the most accurately measured one. Proper motions and radial velocities (Ghez et al., 2004; Schödel et al., 2003; Genzel, Eisenhauer, and Gillessen, 2010; Meyer et al., 2013) of the individual stars rotating around the SgrA* were estimated from high-resolution near-IR observations, and the mass of the central source is estimated to be $4.1(\pm 0.4) \times M_{\odot}$. The black hole masses can also be estimated accurately from the gravitational effect that they have on the surrounding gas and stars. Being closest to us, the SMBH in the center of Milky way provides us meaningful informations about black holes in the centres of galaxies.

H_2O megamaser dynamics

The second most precise measurement of the M_{BH} is the one of the black hole in the center of Seyfert 2 galaxy NGC 4258 (Greenhill et al., 1995; Miyoshi et al., 1995), using the H_2O megamaser dynamics. Water masers (Microwave Amplification by Simulated Emission of Radiation) produce coherent electromagnetic waves on the principle of stimulated emission and can be formed in the AGN torus (Neufeld, Maloney, and Conger, 1994). They are produced when the gas surrounding the central SMBH is heated by X-ray radiation from the inner accretion disk. The warped circlumnuclear molecular gas disk may then be formed, producing H_2O emission at 22 GHz. Such molecular disk can be probed within miliarcseconds from the central SMBH.

The downside of this method is that masers are very rare (Ferrarese and Ford, 2005) and can only be detected in Seyfert 2 galaxies and LINERs with edge-on oriented accretion disks (Braatz, Wilson, and Henkel, 1996; Braatz, Wilson, and Henkel, 1997; Henkel, Greene, and Kamali, 2018; Hagiwara et al., 2018), since for the strong megamaser signal to be detected, a large path-length is required. The most comperhensive maser study up to date is the Mahamaser Cosmology Project (Reid et al., 2009), consisting of 180 galaxies with detectable megamasers.

The most interesting observation when studying megamasers is that the SMBH masses estimated from their dynamics appear to be lower when compared to other methods for the same objects. Also, masers are usually detected in low-mass S0-Sbc barred galaxies (Greene et al., 2016). In the past several years, few more black hole masses are estimated using this method (Pastorini et al., 2007; Greene et al., 2010; Kuo et al., 2011; Greene et al., 2016; Gao et al., 2016; Gao et al., 2017; Pesce et al., 2018; Zhao et al., 2018). Whether the mass discrepancy is the result of the sample selection or there is an underlying inaccuracy present in other methods, is still unknown.

Gas kinematics

Some galaxies have disks of ionized gas in their nuclear regions (Tran et al., 2001), which can be used to estimate the masses of central SMBHs. The ionized gas motion is detected in the optical nebular emission lines (Balmer Hydrogen lines and forbidden lines of [OIII] and [NII]), therefore the high angular resolution is not required. The advantage of the gas dynamics is that a gas settles more quickly into the rotating disk-like structure than stars (Peterson, 2014). This method has been applied to several elliptical (Ferrarese, Ford, and Jaffe, 1996; Macchetto et al., 1997; Barth et al., 2001; Capetti et al., 2005; Shapiro et al., 2006; Francesco, Capetti, and Marconi, 2006; Francesco, Capetti, and Marconi, 2008; Dalla Bontà et al., 2009) and spiral galaxies (Sarzi et al., 2001; Devereux et al., 2003; Marconi et al., 2006; Coccato et al., 2006;

Neumayer et al., 2007; Beifiori et al., 2009; Walsh, Barth, and Sarzi, 2010; Walsh et al., 2013), as well for a galaxy pairs (Hekatelyne et al., 2018).

In order to estimate SMBH mass using gas kinematics, the central region of the galaxies is mapped spectroscopically, and then the dwo-dimensional velocity field is reconstructed from the measured emission line strengths and fitted to the data. Assuming thin rotating disk of the ionized gas that is projected in the line-of-sight, the modeled rotational velocity is calculated from the stellar density, the contribution of the ionized gas disk, and the gravitational potential of the central source. The mass of the central SMBH is then estimated from the fit. Although ionized gas is easy to model, it assumes that we know the inclination angle of the disk, otherwise the error in the mass estimate will be significantly large. Also, presence of the magnetic fields, radiation pressure and dust, and processes such as turbulence and shocks can change the flow of the gas from the Keplerian orbits, implying inaccurate black hole mass estimations (Neumayer et al., 2007; Mazzalay et al., 2014; Jeter, Broderick, and McNamara, 2019; Slater et al., 2019).

Stellar kinematics

Ionized gas disks are only present in the fraction of galaxies, therefore the black hole masses can be determined only for those galaxies that contain such disks. On the other hand, dynamical modeling of stellar kinematics can be applied on all galactic systems, since they don't require any additional components to be present. In the most simple scenario, galaxies can be treated as collisionless systems, whose stellar motion is driven purely by the gravitational force. Therefore, the stellar motion is defined by the gravitational potential of all stars in the galaxy, the central SMBH and the dark matter. The black hole mass then can be estimated from these stellar motions. Realistically, the complexity of the model arises when effects of dust, spiral structures or triaxial gravitational potential are present, therefore this method is mainly used for determining SMBH mass in early-type galaxies.

In order to derive the stellar kinematics of the system, stars can be represented by the distribution function, determined on the line-of-sight velocity distribution. Assuming dynamical equilibrium, velocity field is connected to the stellar gravitational potential. Stellar gravitational potential can be represented as a function of stellar mass density, which can be estimated from the observed luminosity of the galaxy. Having the distribution function determined from the observations, the gravitational potential of the entire system can then be easily estimated. Linking the stellar gravitational potental to the total, the mass density of the entire system can then be estimated from the Poisson equation. The total mass density consists of the stellar, black hole and dark matter mass densities, while dark matter is usually excluded from the dynamical models, implying that the SMBH mass can then be estimated directly from the stellar mass density. The reality is that not all of the components of distribution function can be estimated from the observations, therefore the additional assumptions are required.

The first black hole mass estimation using the stellar kinematics dynamical models was performed for the case of M 87 galaxy (Sargent et al., 1978; Young et al., 1978), assuming spherical symmetry and isotropy of the non-rotating system. This is the most simple model where the distribution function can be described only by one inteegral of motion – the total energy of the system. A somewhat more complex Jeans model assumes the anisotropic velocity distribution (Binney, Davies, and Illingworth, 1990; Marel et al., 1998; Cappellari, 2008). The distribution function the

depends on two integrals of motion – the total energy and the verticular component of the angular momentum.

The most common approach is the so-called Schwarzschild (1979) method where the distribution function also depends on the third integral of motion. Assuming this method, the orbital library is computed from a given gravitational potential of the galaxy. The large number of orbits is computed in order to represent the kinematics and find the best fit that accurately represents the actual distribution of the starlight.

The advantage of the Schwarzschild model is that it allows for more complex potentials to be calculated, such as axisymmetric and triaxial potentials (Bosch et al., 2008; Bosch and Zeeuw, 2010), or additional dark matter component (Gebhardt and Thomas, 2009; Schulze and Gebhardt, 2011; Rusli et al., 2013). This technique is widely applied nowadays for the estimating of the SMBH mass in the quiescent galaxies (Marel et al., 1998; Gebhardt et al., 2003; Shapiro et al., 2006; Gültekin et al., 2009; Thater et al., 2017; Thater et al., 2019). The method, unfortunately, suffers from uncertainties, and therefore can only be used for regular early-type galaxies. It requires the knowledge of the inclinations of galaxies, which is rarely known with high precision. Presence of dust and LLAGN can also further introduce additional complications to the model.

Reverberation mapping

Direct measurement of black hole masses is limited only to the closest luminous quiescent galaxies, since they require for the black hole sphere of influence to be resolved. The very accurate method for determining the black hole masses of type 1 AGN is the, so-called Reverberation Mapping of the BLR (Blandford and McKee, 1982; Koratkar and Gaskell, 1991; Peterson, 1993). This technique uses the variability of type 1 AGN in order to estimate time lags between the changes in continuum and corresponding emission line fluxes.

The gas in the BLR is ionized by nonthermal radiation from the accretion disk surrounding the central SMBH, and is therefore influenced by its gravitational field, and, as such, can be used to trace SMBH activity and estimate its mass. Flux changes in UV ionizning continuum of an AGN will result in changes in the flux of the BELs, with a time delay required for the light to travel through the BLR. Measuring these lags will allow us to accurately estimate the size of the BLR as $R_{BLR} = c\tau$, where R_{BLR} is the radius of the BLR. Reverberation mapping revealed that the emission lines respond rapidly to the continuum changes, implying a small size and high gas density of the BLR, since the recombination time is significantly shorter than the light-travel time (Peterson, 2014).

Assuming the virial equilibrium of the central source, meaning that the motion is dominated by gravity and that the radiation pressure can be neglected, the mass of the central SMBH can then be estimated from:

$$M_{BH} = f \, \frac{R_{BLR} \, v^2}{G} \tag{1.5}$$

where v is the gas velocity in the BLR, and f is the virial scaling factor which depends on geometry, kinematics and inclination of the BLR. The gas velocity is usually represented by the width of broad Hβ line, expressed in km s^{-1}. Although different lines have different time delays and different line widths, they approximately follow the $\tau \propto v^2$ law (Wandel, Peterson, and Malkan, 1999; Peterson and Wandel, 2000; Onken and Peterson, 2002).

The dimensionless scaling virial factor is usually the order of unity, although it is the parameter with highest uncertainty in the equation, since it represents everything that we do not know about the BLR. Since the virial factor f depends on so many factors, it may also vary with each individual object. Individual values of f can be determined from velocity-delay maps, where the dynamics of the BLR is modeled, resulting in a black hole mass or virial factor estimate. So far this is done only for two AGN (Brewer et al., 2011; Pancoast et al., 2012). Another way to individually estimate f is to determine the black hole mass from another method, of which the most commonly used is the relationship between the mass of the central SMBH and stellar velocity dispersions from the bulge, better known as the $M_{BH} - \sigma_*$ correlation (Gebhardt et al., 2000a; Gebhardt et al., 2000b; Ferrarese and Merritt, 2000; Ferrarese et al., 2001; Nelson et al., 2004), which will be discussed in greater detail in Section 1.3.1.

Assuming that the $M_{BH} - \sigma_*$ correlation is the same for quiescent and active galaxies, it is possible to calculate the mean virial factor. This is done by several authors (Onken et al., 2004; Collin et al., 2006; Woo et al., 2010; Graham et al., 2011; Park et al., 2012; Grier et al., 2017), where they normalized the reverberation mapping masses to the $M_{BH} - \sigma_*$ correlation of the quiescent galaxies. However, assuming that both quiescent and active galaxies follow the same $M_{BH} - \sigma_*$ correlation turned out to be inaccurate. Woo et al. (2013) and Shankar et al. (2016) showed that inconsistency in the $M_{BH} - \sigma_*$ correlation of quiescent galaxies and AGN is a consequence of the selection bias introduced in dynamically measured black hole masses of the quiescent galaxies. Since the $M_{BH} - \sigma_*$ correlation is out of the scoop of this section, this will be discussed in more detail in Section 1.3.1. The calibration of the reverberation mapped masses therefore cannot be applied with any accuracy to individual sources without knowing the exact geometry and inclination of the BLR (Peterson, 2014).

Another uncertainty in the estimation of the reverberation mapping based masses comes from the estimation of the gas velocity in the BLR v, more precisely, which line width to use as its representation. Peterson et al. (2004) found that the virial relationship $\tau \propto v^2$ is more accurately reproduced when using σ_{line} from the root-mean-square (rms) spectrum, than the FWHM of the same line. Collin et al. (2006) estimated f using both σ_{line} and FWHM, and concluded that for σ_{line} the virial factor is independent of the line shape, implying that it is a less biased width estimate than the FWHM.

The first reverberation mapping program was conducted by the, so-called, International AGN Watch (Clavel, 1991; Peterson et al., 1991; Maoz et al., 1993; Dietrich et al., 1993; Alloin et al., 1994). Unfortunately, reverberation mapping is not applicable for large number of objects, since it requires long observation time, therefore the black hole mass measurements are available only for $\sim$ 50 objects. (Peterson et al., 2004) provided the most comprehensive measurements of the reverberation mapping SMBH masses. More recent studies include the Lick AGN Monitoring Program (LAMP,Bentz et al. (2009), Barth et al. (2011), Barth, Pancoast, and Collaboration (2012), Barth, Pancoast, and Collaboration (2013), Pancoast et al. (2014), Skielboe et al. (2015), and Williams et al. (2018)).

Virial method

Although reverberation mapping is a direct measurement of the SMBH masses in type 1 AGN, measuring the actual time lags between the continuum and the emission-line flux changes can be time consuming and is possible only for the closest luminous objects. It is therefore necessary to use certain scaling relationships in order to estimate the size of the BLR R_{BLR}.

Kaspi et al. (2000), Kaspi et al. (2005), and Bentz et al. (2006) found that there is a strong correlation between R_{BLR} and continuum luminosity of an AGN at 5100 Å:

$$R_{BLR} \sim L^{\gamma} \tag{1.6}$$

where γ is a factor $\sim$ 0.5 (Bentz et al., 2006; Bentz et al., 2009; Bentz et al., 2013). By introducing these assumptions to the Equation 1.5, it became possible to estimate black hole masses for a large number of objects (McLure and Dunlop, 2004; Vestergaard, 2004; Shen et al., 2008). On Figure 1.3 we present the radius – luminosity relationship established by Bentz et al. (2013) for a sample of 41 nearby reverberation mapped AGN. Bentz et al. (2013) established this correlation for the lowest luminosity AGN for which the AGN continuum luminosity at 5100 Å can still be measured in the spectrum.

The uncertainty of these virially estimated black hole masses are quite large comparing to the reverberation mapped masses, being of order of $\sim$ 0.4 dex (Vestergaard and Peterson, 2006). Therefore, the method may not be very precise, but it can be used to estimate black hole masses for large samples of type 1 AGN. As we already mentioned in the previous subsection, the most commonly used proxy for the gas velocity is the width of broad Hβ line. Estimating black hole masses at higher redshifts using the Hβ will require the observations in near-IR, due to Hβ being redshifted out of the optical domain (Netzer et al., 2007; Greene et al., 2010), or using other emission lines as a proxy, of which the most common are MgII and CIV. For the nearest LLAGN ($z \approx 0$) the broad Hα line can be used with high precision, since the broad Hβ is too weak to be detected in these objects. Greene and Ho (2005) found that there is a correlation between the luminosities of the broad Hα and Hβ lines, as well as their FWHMs.

Although it can be used for large AGN samples, the virial method introduces too many approximations that its validity may be questioned for different samples of AGN. As we will show in our work, this method appears to be inaccurate for the lowest-luminosity AGN at $z \approx 0$.

1.3 SMBH - host galaxy coevolution

1.3.1 SMBH - host galaxy's bulge correlations

Dynamical studies of local galaxies showed that black hole masses in massive galaxies tightly correlate with host galaxies' properties, implying that there is a coevolution of SMBHs and their hosts. (Dressler, 1989) was the first to initiate the existence of the correlation between SMBH masses and the bulge luminosity of the host galaxies, while few years later, Kormendy (1993) derived the correlation for a slightly higher number of objects.

Similarly, Kormendy and Richstone (1995) observed the correlation between dynamically measured black hole masses and luminosities of spheroid component of the host galaxies. In case of spiral galaxies, the spheroid component refers to the central bulge, while in case of elliptical galaxies, it represents the entire galaxy. Later,

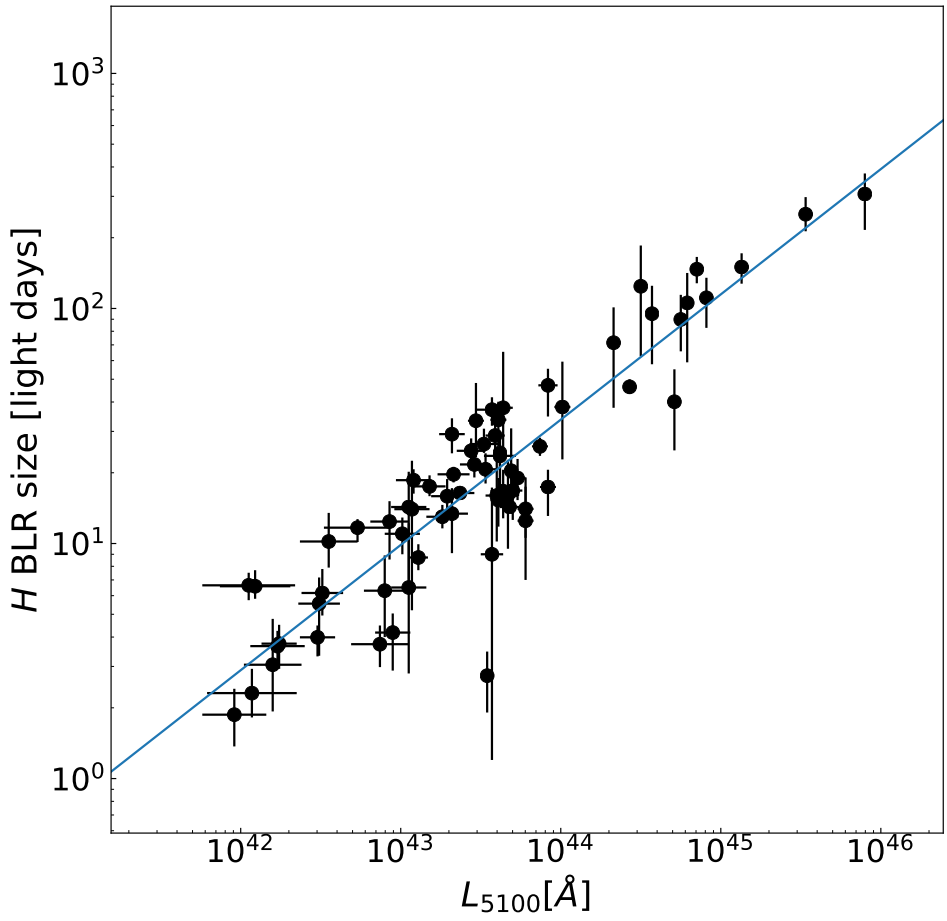

FIGURE 1.3: Correlation between continuum luminosity at 5100 Å and the size of the BLR, established by Bentz et al. (2013) for a sample of 41 nearby reverberation mapped AGN. The BLR size is measured from Hβ time lags. The solid blue line represents the best fit to the data.

Magorrian et al. (1998) used dynamical models and found a correlation between black hole mass and host galaxy's bulge mass. Bulge masses are estimated from the virial theorem:

$$M_{bulge} \propto r_e \sigma_*^2 \tag{1.7}$$

where r_e is the effective radius, and σ_* is the stellar velocity dispersion of the bulge component, estimated from dynamical modeling (Magorrian et al., 1998; Häring and Rix, 2004). The correlations between black hole mass and bulge luminosity, on one side, and black hole and bulge mass on another, are probably just two different manifestations of the same relationship, while bulge luminosity is significantly easier to measure than the bulge mass. Further work in this field is conducted by Ferrarese et al. (2001), Merritt and Ferrarese (2001), Gültekin et al. (2009), Kormendy and Ho (2013), and Davis, Graham, and Cameron (2018).

Another fundamental host galaxy's bulge property that appears to have the tightest correlation with quiescent SMBH mass is the bulge stellar velocity dispersion σ_*

(Gebhardt et al., 2000a; Gebhardt et al., 2000b; Ferrarese and Merritt, 2000; Tremaine et al., 2002; Häring and Rix, 2004; Nelson et al., 2004; Gültekin et al., 2009; McConnell and Ma, 2013; Kormendy and Ho, 2013; Saglia et al., 2016). The $M_{BH} - \sigma_*$ correlation has the smallest scatter ($\epsilon_0 = 0.44$, Gültekin et al. (2009)) from all SMBH – bulge correlations. The $M_{BH} - -\sigma_*$ correlation can be represented as:

$$M_{BH} = k\sigma^p \tag{1.8}$$

where p is the slope that depends mainly on the sample selection, and in praxis has values between 3.6 and 5.3 (Bhattacharyya and Mangalam, 2018).

Gebhardt et al. (2000b), Ferrarese et al. (2001), and Onken et al. (2004) observed a consistent correlation between M_{BH} and σ_* of AGN, to the one found for the dynamically measure black hole masses. This result indicated that AGN and quiescence are just different phases in one galaxy's life cycle, where $M_{BH} - \sigma_*$ correlation is probably established during the AGN phase, in which SMBH accretion limits gas supply for building BH and host galaxy mass simultaneously (Silk and Rees, 1998).

Taking into account larger AGN samples and more sensitive surveys, Greene and Ho (2006), Woo et al. (2010), Xiao et al. (2011), Woo et al. (2013), Bennert et al. (2015), Shankar et al. (2016), and Sexton et al. (2019) showed that $M_{BH} - \sigma_*$ correlation of active galaxies has a shallower slope and lower normalization compared to the ones estimated for the samples of quiescent galaxies. Shankar et al. (2016) observed a similar $M_{BH} - \sigma_*$ behavior for the sample of local galaxies, selected from SDSS. Woo et al. (2013) and Shankar et al. (2016) argued that the discrepancy is a direct consequence of the selection biases introduced in dynamically measured black hole masses of quiescent galaxies, and performed simulations where the same bias is introduced in AGN samples and local SDSS galaxies. The simulations showed that the corresponding $M_{BH} - \sigma_*$ correlations would be consistent with those estimated from dynamically measured black hole masses. They provide more accurate $M_{BH} - \sigma_*$ correlations for AGN samples. On Figure 1.4 we present the $M_{BH} - \sigma_*$ correlation established by Woo et al. (2013), which we will further use in our work for the purpose of estimating SMBH masses. Woo et al. (2013) established the $M_{BH} - \sigma_*$ correlation a sample of 25 nearby reverberation-mapped AGN located mainly in spiral galaxies, with data obtained form Keck, Palomar and Lick Observatories.

The observed black hole mass – bulge correlations, beside the fact that they imply a tight coevolution of SMBHs and their hosts, can be used as reliable black hole mass estimators across various redshift ranges. The most commonly used is the $M_{BH} - \sigma_*$ correlation, since stellar velocity dispersion is the easiest to measure of all bulge parameters.

On the other hand, while ellipticals and bulges of spiral galaxies correlate very tight with SMBH mass, the respective correlation is not found in case of pseudobulges (Hu, 2008; Gadotti, 2009; Greene et al., 2010; Kormendy and Ho, 2013). Zubovas and King (2012) also showed that different environments effect the scatter of black hole mass – bulge correlations.

The underlying physics behind observed correlations, or the lack of them, is, as we already mentioned, the coevolution of SMBHs and their hosts. Central SMBHs are believed to regulate the growth and evolution of their host galaxies through AGN feedback. Galaxies' mergers, as well as secular evolution processes, such as bar instabilities in isolated galaxies, are probably an important mechanisms for the process of SMBH feeding and its growth. Major mergers trigger star formation and redirect gas flow towards the center where SMBH is being fed through the process of accretion. At this stage, the large amount of energy is produced through accretion

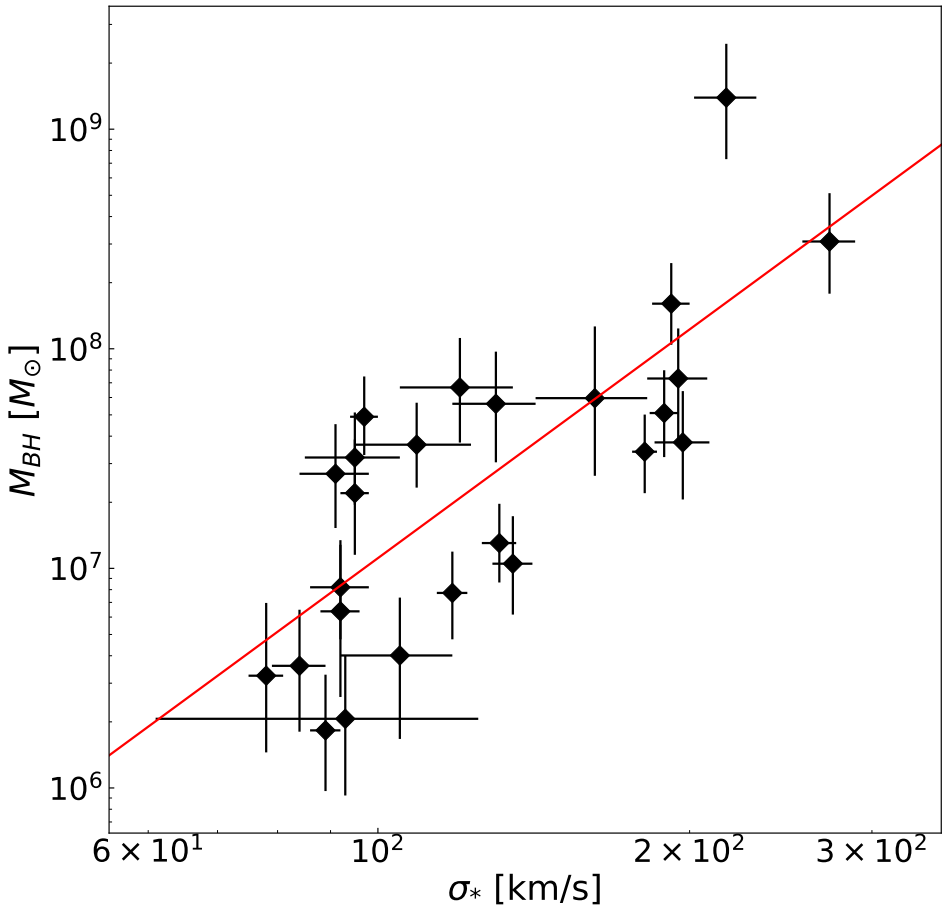

FIGURE 1.4: The $M_{BH} - \sigma_*$ correlation (solid red line) estimated by Woo et al. (2013) for a sample of 25 local reverberation mapped AGN from Keck, Palomar and Lick Obervatories surveys (black diamonds). The intrinsic scatter of the correlation is $\epsilon_0 = 0.41 \pm 0.05$, consistent with $M_{BH} - \sigma_*$ correlations estimated for samples of dynamically measured black hole masses of quiescent galaxies.

and part of that energy is turned into heat and unbind the gas in the galaxy. Further on, the black hole will self regulate its growth by quenching its gas supply through released energy.

Such rapid black hole growth through radiativelly efficient accretion probably took place in the massive galactic systems, of which the majority is quenched in the current epoch, implying that the epoch of efficient SMBH growth is now mostly over (Kormendy and Ho, 2013). AGN feedback mechanisms are in general poorly understood due to their complex nature, but are considered to be the main driver of the slope of the SMBH – bulge correlations. Detailed studies of AGN feedback are conducted by Croton et al. (2006), Lagos, Cora, and Padilla (2008), Fabian (2012), McNamara and Nulsen (2012), Ishibashi and Fabian (2014), and Baron et al. (2018).

1.3.2 Correlation between SMBH masses and total galaxies' stellar masses

Although SMBH – bulge properties correlations show great consistency between each other, bulge measurements cannot be established for large statistical samples, and especially on high redshifts, due to insufficient telescopes' spatial resolution and sensitivity (Sanghvi et al., 2014). Therefore it is useful to seek for correlation between SMBH masses and other parameters that can be measured at greater distances and for larger samples.

Several studies have pointed out to the correlation between the central SMBH mass and the total stellar mass of the host galaxy M_*, that is usually estimated from assumed mass-to-light ratio or SED fitting. Magorrian et al. (1998) were the first to introduce such correlation, although they found a significantly large scatter ($\sim$ 0.51 dex). Using data of higher quality, (Häring and Rix, 2004) implied that the scatter of $M_{BH} - M_*$ relationship is actually comparable to the one of M_{BH} - σ_* correlation ($\sim$ 0.3 dex. Several other authors analyzed this correlation for different black hole samples at different redshifts (Merritt and Ferrarese, 2001; Marconi and Hunt, 2003; Häring and Rix, 2004; Jahnke et al., 2009; Cisternas et al., 2011; Targett, Dunlop, and McLure, 2012; Merloni et al., 2010; Lamastra et al., 2010; Bongiorno et al., 2014; Reines and Volonteri, 2015).

The recent work of Reines and Volonteri (2015) (corrected in Erratum: Reines and Volonteri (2019)) showed that $M_{BH} - M_*$ correlation is also observed for different samples of $\sim$ 250 broad-line AGN. Their combined sample includes measurements of black hole and total galaxy stellar masses for around 350 local galaxies ($z < 0.055$), including dynamically measured black hole masses, dwarfs, type 1 and reverberation-mapped AGN. Black hole masses of type 1 AGN were estimated using the virial assumption. On Figure 1.5 we show their result for respective samples of galaxies. They found that there is an apparent discrepancy between active and quiescent SMBH hosts, where AGN fall significantly bellow quiescent ellipticals and spirals with classical bulges, as seen on the figure as red dots. Also, they noticed a slight difference in slopes of AGN hosts of different morphologies, suggesting two separate $M_{BH} - M_*$ correlations for ellipticals and spirals. They as well propose a one unified $M_{BH} - M_*$ correlation for local type 1 AGN, which we used for the purpose of this thesis. Similarly, it is shown (Häring and Rix, 2004; Greene et al., 2010; McConnell and Ma, 2013; Kormendy and Ho, 2013) that AGN and galaxies with pseudobulges also fall below $M_{BH} - M_{bulge}$ correlations established for quiescent early-type galaxies.

Shankar et al. (2016) also noticed the similar discrepancy between the $M_{BH} - M_*$ correlations of dynamically measured black hole masses and the local SDSS galaxies. They analyzed 5 different black hole samples with dynamical black hole mass measurements and early-type SDSS galaxies at $0.05 < z < 0.2$. As we already discussed in Section 1.3.1, they showed that the dynamically measured black hole masses are biased towards the galaxies with larger stellar velocity dispersions, therefore implying the bias towards the more massive systems. The correlation between M_{BH} and M_* as a consequence has a higher normalization factor than what is observed for SDSS galaxies in their sample, with the bias being more prominent in $M_{BH} - M_*$ than in $M_{BH} - \sigma_*$ correlation. They established the, so-called, intrinsic $M_{BH} - M_*$ correlation that shows a slight curvature, which is a direct consequence of the curvature observed in their $\sigma_* - M_*$ correlation. Both (Shankar et al., 2016) and Fontanot, Monaco, and Shankar, 2015 observed the similar curvature and concluded that the shape is due to galaxy formation physics, and does not imply anything fundamental about black hole formation.

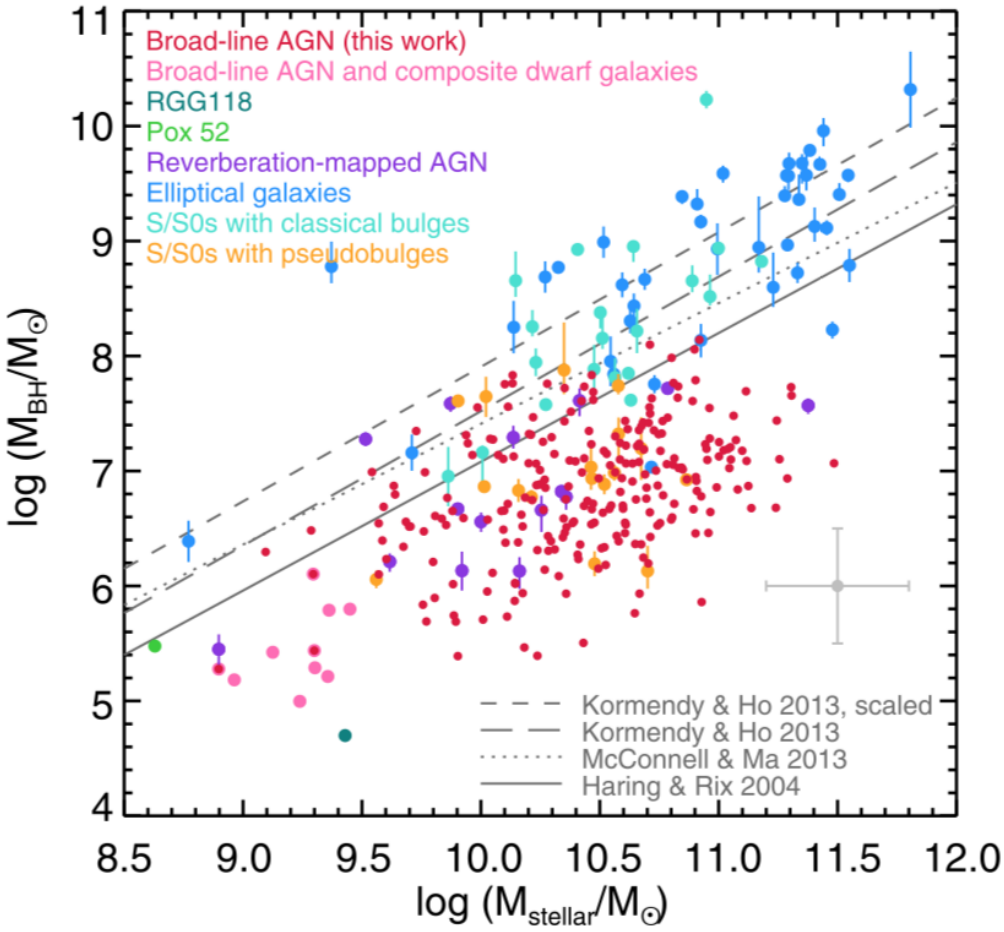

FIGURE 1.5: Correlation between M_{BH} and M_* (estimate from color-dependant mass-to-light ratios from Zibetti, Charlot, and Rix (2009) for multiple galaxy samples. The image is taken from Reines and Volonteri (2015), where they present a combined sample, consisting of: 244 type 1 AGN with virially estimated black hole masses (red dots), 15 reverberation mapped AGN (purple dots), 10 type 1 AGN and composite dwarf galaxies from (pink dots), two dwarf galaxies with low black hole masses – RGG 118 and Pox 52 (dark green and light green dots, respectively), and dynamical black hole masses hosted by ellipticals (blue dots), S/S0 galaxies with classical bulges (turquoise dots), and S/S0 galaxies with pseudobulges (orange dots). The respective M_{BH} measurements were obtained by various authors, for which we refer to the Reines and Volonteri (2015) paper for more detail. The gray lines represent various $M_{BH} - M_*$ correlations estimated by authors mentioned on the plot. The gray error bar indicates uncertainties applied to all stellar masses.

(Lauer et al., 2007) analyzed the biases introduced in SMBH – host galaxy correlations for a multiple samples at different redshifts and different selection criteria. The correlations between SMBH masses and host galaxy properties beyond the bulge may provide insightful information about their coevolution, especially for sample where bulge properties cannot be estimated with high precision.

Beside already mentioned correlations between the mass of the central SMBH and its host galaxy's parameters, there are numerous other SMBH – host galaxy scaling relationships that are not as widely used as previously discussed ones. These are

correlations of SMBH with the bulge optical or near-IR luminosity (Kormendy and Richstone, 1995; Marconi and Hunt, 2003; Läsker et al., 2014), the galaxy's light concentration (Graham et al., 2001), the galaxy's total luminosity (Kormendy and Gebhardt, 2001; Kormendy, Bender, and Cornell, 2011; Läsker et al., 2014),the galaxy's Sérsic index (Graham et al., 2001; Graham et al., 2007; Savorgnan et al., 2013), the dark matter halo (Ferrarese, 2002), the gravitational binding energy (Aller and Richstone, 2007), pitch-angle for spiral galaxies (Seigar et al., 2008; Berrier et al., 2013; Davis, Graham, and Seigar, 2017), and the number of globular clusetrs (Burkert and Tremaine, 2010).

1.4 Growth of SMBHs and AGN evolution through cosmic history

1.4.1 AGN luminosity function

Growth of SMBH across cosmic time is the key to understanding galaxy formation and evolution processes, and it is important to study them both in their active and quiescent phases. Black holes grow mainly through mass accretion in their active phase, where AGN bolometric luminosity reflects the accretion rate, as described by Equation 1.1. The accretion rate is usually expressed through Eddington ratio (Equation 1.3, as normalized AGN bolometric luminosity). Eddington luminosity L_{Edd} (described by Equation 1.2) is an upper limit that a source of mass M_{BH} can achieve in order to maintain balance between the radiation pressure and the gravitational force. From L_{Edd} we can obtain the growth rate of the black hole of mass M_{BH} as:

$$\dot{M}_{BH} = \frac{(1-\eta)}{\eta c^2} L_{bol}$$

where $(1-\eta)$ represents the fraction of the energy that is not radiated, and contributes to the black hole growth. Therefore, in order to trace black hole growth it is important to understand how AGN with different luminoisties evolve across different redshifts, which is represented by the AGN luminosity function (AGNLF). AGN luminosity function is defined as AGN number density at a given volume for a given luminosity interval:

$$\phi(L,z) = \frac{d^2N}{dVdL}(L,z). \tag{1.9}$$

As we already mentioned in Section 1.2.1, bolometric luminosity of AGN cannot be directly measured due to their wide SED, instead, certain luminoisty bands or emission lines can be used as good proxies for representation of AGNLF. The most accurate luminosity function is estimated from hard X-ray band, where X-ray surveys (XMM-Newton, Chandra, ROSAT, ASCA) provide the most insightful data. Some of the X-ray AGN luminosity functions from hard and soft X-rays are conducted by Miyaji, Hasinger, and Schmidt (2000), La Franca et al. (2002), Cowie et al. (2003), Fiore et al. (2003), Barger et al. (2003), Ueda et al. (2003), Hasinger, Miyaji, and Schmidt (2005), Barger et al. (2005), Sazonov and Revnivtsev (2004), Nandra, Laird, and Steidel (2005), Ebrero et al. (2009), Aird et al. (2010), Fiore et al. (2012), Pović et al. (2013), Ballantyne (2014), Ueda et al. (2014), Vito et al. (2014), Miyaji et al. (2015), Aird et al. (2015b), Aird et al. (2015a), Georgakakis et al. (2015), Ranalli

et al. (2016), and Fotopoulou et al. (2016), and they all imply that cosmic evolution of AGN strongly depends on AGN X-ray luminosity (Hirschmann et al., 2012).

AGN luminosity function is relatively well established for luminous QSOs at high redshifts (Schmidt and Green, 1983; Marshall et al., 1983; Boyle, Shanks, and Peterson, 1988; Boyle et al., 2000; Hewett, Foltz, and Chaffee, 1993; Schmidt, Schneider, and Gunn, 1995; Hawkins and Veron, 1995; Wisotzki, 1999; Fan et al., 2000; Richards et al., 2006b; Croom et al., 2009; Palanque-Delabrouille et al., 2013), and directly traces the growth of SMBH accros cosmic history. Therefore, AGNLF can be used to estimate the SMBH density that is accreted during bright QSO phase:

$$\rho(z) = \int_z^\infty \int_0^\infty \frac{1-\eta}{\eta c^2}\, L_{bol}\, \phi(L,z) \frac{dt}{dz} dL dz \tag{1.10}$$

Yu and Tremaine (2002), Marconi et al. (2004), and Shankar, Weinberg, and Miralda-Escudé (2009) showed that the amount of material accreted by the central SMBH estimated by integrating AGNLF over luminosity and redshift ranges is consistent with the mass density of quiescent SMBHs in the local Universe ($\rho(z=0)$). Shankar, Weinberg, and Miralda-Escudé (2009) obtained $\rho(z=0) = (3.2-5.4)\times 10^5\, M_\odot\, \mathrm{Mpc}^{-3}$, while Marconi et al. (2004) estimated average growth curves of SMBHs as function of redshift. Their results imply the rapid growth of SMBHs, where the most massive QSOs accreted their mass faster and at higher redshifts, while the lower-mass black holes accrete at the significantly lower level in the local Universe. The "era of QSOs" peak at at $z \approx 2$. Such phenomenon is known as "AGN cosmic downsizing" or "anti-hierarchical growth of black holes" (Soltan, 1982; Salucci and Persic, 1999; Ueda et al., 2003; Steffen et al., 2003; McLure and Dunlop, 2004; Merloni, 2004; Merloni and Heinz, 2008), implying that the era of massive QSOs and rapid SMBH growth is now mainy over, and that the local Universe is populated mostly by lower-mass SMBH accreting at low Eddington ratios.

AGN downsizing imposes a characteristic behaviour of AGNLF, where various AGN studies at different redshift and luminosity ranges show the peak being shifted towards lower redshifts for fainter objects. However, majority of the studies agree that AGNLF can be parametrized and described by a double power law with different slopes for faint- and bright-end:

$$\phi(L) = \frac{\phi_* / L_*}{(L/L_*)^\alpha + (L/L_*)^\beta} \tag{1.11}$$

with α and β describing the bright- and faint-end slopes respectively, and L_* is the characteristic breaking luminosity at ϕ_*. The downsizing trend is observed in both optical and X-ray luminosity functions.

In order to fully understand AGN evolution and SMBH growth across cosmic history, it is necessary to establish the AGNLF in the local, as well as high redshift Universe. Local AGNLF not only shows us how these objects fit into the bigger picture of AGN evolution over cosmic time, but may also serve as a zero-point for higher redshift AGN and QSO luminosity function studies. As we already mentioned in Section 1.1.4, LLAGN in the local Universe are extremely faint compared to the luminous QSOs at high z. Therefore, estimation of their luminoisty function imposes additional challenges, and is generally poorly known.

A good proxy of the total AGNLF is the emission-line luminosity function of broad lines, characteristical for type 1 AGN. Koehler et al. (1997) obtained the first AGNLF for a small sample of local type 1 AGN, as is later followed by works of Vila-Vilaro (2000), Ulvestad and Ho (2001), Hao et al. (2005a), Greene and Ho (2007),

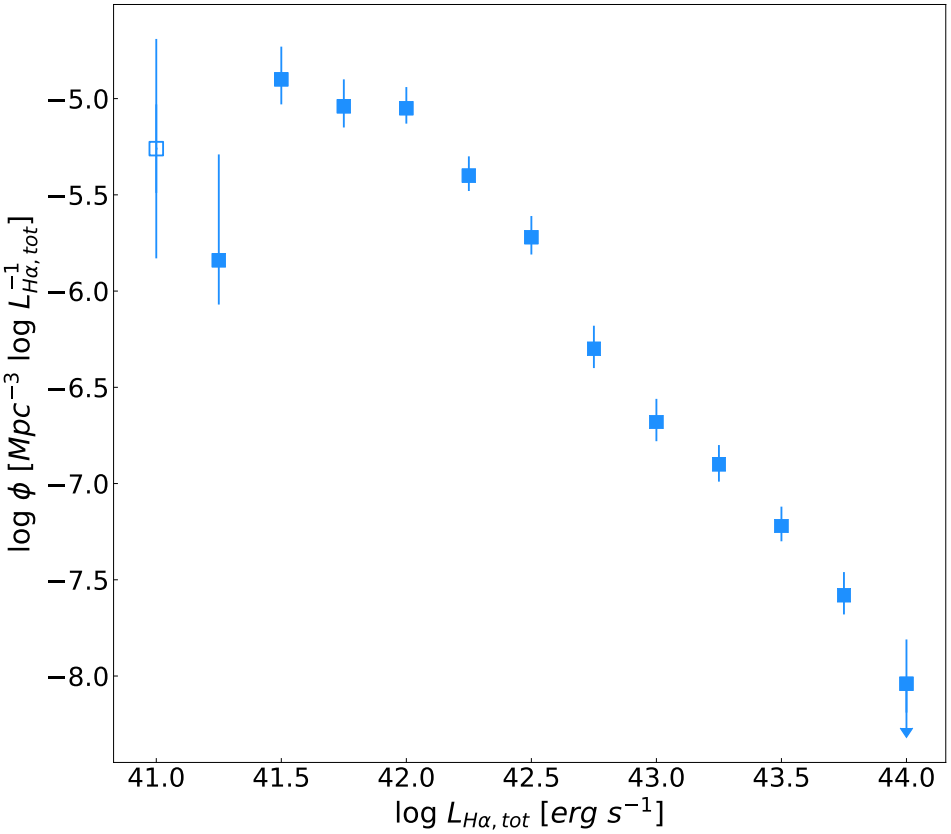

FIGURE 1.6: Broad Hα luminosity function as a representation of type 1 AGNLF obtained by Schulze, Wisotzki, and Husemann (2009) for a sample of $\sim$ 300 AGN from Hamburg/ESO survey, in luminosity range $(10^{40.5} - 10^{44})$ erg s^{-1} and redshifts $0.01 < z < 3.3$. The idea for the plot is adopted from Schulze, Wisotzki, and Husemann (2009).

Vestergaard et al. (2008), Vestergaard and Osmer (2009), and Schulze, Wisotzki, and Husemann (2009) for larger samples and better survey quality.

Schulze, Wisotzki, and Husemann (2009) compared their local AGNLF and luminosity functions from Bongiorno et al. (2007) and Croom et al. (2009), estimated for AGN at higher redshifts and found an apparent disagreement, where Bongiorno et al. (2007) and Croom et al. (2009) high-z luminosity functions predicted significantly higher space density of luminous AGN in the local Universe. Therefore, a proper estimation of the local AGNLF is important as it may provide us with more information, that is often not accounted in luminosity function extrapolations. This will help us gain deeper understanding of the entire AGN evolution.

On Figure 1.6 we used the example from Schulze, Wisotzki, and Husemann (2009), which shows AGN luminosity function of $\sim$ 300 type 1 AGN from Hamburg/ESO Survey, within redshifts $0.01 < z < 3.3$ and in luminosity range $(10^{40.5} - 10^{44})$ erg s^{-1}. We used the work from Schulze, Wisotzki, and Husemann (2009) to compare with our own results and gain deeper understanding of how AGNLF behaves at lowest broad Hα luminosities and $z \approx 0$.

1.4.2 Active black hole mass and Eddington ratio distribution functions

Although AGNLF provides us with the meaningful insight of growth history of SMBHs, it is based on the numerous assumptions, that may, as we mentioned at the end of the previous subsection, introduce large uncertainties when extrapolated over larger redshift and luminosity ranges. In order to estimate AGNLF, the single value of Eddington ratio is assumed for the entire SMBH population. However, it is now know that SMBHs accrete at very wide range of λ, with no preferred value (Yu, Lu, and Kauffmann, 2005; Ho, 2009). In order to avoid such biases that would introduce additional uncertainties, it is useful to separate AGNLF into two parts: the active black hole mass function (BHMF) and the Eddington ratio distribution function (ERDF).

While AGN luminosities can be estimated with relatively high precision, black hole masses are something that we cannot measure directly. As we already discussed, dinamically and reverberation-mapping measured black hole masses are estimated for only a limited number of objects, while for larger AGN samples, indirect methods of M_{BH} estimation have to be used.

First estimation of BHMF were made by McLure and Dunlop (2004), for a sample of type 1 QSO from SDSS survey and Heckman et al. (2004), for low-redshift type 2 AGN, followed by more detailed studies for different type 1 AGN samples (Greene and Ho, 2007; Greene and Ho, 2009; Vestergaard et al., 2008; Vestergaard and Osmer, 2009; Labita et al., 2009; Schulze and Wisotzki, 2010; Shen and Kelly, 2012; Kelly and Merloni, 2012). These studies are consistent with the results obtained from the AGNLF, implying an antihierarchical SMBH growth scenario.

Eddington ratio, besides the black hole mass, is the main drive of the SMBH growth through accretion. Therefore, in order to obtain a complete picture of SMBH growth history at all stages of their activity, it is essential that we also know the evolution of ERDF across different redshifts. Figure 1.7 from Merloni and Heinz (2008) shows the evolution of their estimated BHMF across different redshifts. The dashed line is the local BHMF and, while the yellow shaded regions represent the uncertainty in the BHMF, which is a direct consequence of uncertainties in AGNLF. We can also notice an apparent trend of antihierarchical SMBH growth, where high mass end of their estimated BHMF is built significantly faster than the low mass end.

So far, only few studies were conducted on ERDF. Yu and Tremaine (2002) estimated ERDF for a sample of local type 2 AGN from SDSS, while Schulze and Wisotzki (2010) used the same sample from Hamburg/ESO survey to derive AGNLF, as well as BHMF and ERDF, which we will compare to our work presented in this thesis. Kelly and Shen (2013) also estimated both BHMF and ERDF of type 1 SDSS QSOs using flexible Bayesian technique In the latest work in this field,Weigel et al. (2017) used theoretical model to show that SMBH growth in the local Universe ($z < 0.1$) can be interpreted by two separate ERDFs, of radiativelly efficient and inefficient accretion.

Both BHMF and ERDF are estimated in the same manner as luminosity function, using the Equation 1.7 with the corresponding parameters. Detailed studies of these distribution functions will further help us gain deeper understanding of the cosmic history and growth of SMBHs.

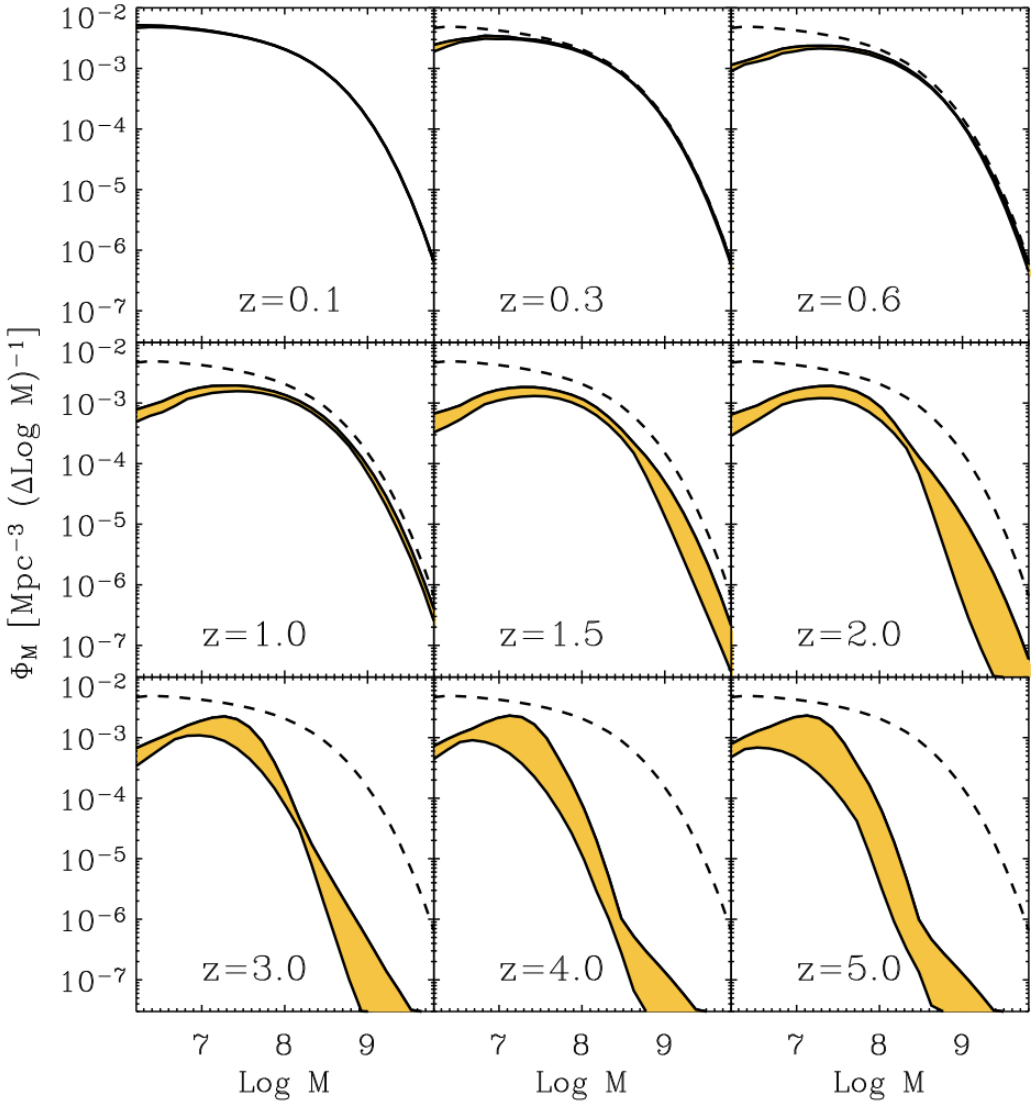

FIGURE 1.7: Representation of SMBH growth across different redshift. The dashed line represents the local BHMF, and yellow shaded regions represent the uncertainties in BHMF estimated by Merloni and Heinz (2008). The AGN downsizing, or antihierarchical SMBH growth scenario reflects itself in redshift evolution of BHMF, where black holes of higher mass are built much more rapidly that the low mass SMBHs. Image credit: Merloni and Heinz (2008).

1.5 Completing AGN census

1.5.1 Multiwavelength surveys

AGN radiate in very broad spectral range, covering wavelengths from the X-ray to the radio domain. Therefore it is essential for understanding of their nature and underlying physics, to study AGN properties in more than one wavelength band. Each band can provide significant information on different phases of AGN activity and help us understand the bigger picture of the AGN phenomenon.

As we already mentioned, AGN are well-known X-ray emitters, whose strong X-ray radiation coming from the compact nucleus may distinguish them from other (quiescent) galaxies. AGN that are too faint or too obscured to be detected in the

optical spectra may reveal themselves in both soft and hard X-ray domain (Loewenstein et al., 2001; Ho, Filippenko, and Sargent, 2003; Ho, 2003; Fabbiano et al., 2004; Pellegrini, Ciotti, and Ostriker, 2008). *Chandra*, XMM – *Newton*, ROSAT, and *Swift* – BAT are among the most noteworthy surveys that collected large samples of both obsucred and unobscured AGN up to redshift $z = 5$ covering over five orders of magnitude in X-ray luminosities Civano et al. (2019), Kollatschny et al. (2008), and Oh et al. (2018)).

Another significant indicator of AGN activity in the centre of a galaxy is the detection of strong compact radio emission in the center of the galaxy or presence of radio jets that might expand over a scale of the entire galaxy. Early studies Sadler, Jenkins, and Kotanyi (1989), Wrobel (1991), Heckman (1980a), and Ho, Filippenko, and Sargent (2003) revealed that compact radio cores are linked to the objects identified as LINERs according to the standard emission-line ratio diagnostic diagrams, while Wrobel (1991) and Slee et al. (1994) pointed out that these objects have SEDs of LLAGN. Later studies (Filho, Barthel, and Ho, 2000; Filho, Barthel, and Ho, 2002; Filho, Barthel, and Ho, 2006; Nagar et al., 2000; Nagar et al., 2002; Filho et al., 2004; Nagar, Falcke, and Wilson, 2005; Krips et al., 2007) also revealed that both Seyfert 2 galaxies and LINERs have similar incidence of compact radio cores.

The most definitive proof of AGN presence in a galaxy is detection of jets in radio domain. Jets are emitted from the compact core, and majority of jetted AGN are discovered to be radio loud, compared to the radio-quiet AGN without jet signature (Padovani, 2017). Detection of jets is strongly linked to the phenomenon of LLAGN, as jets are formed as a consequence of a modified accretion disk structure that we already described Section 1.2.1 of this chapter. Originally these objects were identified as Low-Excitation Radio Galaxies (LERGs, Hine and Longair (1979)) having extremely low Eddington rates and lacking the typical AGN features such as disk or torus, while in the optical domain such behaviour is linked to LLAGN and LINERs (Hardcastle, Evans, and Croston, 2007; Hardcastle, Evans, and Croston, 2009; Best and Heckman, 2012; Mingo et al., 2014; Paggi et al., 2016).

Among most notable surveys significant for radio-AGN detection are NRAO VLA Sky survey (NVSS, Condon et al. (1998)) and FIRST (Becker, White, and Helfand, 1995; Helfand, White, and Becker, 2015).

1.5.2 Extended AGN

Another interesting feature of AGN is that sometimes their emission can be detected in farther galactic regions, up to 10 – 20 kpc from the nucleus Husemann et al. (2008), Husemann et al. (2013), and Husemann et al. (2014). Such regions are usually referred to as Extended Emission-Line Regions (EELRs) or Extended Narrow-Line Regions (ENLRs) of ionized gas and have emission-line ratios typical for central Seyfert or LINER-like emission. As these regions are insensitive to the obscuration of the nucleus, their detection might reveal certain hidden AGN that we previously missed while observing only central galactic regions. This topic came to rise with the development of IFS, which enabled us to study both central and spatially resolved properties of the galaxies in great depth.

There are few scenarios that might explain this extended AGN emission. In case that the detected extended AGN emission has conical or bi-conical shape, usually aligned with radio jets, the most likely explanation is that this is generated by outflows in form of jets (Morganti, Oosterloo, and Tsvetanov, 1998; Stockton, Fu, and Canalizo, 2006; Morganti et al., 2007; Morganti et al., 2015). Another explanation is that these regions actually point out to the historical view indicating former AGN

activity. In such scenario, central AGN has recently turned off while its relic ionized material is spread across the galaxy, forming the "light echos" that we detect as extended AGN emission (Shapovalova et al., 2009; Dadina et al., 2010; McElroy et al., 2016). In this case a galaxy might have a non-AGN mechanism responsible for the excitation of central regions. And final, and very likely explanation of this phenomenon is that central regions of these galaxies are just heavily obscured, preventing detection of AGN. Many studies have revised this topic (Heckman et al., 1981; McCarthy et al., 1987; Cracco et al., 2011; Keel et al., 2012; Keel et al., 2015; Obied et al., 2016; Belfiore et al., 2016; Wylezalek, 2017; Hviding et al., 2018) of which the most detailed work is done by Belfiore et al. (2016) on a sample of $\sim$ 650 MaNGA galaxies. We followed their approach in this thesis and constructed spatially resolved emission-line ratio diagnostic diagrams in order to detect extended AGN.

Studying different wavelength bands and having multiple approaches in AGN detection is essential in their proper identification, as each method and wavelength band carry certain biases and limitations. Like this we are able to gather as much information as possible in order to improve our understanding of AGN phenomenon in its different activity and historical stages.

1.6 The CALIFA sample

For the purpose of investigating LLAGN in the local Universe in this thesis we used the data from the Calar Alto Legacy Integral Field Area (CALIFA) survey (Sánchez et al., 2012; Walcher et al., 2014; García-Benito et al., 2015; Sánchez et al., 2016). The CALIFA survey observations were conducted with the Potsdam Multi Aperture Spectrograph (PMAS, Roth et al. (2005)) mounted at the 3.5 m telescope at Calar Alto Observatory. PMAS uses the PPAK Integral Field Unit (Verheijen et al., 2004; Kelz et al., 2006), with a hexagonal field of view of $74'' \times 64''$ that consists of 331 science fibres with diameter of $2\farcs7$ each. The spectroscopic observation made by the CALIFA survey enable us to study both integrated and spatially resolved properties of the galaxies from the sample. The survey targets galaxies in nearby Universe, in redshift range $0.005 < z < 0.03$.

The entire CALIFA sample consists of 939 galaxies – called the "mother sample", that was selected from the SDSS data release 7 (DR7), with isophote major axis at 25 mag per square second in the r band ($isoA_r$) to satisfy the criteria: $45'' < isoA_r < 79.2''$, cut in the Galactic latitude to exclude the Galactic plane: $b > 20$ or $b < -20$, and $petroMag_r < 20$, to exclude very faint objects. The galaxies were observed with two spectral setups: a low-resolution (V500) that has a wide spectral coverage (4240 Å–7140 Å unvignetted) at a spectral resolution of 6 Å, and midium-resolution (V1200) that covers the wavelength range 3650 Å–4620 Å, and is observed at higher spectral resolution of 2.3 Å. After a three-point dithering pattern the CALIFA data reduction pipeline translated the fibre-fed spectra into combined datacubes that oversample the spatial domain by adopting spatial pixels (spaxels) of $1'' \times 1''$.

The CALIFA survey produced three data releases, of which for the purpose of this thesis we used the final Data Release 3 (DR3, Sánchez et al. (2016). As we were interested in wide spectral range, we used the V500 setup which consist of 542 galaxies selected from the mother sample. The detailed sample selection and data processing descriptions are given in the survey presentation papers (Sánchez et al., 2012; Walcher et al., 2014; García-Benito et al., 2015; Sánchez et al., 2016). On Figure 1.8 we show an example of one LLAGN from CALIFA (galaxy NGC 0499)

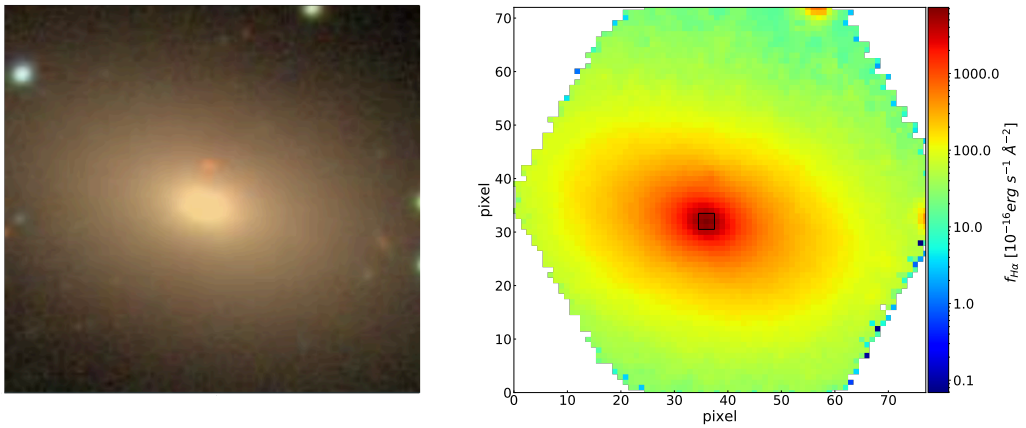

FIGURE 1.8: An example of CALIFA LLAGN (NGC 0499). The left panel shows the galaxy in the white light, while the right panel represents a CALIFA datacube slice at Hα wavelength ($\sim$ 6562 Å). The right panel is colorcoded for the strength of the measured Hα line from the raw spectrum, without stellar component subtraction and emission line fitting. The red regions correspond to the strong Hα signatures, while blue signifies that no traces of Hα line have been detected. The central square marks to the nuclear region of the galaxy ($3'' \times 3''$), which is an aperture size that we used in order to detect potential AGN activity in the centers of CALIFA galaxies.

in white light (left), obtained from the CALIFA website[1], and a datacube slice at Hα wavelength $\sim$ 6562 Å (right). The right panel is colorcoded for the strength of the measured Hα line, obtained from the raw spectrum, therefore stellar component subtraction and emission line fitting were not performed on the datacube slice, since this image serves only for the presentation purpose. The central square on the right panel corresponds to the nuclear region of the galaxy ($3'' \times 3''$), an aperture that we adopted in our work for the purpose of detecting potential activity in the centers of galaxies.

1.7 Outline of this thesis

The main goal of this thesis is to search for the LLAGN in our local Universe and study their properties and underlying physics behind their characteristical appearance. For this purpose we used the data from the CALIFA survey DR3. The thesis is divided into chapters, each focusing on the specific topic that we analyzed in greater detail. The chapters are written as paper drafts, of which each has its own introduction, discussion and conclusions, therefore a certain level of redundancy is unavoidable.

- In Chapter 2 we set the ground for our research, focusing mostly on detection of local LLAGN, and their proper separation from other emission-line galaxies. For this purpose we were interested only in the central regions of the CALIFA galaxies, adopting an inner $3'' \times 3''$ aperture diameter, which corresponds to the central diameter of $\sim 100 - 500$ pc. We used the standard emission-line ratio diagnostic diagrams to separate galaxies with Seyfert 2 nuclei, as well as broad-line fitting techniques, in order to detect possible broad component of Hα emission line.

[1] https://califaserv.caha.es/CALIFA_WEB/public_html/?q=node/1

- Chapter 3 is focused on the detected type 1 LLAGN in the CALIFA survey, and resolves around their properties such as the masses of the central SMBHs and their Eddington ratios. We valued on the $M_{BH} - \sigma_*$ correlation and the virial method as SMBH estimators of the local LLAGN, and discussed their reliability for our sample.
- Chapter 4 extends to the Chapter 3, where we established AGNLF, active BHMF, and ERDF of type 1 AGN that we have mass and Eddington ratio estimations for.
- In Chapter 5 we construct the AGN census in the local Universe, that beside already detected Seyfert 2 and type 1 AGN, now includes X-ray and radio AGN from multiwavelength surveys, as well as spatially extended AGN.
- The final chapter contains the overall summary and discussion of the entire thesis, and provides a brief outlook on possible future studies and perspectives.

CHAPTER 2

Large fraction of low-luminosity type 1 AGN in the CALIFA survey

ABSTRACT

We present a search for AGN signatures in the central spectra of 542 galaxies in the Calar Alto Legacy Integral Field Area survey (CALIFA). We adopted an aperture of $3'' \times 3''$ corresponding to $\sim$100–500 pc for the redshift range of the galaxies, $0.005 < z < 0.03$. 526 galaxies were found to have significant emission lines. After modelling the spectra with the stellar population synthesis code PyParadise and subtracting the stellar continua we fitted the emission lines with Gaussian profiles. In 89 of our galaxies we found evidence that an additional broad component in Hα resulted in a significant improvement of the fit. Using standard emission line ratio diagnostic diagrams we first classified the galaxies on the basis of only their narrow emission lines into star-forming, LINER-like, AGN, and intermediates. More than 60% of the objects with broad emission lines in their central spectra are located in the LINER-like region of the diagnostic diagrams. The broad lines are mostly very faint, with luminosities in range of 10^{38}–10^{41} erg s^{-1}, but they have widths of 1000–6000 km s^{-1}, with distribution typical for broad lines in type 1 AGN. Our results show that broad-line AGN are actually very common among galaxies with LINER spectra, and contribute to non-negligible fraction of galaxies in the local Universe.

2.1 Introduction

Active Galactic Nuclei (AGN) are spread over a wide range of luminosities, from the most luminous quasars with $L_B = 10^{11} - 10^{14} L_\odot$, to the nuclei of Seyfert 1 galaxies with significantly lower luminosities of $L_B = 10^8 - 10^{11} L_\odot$. Being much fainter than QSOs, typical Seyfert 1 nuclei are still quite bright with $L_{\mathrm{H}\alpha} \approx 10^{42}$ erg s^{-1} . Although AGN luminosities extend to even fainter values than those of Seyferts, to which point this phenomenon expands is still not entirely known. In their studies Filippenko (1989) and Ho (1996) point out that this faint AGN are quite frequent in our local Universe. Due to relatively low luminosities of their central engines ($L_{\mathrm{H}\alpha} \leq 10^{40}$ erg s^{-1}), the accreting gas may often be ionized by mix of non-thermal and star-forming ionization processes (Bennert et al., 2006; Villar-Martín et al., 2008).

Very interesting and purely understood class of objects are so-called Low-Ionization Nuclear Emission-Line Regions (LINERs), postulated by Heckman (1980b). The optical emission-line spectra of LINERs have strong lines of the lower ionization levels ([OI], [OII], [SII]). The power source of LINERs is still under a debate. In their work, Ho et al. (1997) assumed that LINERs are actually genuine AGN and that they are an significant constituent of the faint end of the AGN luminosity function (AGNLF). Due to uncertainty of the origin of their powering source other ionization mechanisms of LINERs are proposed as well: fast shocks (Heckman, 1980b; Dopita and Sutherland, 1995; Lípari et al., 2004), hot stars (Filippenko and Terlevich, 1992; Shields, 1992; Maoz et al., 1998; Barth and Shields, 2000), hot, old, luminous, metal-rich evolved stars (Alonso-Herrero et al., 2000; Taniguchi, Shioya, and Murayama, 2000), or post asymptotic giant branch (pAGB) stars (Kehrig et al., 2012; Singh et al., 2013; Papaderos et al., 2013).

The emission line spectroscopy of the central regions of galaxies holds key information on the ionization mechanism responsible for the spectral features that we observe. Nuclear ionization can be stellar or non-stellar in origin, or powered by shock waves. For non-stellar ionization, a source with "harder" ionizing spectrum, that extends further into the UV part, such as AGN power-law continuum, must be present (Osterbrock and Ferland, 2006). Main ionization mechanism of the gas surrounding AGN is photoionization by accretion of the gas onto the central SuperMassive Black Hole (SMBH). The spectra of AGN can be identified by the presence of a starlike nuclei, a blue featureless continuum, strong or broad emission lines (BELs) coming from the Broad Line Region (BLR), or strong radio or X-ray emission (Ho, 2008). If nuclear gas is ionized by non-stellar mechanism, forbidden emission lines of metals, such as [OI] λ6300, [OII] $\lambda\lambda$3726, 3729, [SII] $\lambda\lambda$6717, 6731, [NII] $\lambda\lambda$6548, 6583 and [OIII] $\lambda\lambda$4959, 5007, arising from the Narrow Line Region (NLR), will be relatively strong in the observed spectrum.

The most popular method to distinguish between the galaxies ionized by star formation and the ones ionized by other non-stellar mechanisms was proposed by Baldwin, Phillips, and Terlevich (1981). The method consist of empirical diagnostic diagrams using two optical emission line ratios (for example: [OI]/Hα, [SII]/Hα, [NII]/Hα and [OIII]/Hβ), well known as the BPT diagrams. The BPT diagrams are revised and improved by Osterbrock and Pogge (1985) and Veilleux and Osterbrock (1987). Kewley et al. (2001) constructed the first theoretical classification scheme to distinguish between the HII regions and AGN. Using combination of modern stellar population synthesis, photoionization, and shock models, they derived the "maximum starburst line" (further in the text: KE01 line), above which the ionization by star formation is theoretically no longer possible. Kauffmann et al. (2003) shifted the KE01 line and made an empirical division between the galaxies dominated by

star formation and others dominated by the non-stellar mechanisms, such as shocks or accretion onto the SMBH.

Objects with extremely low luminosities are target of many observational challenges and they are still not properly studied and understood. Whether they are genuine, but less active AGN, or a completely different class of objects is still unknown. Quasars and Seyfert 1 galaxies at high redshifts distinguish themselves by the presence of the characteristic permitted BELs with the Full Width at Half Maximum (FWHM) of a few thousand kilometres per second. If these broad lines can be detected in the spectra of low-luminosity AGN (LLAGN), then there must be a certain physical connection between these objects and high-redshift Seyfert 1 galaxies and QSOs. But due to the relatively low luminosities of the LLAGN, their emission is often highly diluted by the light coming from their host galaxies. On the other hand, if these objects are indeed detected, they might be extremely useful for studying the coevolution of the central SMBHs and their host galaxies, because in this case, the AGN light wouldn't dominate the spectrum and the host galaxy properties could be measured.

The main purpose of our research is to investigate physical properties of LLAGN in our local Universe, using the central spectra of the galaxies. Previous work in this field, conducted by Ho, Filippenko, and Sargent (1995), consists of monitoring the central regions of around 400 nearby galaxies from Palomar survey in order to search for LLAGN and quantify their luminosity function (Ho et al., 1997). They found that the broad component of the Hα emission line is present in 20% of active galaxies in their sample and that more than a half of them belonged to the LINER part of the standard diagnostic diagrams (Ho, Filippenko, and Sargent, 1997a). Their research is performed on the long-slit spectra of moderate resolution. In order to improve the sensitivity and probe even weaker emission lines, better image quality is required. For the purpose of our research we used the Calar Alto Legacy of Integral Field Array (CALIFA) survey Integral Field Spectroscopy (IFS) with moderate spectral resolution. The IFS has a better image quality and is able to detect weaker emission lines than long-slit spectroscopy. The CALIFA survey also probes even lower redshifts than the other surveys theat were previously used in similar studies. The latest research in this field, conducted by Eun, Woo, and Bae (2017), shows much lower fraction of type 1 AGN in the local Universe – only 3% of Sloan Digital Sky Survey (SDSS) galaxies originally categorized as Seyfert 2 type. Using the CALIFA sample, we found this fraction to be significantly higher (around 35%).

The paper is organised as follows: In Section 2.2 we present the CALIFA data sample and analysis that we performed on it. In Section 2.3 we present our results and in discuss them in Section 2.4; and, finally in Section 2.5, we summarise our work and draw our conclusions.

Cosmological parameters that we used are: $H_0 = 70$ km s^{-1}Mpc^{-1}, $\Omega_M = 0.3$ and $\Omega_\Lambda = 0.7$.

2.2 Dataset and spectral analysis

2.2.1 The CALIFA survey

The CALIFA project (Sánchez et al., 2012; Sánchez et al., 2016) has provided wide-field integral-field spectroscopic data of 667 galaxies in the local universe, covering a wide range of morphological types and stellar masses. The so-called CALIFA mother sample consists of 939 target galaxies selected from the SDSS DR7 photometric catalogue (Abazajian et al., 2009). The mother sample was constructed to

be representative for the general non-dwarf galaxy population in the local universe (Walcher et al., 2014), including the possibility to perform volume corrections and reconstruct intrinsic distribution functions. On the basis of the mother sample, galaxies were selected for observations only according to their visibility in the sky. The final CALIFA sample therefore constitutes basically a random subset of the mother sample. The data were made public in three data releases, DR1 (Husemann et al., 2013), DR2 (García-Benito et al., 2015), and DR3 (Sánchez et al., 2016). Here we use the 542 galaxies in the final DR3 of the CALIFA Main sample.

The observations were conducted with the Potsdam Multi Aperture Spectrograph (PMAS, Roth et al., 2005) mounted at the 3.5 m telescope at Calar Alto Observatory, Spain, employing the PPAK Integral Field Unit (Verheijen et al., 2004; Kelz et al., 2006). PPAK has a hexagonal field of view of $74'' \times 64''$ consisting of 331 science fibres with an individual diameter of $2\farcs7$. Each CALIFA galaxy was observed with two spectral setups: A low-resolution grating (V500) provided wide spectral coverage (4240 Å –7140 Å unvignetted) at a spectral resolution of 6 Å, while the wavelength range 3650 Å –4620 Å was observed at somewhat higher spectral resolution of 2.3 Å (V1200 setup). After a three-point dithering pattern the CALIFA data reduction pipeline translated the fibre-fed spectra into combined datacubes that oversample the spatial domain by adopting spatial pixels (spaxels) of $1'' \times 1''$. For further details of the data processing see Sánchez et al. (2016) and references therein.

In this paper we focus on the nuclear spectra of galaxies. Given the fibre size of $2\farcs7$, the median seeing on $1\farcs0$ (FWHM), and the $1\farcs8$ (FWHM) interpolation kernel used in the construction of the datacubes, we adopted an aperture of 3×3 spaxels as an adequate representation of the nuclear regions, with the central spaxel in each case defined by the centroid of the of the galaxy in the SDSS *R* band image. Each galaxy thus provided one spectrum consisting of the co-added flux densities of each of these 9 spaxels.

2.2.2 Stellar continuum modelling

The optical spectra of many galaxies are a superposition of emission lines and underlying starlight. A crucial step before measuring emission line spectra and parameters is therefore a proper subtraction of the stellar continuum and absorption lines. Any significant imperfections in this subtraction could severly affect the apparent properties of the residual emission line spectra. In line with current practice we modelled the stellar spectra by means of a population synthesis code. We used the PyParadise spectral fitting code, developed by Husemann et al. (in prep.), building on previous work by Walcher et al. (2006) and Walcher et al. (2009). PyParadise obtaines the stellar population spectrum and the gas emission lines in two separate iterative steps. The code uses a basis of single stellar population (SSP) templates from the Bruzual and Charlot (2003) library to obtain a set of coefficients which represent the best-fitting linear combination to the observed spectra. We used template spectra from Vazdekis et al. (2012) which has a spectral resolution of 2.51 Å, sufficient for the CALIFA dataset. The SSP library consisted of 84 models covering 6 metallicities (Z = 0.0004, 0.001, 0.004, 0.008, 0.019, and 0.03) and 14 ages, from 0.063 to 17.8 Gyr. After a preliminary model has been obtained, the kinematic solution is determined using a non-linear Monte Carlo Markov Chain fitting process. For the stellar population modelling all strong emission line regions are masked. Upon output the final stellar component model, which, when subtracted from the original spectrum, gives us the desired residual emission line spectrum. In Figure 2.2.1 we illustrate this process and the typical data quality.

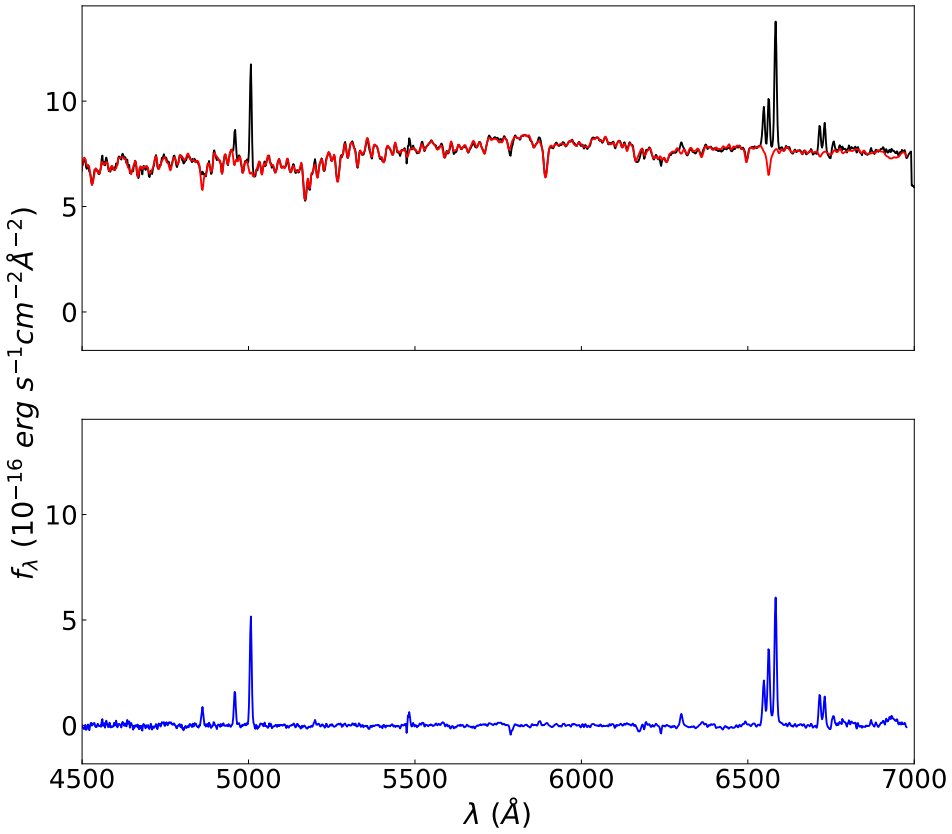

FIGURE 2.1: Example of the stellar continuum modelling process with PyParadise. Upper panel: Central spectrum of the galaxy NGC1093 (black line), overplotted by the best-fit spectrum (red line). Lower panel: Residual pure emission line spectrum after subtraction of the stellar component model fit (blue line).

2.2.3 Emission line fitting

We then proceeded to measure the emission line properties of the central regions of our galaxies. We assume that the dominant mechanism for any line broadening is random Doppler motion of the gas and model each emission line with Gaussians. We focused on the usual strong lines in the optical range: Balmer Hα and Hβ; [NII] $\lambda\lambda$ 6548, 6583; [OIII] $\lambda\lambda$ 4959, 5007; [SII] $\lambda\lambda$ 6716, 6731; and [OI] $\lambda\lambda$ 6300, 6363. As all these lines are contained in the V500 spectral range of CALIFA, we only analysed the spectra from this setup.

Single Gaussian fits

As a baseline approach we assumed that all emission lines originate from the same spatial region and can be represented by single Gaussians of identical line widths and at identical redshifts. We designed a spectral fitting code in order to obtain emission-line models of the central galactic regions. The code uses χ^2 minimization routine to determine the best fit model. The initial values for the velocity dispersions were taken from the prior fit to the stellar kinematics. The line fluxes were left as free parameters, except for the [NII] and [OIII] doublets where the flux ratios were fixed to the quantum mechanical value of 3 in both cases.

In order to estimate errors of the measured parameters, we added random Gaussian noise scaled by the associated error spectra to the emission line model and refitted the lines. We repeated this procedure 100 times for each object and calculated the dispersions of each refitted parameter. We performed visual eye inspection of each fit, and, while overall quality is very good, we noticed that some spectra have slight asymmetries that cannot be captured by single Gaussian fit. These asymmetries then get highlighted when the emission-line fit model is subtracted from the spectrum.

Of the 542 galaxies in the sample, we did not detect any emission lines in the central spectra of 16 of them. Among the remaining 526 galaxies, 43 only showed very weak Hα and no other emission lines. 483 galaxies revealed also detectable emission from [NII], and 447 galaxies presented a detectable [SII] doublet, enabling us to classify them through standard emission line ratios as discussed in Section 2.3 below, and 432 of them had detectable [OI] emission line in their central spectra.

Broad Hα emission

Inspecting the single-Gaussian emission line fits we noticed that in the Hα+[NII] spectral region, several spectra displayed an apparent excess around the [NII] λ6548 line, while at the same time Hα appeared to be overfitted. While one might first suspect an overall profile mismatch given the simple template shape as single Gaussians, we also noted that the excess was typically less pronounced in the brighter [NII] λ6583 line, which is opposite to what one would expect for template mismatch. Instead, adding a single broad component only in Hα to the fit provided a very significant improvement in such cases. This is illustrated in Figure 2.2, especially in the middle panels: Although the additional broad line is quite weak, the excess emission around λ6548 is significant, and a broad hump centred on Hα can be discerned already in the left panel. We emphasize that it is in general only the Hα line that requires such an additional component; we generally do not detect strong indications for broad components in [NII] or other forbidden lines. In a 2 objects we also find hints of a broad Hβ component, but as these are generally much weaker and less convincing, we did not consider them any further.

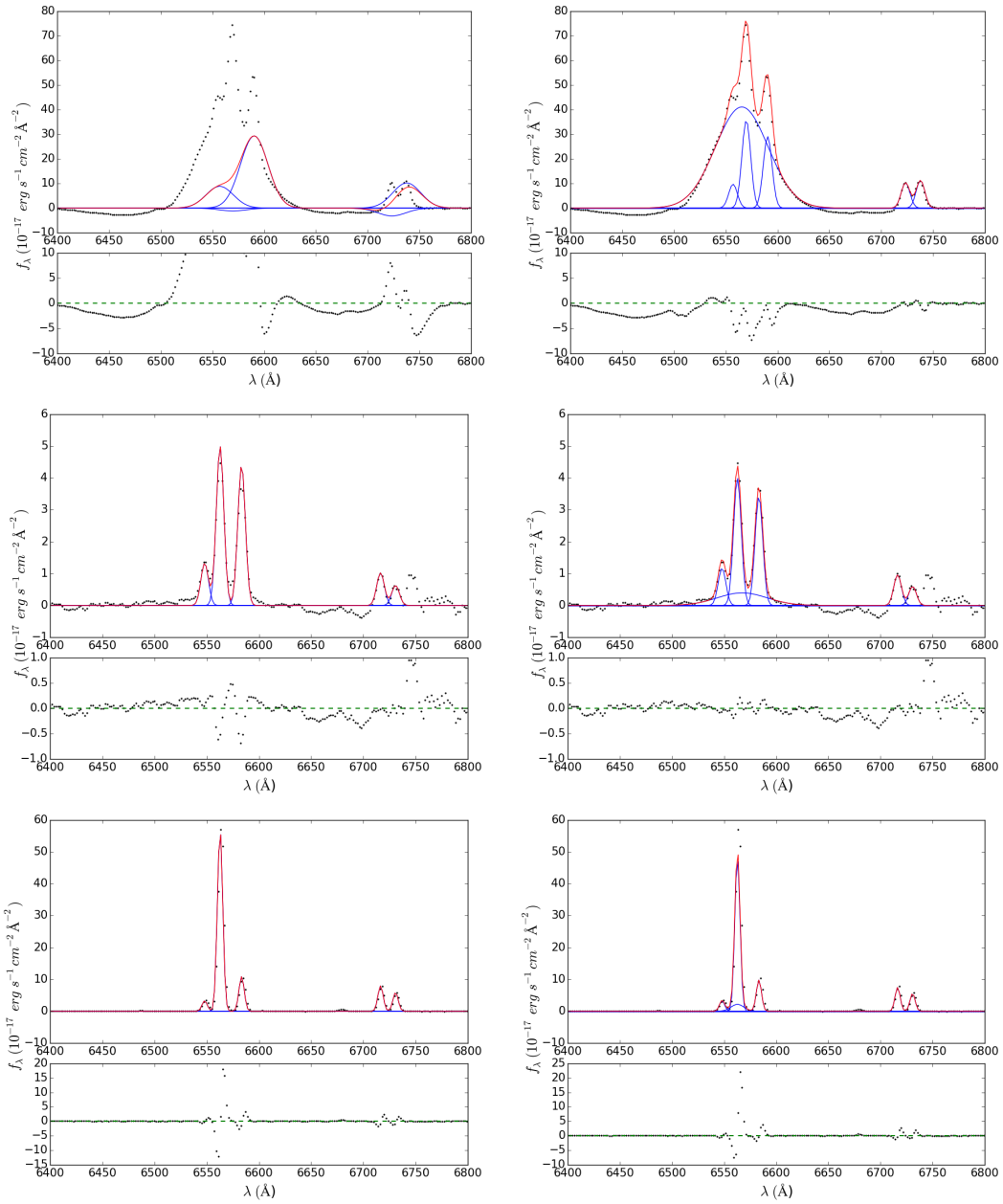

FIGURE 2.2: Examples for the emission line fits of the Hα + [NII] region, without (left panels) and with a broad Hα component included in the fits (right panels). The black dots represent the data points of the spectra after subtracting the stellar component. The red lines show the best-fit models, while blue lines trace the individual fit components. The smaller panels below each main panel show the fit residuals. The top row presents a clear case of a type 1 AGN (UGC 03973 or Mrk 79) in the sample where the broad Hα component is obvious. The middle panels illustrates a typical example for the objects of special interest in this paper, where the fit with only narrow lines is overall not bad, but improves significantly when adding a weak broad component. The representing object is MCG-02-51-004. The bottom row shows a case where the additional broad Hα component does not improve the fit and is therefore rejected; this object (NGC 2480) is counted as having only narrow emission lines. More BEL fit examples can be found in Appendix B.

We found that for 89 galaxies in our sample a broad Hα component was needed to make the fit to the [NII] doublet acceptable. When included in the fit, the broad emission line component added three free parameters: line width, wavelength centroid, and line flux. Table A provides the best-fit broad line parameters for all 89 galaxies in our CALIFA sample. The line widths were approximately corrected for instrumental broadening. BEL fits of our type AGN are shown in the Appendix B.

The presence of a weak broad Hα component in the nuclear spectrum of several of our galaxies suggests that these object may harbour faint AGN. We discuss the arguments in support of this hypothesis in Section 2.3.2

Detection limits for broad emission lines

As many of the detected Hα broad emission line components in our data are quite weak, we made the following experiment to asses the minimum strength of a broad component in order to be detected with our method. For this purpose we selected 100 galaxies from our sample that appeared to show pure narrow emission line central spectra. We then added a sequence of broad Hα components to each spectrum, with gradually increasing line fluxes and also varying the other line parameters. The minimum flux considered was $1 \times 10^{-17}\,\mathrm{erg\,s^{-1}}$ and incremented by half that value up to a maximum of $120 \times 10^{-17}\,\mathrm{erg\,s^{-1}}$. The line widths (FWHM) were varied over the range of 700–9100 $\mathrm{km\,s^{-1}}$, with a step size of 300 $\mathrm{km\,s^{-1}}$, and the line centroid was shifted between $\pm 1000\,\mathrm{km\,s^{-1}}$ relative to the narrow lines, stepped by 10 $\mathrm{km\,s^{-1}}$. Each of those artificial spectra was refitted twice, with and without a broad component.

For each fit we calculated the reduced χ^2_{red} value over the wavelength range 6460–6670 Å and compared the values with and without the additional broad Gaussian. If χ^2_{red} was improved by more than 20% we assumed the fake broad Hα to be detected; otherwise we considered it undetected.

Repeating this procedure for all 100 spectra, we estimated the detection frequency in dependence of flux, FWHM and line shift. Figure 2.3 shows the resulting detection probability as a function of line flux after marginalising over all line widths and shifts. We approximated the probability dependence on flux by the fitting function

$$p(f) = \frac{1}{1 + e^{-k(f - f_0)}} \tag{2.1}$$

where f_0 characterises the location of the turnover from essentially zero to essentially unit detection probability. This fitting function is overplotted in Figure 2.3. We found that the location of the turnover probability is fairly invariant with respect to variations of the line width and shift and mainly depends on the line flux.

Figure 2.3 reveals that a 50% detection limit corresponds roughly to a broad line flux limit of about $1.5 \times 10^{-16}\,\mathrm{erg\,s^{-1}}$. Also depicted in Figure 2.3 are the actually measured broad line fluxes of the objects in our sample. In fact only the weakest lines are plotted, as most of the detected lines have fluxes outside the plot limits and correspond to a detection probability of essentially one. Of the 89 objects in our broad line subsample, only 14 have marginalised detection probabilities below unity, and none has a probablity of less than 0.4. This shows that while our dataset is probably somewhat incomplete at the level of the faintest detected lines, the overall sample has a very high degree of completeness.

We also tested whether the detected broad emission lines were limited to the central region. While an analysis of the spectra over the full spatial extent of the galaxies is beyond the scope of the present paper, we extracted centrally positioned

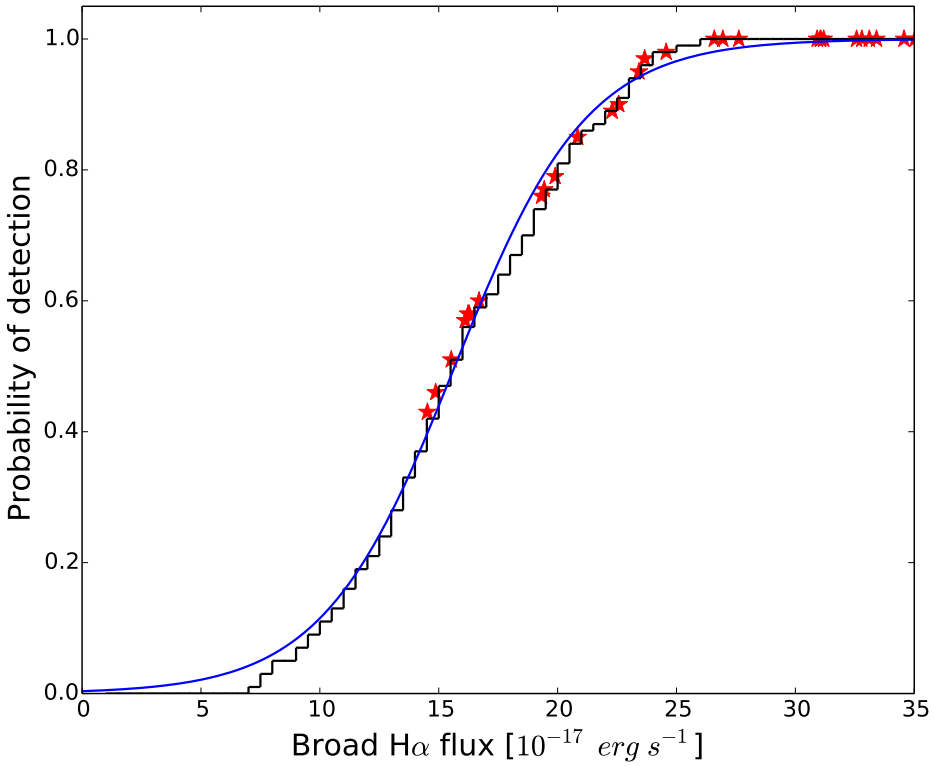

FIGURE 2.3: Detection probability of the broad Hα fluxes, obtained by adding the variety of broad Hα components to the pure narrow line central spectra of 100 galaxies, in order to determine the point from which the broad line fluxes could be detected. The cumulative function (black solid line) represents broad line flux detection probability averaged over FWHM and intrinsic shift range. The blue solid line represents a curve fit of the data, and the red stars are the data points that we measured in the real broad line spectra of CALIFA survey, by applying the same procedure as for the artificial line fluxes.

test apertures of 11″ in diameter, but with excluded central 3″ × 3″ region. These spectra always showed either no broad line at all, or a much weaker signal than in the central spectra as expected from a blurred point source.

2.2.4 Corrections for dust reddening

Before proceeding to calculate emission line ratios we corrected all fitted line fluxes for extinction using the Balmer decrement Hα/Hβ. As HII regions and AGN have slightly different intrinsic values of this ratio and also somewhat different extinction curves, we used the line ratio classifications presented in Section 2.3 to differentiate. Based on the standard diagnostic diagram [OIII]/Hβ vs. [NII]/Hα and the empirical separation curve from Kauffmann et al. (2003, KA03 hereafter) we identified galaxies that are possibly hosting AGN. We adopted the extinction curve from Cardelli, Clayton, and Mathis (1989) for star-forming galaxies and the curve by Gaskell and Benker (2007) for objects above the KA03 line. Following usual practice we assumed the intrinsic Hα/Hβ ratio to be 2.86 in the former, corresponding to case B recombination in a photoionized nebula with electron density $n_e = 10^2\,cm^{-3}$ and temperature $T = 10^4$ K (Brocklehurst, 1971). For the objects in the potential AGN region

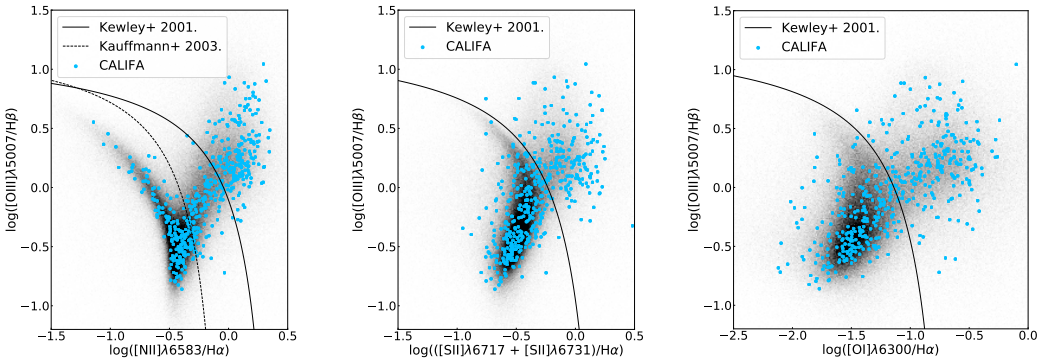

FIGURE 2.4: Diagnostic diagrams of emission line ratios, always showing the [OIII]/Hβ ratio on the y axis and three different lower ionization ratios on the x axis – from left to right: [NII]/Hα, [SII]/Hα, [OI]/Hα. The blue dots represent our measurements in the central spectra of CALIFA galaxies. The underlying grey-shaded regions show the distributions of SDSS DR7 galaxies, with darker shades indicating higher object densities. The solid lines represent the theoretical "maximum-starburst lines" by Kewley et al. (2001), and the dashed line traces the empirical demarcation curve by Kauffmann et al. (2003) in the left panel.

we adopted Hα/Hβ = 3.1 (Halpern and Steiner, 1983; Gaskell and Ferland, 1984). In cases where the measured Balmer decrement was less than the adopted intrinsic value we assumed that no extinction is present. We left the broad emission line fluxes uncorrected for extinction.

2.3 AGN candidates in CALIFA

2.3.1 Emission line ratio diagnostics

To identify likely AGN among the CALIFA galaxies we first followed the usual approach of consulting diagnostic diagrams based on emission line ratios. We employ the three standard diagrams established by Veilleux and Osterbrock (1987), each of which combines the high-excitation [OIII]/Hβ ratio with the ratio of a low-excitation line to Hα. Figure 2.4 presents the resulting distributions of our measured line ratios. For these diagrams we used only the narrow components of the Balmer emission lines, even if a broad line was included in the best fit. For comparison we also show the data for nearly 10^6 galaxies in SDSS DR7. We stress the differences in the captured spatial scales between SDSS and our CALIFA central spectra: Although the *angular* spectral apertures are of the order of 3″ in both cases, the typical redshifts of CALIFA galaxies (the median z is ~ 0.015) are lower by a factor of ~ 6 than those in the full SDSS DR7 sample, implying that the CALIFA central spectra cover a correspondingly smaller region of typically only a few 100 pc in radius.

We first focus on the classical [OIII]/Hβ vs. [NII]/Hα diagram (Figure 2.4, left panel): Of the 483 CALIFA galaxies with central spectra showing these lines, 196 (37%) have line ratios putting them above the "extreme starburst line" of Kewley et al. (2001, ; KE01 hereafter), putting them in the AGN/LINER domain and indicating that excitation by young stars is unlikely to be the dominant mechanism in the nuclear regions of these galaxies. Basically an equal proportion of objects (179/483 $\approx$ 37%) have central spectra that place them into the star-formation domain below the Kauffmann et al. (2003, ; KA03 hereafter) line in this diagram. The

remaining 108 objects (21%) have intermediate line ratios. In contrast, more then 2/3 of SDSS galaxy spectra are found on the star-forming branch, and only 15% are located to the right of the KE01 line.

The other diagnostic diagrams in Figure 2.4 show a qualitatively similar pattern, in the sense that the fraction of points in the AGN/LINER region is substantially higher for the CALIFA central spectra than for the SDSS DR7 datapoints. This is presumably a consequence of the above mentioned aperture differences, highlighting that in many galaxies the physical conditions change significantly when zooming into their central zones. It is also noteworthy that the star-forming sequence in the [SII]/Hα and [OI]/Hα diagrams basically becomes inconspicuous in the CALIFA data, due to the low number of objects in these parts of the diagrams. This trend is probably enhanced by differences in the distributions of stellar masses between SDSS DR7 and CALIFA, the latter containing a larger proportion of massive galaxies than the former.

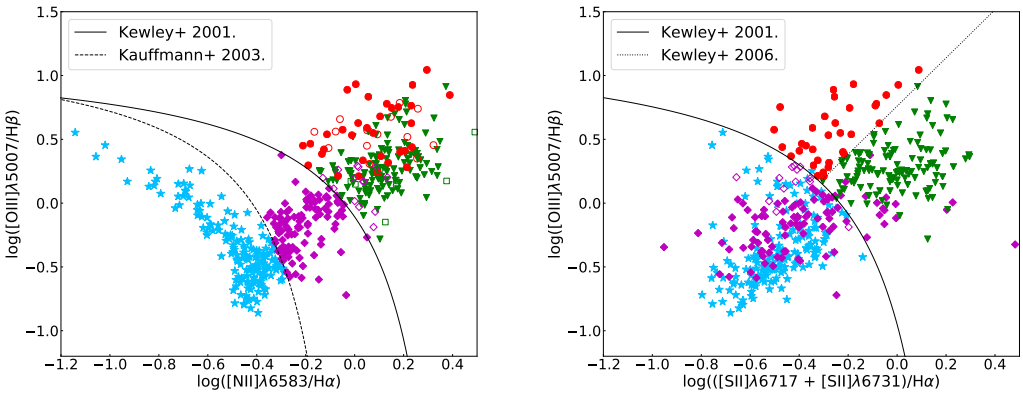

FIGURE 2.5: The central emission line ratios of the CALIFA galaxy sample represented on the [OIII]/Hβ vs. [NII]/Hα (left) and [OIII]/Hβ vs. [SII]/Hα (right) standard diagnostic diagrams. The galaxies with star-forming nuclei, determined using the empirical Kauffmann et al. (2003) line (dashed line, left) on the [OIII]/Hβ vs. [NII]/Hα diagnostic diagram, are marked with blue stars. Seyfert 2 nuclei, located above the theoretical Kewley et al. (2001) "maximum-starbust line" (solid line) and left from the Kewley et al. (2006) "Seyfert-LINER classification line" (dotted line, right) on the [OIII]/Hβ vs. [SII]/Hα diagram, are represented with red dots, while LINER-like nuclei (above the Kewley et al. (2001) line and right from the Kewley et al. (2006) line on the [OIII]/Hβ vs. [SII]/Hα diagram) are marked with green triangles. The additional "intermediate nuclei" (located above the Kauffmann et al. (2003) line on the [OIII]/Hβ vs. [NII]/Hα, and below the Kewley et al. (2001) line on the [OIII]/Hβ vs. [SII]/Hα diagram) are represented with purple diamonds. Empty red circle and green triangle symbols represent objects that we classified as either Seyfert or LINER-like according to their [OIII]/Hβ ratio as they are missing [SII] lines in their central spectra to be classified according to the [OIII]/Hβ vs. [SII]/Hα diagram. Empty diamonds represent those objects that are located below Kewley et al. (2001) line on [OIII]/Hβ vs. [SII]/Hα and above Kewley et al. (2001) on [OIII]/Hβ vs. [NII]/Hα diagram.

A more refined view of the information contained in these diagnostic diagrams is provided by Figure 2.5, where we used different colours and symbols to mark certein regions in the diagrams. We leave out [OI]/Hα from these considerations as [OI] is the weakest of these lines and too often undetected or very noisy in our spectra. Of the remaining two low-ionization line ratios, [NII]/Hα is very efficient

in separating the star-forming from the AGN/LINER branch, whereas [SII]/Hα has higher discriminative power within the latter domain. This was demonstrated by Kewley et al. (2006, ; hereafter KE06) who proposed an empirical dividing line between AGN and LINER (or LINER-like) spectra which is also plotted in the lower panel of Figure 2.5. If we apply this classification to the 160 objects having detectable [SII] line above the KE01 separation on [SII]/Hα diagram, we find 33 objects on the AGN side (red circles on Figure 2.5) and 127 on the LINER-like side (green triangles) of the K06 dividing line. The left panel of Figure 2.5 shows that the objects classified as AGN in the [SII]/Hα diagram are still above the LINER-like objects in [NII]/Hα, but with significant overlap. We classified additional 22 objects that lack [SII] emission in their central spectra according to their [NII]/Hα diagram and [OIII]/Hβ line ratios. Adopting the criterion [OIII]/Hβ = 3 from Heckman (1980b), we classified objects above this limit as Seyferts (14 objects), and below as LINERs (8 objects). There is one object in the far LINER region that has [OIII]/Hβ > 3, which we attributed to LINERs. These objects are marked with corresponding empty symbols on [NII]/Hα diagram. This resulted in total 47 objects with Seyfert 2 and 135 with LINER-like nucleus.

For the 108 objects with intermediate line ratios in the [NII]/Hα diagram (magenta diamonds on Figure 2.5), the [SII]/Hα ratio appears not to provide much additional discriminatory power, as most of these objects are scattered over much the same region as the star-forming galaxies in the lower panel of Figure 2.5. These objects have weak [SII] lines, while their [NII] lines are still relatively strong, setting them apart from the star-forming branch. Additional 14 objects are located below KE01 line on the [SII]/Hα diagram, placing them on star-forming region, while on the [NII]/Hα diagram they are located above KE01 line, which we used to separate AGN-LINER region from star-forming and intermediate galaxies. We attributed these objects to the intermediate class (marked with empty magenta diamonds), resulting in total of 122 galaxies with intermediate nucleus. Several of these objects probably have composite spectra, with emission lines powered by young stars as well as other mechanisms. It is also possible that this category contains centrally obscured AGN that might be detectable by their radiative influence on other parts of their host galaxies. This will be studied in another chapter.

2.3.2 Broad emission line objects

We now consider the 89 objects of our sample where we detected a broad Hα line. In Figure 2.6 these objects are marked by black circles. Interestingly, the vast majority of them (59/89) are located in the LINER-like part of the diagnostic diagrams, followed by 18 objects located in the Seyfert region and 12 located in the "intermediate" region. None of them is classified as purely star-forming. Assuming that our broad line objects are genuine low-luminosity type 1 AGN increases the AGN fraction of our CALIFA sample considerably. We return to this point in Section 2.4 below.

We converted all broad Hα fluxes to luminosities, shown as a histogram in Figure 2.7. The object with the lowest broad Hα luminosity is NGC 0955 with only 2×10^{38} erg s^{-1}; the most luminous (by far) is the well-known Seyfert 1 galaxy UGC 03973 = Mrk 79. The median luminosity for our sample is 2.6×10^{39} erg s^{-1}. Comparing these luminosities with those of the SDSS-selected local broad-line AGN sample of Hao et al. (2005a) and Hao et al. (2005b), our objects are among the lowest luminosity (in broad Hα) AGN known.

The distribution of broad line widths for our sample, on the other hand, is quite similar to that of other broad-line AGN samples, as shown in Figure 2.7. The values

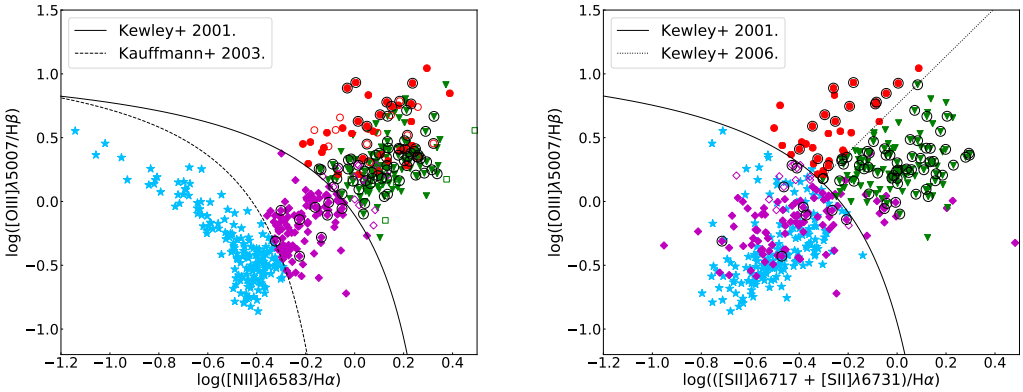

FIGURE 2.6: As Figure 2.5, but marking all objects by a black circle where we detected a broad Hα component in the central spectrum.

range from a minimum of 1000 km s^{-1} (NGC 5056) to a maximum of 6000 km s^{-1} (NGC 0499); the mean value is 3000 km s^{-1}. On Figure 2.7 (right) we see the distribution of FWHMs of CALIFA type 1 AGN compared to the FWHMs obtained by Hao et al. (2005a), normalized for the same number of objects. Hao et al. (2005a) obtained this distribution for a sample $\sim$ 1300 AGN selected from SDSS catalogue. We can notice that our LLAGN width distribution clearly resembles the one of the "genuine" AGN. This is further proof that the BELs that we detected are in fact, an actual representation of the BLR in these objects.

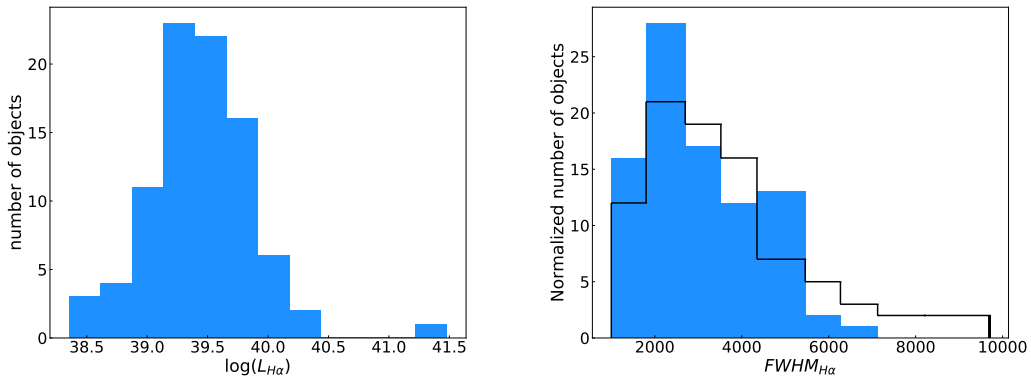

FIGURE 2.7: Left: Histogram of broad Hα luminosities of our 89 objects, in logarithmic units $\log(L/\mathrm{erg\ s^{-1}})$. Right: Histogram of line widths (FWHM) for the 89 detected broad emission lines from CALIFA (blue) compared to distribution of luminous type 1 AGN selected from SDSS and normalized for the same number of objects, obtained by Hao et al. (2005a).

2.3.3 HeII as AGN indicator

We also considered HeII λ4686 emission as an additional potential AGN indicator. Due to its high ionisation potential (54.4 eV compared to 35.2 eV for [OIII]), HeII is sensitive to hard ionizing spectra and can be used to separate AGN from star forming galaxies (Baer, Schawinski, and Weigel, 2016). The downside of this line is that it is typically quite faint and therefore hard to detect. Only 13 objects in our

CALIFA sample showed HeII emission in their central spectra, all of which were already classified as an AGN by either diagnostic diagrams or the detection of a broad Hα component.

2.3.4 Summary of classification results

We combined the results from the diagnostic emission line ratio diagrams and the detections of broad emission lines into a final classification in the following way:

- All objects to the right of the KE01 line in the [NII]/Hα diagram and above the KE06 line in the [SII]/Hα diagram, as well as the objects with [OIII]/Hβ > 3 that do not have [SII] lines in their nuclear spectra, were tagged as AGN, with or without broad lines (47 objects in total). Of these, 18 show a broad Hα component and 29 do not.
- Of the objects to the right of the KE01 line in the [NII]/Hα diagram and below the KE06 line in the [SII]/Hα diagram, i.e. in the LINER region, as well as those with [OIII]/Hβ < 3 with no [S]II], 59 were found to have broad Hα lines and were therefore also counted as AGN. The remaining 76 have LINER spectra without detected evidence for an AGN.
- Of the 122 'intermediate' objects between the KA03 and KE01 lines in the [NII]/Hα diagram, and below KE01 line on line on [SII]/Hα and above KA03 line on [NII]/Hα diagram, 12 have broad Hα and get added to the AGN category; this leaved 110 intermediate objects with unclear or composite excitation mechanism.
- And finally, 179 galaxies in the CALIFA main sample are classified in their central spectra as purely star-forming.

2.3.5 Total stellar mass of CALIFA AGN

We analyzed dependence between our AGN types and total stellar mass $M_\star$ of host galxies, estimated by the CALIFA colaboration (Walcher et al., 2014) using Sloan Digital Sky Survey (SDSS) ugriz growth curve magnitudes. (Walcher et al., 2014) used Bruzual and Charlot (2003) models with a Chabrier (2003) Initial Mass Function (IMF) to calculate total stellar masses, where possible bursts and different amounts of dust extinction were accounted.

We noticed that type 1 AGN in CALIFA have the highest stellar masses in the sample, from $(10^{10.2} - 10^{11.9})\ M_\odot$, with an average of $10^{11}\ M_\odot$. Seyfert 2 galaxies have M_* in range $(10^{9.8} - 10^{11.7})\ M_\odot$. This shows that large number of the most massive galaxies in CALIFA are in fact AGN hosts, where even though these LLAGN are significantly faint, they still prefer massive galactic systems.

On Figure 2.8 we present the distribution of total galaxy stellar masses M_* of both Seyfert 2 and type 1 AGN. On the left we have a standard histogram of stellar masses for the full sample. We gave priority to type 1 AGN, meaning that objects that are identified as both Seyfert 2 and type 1 AGN are attributed to the type 1 AGN. On the right we show the mass-dependant fraction of both AGN types, where full bin contains all emission line galaxies within that M_* range. As we can see, AGN contribute to the large fraction of higest M_* bins in the CALIFA galaxy sample.

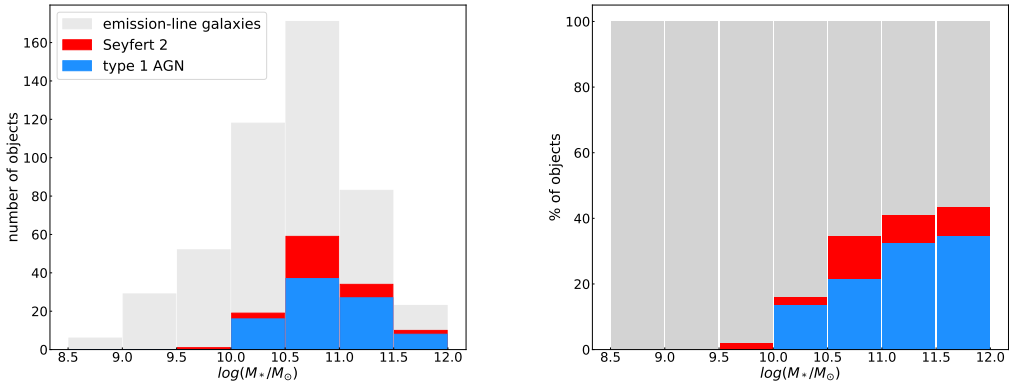

FIGURE 2.8: Left: Histogram showing total stellar masses M_* of AGN hosts (Seyfert 2 + type 1 AGN) in CALIFA, compared to the all emission-line galaxies in the sample. Right: Seyfert 2 and type 1 AGN given as a mass-dependant fraction of all emission-line galaxies in CALIFA.

2.4 Discussion

2.4.1 The frequency of low-luminosity type 1 AGN

The occurrence of AGN is clearly heavily biased towards massive galaxies as we showed in previous section. For stellar masses of $\log(M_\star/M_\odot) > 9.5$ we obtain a mean AGN fraction of 27% and up to 42% for one bin. The mean type 1 AGN fraction is 21%. Walcher et al. (2014) showed that for a range of stellar masses of $9.7 < \log(M_\star/M_\odot) < 11.4$, the CALIFA sample can be taken as representative for the local galaxy population, but with very different survey volumes and therefore subsample sizes for different masses. At any given mass within this range, the AGN fraction obtained from CALIFA should therefore be a valid estimate for galaxies in general.

The total number of AGN among 542 galaxies in the CALIFA main sample, identified from their central spectra, is 118 or 22%. The fraction of only the type 1 AGN is 16%. This is much higher than the fraction measured by Eun, Woo, and Bae (2017) who looked for broad Hα lines among $z < 0.1$ SDSS galaxies classified by their emission line ratios as type 2 AGN and found that only 3% of the type 2 objects revealed a broad line. Presumably this difference is partly caused by the strong dilution effects in more distant galaxies when using a 3″ aperture. As mentioned already in Section 2.2.3, we investigated such dilution effect in our data by extracting spectra through apertures slightly offset from the central position and found that the detectability of broad lines decreases very rapidly. But another explanation for the low fraction of broad-line objects is probably also that they searched for such lines only among already confirmed type 2 AGN, whereas we find most of the broad-line AGN in galaxies classified as LINERs from their narrow emission lines.

On the other hand, our numbers are in good agreement with the survey by Ho, Filippenko, and Sargent (1997a) who analysed nuclear slit spectra of nearly 500 nearby galaxies and found broad Hα emission lines in 10% of all galaxies. In fact our approach can almost be seen as a modern "remake" of the Palomar survey conducted by Ho et al., using integral field rather than long slit spectroscopy and also employing other analysis techniques such as full spectral fitting of population synthesis models instead of matching empirical template spectra to subtract the stellar

continuum. We speculate that these technical improvements benefited our search in terms of sensitivity for weak broad emission lines, which may well explain our even somewhat higher detection fraction.

2.4.2 The nature of LINER galaxies

As discussed already in the Introduction, the LINER class of galaxies is very difficult to characterise and explain in terms of the dominant powering mechanism. While this conundrum has only been deepened by the discovery of LINER-like emission from galactic regions far outside the nuclear zone (Sarzi et al., 2006; Sarzi et al., 2010; Singh et al., 2013; Belfiore et al., 2016), we emphasize that in the present chapter we are only discussing nuclear emission regions and thus genuine LINERs.

A very interesting result of our analysis is the location of so many broad-line objects in LINER region of the standard diagnostic diagrams. In fact, more than 40% of all LINER-classified objects were found to show broad-line nuclear emission. Again the venerable Palomar survey already came to a very similar conclusion (Ho et al., 1997): 50% of the type 1 AGN detected by them belong to the LINER part of the diagnostic line ratio diagrams. If we take these broad lines detected in LINERs as signposts of nuclear activity, i.e. objects powered by accretion onto central SMBHs, then at least half of all LINERs are indeed weak AGN. Of course this still leaves open the possibility that the other 50% have different and possibly diverse origins.

2.4.3 On the ratio of type 1 to type 2 AGN

An interesting finding of this chapter is that the ratio of type 1/type 2 AGN is quite high (3 : 1) in CALIFA. This ratio is also high even for the Seyfert region of the standard diagnostic diagrams, as 40% of Seyfert 2 galaxies have broad Hα line in their central spectra. There is a possibility that the emission-line ratio method "picks" more luminous AGN in the sample, while rest of the type 2 objects are "masked" as intermediate. Also noteworthy is, that for such faint AGN as we have in CALIFA, host galaxy contamination plays a huge role. BELs are insensitive to the stellar contamination, as they can only be produced by accretion onto the central SMBH.

Another important factor to analyze is the dust obscuration. According to the Unified AGN model, the central source is surrounded by optically thick dusty torus. In "typical" luminous AGN this dusty tours blocks the emission coming from the BLR, while the NLR which is located outside of the tours, still remains "visible". As a result, in luminous AGN we observe only the emission coming from the NLR, correspondingly classifying these objects as type 2 AGN. The theoretical work of Elitzur and Shlosman (2006) implies that in very faint AGN with bolometric luminosities below $L_{bol} \sim 10^{42}$ erg s^{-1}, accretion can no longer sustain required cloud outflow rate (González-Martín et al., 2015).

Several studies found the correlation between AGN bolometric luminosities and dust covering factor C_T in optical and X-ray AGN studies (Simpson, 2005; Ueda et al., 2003; Ueda et al., 2011; Ricci et al., 2013). However, more recent studies (Ichikawa et al., 2019; Netzer et al., 2016; Stalevski et al., 2016) actually showed that the correlation between L_{bol} and C_T is in fact really weak to non-existing. Almeida et al. (2011) showed that type 2 AGN have larger C_T than type 1. The most likely scenario is that the torus structure disappears for $L_{bol} < 10^{42}$ erg s^{-1}, while the BLR still persists at very low level, resulting in detection of BELs that were hidden in more luminous AGN. As a consequence we have a higher fraction of type 1 than type 2 LLAGN. More insight into this topic will be presented in the next chapter.

2.5 Conclusions

We analyzed the central spectra of the CALIFA sample, a representative set of galaxies in the local universe, with respect to the occurrence of AGN signatures. We pursued two different methods to identify AGN from the spectra: By placing characteristic emission line ratios into diagnostic diagrams, and by searching for broad emission lines, in particular from Hα. We find 47 AGN by the first method, based on their narrow lines alone, and another 89 likely broad-line AGN. Out of these 47 objects 18 have detectable broad Hα in their central spectra, which we then classified as type 1 rather than Seyferts, leaving us with 29 Seyfert 2 and 89 type 1 AGN, out of 542 galaxies investigated. These fractions show that AGN are actually widely present in the local Universe, once the bar is sufficiently low that even very weak AGN can be detected.

In fact our tally of AGN in CALIFA galaxies is almost certainly still incomplete, because here we investigated only the central spectra of our galaxies. However, some objects may not display any significant emission from photoionized material in their centres due to obscuration, or if the material was blown away into the outer regions of the galaxy (Congiu et al., 2017; Stockton, Fu, and Canalizo, 2006; Morganti et al., 2007; Morganti et al., 2015) It might even happen that the central AGN has recently "turned off" (Shapovalova et al., 2009), in which case photoionized material can only be detected outside the central region (Keel et al., 2012; Keel et al., 2015). With the integral field spectroscopic coverage of the CALIFA data we will be able to investigate this possibility for the entire sample; this will be the topic of a another chapter. Further clues to possible AGN might come from the X-ray and radio domains. Only then will we be approaching a complete AGN census of our sample.

CHAPTER 3

Black hole mass scaling relations for type 1 AGN from CALIFA

ABSTRACT

We found that significant fraction of galaxies in the CALIFA sample host type 1 AGN. These AGN are extremely faint, with broad Hα luminosites $\sim 10^{39}$ erg s^{-1}, which makes them very hard to detect in optical domain. We estimated masses of central black holes of these type 1 low-luminosity AGN, using both virial assumption and $M_{BH} - \sigma_*$ correlation established for active galaxies. We obtained that the masses estimated using the virial assumption are on average for a factor ~ 10 smaller than the ones estimated from $M_{BH} - \sigma_*$ correlation, while the Eddington rations are for more than a factor of 10 larger. This would imply that either $M_{BH} - \sigma_*$ correlation or the virial assumption and virial scaling relationships break down at these extremely low luminosities, and therefore cannot be applied for black hole mass estimation of the local low-luminosity AGN. We discussed the likelihood of each scenario, and investigated how well our black hole mass estimates agree with previously established $M_{BH} - M_*$ correlations. Virial black hole masses seem to fall off of both $M_{BH} - \sigma_*$ and $M_{BH} - M_*$ correlations, implying that they are probably underestimated. The most probable scenario is that the virial scaling relationships are no longer linear in this low-luminosity regime. Detection of broad emission lines in these low-luminosity AGN implies that they are still able to form the broad line region, despite their extremely low Eddington ratios. According to this scenario, low-luminosity AGN in the local Universe still appear to be scaled-down version of luminous AGN at high redshifts, with certain modifications in structure of the central engine.

3.1 Introduction

Super Massive Black Holes (SMBHs), with masses between 10^6 and 10^9 $M_\odot$, reside in the centers of majority of massive galaxies. When the central SMBH is in its active phase, its gravitational pull of the surrounding material – accretion is considered to be the primary powering source of an Active Galactic Nucleus (AGN). Typical luminous AGN distinguish themselves from other galaxies by the presence of Broad Emission Lines (BELs) in their central spectra. These BELs have Full Widths at Half Maximum (FWHMs) in order of few thousands km s^{-1}. BEL components are formed in the Broad Line Region (BLR), which is located in vicinity of the central SMBH.

Filippenko (1989) and Ho (1996) were the first to point out that significant AGN fraction in our local Universe reaches even fainter luminosities than those of Seyferts (with the broad Hα luminosity $L_{H\alpha} < 10^{42}$ erg s^{-1}). But even still, detection of these Low-Luminosity AGN (LLAGN) is quite challenging due to their very weak emission lines, and absence of the characteristical power-law continuum. Host galaxy stellar light might then dominate the spectrum, and AGN contribution may be underestimated or completely omitted. Therefore, it is very important that the stellar component is properly subtracted and that the emission-line detection method is of high sensitivity.

Although AGN can be identified with multiple methods, our knowledge of black hole demographics still remains incomplete. First obstacle is that direct measurement of black hole masses is limited only to the closest luminous objects. The most accurate technique of active black hole mass estimation is the Reverberation Mapping (RM) of the BLR (Blandford and McKee, 1982; Koratkar and Gaskell, 1991; Peterson, 1993). RM method consists of measuring time lags between flux variations in continuum and BELs, that correspond to the light-travel time through the BLR, allowing us to estimate its size. Assuming virial equilibrium of the central source, black hole masses can be estimated from:

$$M_{BH} = f \, \frac{R_{BLR} \, v^2}{G} \tag{3.1}$$

where G is the gravitational constant, R_{BLR} is the size of the BLR, v is the gas velocity in the BLR usually represented by the width of broad Hβ line, expressed in km s^{-1}, and f is the virial scaling factor which depends on geometry, kinematics and inclination of the BLR. RM method is not applicable for large number of objects, since it requires long observational time, hence the black hole mass measurements are available only for ~ 50 objects.

On the other hand, Kaspi et al. (2000), Kaspi et al. (2005), and Bentz et al. (2006) found that there is a strong correlation between R_{BLR} and continuum luminosity of an AGN:

$$R_{BLR} \propto L^{\gamma} \tag{3.2}$$

where γ is a factor ~ 0.5. By introducing these assumptions to the virial theorem, it became possible to estimate black hole masses for large number of objects.

Dynamical studies of local galaxies showed that black hole masses in massive galaxies are tightly correlated with host galaxies' properties, such as bulge stellar velocity dispersion σ_* and bulge stellar mass M_{bulge} (Ferrarese and Merritt, 2000; Gebhardt et al., 2000a; Gebhardt et al., 2000b; Ferrarese et al., 2001; Merritt and Ferrarese, 2001; Tremaine et al., 2002; Onken et al., 2004; Gültekin et al., 2009; Kormendy and Ho, 2013; McConnell and Ma, 2013). Gebhardt et al. (2000b), Ferrarese

et al. (2001), and Onken et al. (2004) observed a consistent correlation between M_{BH} and σ_* of AGN. This further provided evidence that AGN and quiescence are just different phases in life cycle of a galaxy, where $M_{BH} - \sigma_*$ correlation is probably established during the AGN phase, in which SMBH accretion limits gas supply for building black hole and host galaxy mass simultaneously (Silk and Rees, 1998). Woo et al. (2010), Woo et al. (2013), and Shankar et al. (2016) showed that $M_{BH} - \sigma_*$ correlation is slightly different for active and quiescent galaxies, due to the selection biases introduced in dynamically measured black hole masses of quiescent galaxies. They provide more accurate $M_{BH} - \sigma_*$ relationships for AGN, which will be used for the purpose of this thesis.

The observed correlation between M_{BH} and σ_* implies the existence of close relationship in coevolution of SMBHs and their host galaxies. Therefore, AGN evolution over cosmic time is important, not only for understanding the accretion mechanism, but the evolution of host galaxies as well.

Beside bulge mass and stellar velocity dispersion, another parameter that correlates with M_{BH} is the total stellar mass of the host galaxy M_*, although many authors are still not convinced in the accuracy of this correlation. Magorrian et al. (1998) were the first to introduce the correlation between these two parameters, although they found very large scatter ($\sim$ 0.51 dex). Merritt and Ferrarese (2001), Marconi and Hunt (2003), Häring and Rix (2004), and Reines and Volonteri (2015) reestablished this relation with more accurate measurements, and found that the scatter is comparable to the one in M_{BH} - σ_*. Due to lack of bulge mass measurements, for the purpose of this chapter we used M_* and corresponding correlations with M_{BH}, and observed how well they represent our data.

Another fundamental characteristic of AGN, besides its black hole mass, is its accretion rate. Accretion rate is often represented by the Eddington ratio and defines the accretion power of an AGN:

$$\lambda = \frac{L_{bol}}{L_{Edd}} \tag{3.3}$$

where L_{bol} is bolometric and L_{Edd} Eddington luminosity of an AGN. The best way to estimate L_{bol} would be to measure it directly from AGN Spectral Energy Distribution (SED), since AGN emit their energy in very broad spectral range. In practice this is not possible, but AGN bolometric luminosity can be estimated from its optical luminosity by applying a certain correction factor (Ho, 2008). Eddington luminosity, or Eddington limit, is defined as the maximum luminosity that AGN with black hole mass M_{BH} can attain so that it remains in hydrostatic equilibrium, where gravitational force is balanced by radiation pressure. There is a range of up to three orders of magnitude in Eddington ratios for given SMBH mass M_{BH} (Woo and Urry, 2002).

Accretion rate shows us in which phase of activity a certain AGN is residing, providing us with information about the structure of the accretion disk and AGN itself. At high Eddington ratios, falling material around SMBH forms geometrically thin and optically thick accretion disk, BELs are evidently present in the spectrum, and the central source is considered to be type 1 AGN according to the unified AGN model. Low Eddington ratios, that are typical for LLAGN, change the structure of the accretion disk, and strong BELs can no longer be detected in the spectrum. As a consequence, M_{BH} is often difficult to estimate in LLAGN. It is usually accepted that below Eddington ratio of $\log(\lambda) \sim -3$ (Nicastro, 2000), central SMBH is considered to be inactive. This limit is still debatable, while with current surveys and fitting procedures, we are able to detect much weaker BELs than it was previously possible.

In Chapter 2 we showed that LLAGN fraction is even higher in the local Universe than what Filippenko (1989) and Ho (1996) estimated in their work. We reached even lower broad Hα luminosities, typically around 10^{39} erg s^{-1}, with some objects going all the way down to even $\sim 10^{38}$ erg s^{-1}. Such low-luminosity regime is out of domain of the virial scaling relationships that are established so far. Therefore, we wanted to investigate the validity of using these scaling relationships for these extreme LLAGN. Luminosities were calculated using the standard cosmological parametars with the following values: $H_0 = 70$ km s^{-2} Mpc^{-1}, $\Omega_M = 0.3$ and $\Omega_\Lambda = 0.7$.

This chapter is organized as follows: in Section 3.2 we briefly present the data sample and analysis that we performed, in Section 3.3 we describe and compare the methods that we used for black hole mass estimations of CALIFA type 1 AGN, in Section 3.4 we investigate the relationship between black hole mass estimations and total stellar masses of their host galaxies. Results are interpreted and discussed in Section 3.5, and, finally, in Section 3.6 we draw the final conclusions and summarize our work.

3.2 Data Sample and Analysis

3.2.1 Sample description

For the purpose of this work we used data from the Calar Alto Legacy Integral Field Area (CALIFA) survey (Sánchez et al., 2012; Walcher et al., 2014), whose observations were made with the Potsdam Multi Aperture Spectrograph (PMAS, Roth et al. (2005)), installed at 3.5m telescope at the Calar Alto Observatory. CALIFA is an Integral Field Spectroscopy (IFS) survey with large hexagonal Field of View (FoV) of $74'' \times 64''$, and sampling of $1'' \times 1''$ per spaxel. This allows us to study both integrated and spatially resolved properties of the sample galaxies. The survey targets galaxies in the nearby Universe, in redshift range $0.005 < z < 0.03$.

Data of each galaxy is stored within two datacubes, one for each spectral setup, a low resolution V500 ($3745 < \lambda < 7500$, R = 6 Å), and a medium resolution V1200 ($3650 < \lambda < 4840$, R = 2.3 Å) one. More detailed description of the data sample can be found in Chapter 2.2.1, as well as in the original CALIFA survey sample papers (Sánchez et al., 2012; Walcher et al., 2014; García-Benito et al., 2015; Sánchez et al., 2016).

We used V500 setup of Data Release 3 (DR3, Sánchez et al. (2016)), which consists of 542 galaxies. Since AGN are located exclusively in the centers of galaxies, we were only interested in the physical processes that take place in this region. Therefore we obtained observed flux densities from the central $3'' \times 3''$ regions of CALIFA datacubes, and estimated total flux density for each galaxy by summing flux densities in these 9 central spaxels. We considered only those spectra that have total central signal to noise ratio S/N > 3.

3.2.2 Spectral fitting

LLAGN have very weak emission lines, especially BELs, that are often masked by host-galaxy stellar light. In order to obtain pure emission line spectrum, it is important that the host galaxy's stellar contamination is properly subtracted. The detailed spectral fitting procedure is described in Chapter 2.2.2 and we will give just a brief summary of the fitting process here.

In order to subtract stellar component from our spectra, we used the pyPARADISE spectral fitting code (Husemann et al. (in prep.), Walcher et al. (2006) and Walcher et al. (2009)), which performs fitting of stellar kinematics and stellar populations in two iterative steps. As an output, the code produces a "model spectrum" that is the best representation of continuum and absorption from host galaxy's starlight. We obtained pure emission line spectrum of galaxy's central region by subtracting stellar component model from the original spectrum.

For emission line modeling we assumed that all Narrow Emission Lines (NELs) originate from the same region – the Narrow Line Region (NLR), and that Doppler motion of the gas around SMBH is dominant mechanism of line broadening. We assigned one Gaussian to fit each NEL, and allowed for a possibility that the Balmer lines, Hα and Hβ, may have broad components, which are then fitted with one additional Gaussian, each. We obtained emission line profiles of both narrow and broad (if present) Hydrogen lines, Hα and Hβ, and narrow-line profiles of [NII] $\lambda\lambda 6548, 6583$, [OIII] $\lambda\lambda 4959, 5007$, [SII] $\lambda\lambda 6717, 6731$ and [OI] $\lambda 6300$. All NELs were set to have same FWHMs, while FWHMs and central wavelengths of the broad lines were left as free parameters, allowing for different line widths and blue- or redshifts of the broad components.

In order to establish detection probability of the broad lines, we performed a test: we added broad Hα line to 100 pure NEL spectra from the sample. This way we created artificial spectra that contain broad Hα component, with different values of fluxes, FWHMs, and central wavelength shifts. We established the detection probability for each broad Hα line flux, FWHM and shift value by taking into account the frequency of how many times the reduced χ^2 was improved after the broad Hα component is added to the fit. Results of our test, as well as detailed description of the emission-line fitting procedure can be found in Chapter 2.2.3.

Galaxies in the CALIFA sample are already corrected for galactic extinction (Sánchez et al., 2012; Husemann et al., 2013). In order to correct obtained emission line fluxes for dust reddening caused by Earth's atmosphere, interstellar medium (ISM) and/or circumnuclear dust, we used the extinction curve from Gaskell and Benker (2007).

3.2.3 Stellar Velocity Dispersions

In order to estimate black hole masses using $M_{BH} - \sigma_*$ correlation, proper measurements of bulge stellar velocity dispersions σ_* of host galaxies are required. Obtaining σ_* is particularly challenging for AGN hosts, because the bright AGN emission dilutes stellar features in galaxy's center. This is not the case with LLAGN, which makes them very convenient for good estimation of σ_*. Méndez-Abreu et al. (2017) performed multi-component photometric decomposition of 404 CALIFA DR3 galaxies, including bulges, bars and disks. From their results we obtained the following bulge properties: effective radius r_{eff}, ellipse axis ratio q, and the position angle PA. With these parameters, we were able to define central ellipses that represent bulges of galaxies that have them as a component. We then binned the data of all spaxels within each ellipse, and obtained average bulge flux density. Finally, we used the pyPARADISE spectral fitting code in order to fit stellar kinematics of each bulge, which provided us with estimations of σ_*.

3.3 Black Hole mass estimation

We used BEL detection method described in Section 3.2.2 in order to separate type 1 AGN from other galaxies in the sample. Out of 483 CALIFA galaxies with detectable emission lines, 89 have broad Hα line present in their central spectra. These are all extremely faint objects, with broad Hα fluxes in range $(13.48 \times 10^{-17} - 26.14 \times 10^{-15})$ erg s^{-1} cm^{-2} Å^{-2}, with the mean value of 82.26×10^{-17} erg s^{-1} cm^{-2} Å^{-2}. On the other hand, FWHMs of these objects are comparable to the FWHMs of "typical" luminous type 1 AGN at high redshifts, occupying the range of values between 1000 km s^{-1} and 6000 km s^{-1}, with the average of 3000 km s^{-1}. We obtained broad Hα luminosities $L_{H\alpha}$ in range $(0.23 - 303.25) \times 10^{39}$ erg s^{-1}, with the average value of 7.21×10^{39} erg s^{-1}. Majority of objects from our sample have extremely low $L_{H\alpha}$, reaching below 10^{39} erg s^{-1}, with exception of Mrk 79 (UGC 03973), being the only relatively luminous type 1 AGN in our sample, with $L_{H\alpha} = 3.03 \times 10^{41}$ erg s^{-1}. The histograms representing broad Hα luminosities can be found on Figure 2.7 Chapter 2.3.1.

3.3.1 $M_{BH} - \sigma_*$ correlation

Tight correlation between black hole masses and bulge stellar velocity dispersions is of high importance for understanding the coevolution of SMBHs and their host galaxies through cosmic time. Establishing this relation is also very useful when M_{BH} cannot be measured directly, which is at higher redshifts or in LLAGN. In that case, black hole masses can be estimated, with high accuracy, from the correlation with bulge stellar velocity dispersions σ_*.

$M_{BH} - \sigma_*$ correlation was primarily established for quiescent galaxies whose M_{BH} were measured directly from stellar or gas kinematics (Ferrarese and Merritt, 2000; Gebhardt et al., 2000a; Gebhardt et al., 2000b; Ferrarese et al., 2001; Merritt and Ferrarese, 2001; Tremaine et al., 2002; Onken et al., 2004; Gültekin et al., 2009; Kormendy and Ho, 2013; McConnell and Ma, 2013). Strong radiation from luminous AGN often contaminates host galaxy's starlight, making σ_* very challenging to measure in these objects. For LLAGN, this is not the case, due to very weak AGN emission. This allows us to estimate host galaxy's properties without AGN contamination, which is important for establishing unbiased correlations between AGN and their hosts.

The assumption of consistent $M_{BH} - \sigma_*$ relationship for quiescent galaxies and AGN was a starting point in establishing the relationship for active galaxies (Gebhardt et al., 2000b; Ferrarese et al., 2001; Nelson et al., 2004). Woo et al. (2010), Greene and Ho (2006), and Xiao et al. (2011) found, on the other hand, somewhat shallower slope and lower normalization of $M_{BH} - \sigma_*$ for different samples of active galaxies. The observed mismatch between correlations for active and quiescent galaxies might be a consequence of biases introduced in sample selections, or it indicates an actual physical difference between AGN and quiescent galaxies, and cooevolution with their hosts.

Woo et al. (2013) and Shankar et al. (2016) showed that dynamically based $M_{BH} - \sigma_*$ correlations are biased towards more massive galaxies with larger σ_*, due to limiting telescope resolution to resolve smaller black hole sphere of influence. Therefore $M_{BH} - \sigma_*$ correlations predicted from dynamically based black hole masses would have higher normalization and would be steeper than those observed for AGN. They showed, using Monte Carlo simulations, that if we include the same bias in AGN samples, relationships between active and quiescent galaxies would be consistent.

For purpose of this research, we used the $M_{BH} - \sigma_*$ correlation established by Woo et al. (2013), for a sample of 25 reverberation-mapped AGN, with data obtained form Keck, Palomar and Lick Observatories. We chose this specific correlation as a black hole mass estimator because their AGN sample consists of nearby spirals, similar to ours. They provide the following equation for black hole mass estimation:

$$\log(\frac{M^{\sigma}_{BH}}{M_{\odot}}) = (7.31 \pm 0.15) + (3.46 \pm 0.61) \log(\frac{\sigma_*}{200 \text{ km s}^{-1}}) \tag{3.4}$$

with intrinsic scatter of $\epsilon_0 = 0.41 \pm 0.05$. The slope that they obtained is flatter than that of quiescent galaxies but is consistent with previous $M_{BH} - \sigma_*$ correlations established for AGN.

Using the method described in Section 3.2.3, we estimated bulge stellar velocity dispersions σ_* of 404 objects, of which 55 have detectable broad Hα component, and are therefore classified as type 1 AGN. Stellar velocity dispersions σ_* of CALIFA type 1 AGN are in range between 118 km s^{-1} and 397 km s^{-1}, with mean value of 212 km s^{-1}. We then applied Equation 3.4 in order to calculate black hole masses M^{σ}_{BH} of these objects. Black hole masses that we obtained have values between 3.3×10^6 $M_{\odot}$ and 2.2×10^8 $M_{\odot}$, with the average of 2.1×10^7 $M_{\odot}$. This result implies that black hole masses lay on the low end of $M_{BH} - \sigma_*$ correlation, which is expected for LLAGN at low z.

In order to estimate bolometric luminosity of an AGN (L_{bol}), we need luminosity measurements at all wavelengths, which is impossible to obtain for LLAGN. We, therefore, used the broad Hα luminosity $L_{H\alpha}$ as a proxy for L_{bol}. Using the correction factor of 9.26 from Richards et al. (2006a) and the relation:

$$L^{\sigma}_{bol} = 130 \, ^{\times 2.4}_{\div 2.4} \times L_{H\alpha} \tag{3.5}$$

from Stern et al. (2012), we obtained L^{σ}_{bol} in range $(3.5 \times 10^{40} - 3.9 \times 10^{43})$ erg s^{-1}, with the average value of 1.2×10^{42} erg s^{-1}. From estimated L_{bol} and $L_{Edd} = 1.25 \times 10^{38}$ $(\frac{M^{\sigma}_{BH}}{M_{\odot}})$ erg s^{-1} (computed for Thompson scattering opacity and pure hydrogen composition, Shankar, Weinberg, and Miralda-Escudé (2013)), we calculated Eddington ratios λ, using Equation 3.3. We obtained wide range of λ, occupying extremely low values $(4.1 \times 10^{-5} - 2.4 \times 10^{-3})$, with an exception of Mrk 79 that has $\lambda = 4.3 \times 10^{-2}$. All measurements are documented in Table A.3 in Appendix.We conclude that the LLAGN in the CALIFA sample occupy the low-mass and the extremely low-accretion rate end of AGN population.

In order to avoid any confusion, we referred to black hole masses, bolometric luminosities, and Eddington ratios estimated from the $M_{BH} - \sigma_*$ correlation established by Woo et al. (2013) as M^{σ}_{BH}, L^{σ}_{bol}, and λ^{σ}, and the ones estimated using the virial method as M^{vir}_{BH}, L^{vir}_{bol}, and λ^{vir}.

3.3.2 Virial Black Hole masses

Assumption that gas motion in the BLR is dominated by gravitational accretion onto the central SMBH enables us to estimate black hole masses using the virial theorem, defined by Equation 3.1 (Peterson and Wandel, 1999; Peterson and Wandel, 2000; Kollatschny, 2003; Peterson et al., 2004; Bentz et al., 2010). Velocity of the gas v in the BLR is usually estimated from FWHM of broad Hβ emission line.

Since changes in flux of BELs follow changes of flux in continuum, it is possible to estimate the size of BLR by measuring time lags between these flux variations. Measuring the actual lags can be time consuming and is possible only for the closest

luminous objects, therefore it is convenient to use some other, secondary mass indicator. The radius – luminosity relationship (Equation 3.2) describes the empirical correlation between BLR size and AGN continuum luminosity at 5100Å. Bentz et al. (2013) established radius – luminosity relationship for low-luminosity end, using RM measurements of 41 nearby AGN:

$$\log(\frac{R_{BLR}}{\text{lt-day}}) = 1.527^{+0.031}_{-0.031} + 0.533^{+0.035}_{-0.033} \log(\frac{L_{5100}}{10^{44}\ \text{erg s}^{-1}}) \tag{3.6}$$

where L_{5100} is AGN continuum luminosity at 5100Å.

The challenge with LLAGN is that their continuum and broad Hβ lines are very weak and, therefore hard, or even impossible, to detect. Greene and Ho (2005) showed that broad Hα luminosity $L_{H\alpha}$ and its FWHM can be used as proxies for L_{5100} and FWHM of Hβ line, respectively. These correlations allow us to estimate black hole masses relying only on the width and luminosity of broad Hα line.

From Greene and Ho (2005) we have:

$$L_{H\alpha} = (5.25 \pm 0.02) \times 10^{42}\ (\frac{L_{5100}}{10^{44}\ \text{erg s}^{-1}})^{(1.133\pm0.005)}\ \text{ergs s}^{-1} \tag{3.7}$$

and

$$FWHM_{H\beta} = (1.07 \pm 0.07) \times 10^{3}\ (\frac{FWHM_{H\alpha}}{10^{3}\ \text{km s}^{-1}})^{(1.03\pm0.03)}\ \text{km s}^{-1} \tag{3.8}$$

which gives us the estimates of L_{5100} and $FWHM_{H\beta}$.

It is worth mentioning that Greene and Ho (2005) used total Hα luminosity in Equation 3.7. The reason for this is that the narrow Hα luminosities from their sample account for only 7% of the total Hα luminosities, and they obtained consistent relationships when they used both broad and total $L_{H\alpha}$. In our case, broad luminosities are much weaker, $\sim$ 50% of the total, therefore we used only the broad component of $L_{H\alpha}$ in Equation 3.7. This is justified by the observation that only BLR traces AGN continuum.

Another parameter that contributes to M_{BH} calculation is the virial factor f. The f factor accounts for geometry, kinematics and inclination of the BLR, and can be a source of the great uncertainty in black hole mass estimation, since these properties are unknown. The virial factor may also vary with each individual object, but that can only be determined if we have some other precise method of estimating M_{BH}. Hence it is much easier and more practical to compute the mean value of f, by scaling RM measurements to $M_{BH} - \sigma_*$ correlation of quiescent galaxies (Onken et al., 2004; Woo et al., 2010; Graham et al., 2011; Park et al., 2012). This procedure, of course, assumes that AGN follow the same $M_{BH} - \sigma_*$ correlation as quiescent galaxies, which is not fully accurate, as discussed in the previous section. In order to estimate black hole masses, we used the most recent value of virial factor $\log(f) = 0.18$, calculated by Grier et al. (2017), using RM measurements of 9 AGN.

Combining equations 3.6 and 3.7, we estimated R_{BLR}, and calculated BLR gas velocity v from Equation 3.8. Including the virial factor of $f = 1.51$ in Equation 3.1, we estimated virial black hole masses M^{vir}_{BH} for all 89 type 1 AGN from the CALIFA sample. These virial black hole masses are in range $(3.5 \times 10^5 - 2.4 \times 10^7)\ M_\odot$, having mean value of $4.3 \times 10^6\ M_\odot$.

In order to estimate L^{vir}_{bol}, we again used broad Hα line as a proxy for AGN luminosity, only this time, we used Equation 3.7 to connect broad Hα and continuum

L_{5100} luminosities, in order to preserve consistency with virial black hole mass estimations. We obtained L_{bol}^{vir} values in range $(1.6 \times 10^{41} - 7.9 \times 10^{43})$ erg s^{-1}, with mean value of 2.6×10^{42} erg s^{-1}. For virial Eddington ratios λ^{vir} we obtained values $5.1 \times 10^{-4} - 2.9 \times 10^{-2}$, with the average of 6.2×10^{-3}.

3.3.3 Comparison between virial black hole masses and the ones estimated from $M_{BH} - \sigma_*$

Using two distinctive methods of black hole mass estimation, we obtained significantly different results. As a next step, we analyzed which of these two methods is more reliable for black hole mass estimation. On Figure 3.1 we compared the distributions of black hole masses (left) and Eddington ratios (right) estimated from both virial method and $M_{BH} - \sigma_*$ correlation of Woo et al. (2013) (further addressed as W13). M_{BH}^{σ} are on average 9 times larger than M_{BH}^{vir}, reaching a factor > 30 for more massive systems.

On the other side, Eddington ratios estimated using virial method λ^{vir} are on average higher than those estimated from $M_{BH} - -\sigma_*$ (λ^{σ}) for a factor of 12 (Figure 3.1 right), which is consistent with the Bondi accretion, where $\lambda \propto 1/M_{BH}$. Virial Eddington ratios λ^{vir} are still in, what is considered, mildly active accretion phase, while λ^{σ} reach values as low as $\log(\lambda) = -4.5$, but majority of objects have values above $\log(\lambda) = -3.75$.

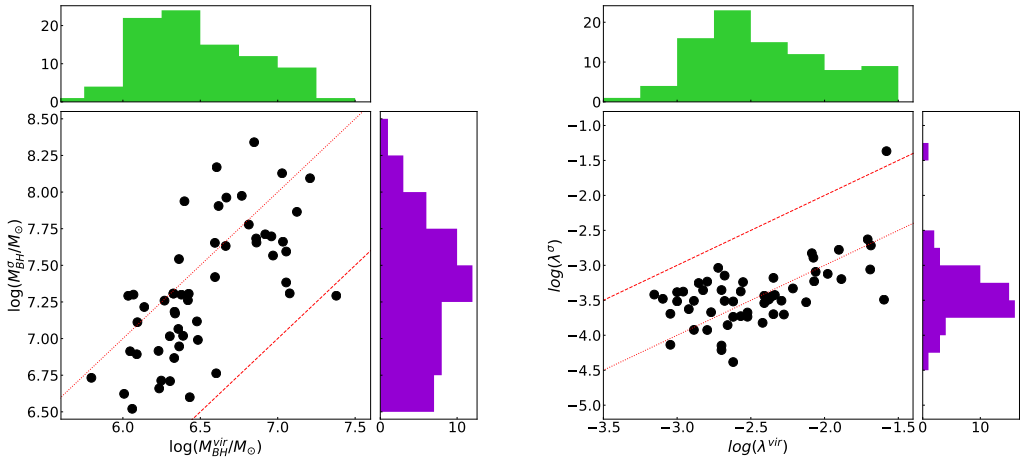

FIGURE 3.1: Left: Comparison between virial black hole masses and those estimated from the $M_{BH} - \sigma_*$ correlation of Woo et al. (2013), and their respective distributions. Green histogram represents M_{BH}^{vir}, while the purple one represents M_{BH}^{σ}. Dashed line is 1 – 1 correlation between M_{BH}^{vir} and M_{BH}^{σ}, while dotted line is the 1 – 10 correlation. M_{BH}^{σ} are on average larger than M_{BH}^{vir} for a factor of 9, reaching a factor of 30 for more massive systems. Right: Comparison between respective Eddington ratios, λ^{vir} and λ^{σ}. In this case dotted line represents 10 – 1 correlation between λ^{vir} and λ^{σ}. λ^{vir} are on average larger than λ^{σ} for a factor of 12.

On Figure 3.2 we wanted to show where virial black hole masses M_{BH}^{vir} fall on some previously established $M_{BH} - \sigma_*$ correlations. We included both $M_{BH} - \sigma_*$ correlation lines from W13 and Shankar et al. (2016) (in further read S16). One can clearly see that discrepancy is larger for objects with larger σ_*. Few objects with the lowest σ_* are located close, but still below, W13 line, while all of them are extremely

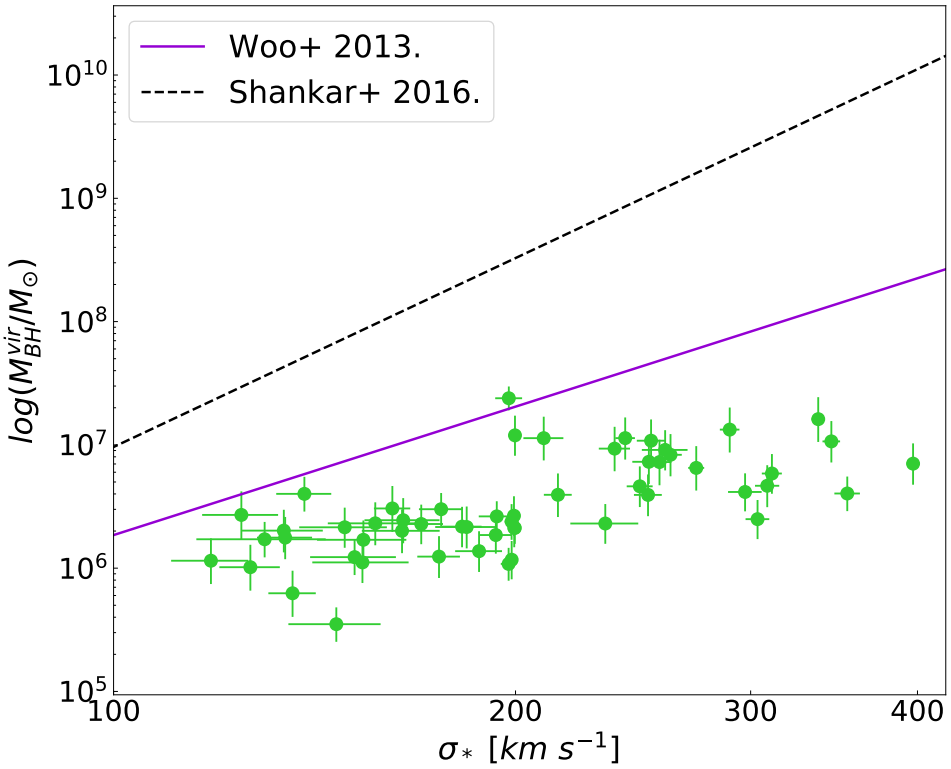

FIGURE 3.2: Virial black hole mass estimates M_{BH}^{vir} (green dots) plotted on the $M_{BH} - \sigma_*$ plane. The purple line is the correlation from Woo et al. (2013) that we used to estimate M_{BH}^{σ}, while the dashed black line is the intrinsic $M_{BH} - \sigma_*$ correlation from Shankar et al. (2016). Majority of M_{BH}^{vir} lie below the two correlation lines, implying underestimated M_{BH}^{vir} (if we assume that $M_{BH} - \sigma_*$ is reliable black hole mass estimator for LLAGN).

far from S16 intrinsic line. The only object that is located slightly above the relation of W13 is Mrk 79. Mrk 79 even has a higher black hole mass and L_{bol} estimated from virial method than from $M_{BH} - \sigma_*$ of W13. Kaspi et al. (2000) obtained RM measurements for this object and reported $M_{BH} = 7.2 \times 10^7\ M_\odot$ and $\log(L_{bol}) = 44.6$. Using the W13 relation we obtained somewhat lower black hole mass and bolometric luminosity ($M_{BH}^{\sigma} = 2 \times 10^7\ M_\odot$, $\log(L_{bol}) = 43.6$), while virial estimation gave $M_{BH}^{vir} = 2.4 \times 10^7\ M_\odot$ and $\log(L_{bol}) = 43.9$. If we use the S16 line, we obtain black hole mass of $5.9 \times 10^7\ M_\odot$, which is closer to the RM value. Still, the S16 line is established for elliptical systems, which are minority in our LLAGN sample. It is also important to mention that RM measurements are slightly biased against LLAGN (Woo et al., 2013), therefore we do not have a clear picture of the exact situation in this regime.

From obtained results, we can conclude that M_{BH}^{vir} are underestimated, according to predictions from $M_{BH} - \sigma_*$ correlations. This implies that we trust that $M_{BH} - \sigma_*$ correlation still holds in such low-luminosity regime. This will be discussed further in Section 3.5.

We wanted to investigate whether the black hole mass ratio $M_{BH}^{\sigma} / M_{BH}^{vir}$ somehow scales with λ^{σ} or λ^{vir}. Due to similarity of results for λ^{σ} and λ^{vir}, we will only discuss

λ^σ, in order to avoid unnecessary repeating. On Figure 3.3 we plotted $M^\sigma_{BH}/M^{vir}_{BH}$ over λ^σ (black dots) and noticed that the area covering low λ^σ ($\log(\lambda^\sigma) < -3.6$) and high mass ratio ($M^\sigma_{BH}/M^{vir}_{BH} > 14$) remains blank (no black dots). In order to establish whether this is due to selection effects or perhaps lack of objects in this area has actual physical meaning, we designed a test that will show us where would the hypothetical objects with low detection probability be located on this diagram. We divided the $M^\sigma_{BH}/M^{vir}_{BH} - \lambda^\sigma$ plane into 4 different areas, and analized FWHMs and broad Hα luminoisities of objects falling into these 4 quadrants. We found that objects with extremely low λ^σ ($\log(\lambda^\sigma) < -3.6$) and smaller discrepancy between black hole masses estimated from virial method and $M_{BH} - \sigma_*$ correlation ($M^\sigma_{BH}/M^{vir}_{BH} < 14$), have the lowest broad Hα luminosities (2.7×10^{38} erg s^{-1} $< L_{H\alpha} < 1.0 \times 10^{39}$ erg s^{-1}). These objects are located in the bottom left quadrant of the diagram. On the other hand, objects located in the top right quadrant of the diagram, with large discrepancy between black hole masses ($M^\sigma_{BH}/M^{vir}_{BH} > 14$) and $\log(\lambda^\sigma) > -3.6$, have the lowest $FWHM_{H\alpha}$ in the sample ($FWHM_{H\alpha} \sim 1000 - 2000$ km s^{-1}). Our detection probability (Chapter 2.2.3) is higher than 50% for luminosities $L_{H\alpha} > 2 \times 10^{39}$ erg s^{-1} and higher than 80% for $FWHM_{H\alpha} > 1000$ km s^{-1}. We then selected objects with the lowest FWHMs and decreased their luminosities $L_{H\alpha}$ for 50%, so that they fall in the range 1.4×10^{38} erg s^{-1} $< L_{H\alpha} < 5.2 \times 10^{38}$ erg s^{-1}, and recalculated virial black hole masses of these hypothesized objects. What we obtained is that these objects have high $M^\sigma_{BH}/M^{vir}_{BH}$ and low λ^σ, which would place them in the blank area of the $M^\sigma_{BH}/M^{vir}_{BH} - \lambda^\sigma$ diagram. These hypothesized objects are represented with cyan stars on Figure 3.3. This quick test showed us that there is no physical reason why we did not observe any objects with extremely low Eddington ratios and high black hole mass discrepancy, since the lack thereof is only due to the selection effects. These objects would have broad Hα fluxes $f_{H\alpha}$ in range $(7-22) \times 10^{-18}$ erg s^{-1} cm^{-2} Å^{-2}, which is between 10% and 50% (20% on average) detection probability of our emission-line fitting code.

3.4 Relationship between black hole masses and total galaxy stellar masses

In order to investigate connection between AGN and their host galaxies beyond the bulge region, we investigated how well our black hole mass estimates fit on the previously established correlations between M_{BH} and total galaxy's stellar mass M_*. These correlations may provide further information about the coevolution of AGN and their hosts.

Total stellar masses were calculated by the CALIFA collaboration (Walcher et al., 2014) from Sloan Digital Sky Survey (SDSS) ugriz growth curve magnitudes. The M_* estimation method used the Bruzual and Charlot (2003) models with a Chabrier (2003) Initial Mass Function (IMF), where possible bursts and different amounts of dust extinction were accounted.

We found that type 1 AGN from CALIFA are hosted by the most massive galaxies in the sample $(10^{10.2} - 10^{11.9})$ $M_\odot$, $M_* \approx 10^{11}$ $M_\odot$ on average. On the Figure 3.4 we present the link between Hubble types of type 1 AGN hosts from CALIFA, and their total stellar masses. As we can see from the figure, these objects cover wide range of morphological classes, but majority of them are distributed between S0 and Sbc Hubble types. This was our motive to use W13 $M_{BH} - \sigma_*$ correlation for black hole mass estimations, since their sample consists mainly of spirals.

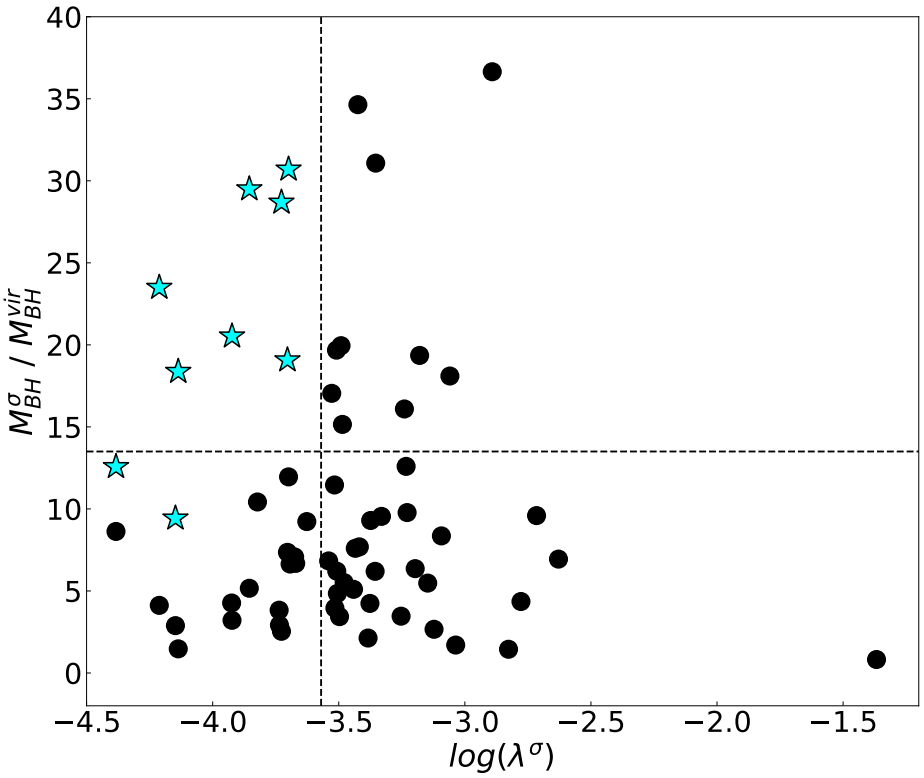

FIGURE 3.3: Graphical representation of type 1 LLAGN selection effect on the $M^{\sigma}_{BH}/M^{vir}_{BH} - \lambda^{\sigma}$ plane. Black dots correspond to BH mass and Eddington ratio estimates of the CALIFA AGN. Objects in the top bottom left quadrant have the lowest broad Hα FWHMs in the sample, while the objects in the top right quadrant have the lowest broad Hα luminosities (below 50% detection probability). We decreased $L_{H\alpha}$ of the objects in the bottom left area for 50% and calculated the hypothetical virial black hole masses (M^{vir}_{BH}) of these objects. The test objects are marked with cyan stars and they fill in the blank area of the $M^{\sigma}_{BH}/M^{vir}_{BH} - \lambda^{\sigma}$ diagram, implying that we do not have data points in this region due to the inability to detect such faint objects, and not for any particular physical reason.

Reines and Volonteri (2015) (further RV15) established the correlation between black hole and total stellar masses of their hosts, for the sample of 341 nearby ($z < 0.055$) galaxies. Their sample includes type 1 AGN, dynamically measured black hole masses, dwarfs and reverberation-mapped AGN. Black hole masses of type 1 AGN were estimated using the virial assumption. They calculated M_* using the procedure from Zibetti, Charlot, and Rix (2009), where total stellar masses were derived from color dependant mass-to-light ratios, which is the method used for M_* estimations at higher redshifts.

In order to investigate whether there may be some discrepancy between Zibetti, Charlot, and Rix (2009) total stellar mass estimation method used by RV15 and ours, we recalculated total stellar masses of the CALIFA galaxy sample, following the procedure described in RV15. We showed on Figure 3.5 that the total stellar masses estimated using the RV15 recipe and the ones estimated by the CALIFA collaboration correlate well with each other. Therefore, any source of discrepancy between black hole mass estimates and $M_{BH} - M_*$ relationships, if present, cannot be due to

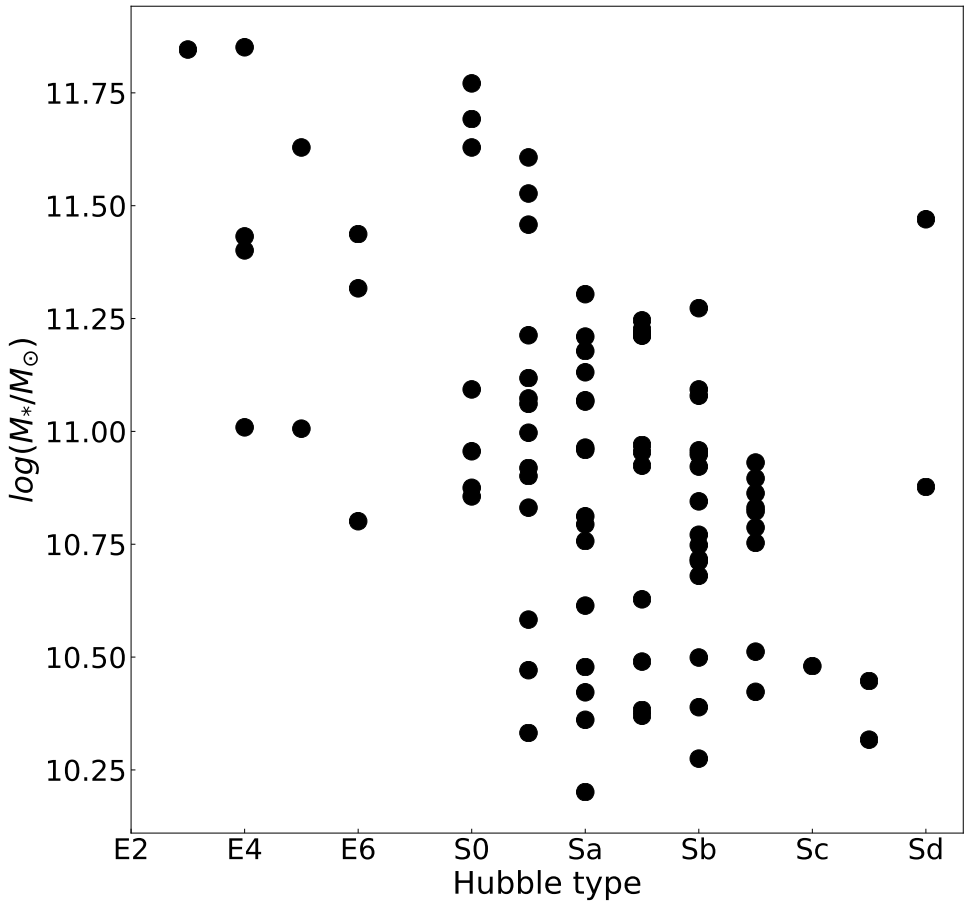

FIGURE 3.4: Connection between total host galaxies' stellar masses M_* and Hubble types of galaxies hosting type 1 LLAGN in CALIFA. Our type 1 AGN are majorly located in spiral galaxies between morphological classes S0 and Sbc.

different methods of estimations of total stellar masses.

S16 also established the, so-called, "intrinsic" $M_{BH} - M_*$ correlation for the sample of local ($0.05 < z < 0.2$) early-type galaxies selected from the SDSS DR7 (Abazajian et al., 2009), and 5 different black hole samples with dynamical black hole mass measurements. They imply, similar to previous discussion about $M_{BH} - \sigma_*$ correlation, that the dynamically measured black hole masses are biased towards galaxies with larger σ_*, therefore, towards the more massive ones. This provides higher normalization factor than what is observed for SDSS galaxies in their sample. S16 states that the bias is much stronger in $M_{BH} - M_*$, than in $M_{BH} - \sigma_*$ correlation. From $\sigma_* - M_*$ and $M_{BH} - \sigma_*$ correlations, they established the intrinsic $M_{BH} - M_*$ correlation that has a slight curvature. They claim that the curvature in $M_{BH} - M_*$ is a consequence of the curvature in $\sigma_* - M_*$ relation, which is due to galaxy formation physics, and does not imply anything fundamental about black hole formation (Shankar et al., 2016; Fontanot, Monaco, and Shankar, 2015).

On Figure 3.6 we showed where our M^{σ}_{BH} measurements are located compared to the $M_{BH} - M_*$ correlations established by RV15 and S16. The data points were

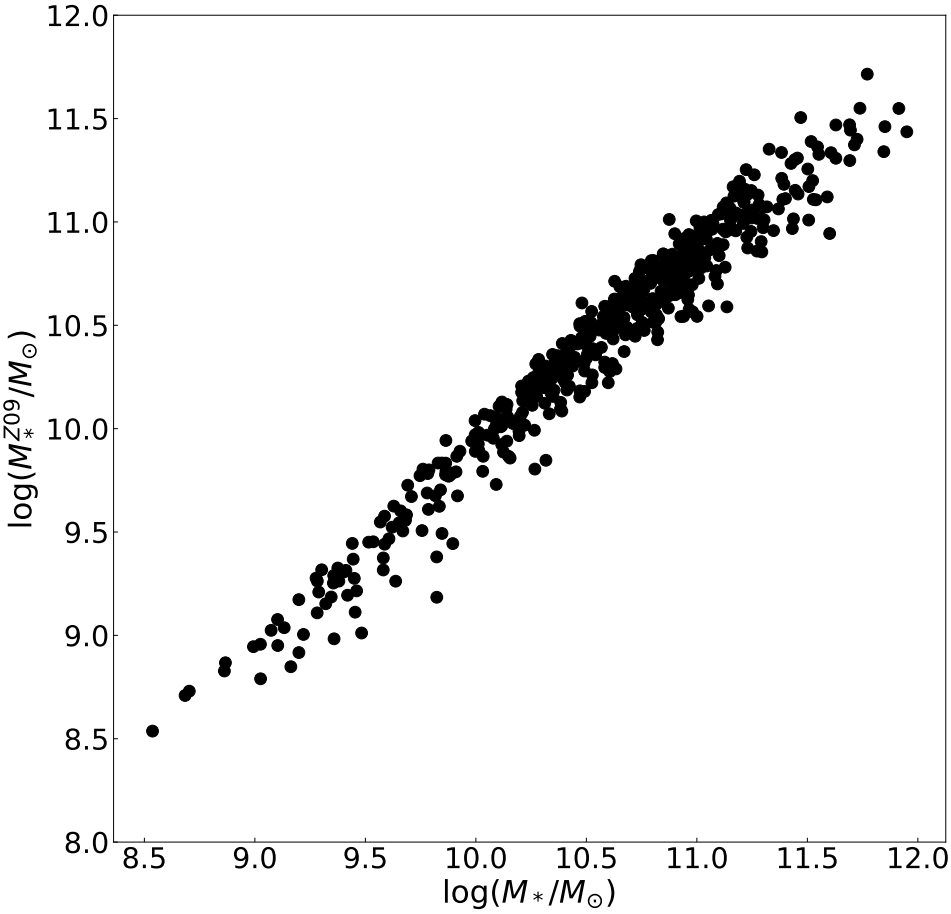

FIGURE 3.5: Correlation between total stellar masses estimated by the CALIFA collaboration M_* and the ones estimated using the recipe from Zibetti, Charlot, and Rix (2009) (M_*^{Z09}). Since the correlation is strong, we conclude that any source of discrepancy between black hole mass estimations and $M_{BH} - M_*$ correlations is not due to different methods of M_* estimations.

color-coded for Eddington ratios λ^σ, where circles represent AGN located in spiral galaxies, and squares the ones located in elliptical galaxies. It is clear that ellipticals host the most massive black holes in the sample. We can also see that there is a slight correlation with λ^σ, corresponding to Bondi accretion model ($\lambda \propto 1/M_{BH}$). We noticed that the objects with the lowest Eddington ratios ($\log(\lambda^\sigma) < -3$) correlate very well with M_{BH}^σ and M_* (yellow to green). On the other hand, the objects with higher λ^σ ($\log(\lambda^\sigma) > -3$) are distributed over almost the entire range of M_{BH} and M_* values (all shades of blue). This is not surprising, considering the fact that one Eddington ratio can cover wide range of black hole masses. Still it is an interesting observation that there is a stronger correlation between black hole and total stellar masses, on one side, and Eddington ratios on the other, in regime where $\lambda^\sigma < 10^{-3}$. This implies that only low-mass SMBHs accrete at these extremely low Eddington ratios. According to the literature (Nicastro, 2000) such low accretion stages imply that black holes are no longer in their active phase. Our results actually point out

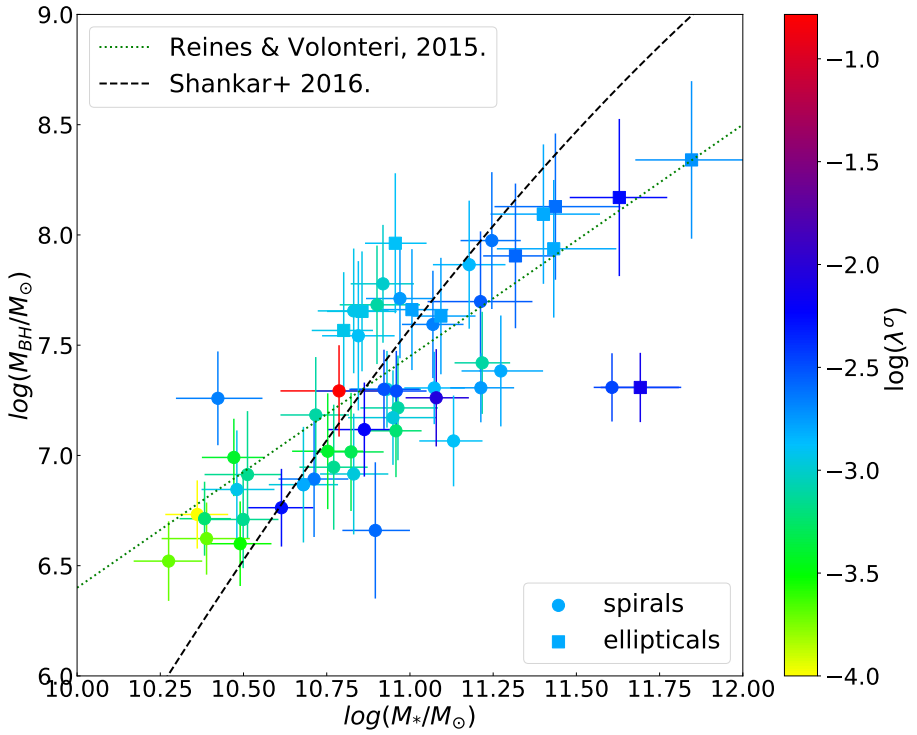

FIGURE 3.6: Distribution of the CALIFA type 1 AGN black hole masses, calculated from the $M_{BH} - \sigma_*$ correlation of Woo et al. (2013). Green dotted line was established by Reines and Volonteri (2015) for a sample of local type 1 AGN, whose black hole masses were estimated using the virial assumption, while the black dashed line is from Shankar et al. (2016), established for a sample of local SDSS galaxies. The data points represent our black hole mass measurements, color-coded for Eddington ratios λ^σ, where circles represent AGN located in spiral galaxies, and squares the ones located in elliptical galaxies. We can see strong correlation for lower Eddington ratios ($\log(\lambda^\sigma) < -3$), while in the range of $\log(\lambda^\sigma) > -3$, one value of λ^σ spreads over a wide range of M^σ_{BH} and M_*.

that this threshold of $\log(\lambda^\sigma) \sim -3$ for black hole activity should be lowered, since it implies that BLR cannot be seen in these objects, which is definitely not the case in our observations. This will be discussed in detail in the next section.

Our M^σ_{BH} measurements fit perfectly on the $M_{BH} - M_*$ correlation of RV15, and have a slightly flatter slope than the $M_{BH} - M_*$ correlation of S16. Our results are in high agreement with the unbiased $M_{BH} - M_*$ correlations of the local galaxies, suggesting that the $M_{BH} - \sigma_*$ relation of W13 can be used a reliable black hole mass estimator of nearby type 1 LLAGN.

RV15 also noticed the difference between slopes of ellipticals and spirals, which we do not observe in our data. This may come from the difference in sample sizes, since we have only 12 type 1 AGN that are classified as ellipticals, which is statistically less significant than the number of data points from RV15.

It is interesting to note that our M^{vir}_{BH} estimates lay significantly below the $M_{BH} - M_*$ correlation of RV15 (Figure 3.7), even though this specific correlation was established for the sample of viral black hole masses. We can also notice that the slope

of M_{BH}^{vir} distribution on the $M_{BH} - M_*$ plane is slightly shallower than both RV15 and S16 correlation lines, and our measurements of M_{BH}^{σ}. This result indicates that M_{BH}^{vir} may be underestimated for an order of magnitude, or even more, for ellipticals, which also agrees with $M_{BH}^{\sigma}/M_{BH}^{vir}$ ratios that we estimated in Section 3.3.3.

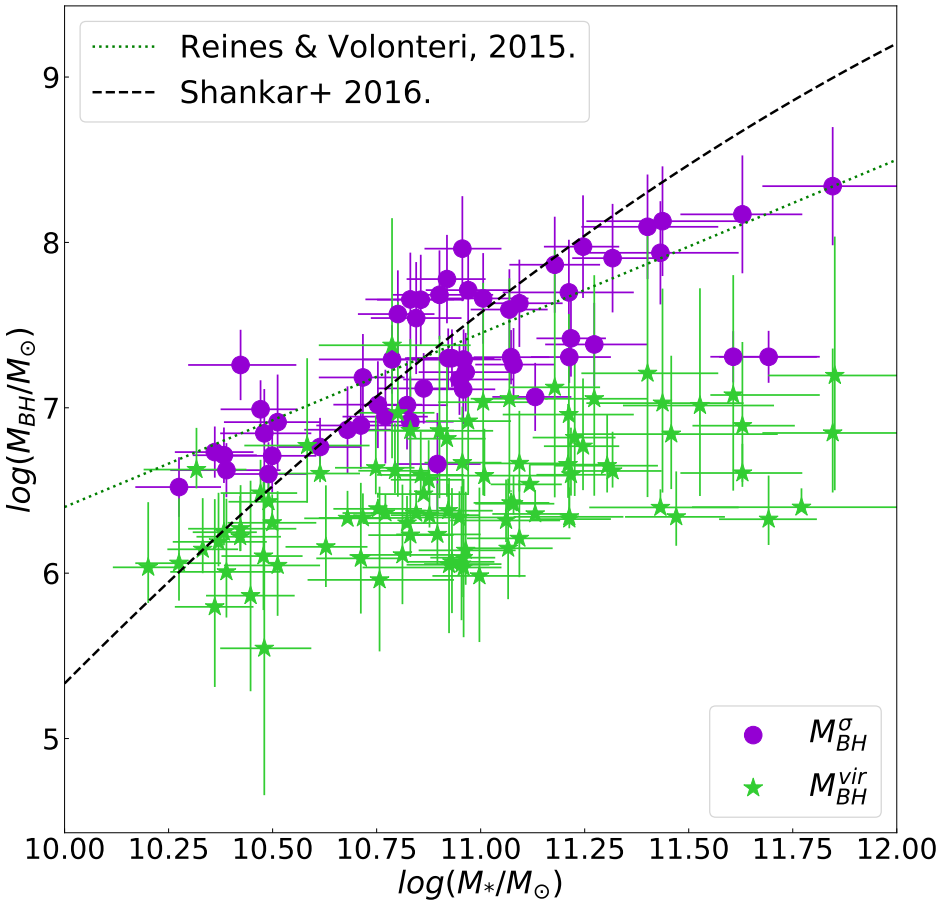

FIGURE 3.7: Distribution of virial black hole masses M_{BH}^{vir} (green stars) and those estimated using the $M_{BH} - \sigma_*$ correlation of Woo et al. (2013) (purple dots), on $M_{BH} - M_*$ plane. We can see that M_{BH}^{vir} lay significantly below (order of magnitude on average) the correlation lines of Reines and Volonteri (2015) and Shankar et al. (2016), and that they have a shallower slope compared to M_{BH}^{σ} distribution on $M_{BH} - M_*$ diagram.

3.5 Discussion

As we showed in Section 3.3.3, black hole masses estimated from the $M_{BH} - \sigma_*$ correlation and the ones estimated from virial assumption are inconsistent with each other. Here we will discuss reliability of the methods that we used and try to offer solutions for the problem of estimating black hole masses in nearby LLAGN.

$M_{BH} - \sigma_*$ correlation is considered to be one of the most reliable black hole mass estimators, since it was established for both quiescent and active galaxies in various redshift ranges. On the other hand, virial method is often used as the most accurate black hole mass estimation technique for nearby AGN. Many authors (Greene and Ho, 2005; Greene and Ho, 2007; Zhang, Dultzin-Hacyan, and Wang, 2007; Woo et al., 2015; Eun, Woo, and Bae, 2017) used virial assumption in order to estimate black hole masses of local LLAGN. However, previous research in this field was done in higher luminosity regime, with $L_{H\alpha} \sim 10^{40}$ erg s^{-1}, than the one that we reached in our work. Our broad Hα luminosities are of order $\sim (10^{38} - 10^{39})$ erg s^{-1}, the regime that remained unexplored so far. Do the established scaling relationships between continuum luminosity and BLR size, or continuum and broad line luminosities still hold in this low-luminosity regime? Or maybe $M_{BH} - \sigma_*$ correlation cannot be applied on such faint sources? In the worse case scenario, can we be sure that the BELs that we detected are actually representing gas motion in the BLR? Could they be an indication of some other line broadening mechanism, or even source of an error?

Results that we obtained could be interpreted with three possible scenarios:

1. We didn't actually detect the BLR feature, rather this is a fitting error or BELs that we detected are produced by some other mechanism, and not by accretion onto the central SMBH

2. Scaling relationships and virial assumption are still valid at extremely low luminosities $\rightarrow$ $M_{BH} - \sigma_*$ correlation breaks down

3. $M_{BH} - \sigma_*$ correlation is reliable black hole mass estimator for nearby low-luminosity AGN $\rightarrow$ virial scaling relationships break down

3.5.1 First scenario: Broad emission lines that we detected are not produced in the broad line region

Let's start with the first scenario where there is still a possibility that the BELs that we detected are not actually a product of the accretion of the material onto the central SMBH, or that the fitting procedure was not precise enough, therefore the detected broad line features are actually not real. This is the most unlikely scenario, because we have solid evidence that these BELs are actually coming from SMBH accretion. This would imply that FWHMs of our LLAGN are underestimated, which is highly unlikely, since our detection probability of FWHMs in range between 1000 km s^{-1} 6000 km s^{-1} is larger than 80%.

One of commonly used methods to distinguish between different types of emission line galaxies are the well known emission-line diagnostic diagrams (Baldwin, Phillips, and Terlevich, 1981; Osterbrock and Pogge, 1985; Veilleux and Osterbrock, 1987; Kewley et al., 2001; Kauffmann et al., 2003; Kewley et al., 2006). This method uses two narrow emission line ratios in order to separate star-forming galaxies from Seyfert 2 AGN, and LINERs. On Figure 2.6 in Chapter 2.3.1 we marked the objects in which we detected broad Hα lines on the diagnostic diagrams, and observed an interesting result, which is that all of them are located in the AGN (Seyfert 2 + LINER)

region on the [OIII]/Hβ over [NII]/Hα diagram. If these BELs are not the product of central SMBH accretion, these broad-line objects would be distributed all over the diagnostic diagrams, without any preferred direction. Some of them even have confirmed counterparts in Radio and X-ray domains, which is the subject of Chapter 5.

We also wanted to compare widths of our LLAGN to the widths of typical luminous type 1 AGN. For that purpose we plotted the distribution of the FWHMs that we obtain over the distribution of FWHMs from Hao et al. (2005a), normalized for the same number of objects (Fig. 11 in Jonić et al. *in preparation*). Hao et al. (2005a) obtained this distribution for a sample $\sim$ 1300 AGN selected from SDSS catalogue. We can notice that our LLAGN width distribution clearly resembles the one of the "genuine" AGN. This is further proof that the BELs that we detected are in fact, an actual representation of the BLR in these objects. This would imply that BLR exists even in this extremely low luminosity and low Eddington ratio regime, which would then bring further questions about the limiting accretion rate. If BLR is accretion driven, then this threshold value of $\log(\lambda) \sim -3$ cannot be used as an indication of activity of the central SMBH.

3.5.2 Second scenario: $M_{BH} - \sigma_*$ correlation breaks down for local type 1 low-luminosity AGN

If we consider the second scenario, and assume that virial black hole masses that we obtained are trustworthy, this would imply that $M_{BH} - \sigma_*$ correlations established so far, break down after a certain point and cannot be applied on nearby LLAGN from our sample. This will result in scenario where we have relatively low black hole masses in nearby Universe, but unlike previous studies (Greene and Ho, 2007; Ho, 2008) that showed that these black holes are hosted by low massive galaxies, our LLAGN are located in high-mass systems.

Zhang, Dultzin-Hacyan, and Wang (2007) also calculated smaller virial black hole masses of the Palomar survey LLAGN, than what is predicted by $M_{BH} - \sigma_*$ correlations. They concluded that this offset of virial black hole masses from $M_{BH} - \sigma_*$ is due to larger BLR of LLAGN. It is also possible that FWHMs of broad Hα lines were systematically underestimated (Ho and Kim, 2016).

Nicastro (2000) proposed a scenario where the BLR is produced by accretion disk wind, that is formed at the critical radius in the transition region between gas and radiation pressure dominated disk. At high accretion rates, the accretion flow forms geometrically thin and optically thick accretion disk (Shakura and Sunyaev, 1973) that is typical for AGN with high luminosities. Low Eddington ratios, that are typical for LLAGN, introduce certain modifications to the accretion disk structure. As λ decreases, the transition region between gas and radiation pressure dominated disk region shrinks, and below the certain point, the critical radius becomes smaller than the innermost stable orbit. For Eddington ratios below 10^{-3}, optically thick and geometrically thin accretion disk transforms into 3-component structure: an inner optically thick disk, a truncated outer geometrically thin disk, and a jet or an outflow. The inner region of the accretion disk truncates (Shakura and Sunyaev, 1976; Esin, McClintock, and Narayan, 1997; Ruan et al., 2019) and forms a quasi-spherical radiatively inefficient accretion flow (RIAF, Quataert (2003)) that is advection dominated (Narayan and Yi, 1994). These accretion flows are radiatively inefficient due to their extremely low densities, at which the radiative processes are much weaker than the energy dissipation.

The existence of the outer truncated thin disk may possibly explain the SED of LLAGN (Ho, 2008). The big blue bump, characteristical for luminous AGN, is evidently absent from the spectra of LLAGN. Instead, there is a peak in the mid-IR part of the LLAGN spectra, forming the so-called big red bump (Lawrence et al., 1985; Willner et al., 1985; Chen and Halpern, 1989; Willner et al., 2004; Bendo et al., 2006; Gu et al., 2007). These changes result in SED of LLAGN to appear shallow in the optical and UV parts, lacking the typical power-law continuum feature. The shift from blue to the red bump may be explained by the cool thermal outer disk emission (Lawrence, 2005).

The last feature of the modified accretion disk – jets or outflows can be confirmed by looking at the images from radio observations. LLAGN are considered to be more radio loud than typical broad-line AGN (Trump et al., 2011). However, this topic is beyond the scoop of this chapter.

The 3-component accretion disk model suggests that the critical radius is located within the RIAF, from which point the disk wind cannot be generated, and therefore the classical BLR cannot be formed. Rather, these low-Eddington ratio LLAGN would have the broadest possible emission lines, that are hidden in the optical spectra (Laor, 2003). Since, according to this model, the BELs disappear for Eddington ratios $\lambda < 10^{-3}$, it would indicate that the black hole mass estimates from the $M_{BH} - \sigma_*$ of W13 would imply inactive black holes, since the BELs that we detected could not be formed in the BLR. Similar model of BLR formation is proposed by Laor (2003), except that in this model, FWHMs of broad lines are the parameter responsible for the correlation between radius of BLR and AGN luminosity, not the accretion rate, as in Nicastro (2000) model.

An interesting discovery of our work is that both virial theorem and $M_{BH} - \sigma_*$ correlation predict AGN with extremely low Eddington ratios. This would imply that local LLAGN accrete at very low level, especially if we consider the black holes from $M_{BH} - \sigma_*$, where λ_σ lie significantly below the threshold value of 10^{-3}. This finding goes in favor of the second scenario. If we were able to detect an actual BLR, then the Eddington ratios of these AGN should be higher than 10^{-3}, according to the models. Virial black hole masses still accrete at sub-Eddington ratios, but majority of them are slightly above the limit. If we assume that LLAGN obey the virial assumption, their black hole mass depends on BLR velocity and its luminosity. If velocities are underestimated, black hole masses would be underestimated as well.

Kormendy and Ho (2013) concluded that rapid SMBH growth by radioactively efficient accretion took place at higher z, in massive galaxies that are majorly quenched today. They suggest that local SMBHs grow their masses by secular processes only, which are not enough to keep black holes coevolving with their hosts. This would imply that local LLAGN are not coevolving with their host galaxies. Still, the obvious correlations between both M_{BH}^{σ} and M_{BH}^{vir} with σ_* and M_* prove otherwise. Nonexistent coevolution may be the case in low-mass galaxies, but AGN hosts from our sample are relatively massive systems, whose total stellar masses correlate well with central SMBH masses. This implies that the second scenario where $M_{BH} - \sigma_*$ correlation breaks down for low-luminosities, and the virial method is still valid black hole mass estimator is unlikely to be true.

3.5.3 Third scenario: Virial assumption can no longer be applied for black hole mass estimations of local type 1 low-luminosity AGN

Finally we consider a scenario where the $M_{BH} - \sigma_*$ correlation of W13 can be trusted as a reliable black hole mass estimator for our local type 1 LLAGN. We have strong

evidence from $M_{BH} - M_*$ correlation to support this. $M_{BH} - \sigma_*$ of W13 and and $M_{BH} - M_*$ correlation of RV15 represent totally independent data samples, therefore there is no reason to believe that somehow black hole mass estimates from $M_{BH} - \sigma_*$ correlation of W13 would be biased towards the $M_{BH} - M_*$ relation of RV15. We already mentioned that it is interesting that our actual M_{BH}^{vir} estimations fall off the $M_{BH} - M_*$ correlation of RV15, which is in fact established for virial black hole masses. We can look at this from reversed perspective: let's assume that the $M_{BH} - M_*$ correlation of RV15 is a valid black hole mass estimator for local LLAGN. If we use this relation to calculate black hole masses, we obtain result that is consistent with the $M_{BH} - \sigma_*$ correlation of W13 (Figure 3.8). This proves that even when black hole masses are estimated using two different methods and correlations, in this case $M_{BH} - \sigma_*$ and $M_{BH} - M_*$, we obtain results that are consistent with each other, which is not the case with virial black hole masses. The possible explanation why virial black hole masses from RV15 are larger than ours may be because their sample consists of AGN in luminosity regime where the scaling relationships are well established. In our work, we probed much fainter luminosities, and it is possible that the scaling relationships do not hold to this point, since we have no data in this regime to prove otherwise. Of course it is possible that both $M_{BH} - M_\sigma$ and $M_{BH} - M_*$ correlations break down at such low luminosities, but it is highly unlikely, since they are two distinctive methods of black hole mass estimation. Also, the fact that there is an actual correlation between M_{BH}^{vir} and σ_*, just with lower normalization and slightly different slope, favors the idea that $M_{BH} - \sigma_*$ correlation can still be used in extremely low-luminosity regime.

The largest uncertainty attributed to $M_{BH} - \sigma_*$ correlation is, which one should be trusted to be adequate in case of LLAGN, considering the variety of them. As we already mentioned, W13 and S16 showed that $M_{BH} - \sigma_*$ correlations of quiescent galaxies are biased towards larger stellar velocity dispersions, therefore they favor galaxies with more massive SMBHs. When they introduced the same bias to AGN in their Monte Carlo simulations, they obtained higher normalization and steeper slope, comparable to $M_{BH} - \sigma_*$ correlations of quiescent galaxies. From this we can conclude that the optimal solution would be to use one of $M_{BH} - \sigma_*$ correlations established for AGN. Still, there are few of them. In this work, we justified using the one from W13 by similarities between objects in their sample and CALIFA.

The first scenario excludes the possibility that virial assumption can be used as black hole mass estimator in this extreme low-luminosity regime. The assumption of validity of $M_{BH} - \sigma_*$ correlations for LLAGN, have more arguments on its side, since virial method requires lot of extrapolations, where each of them may contribute to the uncertainty in black hole mass estimation of these faint AGN. The first contribution to an error in black hole mass estimation may come from virial scaling factor f. We already mentioned that f factor accounts for kinematics, geometry and inclination of BLR, which are the properties that we cannot estimate with current methods. Yong, Webster, and King (2016) performed Monte Carlo simulations of two BLR disk wind models, in order to recover virial factor f. Their result implies that f strongly correlates with inclination angle of BLR, where larger values of f are associated with smaller inclination angles, and smaller values of f – with larger inclination angles. This shows that the standard assumption of one average value of f may introduce significant error in black hole mass estimation. Still, virial factor alone cannot be responsible for M_{BH}^{vir} offset from $M_{BH} - \sigma_*$ or $M_{BH} - M_*$, that is of an order of magnitude or larger.

Other contribution to uncertainty of virial assumption may come from the virial

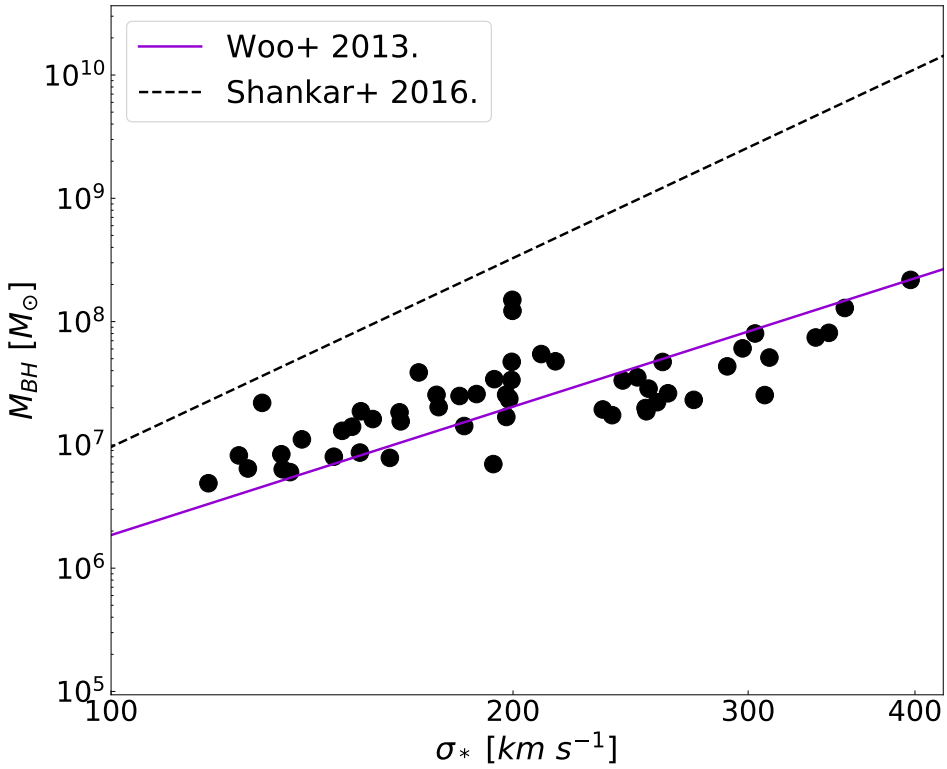

FIGURE 3.8: Black hole masses estimated from the RV15 $M_{BH} - M_*$ correlation, represented on $M_{BH} - \sigma_*$ plane. The respective lines are from $M_{BH} - \sigma_*$ correlations established by Woo et al. (2013) (solid purple line) and Shankar et al. (2016) (dashed black line).

scaling relationships (Equations 3.6 and 3.7). It is important to investigate the accuracy of these relationships if they are extrapolated beyond regions in which they were established. $L_{H\alpha} - L_{5100}$ from Greene and Ho (2005) and $R_{BLR} - L_{5100}$ from Bentz et al. (2013) correlations were established for $L_{H\alpha} > 10^{40}$ erg s^{-1}. In our sample we have only one object with $L_{H\alpha}$ in this regime – Mrk 79. Virial black hole mass estimation of this object fits well on the $M_{BH} - \sigma_*$ correlation of W13. This is, although statistically insignificant, proof that both virial scaling relationships and the $M_{BH} - \sigma_*$ of W13 are valid in this luminosity regime. Also, some previous studies at significantly higher luminosities than ours (Gebhardt et al., 2000b; Ferrarese et al., 2001; Nelson et al., 2004; Onken et al., 2004) showed that virial black hole masses are consistent with $M_{BH} - \sigma_*$ correlations of quiescent galaxies.

In order to investigate whether a slight change of one or both scaling relationships might provide virial black hole mass measurements that are consistent with M^{σ}_{BH}, we varied the slopes and normalizations of $R_{BLR} - L_{5100}$ and $L_{H\alpha} - L_{5100}$, individually and together, and recalculated M^{vir}_{BH}. Assuming that the relationships are still linear, they would have to be changed so drastically that they would not be applicable in higher luminosity domain, at which they are established in the first place. This may indicate a turnover in scaling relationships, implying non-linear correlation that would satisfy accounting of the faintest sources. Unfortunately AGN

continuum of these objects is so weak that it is impossible to measure its luminosity, which is necessary for establishment of these scaling relationships for broad Hα luminosities below 10^{40} erg s^{-1}.

The assumption of $M_{BH} - \sigma_*$ being a valid black hole mass estimator for LLAGN would imply that these objects are still able to form the BLR, although the structure of their central engine is probably modified to a certain extent. The most likely scenario is that there is a smooth transition between classical optically thick and geometrically thin accretion disk to the 3-component structure where we can no longer detect the broad emission lines. According to this, low-luminosity local AGN are weak scaled-down versions of luminous high-z AGN, which disagrees with the claims of Ho (2008). Still, the objects that Ho used in his research (see also Greene and Ho (2007)) are located in significantly less massive galaxies than AGN from our sample. Type 1 LLAGN that we detected with CALIFA are accreting below traditionally used "treshold" value of SMBH activity ($\log(\lambda) \sim -3$), implying that their accretion mechanism is consistent with the one of the typical luminous AGN. Considering our LLAGN as genuine type 1 AGN would require lowering of this limit, implying that the current BLR formation and accretion models need to be reexamined.

3.6 Conclusions

Local type 1 LLAGN are extremely difficult objects to detect due to their weak emission lines and non-existent typical power law AGN continuum. Yet, they are very important for improving our understanding of black hole demographics across cosmic time, and coevolution of AGN and their host galaxies.

We used the CALIFA survey in order to detect these faint objects in the local Universe. We found that more than 16% of CALIFA galaxies host BELs in their spectra. These BELs are extremely weak ($L_{H\alpha} \sim 10^{39}$ erg s^{-1}), but have FWHMs comparable to the "typical" high-luminosity high-z type 1 AGN (3000 km s^{-1} on average). We also estimated bulge velocity dispersions σ_* and total stellar masses M_* of the host galaxies of these objects, which helped us gain insight into the correlations between these parameters and black hole masses.

We estimated black hole masses of these type 1 LLAGN using the $M_{BH} - \sigma_*$ correlation of Woo et al. (2013), on one hand, and virial assumption, on another. We obtained significant discrepancy between the results. Our virial black hole masses are on average $\sim$ 10 smaller than the black hole masses estimated from $M_{BH} - \sigma_*$ correlation, while the Eddington ratios are on average 12 times larger. The discrepancy is the smallest for the low-mass spiral galaxies, and reaches more than a factor of 30 in black hole mass for the massive elliptical systems.

These results lead to three possible scenarios: the BELs that we detected are not produced in the BLR by the accretion of the material onto the central SMBH, they can be produced by some other mechanism or they represent a systematic error introduced by fitting procedures; the virial assumption and virial scaling relationships are a valid black hole mass estimator for LLAGN and $M_{BH} - \sigma_*$ correlations break down; or $M_{BH} - \sigma_*$ correlation is still valid in this extreme low-luminosity regime and the scaling relationships are probably no longer linear and therefore cannot be applied for black hole mass estimation.

The scenario where $M_{BH} - \sigma_*$ correlation is still a valid black hole mass estimator, even for the faintest AGN, is probably the most likely one, while the virial theorem requires lot of assumptions and extrapolations beyond the established luminosity

regime. Also, the location on the emission-line diagnostic diagrams and the distribution of FWHMs of the objects with detected broad Hα imply that these are in fact AGN. Another factor that favors the $M_{BH} - \sigma_*$ correlation is that the black hole masses estimated from it correlate very well with previously established $M_{BH} - M_*$ correlations for local type 1 AGN. If $M_{BH} - \sigma_*$ correlation is still valid black hole mass estimator, this would imply that these objects are weak scaled-down versions of genuine luminous type 1 AGN originating at high redshifts, and that there are no drastic changes of LLAGN accretion disk structure. They are still able to form the BLR that produces very faint, yet still detectable BELs. Accretion disk most likely changes smoothly from optically thick and geometrically thin structure, to the 3-component model consisting of inner RIAF, an outer geometrically thin disk, and a jet or an outflow. The virial scenario would require modifications of the central engine, where the accretion disk is probably decomposed into this 3-component structure, in which case, LLAGN would have to be different type of objects than luminous high-z AGN.

We can not claim with 100% accuracy that one of the three proposed scenarios is certainly the correct one. In order to derive such statement, further studies of LLAGN are necessary. Still we gained some new insight on the LLAGN in the local Universe.

Our results can further be used to establish the faint end of AGN luminosity function, as well as black hole mass function and Eddington ratio distribution function. This will help us gain better insight into the AGN population as a whole and study AGN and SMBH phenomenon on the entire redshift range.

CHAPTER 4

Luminosity and distribution functions of the CALIFA type 1 AGN

ABSTRACT

We applied $1/V_{max}$ method to estimate AGN luminosity function (AGNLF), as well as black hole mass (BHMF) and Eddington ratio distribution (ERDF) functions of local type 1 AGN, using the CALIFA survey ($0.005 < z < 0.03$). For a sample of 89 type 1 AGN we estimated both broad and total Hα emission-line luminosity functions, and combined our result with previous studies in this field, in order to obtain local AGNLF for a wide range of luminosities. We found double power law to be good representation of our binned AGNLF. The shape of AGNLF shows an apparent flattening for $L_{\mathrm{H}\alpha} \lessapprox 10^{40}$ erg s^{-1}, indicating that we approached the upper limit of AGN number density in the local Universe. BHMF and ERDF were estimated for a sub-sample of 55 type 1 AGN, for which we had measurements of stellar velocity dispersions. BHMF is well described both by a double power law and the Schecter function. Consistently with the shape of AGNLF, we observed clear flattening of both BHMF (for $\log(M_{BH}) < 7.7$ in units of $M_{\odot}$) and ERDF ($\log(\lambda) < -3$), depicting the peak of low-mass and low-activity SMBHs at $z \approx 0$. Comparing our active black hole mass function with the one of local quiescent black holes, we estimated the fraction of active SMBHs in CALIFA. The active fraction decreases with increasing black hole mass, agreeing with the scenario of anti-hierarchical growth of black holes, or AGN downsizing. We showed that both BHMF and ERDF contribute to the downsizing, and signified the importance of including black holes in the lowest stages of their activity in order to fully understand their growth history.

4.1 Introduction

Growth of Super Massive Black Holes (SMBH) across cosmic time is the key to understanding formation and evolution processes of galaxies. In order to fully comprehend black hole growth, it is essential that we study them in different stages of their activity. Active Galactic Nuclei (AGN) represent important phase in black hole and galaxy's activity cycle and can provide significant insight into demographics of SMBHs.

Correlations between black hole masses and their host galaxies' properties, such as stellar velocity dispersion (Ferrarese and Merritt, 2000; Gebhardt et al., 2000a; Gebhardt et al., 2000b; Tremaine et al., 2002; Nelson et al., 2004; Onken et al., 2004; Gültekin et al., 2009; Kormendy and Ho, 2013; McConnell and Ma, 2013), bulge mass or bulge luminosity (Ferrarese et al., 2001; Merritt and Ferrarese, 2001; Gültekin et al., 2009; Kormendy and Ho, 2013), or galaxy's total stellar mass (Magorrian et al., 1998; Merritt and Ferrarese, 2001; Marconi and Hunt, 2003; Häring and Rix, 2004; Reines and Volonteri, 2015), imply that there is a strong coevolution of central SMBHs and their hosts. In previous chapter, we showed that this coevolution persists until present epoch for SMBHs in massive galactic systems. The correlation between black hole mass M_{BH} and bulge stellar velocity dispersion σ_* (the $M_{BH} - \sigma_*$ correlation) is proven to be reliable black hole mass estimator across various redshift ranges. Greene and Ho (2006), Woo et al. (2010), and Xiao et al. (2011) found that $M_{BH} - \sigma_*$ correlations of active galaxies show shallower slope and lower normalization than the ones established for samples of quiescent galaxies. The same discrepancy is observed for the sample of local galaxies, selected from Sloan Digital Sky Survey (SDSS) database (see Shankar et al. (2016)). Woo et al. (2013) and Shankar et al. (2016) pointed out that this inconsistency is a consequence of selection biases of $M_{BH} - \sigma_*$ correlations established for dynamically measured black hole masses of quiescent galaxies. Their simulations showed that, if the same bias is introduced to the samples of AGN and local SDSS galaxies, the corresponding $M_{BH} - \sigma_*$ correlations would be consistent with those estimated from dynamically measured M_{BH}.

AGN luminosity function

In order to properly understand the growth of AGN population, it is necessary to establish the AGN luminosity function (AGNLF) at different redshifts and luminosities. AGNLF represents AGN number density at a given volume for a given luminosity, and is relatively well established for the luminous QSOs at high z (Schmidt and Green, 1983; Marshall et al., 1983; Boyle, Shanks, and Peterson, 1988; Boyle et al., 2000; Hewett, Foltz, and Chaffee, 1993; Schmidt, Schneider, and Gunn, 1995; Hawkins and Veron, 1995; Wisotzki, 1999; Fan et al., 2000; Richards et al., 2006b; Croom et al., 2009; Palanque-Delabrouille et al., 2013). Low-Luminosity AGN (LLAGN) are extremely faint when compared to luminous QSOs at high redshifts, making them consequently much harder, or even impossible, to detect with methods that are used for QSO identification. This is the reason behind our lack of proper knowledge of AGNLF at $z \approx 0$ and in lower luminosity regimes (Ho, 2008). Another important factor is that the weak LLAGN emission can often be heavily diluted by its host galaxy starlight. This requires very precise stellar continuum and absorption modeling and their proper subtraction from the observed spectrum.

Objects that are particularly useful for luminosity function studies are type 1 AGN, that distinguish themselves by the presence of permitted broad emission lines

(BELs) in their central spectra. Most commonly used BELs for black hole mass estimations are the Balmer series lines of Hydrogen, Hα and Hβ. Such lines with Full Widths at Half Maximum (FWHMs) of few thousands km s^{-1} can only be produced by accretion of the material onto the central active SMBH, therefore they remain unaffected by host galaxy's stellar contamination.

On the other hand, weak emission of LLAGN is very useful for studying the properties of central SMBHs and their hosts separately, since black hole emission doesn't prevail over host galaxy's starlight. Hence, the detection of type 1 LLAGN is extremely important for establishing unbiased correlations between central SMBHs and their host galaxies, and for determining the faint-end of AGNLF.

Koehler et al. (1997) were the first to obtain luminosity function for a small sample of local type 1 AGN, followed by works of (Vila-Vilaro, 2000; Ulvestad and Ho, 2001; Hao et al., 2005a; Greene and Ho, 2007; Schulze, Wisotzki, and Husemann, 2009). For the purpose of our work, we used the data from the Calar Alto Integral Field Survey (CALIFA, Sánchez et al. (2012), Husemann et al. (2013), Walcher et al. (2014), and García-Benito et al. (2015)), and probed even weaker luminosity broad Hα regime than previous studies in this field. This allowed us to establish the faint-end of AGNLF at $z \approx 0$, for a sample of 89 type 1 LLAGN from the CALIFA survey.

Local AGNLF not only show us how these objects fit into a bigger picture, but also serve as a zero-point for higher redshift AGN and QSO luminosity function studies. If AGNLF is well established for a wide range of luminosities at different redshifts, it can be used for studying of evolution of entire AGN population over cosmic time.

Schulze, Wisotzki, and Husemann (2009) estimated type 1 AGN luminosity function at $z < 0.3$ and performed a comparison between their local AGNLF and luminosity functions from Bongiorno et al. (2007) and Croom et al. (2009), estimated for AGN at higher redshifts. They extrapolated these high-z luminosity functions to $z \approx 0$ and found disagreement with their local AGNLF. Bongiorno et al. (2007) and Croom et al. (2009) luminosity functions predicted significantly higher space density of luminous AGN in local Universe. This emphasises the importance of estimating AGNLF at $z \approx 0$, as it may give us additional information on AGN distribution through cosmic history.

One important aspect of comparing high-z luminosity functions to the local ones is that there is a clear difference in their respective shapes. The breaking point, typical for high-z AGNLF, occurs at significantly higher luminosities than in case of local luminosity function. This so called "AGN downsizing" scenario (Ueda et al., 2003; Steffen et al., 2003; McLure and Dunlop, 2004; Merloni, 2004; Merloni and Heinz, 2008) implies that the majority of luminous AGN with high-mass SMBHs are mainly formed earlier in cosmic history, while in current epoch the majority of LLAGN with lower black hole masses are accreting at significantly lower rate.

Black hole mass and Eddington ratio distribution functions

Although AGNLFs are particularly important for studies of black hole demographics and their growth history across cosmic time, they require numerous assumptions in order to be established in the first place. The most common one is assuming the same Eddington ratio for the whole SMBH population which implies that at different redshifts SMBHs of all mass ranges are accreting at the same level. The history of SMBH mass growth would then directly depend on AGN luminosity, independent on the stage of their activity (Nobuta et al., 2012). This is, however, far from realistic scenario. Kauffmann and Heckman (2009) and Schulze and Wisotzki (2010)

showed that local AGN have wide range of Eddington ratios, while in Chapter 3 we concluded that LLAGN of CALIFA accrete at extremely low level. In order to avoid these biases that would introduce additional uncertainties in understanding of the AGN population, it is useful to divide AGNLF into two parts: the active black hole mass function (BHMF) and the Eddington ratio distribution function (ERDF). This will further help us gain deeper understanding of SMBH population growth.

Estimation of active BHMF requires that we already have known black hole masses which is something that cannot be estimated directly. The BHMF of local active galaxies from our sample can be estimated by relying on the correlations between black hole masses and host galaxies' bulge properties, such as bulge mass or bulge stellar velocity dispersion (Salucci and Persic, 1999; Yu and Tremaine, 2002; Shankar et al., 2004; Marconi et al., 2004). Correlation between black hole masses and host galaxies' stellar velocity dispersions σ_* is originally established for samples of quiescent galaxies that have M_{BH} measurements obtained directly from stellar or gas kinematics (Ferrarese and Merritt, 2000; Gebhardt et al., 2000a; Gebhardt et al., 2000b; Ferrarese et al., 2001; Merritt and Ferrarese, 2001; Tremaine et al., 2002; Onken et al., 2004; Gültekin et al., 2009; Kormendy and Ho, 2013; McConnell and Ma, 2013). Further research showed that $M_{BH} - \sigma_*$ correlation can also be applied on samples of active galaxies (Gebhardt et al., 2000b; Ferrarese et al., 2001; Nelson et al., 2004; Greene and Ho, 2006; Woo et al., 2010; Xiao et al., 2011), when certain selection biases are taken into account and eliminated (more in Chapter 3.3.1 and in the original works of Woo et al. (2013) and Shankar et al. (2016)). Emission of luminous AGN often dominates the spectrum and outshines host galaxy's stellar component, which introduces challenges in measuring bulge stellar velocity dispersion. On the other hand, LLAGN have significantly weaker emission, which allows us to properly measure σ_* of their host galaxies, while undiluted AGN emission can be measured from BELs of type 1 objects. It is for that reason our sample of type 1 LLAGN is of great use for setting the zero-point of active BHMF. Another commonly used method, especially for local AGN, is the virial assumption, but as we discussed in Chapter 3, this method appears to be unreliable black hole mass estimator for CALIFA type 1 AGN.

First BHMF estimation were made by McLure and Dunlop (2004), for a sample of type 1 QSO from SDSS survey and Heckman et al. (2004), for low-redshift type 2 AGN. Later studies (Greene and Ho, 2007; Vestergaard et al., 2008; Labita et al., 2009; Schulze and Wisotzki, 2010) showed there is an evidence of cosmic downsizing or antihierarchical growth of SMBHs, consistent to the one observed in AGN luminosity functions. Marconi et al. (2004) derived the first local BHMF, by applying correlations between M_{BH} and bulge luminosity and stellar velocity dispersion. Further works in this field (Graham et al., 2007; Vika et al., 2009; Shankar, Weinberg, and Shen, 2010; Li, Ho, and Wang, 2011) used different data sets and appeared to be in great agreement with results of Marconi et al. (2004).

Considering ERDF, there are only few studies conducted so far on this topic, of which the one estimated by Schulze and Wisotzki (2010) for a sample of local type 1 AGN from Hamburg/ESO survey (HES, Wisotzki (1999)) is the most connected to our work.

The main goal of this chapter is to explore how AGNLF, BHMF and ERDF of CALIFA type 1 AGN fit into a bigger picture, by comparing them to the previous results in slightly higher luminosity regime. Throughout this chapter we assume Hubble constant of $H_0 = 70$ km s^{-1} Mpc^{-1}, and cosmological density parameters: $\Omega_M = 0.3$ and $\Omega_\Lambda = 0.7$.

The outline of this chapter is as follows. In Section 4.2 of this chapter we briefly describe our data sample and the method that we used for its volume correction. In Sections 4.3, 4.4 and 4.5 we discuss our methods and present the results of emission-line AGNLF, BHMF and ERDF, respectively. In Section 4.6 we discuss our results and weight on how they agree with the previous studies in this field, and in Section 4.7 we summarize our work and draw the final conclusions.

4.2 CALIFA survey and type 1 AGN sample

4.2.1 Survey area

The detailed description of the CALIFA survey and its galaxy sample selection is given in Chapter 2.2.1. Here, we will only give a brief information about the survey area and selection criteria.

The CALIFA survey observations were conducted with the Potsdam Multi Aperture Spectrograph (PMAS, Roth et al., 2005) mounted at the 3.5 m telescope at Calar Alto Observatory, Spain, employing the PPAK Integral Field Unit (Verheijen et al., 2004; Kelz et al., 2006). PPAK has a hexagonal field of view of $74'' \times 64''$, and the sampling is $1'' \times 1''$ per spaxel. The survey covers $\Omega_C = 8700$ deg^2 area on the sky, which, in its redshift range ($0.005 < z < 0.03$), this corresponds to $\sim 1.7 \times 10^6$ Mpc^3 of comoving volume (Walcher et al., 2014). The entire galaxy sample of CALIFA consists of 939 galaxies, which is called the "mother sample". Mother sample was selected from the SDSS data release 7 (DR7), with isophote major axis at 25 mag per square second in the r band ($isoA_r$) to satisfy the criteria: $45'' < isoA_r < 79.2''$, cut in the Galactic latitude to exclude the Galactic plane: $b > 20$ or $b < -20$, and $petroMag_r < 20$, to exclude very faint objects.

4.2.2 Sample selection

For the purpose of this research we used Data Release 3 (DR3, Sánchez et al. (2016)) of CALIFA survey sample, which consists of 542 galaxies. We extracted spectra from the central 3×3 spaxel ($3'' \times 3''$) aperture of these galaxies. We performed spatial binning of the data within these 9 central spaxels, at each wavelength, in order to obtain total flux density of the nuclear galactic regions, since this nuclear region corresponds to approximately 100 - 500 pc at CALIFA redshifts, which is comparable to the size of the central AGN. Further we conducted spectral analysis of these central regions, consisting of, first, host galaxy's stellar continuum and absorption modeling, and, secondly, emission line modeling. In order to remove host galaxy's stellar component from the spectrum of interest, we used the PyParadise (Husemann et al. (in prep.),Walcher et al. (2006) and Walcher et al. (2009)) spectral fitting code, which generates a model spectrum that represents stellar continuum and absorption coming from the host galaxy. After the stellar component model is properly subtracted from the original spectrum, what remains is pure emission line spectrum of the galactic central region. In order to obtain emission-line model spectrum and measure the emission-line parameters, we designed a code that detects and fits broad component of Hα emission line, if one is present in the spectrum.

Detailed description of the the PyParadise fitting procedure can be found in Chapter 2.2.2, and, of course, in PyParadise description papers (Husemann et al. (in prep.)), while the emission-line fitting procedure is described in Chapter 2.2.3.

By applying this broad line fitting procedure, we detected the broad Hα component in 89 central spectra of the CALIFA DR3 galaxies. These BELs appear to be very

weak, but their FWHMs $(1000 - 6000)$ km s^{-1} are comparable to those of "typical" type 1 AGN (detailed discussion in Chapter 2.3.2). Correspondingly, we classified these objects as type 1 AGN, and established their luminosity and distribution functions.

4.3 AGN luminosity function of CALIFA type 1 AGN

Establishing AGNLF at $z \sim 0$ is essential for AGN evolution studies, as it may serve as a zero-point of QSO luminosity functions. The AGNLF, $\phi(L)$, represents the number of objects, N, per unit comoving volume, V, per unit luminosity, L:

$$\Phi(L, z) = \frac{d^2N}{dL\, dV} \tag{4.1}$$

Before establishing luminosity function for a sample of objects from a diameter-limited survey, it is important to introduce a correction for the volume effect. This is an effect where at certain apparent brightness, brighter objects have larger volume over which they could be detected, as more luminous objects can be observed at greater distances, resulting in their higher fraction in the survey.

In order to correct for this bias, it is necessary to perform volume correction that uses a weighed mean to properly account for its relative contributions at all magnitudes. In our work, we obtained space densities of the objects in the sample by using the $1/V_{max}$ estimator (Schmidt, 1968; Felten, 1976; Avni and Bahcall, 1980). V_{max} represents the calculated maximal volume that galaxies could have inhabited in certain redshift range, in order to still be observable.

We used the V_{max} values estimated by the CALIFA collaboration (Walcher et al., 2014), for a sample of 937 CALIFA galaxies. V_{max} for each galaxy is estimated as:

$$V_{max} = \int_{z_{min}}^{z_{max}} \Omega_{eff}(m) \frac{dV}{dz} dz \tag{4.2}$$

where Ω_{eff} is the effective survey area, and z_{min} and z_{max} are minimum and maximum redshift for which an object of the same linear size D_{iso} would still be captured by the CALIFA selection criteria. Equation 4.1 assumes that probability of finding AGN in the survey is independent from redshift, which is justified for a narrow redshift range of CALIFA. By implementing such volume correction, we secured that our sample is not affected by Malmquist bias Malmquist (1922) and volume effects.

Since type 1 AGN with measured black hole masses consists only of a fraction (55 objects) of the entire type 1 AGN sample from CALIFA, it is important to account for this reduction of the entire type 1 AGN sample when performing a volume correction. The effective solid angle Ω_{eff} is then given as $\Omega_{eff} = f \times \Omega_C$, where f represents the completeness of spectroscopic coverage of the sample. In the case of DR3 galaxy sample the completeness amounts $f = 55/89 \approx 61.8\%$.

In the sense of logarithmic luminosity, log(L), Equation 4.2 becomes:

$$\Phi(L) = \frac{1}{\Delta \log L} \sum_k \frac{1}{f\, V_{max}^k} \tag{4.3}$$

where $\Delta \log L$ is luminosity bin size.

The most common parametrization of AGNLF is done using a double power law (Marshall, 1987; Boyle et al., 2000) defined as:

$$\phi(L) = \frac{\phi^*/L^*}{(L/L^*)^{-\alpha} + (L/L^*)^{-\beta}} \tag{4.4}$$

where ϕ represents a non-logarithmic form of LF, and is connected to the binned luminosity function $\Phi(L)$ by $\phi(L) = \log e\ \Phi(L)/L$. ϕ^* is the normalization, L^* is a characteristic break luminosity, and α and β represent bright-end and faint-end slopes, respectively.

In order to obtain AGNLF, we would need estimates of AGN bolometric luminosities L_{bol}, which would require luminosity measurements at all wavelengths. As this is impossible for such LLAGN as we have in CALIFA, broad Hα luminosity $L_{H\alpha}$ might serve as a proxy for L_{bol}, when certain corretion factor is applied (Richards et al., 2006a). We calculated broad Hα luminosities of our type 1 AGN, adapting cosmological parameters mentioned in Section 4.1. We obtained remarkably low values of $L_{\mathrm{H}\alpha}$, in range $(2 \times 10^{38} - 3 \times 10^{41})$ erg s^{-1}, with the average value of 7.2×10^{39} erg s^{-1}. This is extremely low luminosity regime, and might serve as a great zero-point for further studies of AGN luminosity function.

In order to understand whether our sample suffers from incompleteness, we refer to the results obtained in the experiment in Chapter 2.2.3, where we determined the minimum strength of broad Hα component required in order for it to be detected with our emission-line fitting method. We concluded that all 89 CALIFA type 1 AGN have probability of more than 40% that their broad Hα lines are genuine BELs formed in the broad line region (BLR) by accretion of the material onto the central SMBH. Therefore our type 1 AGN sample overall has a very high level of completeness, but might still suffer from the incompleteness for the lowest luminosities ($\log(L_{\mathrm{H}\alpha}) < 38.5$). By marking CALIFA galaxies with detectable BELs on the standard emission-line ratio diagnostic diagrams (Chapter 2.3.1) we showed that they are located in AGN – LINER-like regions, which may serve as a valid confirmation that these objects are indeed genuine AGN. The BEL recovery test that we performed and the location of CALIFA galaxies with BELs on the diagnostic diagrams show that such weak BELs that we detected are real and that we can detect them in AGN.

On Figure 4.1 we show binned emission-line luminosity function of broad Hα component combined with broad $L_{H\alpha}$ histogram. Binned broad AGNLF is calculated for a sample of 89 CALIFA type 1 AGN. Bin size is 0.25 dex in $\log(L_{\mathrm{H}\alpha})$. The errors of AGNLF were estimated from Poisson statistics, but in case of the lowest luminosity bin, which might suffer from sample incompleteness, and two highest luminosity bins that contain only a single object per bin, realistic errors are larger than Poissonian's. The object that distinguish itself from others by apparently higher broad Hα luminosity is Mrk 79, the only well known type 1 AGN in the CALIFA survey. This is the only measurement in the highest luminosity bin, and, although a single object, it can be used for comparison with other higher-luminosity studies, in order to test our results. Binned AGNLF of CALIFA is documented in Table 4.1.

We fitted our binned broad AGNLF with double power law function (Equation 4.4), and obtained $\phi_* = 6.94 \times 10^{-4}$ Mpc^{-4}, with a breaking point at $\log(L_*) = 39.65$, $\alpha = -0.92$ describing the faint-end, and $\beta = -4.18$ bright-end slopes, and reduced chi-square value of $\chi^2_{red} = 2.83$. We excluded two highest luminosity bins from the fit as they contain only one object each, therefore we cannot statistically weight them in, as well as the lowest luminosity bin due to incompleteness. Although we can not accurately describe the high-luminosity end of AGNLF, it is evident from the fit that the shape of the double power law and the data indicates a flattening of AGNLF at

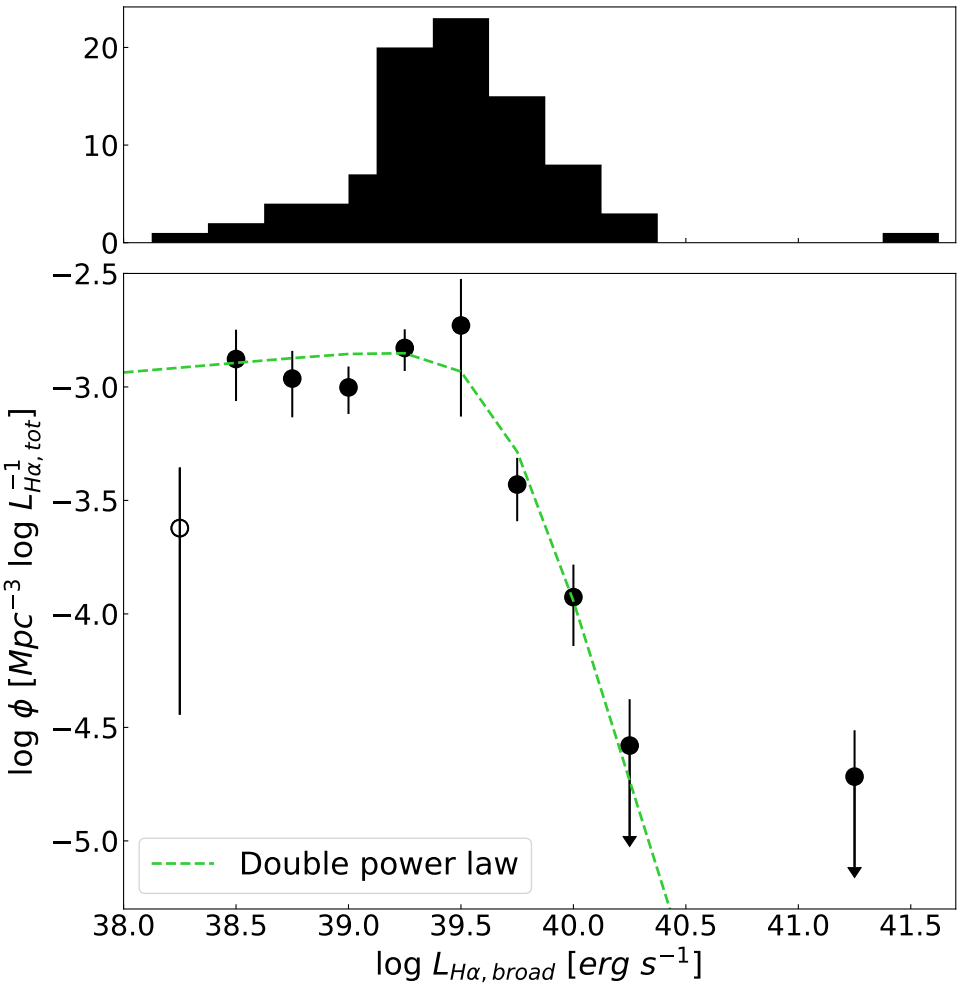

FIGURE 4.1: Top: Histogram of broad Hα luminosities of 89 type 1 AGN from the CALIFA sample. Luminosity range is $(2 \times 10^{38} - 3 \times 10^{41})$ erg s^{-1}. Bottom: Binned emission-line AGNLF of these objects estimated using $1/V_{max}$ method, and fitted with double power law (dashed green line), excluding the two highest luminosity as well as the lowest luminosity bins. The bin size of 0.25 dex. Open symbol represents an incomplete bin, while arrows on errorbars indicate that respective bins contain only a single object.

low-luminosity end. The flattening occurs approximately at 39.5 in log$\Phi(L)$ units, and is crucial to describing and understanding the local AGNLF. Therefore, in order to properly describe the shape of the local AGNLF, and understand its evolution, it is necessary to combine our results with other studies at $z \approx 0$ that are established in slightly higher luminosity regimes. This will be analyzed in detail in Section 4.6.1, where we will perform parametrization of the combined AGNLF, consisting of our data points and the results obtained by Schulze, Wisotzki, and Husemann (2009) and Hao et al. (2005b).

Comparison between luminosity function and a histogram that we see on the figure highlights the importance of including volume corrections in order to properly

understand distribution of objects in certain luminosity and redshift range. As we can see, fraction of AGN with broad Hα luminosities below $10^{39.5}$ erg s^{-1} is significantly higher in the local Universe than what it can be concluded from the histogram of luminosities. As we can detect brighter sources at larger distances, it appears that they are much more common in the local Universe than fainter objects, which introduces a bias in our understanding of AGN demographics.

TABLE 4.1: Binned broad Hα emission-line AGN luminosity function of 89 CALIFA type 1 AGN. N is the number of objects per bin.

$\log L_{\mathrm{H}\alpha,\mathrm{broad}}$ [erg s^{-1}]	N	$\log \Phi$ [Mpc^{-3} $\log L^{-1}_{\mathrm{H}\alpha,\mathrm{broad}}$]
38.25	2	$-3.62^{+0.27}_{-0.82}$
38.50	4	$-2.70^{+0.13}_{-0.18}$
38.75	5	$-2.96^{+0.12}_{-0.17}$
39.00	12	$-3.00^{+0.09}_{-0.12}$
39.25	28	$-2.83^{+0.08}_{-0.10}$
39.50	18	$-2.73^{+0.21}_{-0.40}$
39.75	13	$-3.43^{+0.12}_{-0.16}$
40.00	4	$-3.93^{+0.14}_{-0.21}$
40.25	1	$-5.06^{+0.20}_{-0.40}$
41.25	1	$-4.72^{+0.20}_{-0.40}$

4.4 Active black hole mass function of CALIFA type 1 AGN

As we showed in Chapter 2, type 1 AGN account for a non-negligible fraction of the entire SMBH population, therefore estimation of active BHMF is important in order to properly understand SMBH growth across cosmic time. CALIFA type 1 AGN provide a great opportunity to study how local SMBHs fit into a bigger picture of black hole demographics.

We constructed the CALIFA active BHMF by applying the same approach as in case of emission-line AGNLF in Chapter 4.3. We used the same $1/V_{max}$ estimator as for AGNLF. Usually, in order to estimate the local BHMF, evolution corrections are necessary, but in case of such narrow redshift range as the one of CALIFA, evolution has no effect on BHMF. We calculated the binned BHMF from the following equation:

$$\Phi(M_{BH}) = \frac{1}{\Delta\log(M_{BH})} \sum_k \frac{1}{f\ V^k_{max}} \tag{4.5}$$

where $\Phi(M_{BH})$ is the binned BHMF, $\Delta\log(M_{BH})$ is the black hole mass bin size, and $f \approx 61.8\%$ is the same factor of spectroscopic coverage of the sample that we used for calculation of luminosity function of CALIFA AGN.

The most common parametrization of BHMF is done using the double power law from the Equation 4.4, adopted for M_{BH} instead of luminosity:

$$\phi(M_{BH}) = \frac{\phi^*/M^*}{(M_{BH}/M^*)^{-\alpha} + (M_{BH}/M^*)^{-\beta}} \tag{4.6}$$

where, similar to AGNLF, ϕ^* is the normalization, M^* is the break black hole mass, and α and β are the low-mass and high-mass end slopes, respectively.

Another function commonly used for BHMF parametrization is the Schecter function (Schechter, 1976) of the following form:

$$\phi(M_{BH}) = \frac{\phi^*}{M^*} \left(\frac{M_{BH}}{M^*}\right)^{\alpha} exp\left(\frac{M_{BH}}{M^*}\right) \tag{4.7}$$

where the parameters ϕ^* and M^* are the same as in Equation 4.6, and α is the slope.

In order to calculate black hole masses residing in centers of our type 1 AGN, we used the $M_{BH} - \sigma_*$ correlation from Woo et al. (2013), estimated for a sample of 25 reverberation-mapped AGN:

$$\log\left(\frac{M_{BH}}{M_\odot}\right) = (7.31 \pm 0.15) + (3.46 \pm 0.61) \log\left(\frac{\sigma_*}{200 \text{ km s}^{-1}}\right) \tag{4.8}$$

In order to estimate stellar velocity dispersions of CALIFA type 1 AGN, we used the results obtained by Méndez-Abreu et al. (2017). They performed multi-component photometric composition of 404 CALIFA DR3 galaxies, and estimated bulge parameters of galaxies that have them: effective radius r_{eff}, ellipse axis ratio q, and the position angle PA. We used these parameters to confine central ellipses that define bulge regions of host galaxies, and binned the flux densities of all spaxels within each ellipse, in order to obtain average bulge flux density of each galaxy. Then, with pyPARADISE spectral fitting code we fitted stellar kinematics of each bulge, which provided us with estimations of σ_*. Unfortunately, the measurements from Méndez-Abreu et al. (2017) lacked data on 44 objects that we classified as type 1 AGN, therefore we calculated σ_* only for 55 CALIFA type 1 AGN. We further applied Equation 4.8 in order to calculate black hole hole masses of these objects. Obtained black hole masses are in range between 3.3×10^6 $M_\odot$ and 2.2×10^8 $M_\odot$, with the average value of 2.1×10^7 $M_\odot$.

Using Equation 4.5 we calculated the binned CALIFA BHMF of these 55 type 1 AGN, using the bin size of 0.25 dex in $\log(M_{BH})$. Similar to AGNLF, the errors were estimated from Poisson statistics, but realistic errorbar at the highest mass end might be significantly larger, since the bin contain only one object. The results of our binned BHMF are documented in Table 4.2 and visualy presented on Figure 4.2.

TABLE 4.2: Binned local BHMF of 55 CALIFA type 1 AGN. N is the number of objects per bin.

$\log M_{BH}$ [$M_\odot$]	N	$\log \Phi$ [Mpc^{-3} $\log M_{BH}^{-1}$]
6.50	7	$-3.14^{+0.14}_{-0.20}$
6.75	8	$-3.23^{+0.14}_{-0.21}$
7.00	8	$-3.35^{+0.13}_{-0.18}$
7.25	12	$-3.17^{+0.13}_{-0.20}$
7.50	10	$-3.19^{+0.12}_{-0.17}$
7.75	6	$-3.41^{+0.13}_{-0.18}$
8.00	3	$-3.98^{+0.15}_{-0.23}$
8.25	1	$-4.62^{+0.20}_{-0.40}$

We fitted our binned BHMF with both double power law and Schechter function, Equations (4.6 and 4.7, respectively). As we can see from the figure, both double power law and Schecter function describe well at our narrow black hole mass range, including as well the highest luminosity bin, even though it was excluded from the fit, due to uncertainty of having only one object. The fitting parameters of both

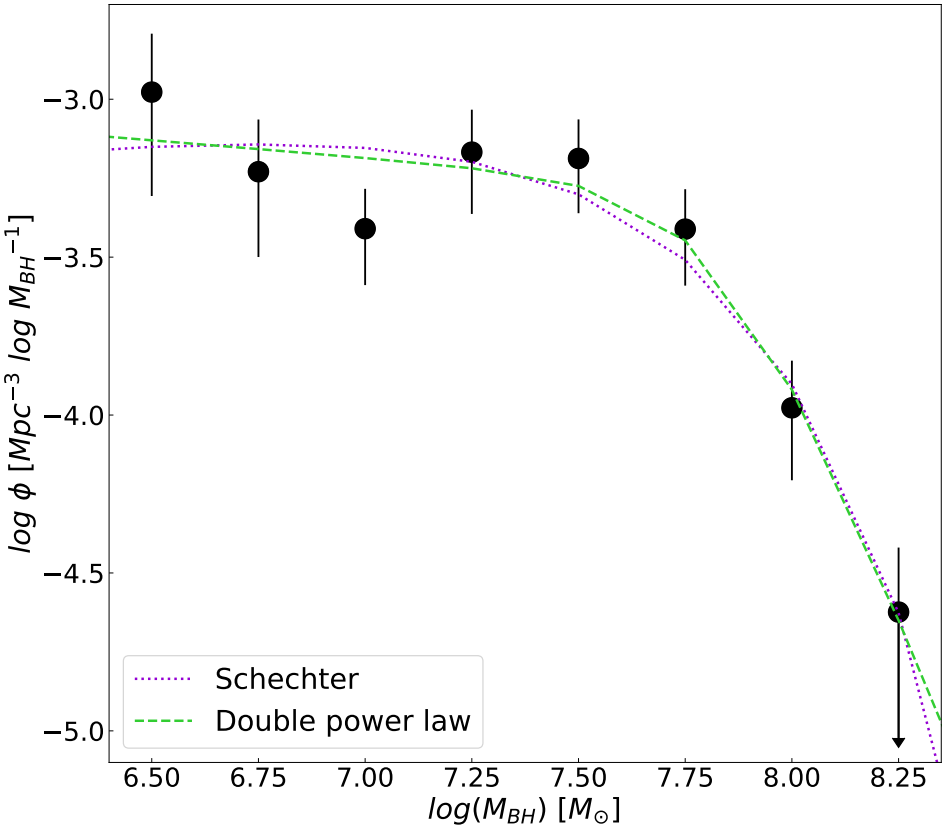

FIGURE 4.2: Binned active BHMF of 55 type 1 AGN from the CALIFA sample, esitmated using $1/V_{max}$ method and bin size of 0.25 dex. M_{BH} are estimated from $M_{BH} - \sigma_*$ correlation of Woo et al. (2013), and are in range between 3.3×10^6 $M_\odot$ and 2.2×10^8 $M_\odot$. Arrow errorbar indicates that a bin contains only one object. Dotted purple line represents the Schechter function fit, and the green dashed line is a double power law.

functions, as well as their calculated reduced chi-square values χ^2_{red} are given in Table 4.3.

The shape of CALIFA BHMF shows indication of flattening towards low mass end, that occurs around $\log(M_{BH}) \approx 7.7$. This agrees with results of our AGNLF, which is an important indicator of consistency between luminosity and mass distribution functions, since black hole masses of CALIFA are estimated independently of AGN luminosity. These AGN properties are however connected through the virial theorem (Chapter 3.3.2), which we dismissed as an accurate black hole mass estimator in case of CALIFA type 1 AGN.

4.5 Eddington ratio distribution function of CALIFA type 1 AGN

As we already mentioned in the Introduction of this chapter, estimation of AGNLF assumes one Eddington ratio for the entire black hole population, which is proven to

TABLE 4.3: Binned local BHMF of 55 CALIFA type 1 AGN. N is the number of objects per bin.

Fitting function	ϕ^* [Mpc^{-3}]	logM^*	α	β	χ^2_{red}
Schechter	4.59×10^{-4}	7.65	-0.87	–	1.40
Double power law	2.29×10^{-4}	7.84	-1.11	-4.31	1.22

be incorrect. Therefore, in order to obtain complete picture of SMBH growth history at all stages of their activity, it is essential that we also estimate ERDF for our type 1 AGN sample.

ERDF is usually described by Schecter function, corresponding to BHMF. We used the following form of the Schecter function from Equation 4.7 to describe our ERDF:

$$\phi(\lambda) = \frac{\phi^*}{\lambda^*} (\frac{\lambda}{\lambda^*})^{\alpha} \, exp(\frac{\lambda}{\lambda^*}) \tag{4.9}$$

where λ^* is the breaking point of ERDF.

Eddington ratio λ is connected to AGN luminosity by the following relation:

$$\lambda = \frac{L_{bol}}{L_{Edd}} \tag{4.10}$$

where L_{bol} is bolometric and L_{Edd} Eddington luminosity of an AGN. Although, due to very wide range of AGN emission, L_{bol} cannot be estimated directly from AGN spectral energy distribution (SED), there are, however, certain corrections that can be introduced in order to estimate L_{bol} with relatively high accuracy. For the purpose of this work we used the broad Hα luminosity $\log(L_{\mathrm{H}\alpha})$ and a correction factor from Richards et al. (2006b). The detailed procedure of calculating λ is described in Chapter 3.3.1.

Using the Eq. 4.10, we calculated Eddington ratios for a sub-sample of type 1 AGN in CALIFA, for which we have black hole mass estimations. This accounts for 55 objects. We obtained very low values of λ, where most of objects have values between 4.1×10^{-5} and 2.4×10^{-3}, with an exception of Mrk 79 that has $\lambda = 4.3 \times 10^{-2}$. This object is a well known Seyfert 1 galaxy, with broad Hα luminosity for a factor of 10 higher than other CALIFA type 1 AGN.

We computed the binned ERDF in the same manner as AGNLF and BHMF, using $1/V_{max}$ method. Following the analogy of equations 4.4 and 4.5, and setting the bin size to be 0.25 dex, we calculated ERDF for our sample of objects. Results are given in Table 4.4. Errors are Poissonian, analogous to estimation of AGNLF and BHMF, but might have larger values at the lowest and the highest λ bin, since both contain one object each.

On Figure 4.3 we present our binned ERDF, with corresponding Schechter function fit (Equation 4.9). The best fit parameters are estimated to be: $\phi^* = 7.77 \times 10^{-4}$ Mpc^{-3}, $\log(\lambda^*) = -3.43$, and $\alpha = -0.50$, with the value of reduced chi-square $\chi^2_{red} = 1.13$. We excluded the highest luminosity bin from the fit due to uncertainty of its error. This may lead to inadequate fit for $\log(\lambda) > 3$, but there is also a significantly lower number of Eddington ratio estimations in this regime. Majority of our objects have Eddington ratios below 10^{-3}, and the data points show a clear flattening of ERDF shape that occurs around $\log(\lambda) \approx 3$. The flattening is consistent with AGNLF and BHMF shapes of CALIFA type 1 AGN, and might indicate that we

TABLE 4.4: Binned local ERDF of 55 CALIFA type 1 AGN. N is the number of objects per bin.

$\log \lambda$	N	$\log \Phi$ [$\mathrm{Mpc}^{-3} \log \lambda^{-1}$]
-4.50	1	$-3.52^{+0.24}_{-0.58}$
-4.25	3	$-3.01^{+0.13}_{-0.19}$
-4.00	4	$-3.22^{+0.15}_{-0.24}$
-3.75	16	$-2.94^{+0.10}_{-0.13}$
-3.50	15	$-3.24^{+0.10}_{-0.12}$
-3.25	10	$-3.20^{+0.14}_{-0.21}$
-3.00	3	$-3.96^{+0.15}_{-0.24}$
-2.75	2	$-4.35^{+0.18}_{-0.30}$
-1.50	1	$-4.72^{+0.20}_{-0.40}$

approached the upper limit in terms of Eddington ratios. This will be discussed in the following section in more detail.

4.6 Discussion

4.6.1 AGN luminosity function in the local Universe

In order to fully understand the shape and evolution of local AGNLF, it is important to see how our result fits into a bigger picture. Previous work in this field is carried out by Schulze, Wisotzki, and Husemann (2009) (S09 in further text), in which they used data from HES in order to establish type 1 AGNLF of bright QSOs across wide range of redshifts. HES sample consists of 329 type 1 AGN in redshift range $0.01 < z < 3.4$, of which 295 of them have detectable broad Hα line with $L_{\mathrm{H}\alpha}$ in range $(10^{40.5} - 10^{44})$ erg s^{-1}. In their work, S09 also compared their type 1 AGNLF with the one obtained by Hao et al. (2005b) (H05). H05 established luminosity function using the maximum likehood method for a sample of $\sim$ 1000 type 1 AGN from SDSS in redshift range $0.01 < z < 0.15$, and in low- to mid-luminosity regime ($L_{\mathrm{H}\alpha}$ between $10^{38.5}$ erg s^{-1} and 10^{43} erg s^{-1}). S09 found that their low-luminosity end overlaps with high-luminosity end of H05 AGNLF. Although, in their work, S09 used only broad Hα component, H05, however used total Hα luminosity, consisting of both broad and narrow components.

For the purpose of maintaining consistency between our results and the low-luminosity end of H05, we calculated the total AGNLF of all 89 type 1 objects in CALIFA, including both broad and narrow components of Hα line. Total Hα luminosities of CALIFA type 1 AGN are in range $(10^{38.5} - 10^{41.5})$ erg s^{-1}. We used the same bin size of 0.25 dex, and errors are Poissonian, consistent with broad Hα luminosity function. We compared our results with binned luminosity functions (estimated using $1/V_{max}$ method) from H05 (adopted to our cosmological parameters) and S09 and presented them on Figure 4.4. Combined Hα luminosities from their works are in range $(10^{38.5} - 10^{43})$ erg s^{-1}.

In order enhance the quality of interpretation of the combined luminosity function, we decided to exclude incomplete bins and bins with only one object from our statistical analysis. As we already mentioned, these bins realistically have larger errors than what is calculated from Poisson statistics. Taking that into account, we can conclude that our luminosity function is in a good agreement with the one

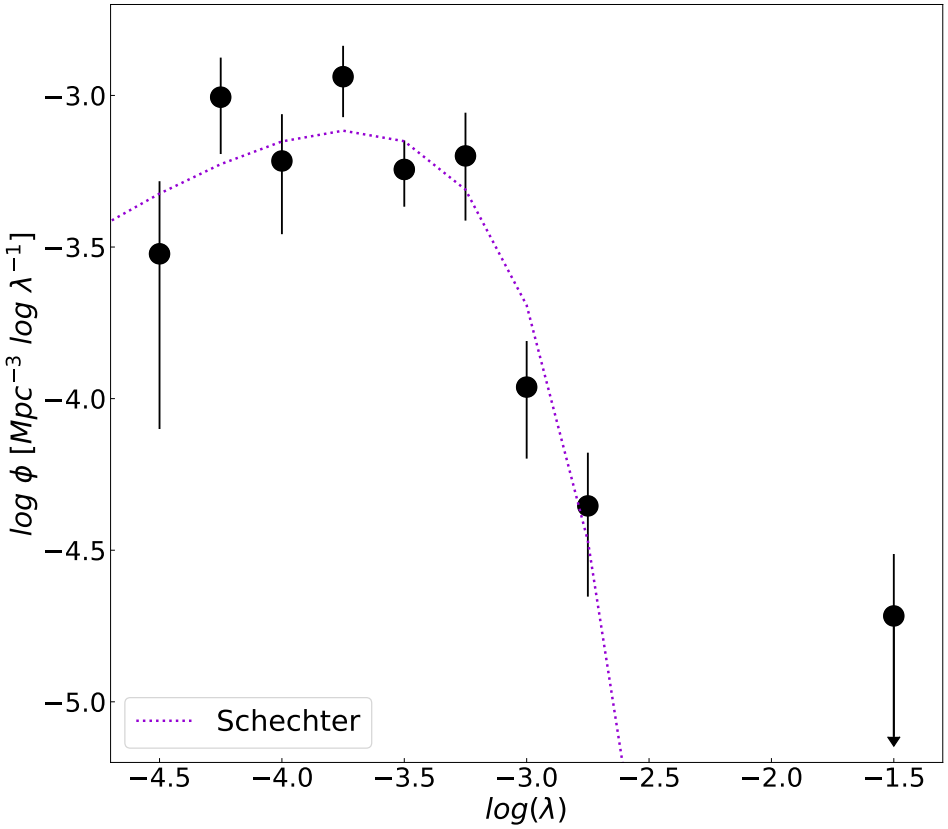

FIGURE 4.3: Binned ERDF for 55 type 1 AGN from the CALIFA sample. Eddington ratios are in range $4.1 \times 10^{-5} - 4.3 \times 10^{-2}$. Equivalent to AGNLF and BHMF, the binned ERDF is estimated using $1/V_{max}$ method with bin size of 0.25 dex. Arrow errorbar indicate bin with only one object. Purple dotted line represents the best fit model of the Schecter function. Green dashed line represents double power law fit of the combined AGNLF.

established by H05 in mid- and high-luminosity range of our sample ($\log L_{\mathrm{H}\alpha,\mathrm{tot}}$ between 39.75 erg s^{-1} and 40.00 erg s^{-1}). The discrepancy arises for the values $\log L_{\mathrm{H}\alpha,\mathrm{tot}} < 39.75$. Since we have no information on the bin completeness for the sample of H05, we decided not to account their last two low-luminosity-end bins into our analysis. If we assume that these data points represent true values of luminosity function, this would indicate that for the luminosities of $\sim 10^{38.7}$ erg s^{-1} we would expect to have up to five times higher number density of type 1 AGN in CALIFA. This scenario is totally unlikely, considering their already high fraction. Also worth mentioning is that, even though the highest luminosity bin in CALIFA sample contains only one object – Mrk 79, it aligns perfectly with both results from H05 and S09. This might serve as a confirmation of the validity of our results. We can conclude that the flattening at the low-luminosity end that we observe is real, unlike constant increasing obtained by H05, as it is impossible to have five times larger number density than what we already observed. This would indicate that in the luminosity regime $\sim 10^{38}$ majority of objects in the local Universe are LLAGN, which is far from realistic picture.

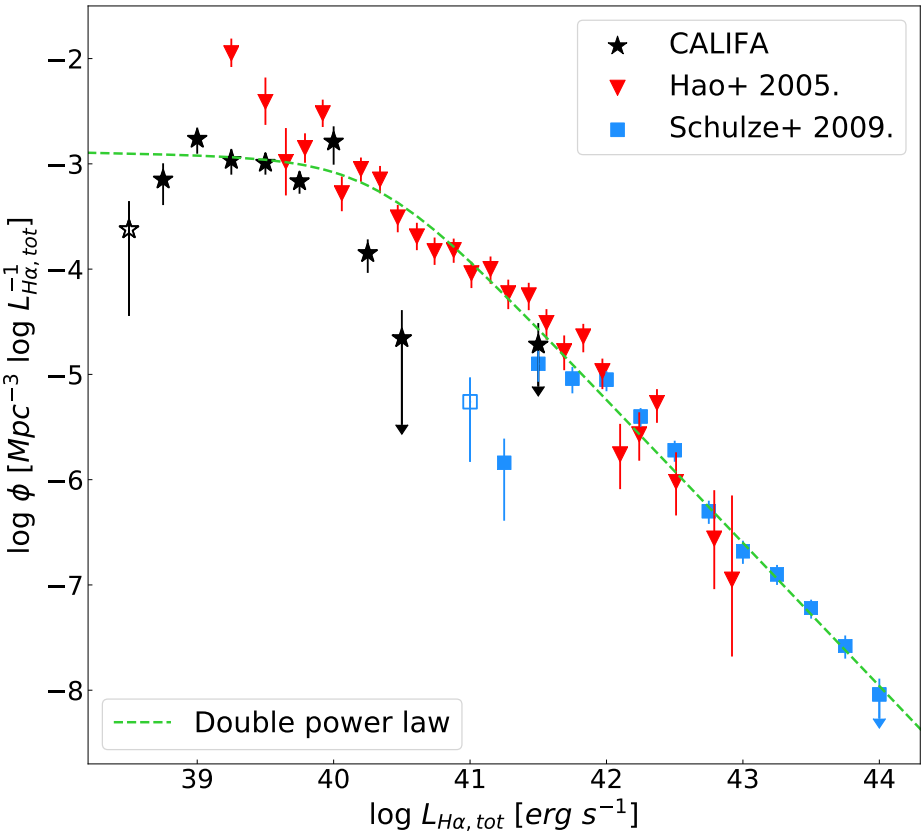

FIGURE 4.4: Binned emission-line AGNLF of Hα line (broad+narrow component). Black stars represent CALIFA type 1 AGN, while red diamonds, and blue squares are luminosity function results obtained by Hao et al. (2005b) and Schulze, Wisotzki, and Husemann (2009), respectively. As in previous figures, open symbols indicate incomplete bins, while arrow errorbars represent bins that contain only a single object.

As we already mentioned in Chapter 4.3, the most commonly used function for AGNLF parametrization is a double power law, given by Equation 4.6. Combining all three data samples, we find best fit parameters of double power slope to be: $\phi^* = 4.89 \times 10^{-4}$ Mpc^{-3}, breaking at log$L^* = 40.31$, $\alpha = -1.03$ describing the faint-end, and $\beta = -2.34$ describing the bright-end slope, with $\chi^2_{red} = 2.13$. The shape of the combined AGNLF, including datapoints from CALIFA, H05 and S09 indicates that there is an apparent flattening, occurring around $L_{\mathrm{H}\alpha,\mathrm{tot}} \approx 10^{40}$ erg s^{-1}. This flattening can be interpreted as an upper limit of AGN number density in the local Universe, and is consistent with AGN downsizing scenario, where at $z \approx 0$ majority of AGN are in low-luminosity regime. This will further be discussed in Chapter 4.6.3.

Another study in this field was performed by Greene and Ho (2007), where they established Hα AGNLF for a sample of $\sim$ 8500 type 1 AGN from SDSS DR4. Since their original work included an error introduced when determining $1/V_{max}$ estimator, they later published the Erratum (Greene and Ho (2009), G09) with correct values of both AGNLF and BHMF. On Figure 4.5 we compare results of our broad Hα luminosity function with the one estimated by G09. While their AGNLF agrees quite well with results from S09, we on the other hand find that there is a divergence between our and G09 luminosity functions for $L_{\mathrm{H}\alpha,\mathrm{broad}} < 10^{40.25}$ erg s^{-1}. This discrepancy is mostly due to survey sensitivities for the lowest luminosity objects, as well as difference in selection of respective samples. G09 analyzed only the objects that are classified as AGN by SDSS categorization, while we already showed that majority of AGN that contain broad Hα line might be labeled as LINERs (Chapter 2). There is also an apparent disagreement between G09 and H05 luminosity functions, where the two AGNLF have significantly different shapes below $L_{\mathrm{H}\alpha,\mathrm{broad}} \approx 10^{41}$ erg s^{-1}, even though they had very similar selection criteria. This is analyzed in detail in Greene and Ho (2009), where they draw the conclusion that SDSS might not be an adequate survey to use for the objects with luminosities below $\sim 10^{40.5}$ erg s^{-1}. This is another argument that goes in favor of trusting the results from the CALIFA survey, which we already discussed in Chapter 2.

4.6.2 Active fraction of CALIFA black holes

The black hole mass active fraction can provide us with significant information about the activity cycle of SMBHs at different redshifts, which could further provide more information on the accreting mechanisms of AGN. In order to understand the census of active SMBHs in our sample, it is useful to compare our derived active BHMF with the local mass function of quiescent galaxies. Estimation of the BHMF of the quiescent galaxies relies on the correlations between black hole masses and properties of their host galaxies, since the sample of dynamically measured quiescent black hole masses is highly limited and biased (we already discussed this in Chapter 3). This approach requires that we have well established relationships between black hole masses and their hosts' bulge properties such as luminosity, stellar velocity dispersion or bulge mass (Salucci and Persic, 1999; Yu and Tremaine, 2002; Marconi et al., 2004; Graham et al., 2007; Vika et al., 2009; Li, Ho, and Wang, 2011). On the other hand, Shankar, Weinberg, and Shen (2010) used a different approach to predict black hole duty cycle at $z \approx 0$, implementing simplified black hole growth models, assuming constant accretion rate. This is in contradiction with observational results proving that black holes accrete at wide range of Eddington ratios, which is an important fact in determining their activity cycle.

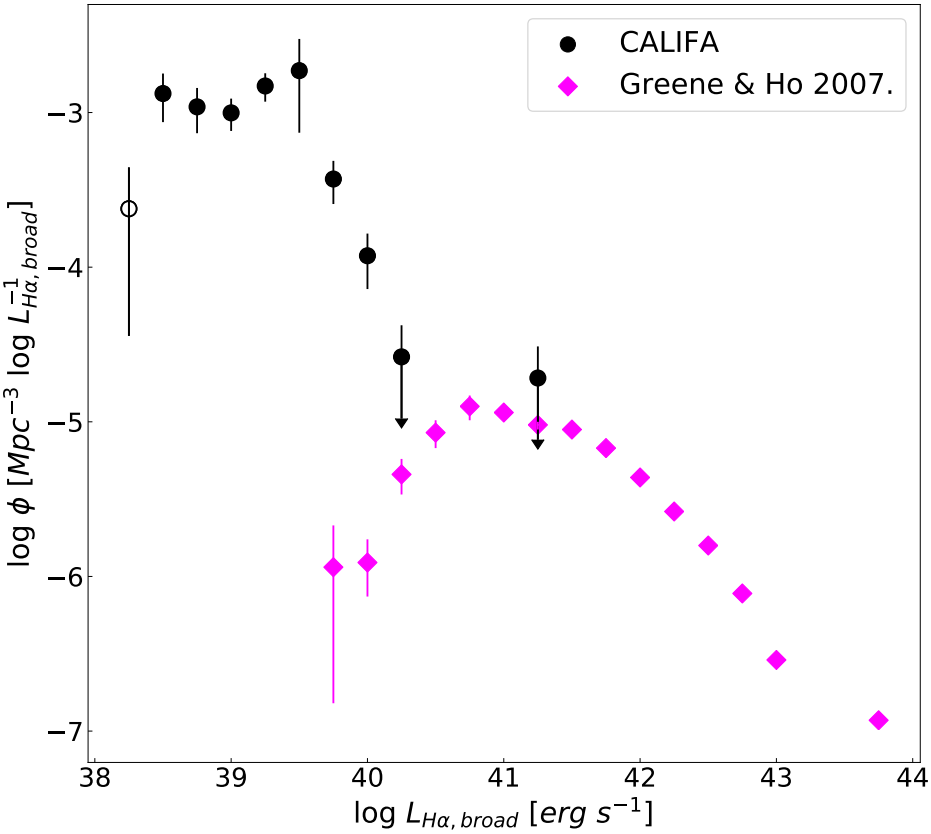

FIGURE 4.5: Binned emission line AGNLFs of broad Hα line. The black dots represent luminosity function of type 1 AGN in CALIFA, while magenta diamonds are the results of binned luminosity function from Greene and Ho (2009). As in previous figure, open symbols and arrows indicate incomplete bins and bins that contain only one object, respectively. Both luminosity functions are calculated using $1/V_{max}$ estimator.

The most commonly used local mass function of quiescent black holes is the one derived by Marconi et al. (2004) (M04). More recent studies of quiescent BHMFs (Vika et al., 2009; Li, Ho, and Wang, 2011) show perfect agreement with M04 results at $z \approx 0$. For this reason, and to maintain consistency with previous studies, we decided to use the quiescent BHMF estimated by M04 in order to determine the active fraction of CALIFA type 1 AGN sample.

On the upper panel of Figure 4.6 we show how the our active BHMF is distributed in comparison with the quiescent BHMF established by Marconi et al. (2004), as well as with some previous studies in this field. Schulze and Wisotzki (2010) (S10) calculated binned BHMF of HES, for a same sample of objects they calculated type 1 AGNLF discussed in previous Section. Greene and Ho (2009) recalculated BHMF of their AGN sample from SDSS. As we already discussed, there is and apparent disagreement between our AGNLF and the one estimated by G09 sample and the ones from S10 and G09 is a direct consequence of different luminosity regimes that are reached with these studies. As in CALIFA we probed significantly lower broad Hα luminosities, this implies proportionally higher number of active black holes that

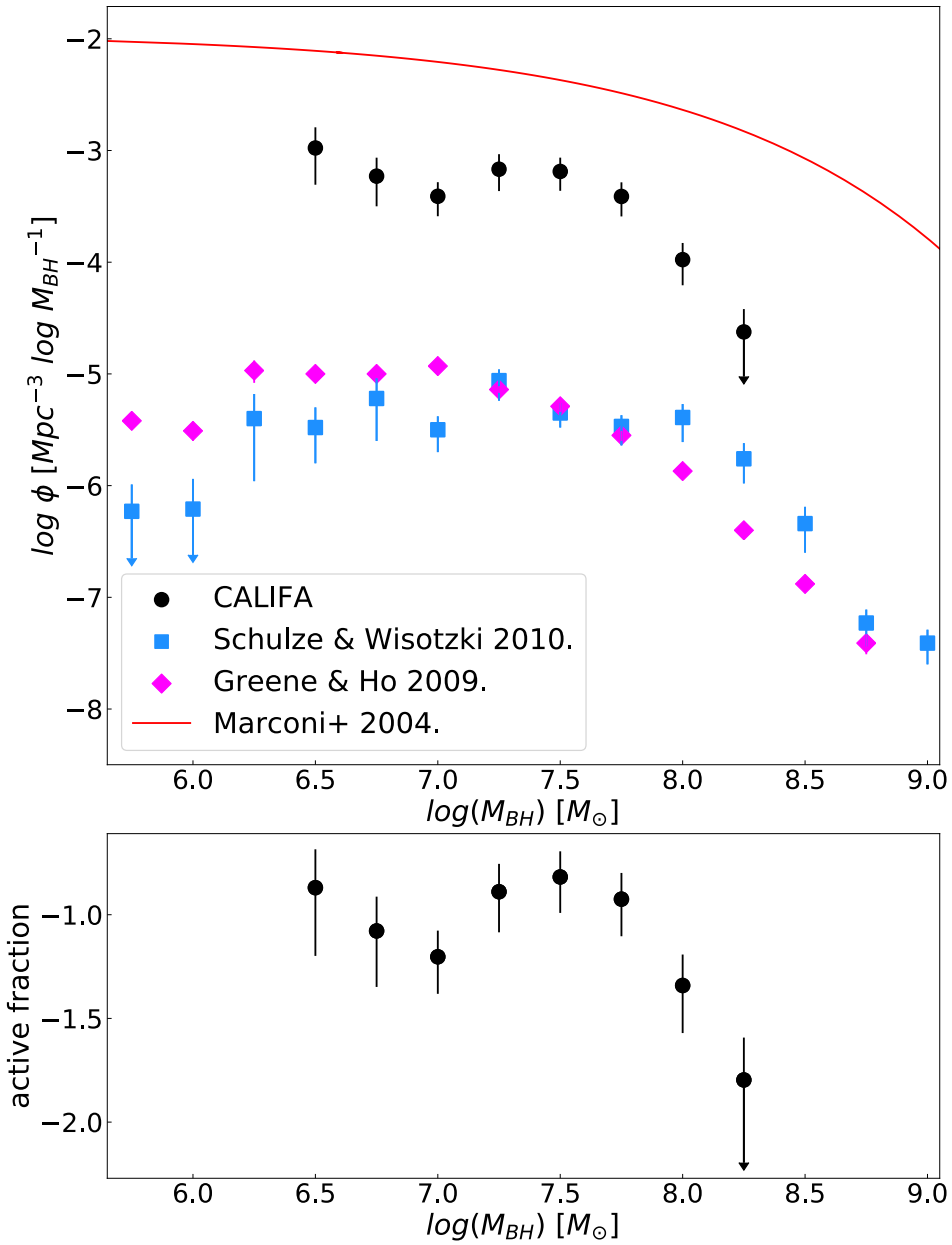

FIGURE 4.6: Upper panel: Comparison of binned broad Hα black hole mass functions (data points) to the BHMF of quiescent galaxies estimated by Marconi et al. (2004) (solid red line). Black dots represent our results for 55 type 1 AGN in CALIFA survey, while magenta diamonds and blue squares are BHMFs estimated for different samples of type 1 AGN, by Greene and Ho (2009) and Schulze and Wisotzki (2010), respectively. Greene and Ho (2009) used a sample of $\approx$ 8500 type 1 AGN from SDSS, while Schulze and Wisotzki (2010) estimated their BHMF for a sample of $\sim$ 300 type 1 AGN from Hamburg/ESO survey. Difference in height between CALIFA BHMF and the ones estimated by Greene and Ho (2009) and Schulze and Wisotzki (2010) is a consequence of different luminosity regimes probed by these studies. Lower panel: Active fraction of CALIFA black holes, calculated by subtracting CALIFA active BHMF from the one of quiescent galaxies of Marconi et al. (2004). As in previous figures, arrow indicates that a respective bin contains only one object.

could not be identified in previous studies. In previous two chapters we already discussed and justified our approach in detecting these objects, proving that these are genuine low-accreting black holes located in extremely LLAGN. Such result imposed a redefinishion of what "active" in AGN stands for, since it is previously considered that AGN with Eddington ratios below 10^{-3} could not form a BLR. As we can see from Figure 4.6, our binned BHMF has similar shape as the quiescent one estimated by M04, indicating the flattening below $M_{BH} \approx 10^{7.7}\ M_{\odot}$. Lack of lower mass black holes in our sample is a consequence of M_{BH} estimation method, where we could only calculate black hole masses of objects we had stellar velocity dispersion parameters estimated by Méndez-Abreu et al. (2017). It is possible that with a larger sample of σ_* we could have reached even lower black hole masses. However, it is important to note that our black hole masses are estimated independently on AGN luminosities, and that the agreement between our AGNLF and BHMF results confirms that $M_{BH} - \sigma_*$ correlation is a good estimator of black hole masses in the CALIFA sample.

Lower panel of Figure 4.6 represents duty cycle or the fraction of CALIFA black holes that are currently in active phase as a function of black hole mass. Our sample asymptotically reaches upper limit of active black holes in local Universe. Consequently, we wouldn't expect the fraction of active black holes to be significantly higher in local Universe than what we estimated. We can clearly see the decrease of our active fraction with increasing black hole mass, especially for $\log(M_{BH}) > 7.5$, which is in direct agreement with scenario of anti-hierarchical growth of black holes, which will be discussed in the next sub-section.

S10 separated their type 1 AGN sample into two categories based on Eddington ratio - objects that have $\log(\lambda) < -1$ and those with $\log(\lambda) > -1$. They showed that there is clear separation in an active fraction of these two groups of objects, implying a higher active fraction of objects with $\log(\lambda) < -1$, and a clear decrease of the active fraction with $\log(\lambda) > -1$ with increasing black hole mass. It is important to note that CALIFA black hole sample contains objects with extremely low Eddington ratios, that would all, except Mrk 79, fit into $\log(\lambda) < -1$ category. This highlights the importance of a survey depth in estimation of active fraction of black holes. For comparison we show the number densities of CALIFA black hole sample Eddington ratios with the ones estimated by S10 on Figure 4.7. We can clearly see that one separated bin at $\log(\lambda) = -1.25$ matches with the ERDF from S10. This is again case of Mrk 79, that can be classified as what is previously thought to be "typical" type 1 AGN. CALIFA objects with lower Eddington ratios ($\log(\lambda) < -3$) have higher number density in local Universe than type 1 AGN used in work of S10. This result emphasizes the importance of including different accretion rates into analysis of black hole demographics, in order to fully understand black hole duty cycle.

4.6.3 Anti-hierarchical growth of black holes and AGN downsizing

In the previous section we showed that in local Universe, we have higher fraction of black holes accreting at lower Eddington ratios, which is in general agreement with scenario of anti-hierarchical growth of black holes (Ueda et al., 2003; Steffen et al., 2003; McLure and Dunlop, 2004; Merloni, 2004; Merloni and Heinz, 2008). According to this scenario the most massive black holes accreted their mass faster and in earlier cosmic times, while in the current epoch low-mass SMBHs, accreting at significantly lower rate, are predominant. This trend is also know as AGN cosmic downsizing, and is originally observed in X-ray luminosity functions of AGN (Cowie et al., 2003; Steffen et al., 2003; Ueda et al., 2003), and is later confirmed in

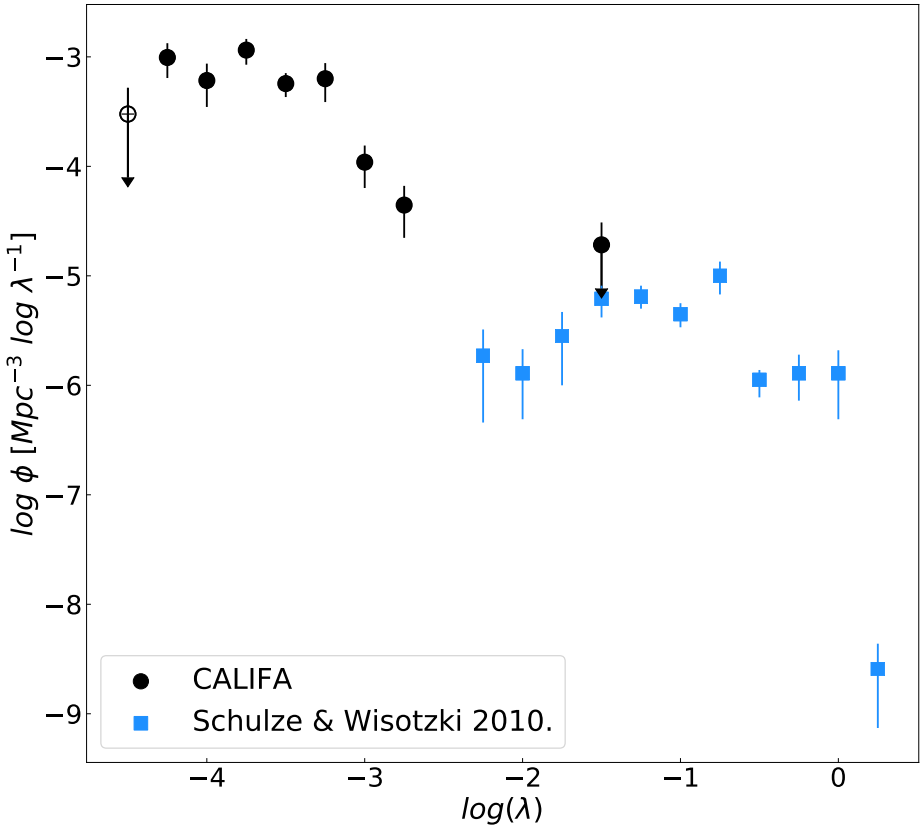

FIGURE 4.7: Comparison of binned Eddington ratio distribution functions from CALIFA (black dots) and Schulze and Wisotzki (2010) (blue squares) type 1 AGN. As in previous figures, open symbols and arrows indicate incomplete bins and bins that contain only one object, respectively. Both luminosity functions are calculated using $1/V_{max}$ estimator. Difference in height between two ERDF is a direct consequence of different luminosity regimes probed by these studies. The flattening of CALIFA ERDF might indicate that we approached the upper limit in terms of Eddington ratios.

optical domain (Wolf et al., 2003; Cristiani et al., 2004; Croom et al., 2004) and NIR (Matute et al., 2006).

Bongiorno et al. (2007), Croom et al. (2009), and Schulze et al. (2015) analyzed AGN luminosity functions at $z \approx 1.5$ in wide luminosity ranges. Their results imply that AGNLF has significantly different shape at $z \approx 1.5$, than what is found for $z \approx 0$. There is an evident break of higher-z luminosity functions that is absent in luminosity functions estimated from local surveys. This proves that the number density of high-mass, luminous AGN was significantly higher at earlier times, while the local Universe is the era of of LLAGN.

However, considering only luminosity function, it is not clear whether AGN downsizing is caused by black hole mass or Eddington ratio evolution, or by a combination of both. In order to understand this, it is important to separate these distribution functions and analyze them individually. As we showed, the behavior of active BHMF and ERDF follow the low-end flattening trend of AGNLF, implying

that both distribution functions are contributing to the AGNLF downsizing. In their work, Schulze et al. (2015) calculated BHMF and ERDF of type 1 AGN from three different optical samples (VVDS, zCOSMOS and SDSS), using the maximum likehood method. Their combined type 1 AGN sample covers wide range of AGN bolometric luminosities (10^{44} erg s^{-1} $< L_{bol} <$ 10^{48} erg s^{-1}) at $1 < z < 2$. They concluded that the downsizing in AGNLF is driven by both downsizing in BHMF and ERDF, while BHMF is more dominant of the two. However we did not evaluate on this topic, since both M_{BH} and λ estimates are highly uncertain in our low-end regime.

We conclude, unanimously to previous results, that there is a strong evidence of AGN downsizing at low-luminosity end of AGNLF of CALIFA type 1 AGN, driven by both black hole mass and Eddington ratio distribution functions. CALIFA type 1 AGN accrete at extremely low level, which probably sets the upper limit of AGN duty cycle. If there were some objects undetected by our method, those would be the ones with even lower black hole masses, in almost inactive accretion stage.

4.7 Summary and Conclusions

We conducted a study of low-luminosity AGN in local Universe ($0.005 < z < 0.03$), using the CALIFA survey data sample, consisting of 89 objects that have detectable broad Hα emission line in their central spectra. We estimated emission-line luminosity function of broad Hα lines, as well as distribution functions of their central black hole masses and Eddington ratios for 55 of these objects. Luminosities, black hole masses and Eddington ratio estimations that we used are previously calculated in Chapter 3.

Broad Hα luminosities of our type 1 AGN sample appear to be distinctly low, having values in range $(10^{38} - 10^{41})$ erg s^{-1}. Applying $1/V_{max}$ method, we estimated binned AGNLF of these objects. We found that double power law fit to the binned luminosity function fails to accurately describe its trend, due to small number of data points, large uncertainties in limiting bins and narrow luminosity range. In order to enhance the probability of obtaining a good fit, we combined our AGNLF with the ones estimated by Schulze, Wisotzki, and Husemann (2009) and Hao et al. (2005b). Hao et al. (2005b) obtained luminosity function for a sample of $\sim$ 1000 low-redshift ($z < 0.15$) type 1 AGN from SDSS. They included both broad and narrow component of Hα emission line, and estimated their luminosities to be in range $(10^{38.5} - 10^{43})$ erg s^{-1}. Schulze, Wisotzki, and Husemann (2009) used the sample of $\sim$ 300 bright ($10^{40.5}$ erg s^{-1} $< L_{\mathrm{H}\alpha} <$ 10^{44} erg s^{-1}) type 1 AGN in redshift range $0.01 < z < 3.4$ from the Hamburg/Eso Survey. In order to preserve consistency between our bright-end and faint-end luminosity function of Hao et al. (2005b), we included total Hα luminosities in the combined AGNLF. Respective luminosities are in range $10^{38.5}$ erg s^{-1} $< L_{\mathrm{H}\alpha,tot} <$ $10^{41.5}$ erg s^{-1}.

We found that combined luminosity function can be well described by a double power law with slope , breaking at $10^{40.31}$ erg s^{-1}. Below this breaking luminosity we can observe an apparent flattening of both combined, and CALIFA only luminosity functions, that can be interpreted as an upper limit of AGN number density in local Universe.

We also compared our AGNLF with the one established by Greene and Ho (2009), for a sample of $\sim$ 8500 type 1 AGN from SDSS. Two luminosity functions appear to be inconsistent with each other for luminosities below $10^{40.25}$ erg s^{-1}. We concluded that the inconsistency is due to survey sensitivities for the lowest luminosities and

different sample selections, where CALIFA is more reliable survey to use for luminosities below $10^{40.5}$ erg s^{-1}.

For a sub-sample of 55 CALIFA type 1 AGN we estimated black hole mass function and Eddington ratio distribution function. Black hole masses of CALIFA sample were estimated using the $M_{BH} - \sigma_*$ correlation established by Woo et al. (2013). We used bulge parameters obtained by Méndez-Abreu et al. (2017) in order to estimate stellar velocity dispersions of our type 1 AGN. The black hole masses of CALIFA type 1 AGN are estimated to lay between 3.3×10^6 $M_\odot$ and 2.2×10^8 $M_\odot$. Eddington ratios are estimated from bolometric luminosities after applying correction factor from Richards et al. (2006b). We found that CALIFA type 1 AGN have extremely low Eddington ratios, having values between 4.1×10^{-5} and 2.4×10^{-3}, with an exception of Mrk 79 that has $\lambda = 4.3 \times 10^{-1}$. This object also has higher broad Hα luminosity for a factor of 10 comparing to other CALIFA type 1 AGN, and its value agrees quite well with all discussed luminosity functions, likely confirming the validity of our results.

Equivalent to approach of estimating AGNLF, we used $1/V_{max}$ method to calculate both black hole mass and Eddington ratio distribution functions. We fitted BHMF with both double power law and Schecter function, and found that both perform well and are in mutual agreement. Eddington ratio distribution function is well described by Schecter function with breaking point at $\log(\lambda) = -3.43$. We excluded Mrk 79 from statistical analysis of ERDF, since it is the only object in the highest λ bin and, therefore its ERDF estimation is highly uncertain. This is the reason why our Schecter function fit has a steep slope for $\log(\lambda) > -3$. In order to complete a picture of local ERDF, we need to include more higher Eddington ratio objects. Unfortunately there are not many studies of ERDF up to date. The one conducted by Schulze and Wisotzki (2010) for HES type 1 AGN has Eddington ratios above -2.25 in logharitmic units, but we find that our estimation of λ for Mrk 79 ($\log(\lambda) = -1.37$) agrees well with their result.

The shape of CALIFA black hole mass and Eddington ratio distribution functions show indication of flattening towards low mass and low-λ end. The flattening is consistent with the shape of AGNLF and occurs around $\log(M_{BH}) \approx 7.7$ in BHMF and around $\log(\lambda) \approx -3$ in ERDF. This result indicates that there is consistency between luminosity and mass distribution functions, taking into account that black hole massses are estimated independently of broad Hα luminosities.

We also compared our active BHMF to the one of quiescent galaxies, estimated by Marconi et al. (2004) and determined the fraction of CALIFA black holes that are currently in active phase, or their duty cycle. Our active fraction decreases with increasing black hole mass for $\log(M_{BH}) > 7.5$, which agrees with the scenario of anti-hierarchical growth of black holes (Cowie et al., 2003; Ueda et al., 2003; Steffen et al., 2003; McLure and Dunlop, 2004; Merloni, 2004; Merloni and Heinz, 2008). Anti-hierarchical growth of black holes, or AGN cosmic downsizing, scenario assumes that the most massive black holes were formed in luminous AGN in early cosmic times, while in the local Universe, these luminous AGN are in less active phase, and low-luminosity low-mass SMBHs contribute to the majority of the AGN population.

Analyzing the flattening trend in both black hole mass and Eddington ratio distribution functions, we concluded that the evolution of both contributes to the AGNLF downsizing, implying that the local Universe consists of high fraction of low-mass SMBH in extremely low accretion regimes. CALIFA type 1 AGN have significantly low Eddington ratios, and would be considered as inactive by the traditional definition of active AGN having $\lambda > 10^{-3}$ (Nicastro, 2000). We reevaluated the validity of this claim, as it would imply that AGN below this Eddington ratio cannot form a

BLR, which is not the case with CALIFA AGN sample. That being said, CALIFA type 1 AGN most likely reach the upper limit of AGN duty cycle in local Universe. We would not expect active fraction to be significantly higher than what we estimated.

We proved once more that AGNLF alone does not give us sufficient information on what may cause the downsizing trend, and has to be disentangled into black hole mass and Eddintgton ratio distribution functions. Aside from that, AGNLF of CALIFA type 1 AGN might serve as a great zero-point for further studies of AGNLF in the local Universe. Our research also stresses the importance of including different Eddington ratios into analysis of black hole demographics, in order to fully understand black hole growth history of SMBH.

CHAPTER 5

Complete AGN census in the CALIFA survey

ABSTRACT

In order to obtain full AGN census in the CALIFA survey galaxy sample, we performed a cross-correlation between 542 CALIFA DR3 galaxies and multiwavelength surveys, *Swift* – BAT 105 month catalogue and NRAO VLA Sky Survey (NVSS), in hard X-ray (15 - 195 keV) and radio (1.4 GHz) domains, respectively. These cross-correlations revealed 6 potential X-ray, and 14 radio-AGN. Additionally, NVSS radio images showed the presence of a jet-like signature in 75% of our radio-AGN candidates. Thirteen of these multiwavelegth AGN candidates were previously already classified as either type 1 or Seyfert 2 AGN, according to the broad Hα emission line present in their nuclear spectra, or standard emission-line ratio diagnostic diagrams. This classification revealed 7 new AGN (1 X-ray and 6 radio-AGN) that we previously missed with the optical classification methods. We also constructed spatially resolved emission-line ratio diagnostic diagrams of all emission-line galaxies from the CALIFA, in order to detect potential extended AGN emission in galactic regions located 10 – 20 kpc from the nucleus. This method revealed in total 6 potential extended AGN, of which only one object was previously not classified as either type 1 or Seyfert 2 AGN. Having five different AGN types enabled us to obtain a highly complete sample of low-luminosity AGN (LLAGN) census in the CALIFA survey, implying that these LLAGN in fact contribute a significant fraction of 24% of the emission-line galaxies in the local Universe.

5.1 Introduction

5.1.1 AGN phenomenology and diagnostics in the optical domain

Supermassive Black Holes (SMBHs) are considered to be the main powering source of active galaxies, and, while in their active stage, they represent an important phase of galaxies' duty cycles. Active Galactic Nuclei (AGN) are spread over wide range of luminosities, from the most luminous QSOs at high redshifts, to the significantly fainter and the most frequent Seyfert galaxies, with luminosities that are 1000 times weaker than those of QSOs. In order to reach the low-end of AGN luminosity distribution, the respective AGN surveys need to be of high sensitivity and spectral resolution. On the contrary to the high-redshift early Universe, the local Universe consists mainly of low-luminosity AGN (LLAGN), with luminosities weaker than even those of Seyfert galaxies. Thes LLAGN impose a challenge in studying of the entire AGN population, but it is essential to understand these objects in order to have a full picture of AGN activity cycle and the growth of their central SMBHs across the entire cosmic history.

Spectral Energy Distribution (SED) of luminous AGN is characterised by the specific power-law shape of index $\alpha \approx 0.5$ (Vanden Berk et al., 2001), the blue featureless continuum, the presence of strong Broad Emission Lines (BELs), and strong emission in X-ray or radio domain. In case of LLAGN, this picture is, however, changed, as the characteristical power-law shape is rather flattened, and the big blue bump disappears from the spectrum (Ho, 1999; Nagar, Falcke, and Wilson, 2005; Eracleous, Hwang, and Flohic, 2010; Younes et al., 2012). Rather, there is a peak at mid-IR wavelengths (big red bump), and in the majority of the faint AGN sources BELs can no longer be detected due to their extremely weak emission. As a consequence the corresponding SED of LLAGN appears to be flatter at the optical and UV wavelengths, lacking the typical power-law feature that is observed in their luminous counterparts. Such SED cannot be explained with radiativelly efficient accretion disk models, rather the optically thick and geometrically thin accretion disk is decomposed into a 3-component structure, consisting of the inner optically thin quasi-spherical structure corresponding to the Radiativelly Inefficient Acretion Flows (RIAFs, Narayan and McClintock (2008), Yuan and Narayan (2014), Narayan and Yi (1994), Blandford and Begelman (1999), and Narayan, Igumenshchev, and Abramowicz (2000)), outer truncated disk and the jet detectable in radio domain. Such picture of the "jetted" LLAGN imposes that these objects are expected to be radio-loud, which is confirmed in early studies (Hota and Saikia, 2006; Gallimore et al., 2006; Del Moro et al., 2013; Singh et al., 2016; Harrison et al., 2015). Therefore in order to properly understand the nature of LLAGN, and how they fit into a bigger picture of the entire AGN population, it is essential that we study these objects from different perspectives, and in multiple wavelength bands, as each may reveal some additional information about their nature.

One of the common methods to separate optically selected AGN from other emission-line galaxies, is to compare the strength ratio of their emission lines. Such criterion, that uses two-dimensional line-ratio strengths was originally proposed by Baldwin, Phillips, and Terlevich (1981), and later adopted and revised by Osterbrock and Pogge (1985) and Veilleux and Osterbrock (1987), consists of empirical diagnostic diagrams that use two optical emission line ratios ([NII]/Hα, [SII]/Hα [OI]/Hα, and [OIII]/Hβ), and are commonly called the BPT diagrams. The BPT diagrams distinguish between star-forming galaxies, Seyfert 2 AGN, and Low Ionization Nuclear Emission Regions (LINERs).

Detection of the permitted BELs, such as Hα, Hβ, MgII and CIV, in nuclear spectra of galaxies is a good indicator of type 1 AGN. These BELs with Full Widths at Half Maximum (FWHMs) in range $1000 - 10000$ km s^{-1} can be produced only by accretion of the material onto the central SMBHs, as other mechanisms could not produce such high gas velocities. This method is therefore widely used to detect luminous type 1 AGN, and with sufficient survey sensitivity, it can be expanded to lower luminosities, typical for LLAGN.

So far, not many studies are conducted on the nature of LLAGN. The most prominent work was performed by Ho, Filippenko, and Sargent (1997a), Ho et al. (1997), Ho, Filippenko, and Sargent (1997b), Ho, Filippenko, and Sargent (1997b), and Ho, Filippenko, and Sargent (2003), where they observed central regions of $\sim$ 400 local ($z < 0.5$) galaxies from the Palomar Survey (Filippenko and Sargent, 1985; Ho, Filippenko, and Sargent, 1995) for the purpose of detecting LLAGN. Their work showed that the broad Hα component is present in $\sim$ 20% of the spectra of galaxies previously labeled as AGN. The latest work in this field, conducted by Eun, Woo, and Bae (2017) indicates that this number is significantly lower, where BELs are detected in only around 3% of Seyfert 2 galaxies. However, the research of Eun, Woo, and Bae (2017) is performed on the sample of local ($z < 0.1$) galaxies selected from Sloan Digital Sky Survey (SDSS, Abazajian et al. (2009)), which may not be the best survey for studying LLAGN (Greene and Ho, 2009), due to its fixed 3″ aperture diameter.

Due to relatively low luminosities of the LLAGN, their emission is often highly diluted by the starlight coming from their host galaxies, and they are often hard to detect in optical spectral domain. An important aspect of AGN is that they emit in very broad wavelength range, usually being strong X-ray and/or radio emitters.

5.1.2 AGN in multiwavelength bands

X-ray AGN

X-ray emission from the central regions of galaxies is one of the key aspects in distinguishing AGN from other powering mechanisms, since most AGN are strong X-ray emitters compared to the non-active galaxies. Therefore the observations in X-ray band play crucial role in AGN diagnostics, as objects that are too weak to be detected in optical domain can easily be identified in X-ray band (Loewenstein et al., 2001; Ho, Filippenko, and Sargent, 2003; Ho, 2003; Fabbiano et al., 2004; Pellegrini, Ciotti, and Ostriker, 2008).

X-ray emission can be divided into two categories – soft X-rays, with energies 2 - 10 keV, and hard X-rays emitting in 15 - 195 keV band. The soft X-ray emission is emitted from a compact central source, while hard X-rays are most probably produced by Compton scattering of the photons from the accretion disk (Haardt and Maraschi, 1991; Zdziarski et al., 2001). Soft X-rays may suffer from the obscuration effects, as X-ray emission of lower energies is more absorbed than that of higher energies. As X-ray emission is sensitive to the amount of absorbing material, it can therefore be used to distinguish between obscured (type 2) and unobscured (type 1) AGN (Padovani, 2017).

As we already mentioned, SED of LLAGN significantly differs than SED of their luminous counterparts, which also reflects on the multiwavelength observations of LLAGN. Soft X-ray features that are typical for luminous AGN, such as rapid variability (Ptak et al., 1998; Pian et al., 2010; Younes et al., 2010; Younes et al., 2011;

González-Martín and Vaughan, 2012; Hernández-García et al., 2014), or characteristical broad Fe Kα lines (Ptak et al., 2004; González-Martín et al., 2009; Younes et al., 2011) are not observed in spectra of LLAGN.

The most prominent X-ray surveys that produced significant results in AGN diagnostics are *Chandra*, XMM – *Newton*, and ROSAT in soft, and *Swift* – BAT survey in hard X-ray band. These surveys have collected a sample of thousands of both obscured and unobscured AGN up to $z = 5$, with a broad range of luminosities (10^{39} erg s^{-1} $< L_X <$ 10^{44} erg s^{-1}, Civano et al. (2019), Kollatschny et al. (2008), and Oh et al. (2018)). Unlike luminous AGN, there are only few studies provided so far on X-ray LLAGN. Terashima and Wilson (2003) analyzed a sample of soft X-ray observations (2 – 10 keV) of 11 LINERs, 3 low-luminosity Seyfert galaxies, and one HII – LINER transition object from *Chandra*, and detected weak ($10^{38} - 10^{42}$ erg s^{-1}) X-ray nucleus in all but one object. They calculated the X-ray–to–Hα luminosity ratios for these objects and found that in majority of cases they are in good agreement with the values characteristical for LLAGN and more luminous AGN. The most recent work on X-ray LLAGN is conducted by Younes et al. (2019), where they performed the analysis of simultaneous *Nu*STAR + XMM – *Newton* observations of two LLAGN (NGC 3998 and NGC 4579), of which both have detectable weak broad Hα line in the optical domain (Ho, Filippenko, and Sargent, 1997b).

Radio AGN

Another very strong indicator of AGN presence in the centre of a galaxy is a strong compact radio emission. Studies of Verry Large Array (VLA) radio continuum of nearby early-type galaxies, conducted by Sadler, Jenkins, and Kotanyi (1989) and Wrobel (1991), revealed high fraction ($30 - 40$ %) of compact radio cores corresponding to AGN, with similar detection rate to optical emission lines (Ho, Filippenko, and Sargent, 2003). These objects are mostly classified as LINERs according to the standard diagnostic diagrams, implying that some LINERs that are actually LLAGN appear to be radio-loud sources. Heckman (1980a) also pointed out to radio-loudness of LINERs, and Wrobel (1991) and Slee et al. (1994) showed that these objects have relatively flat spectral indices, corresponding to the LLAGN SED.

Few studies in the past decade investigated the radio-emission of nearby LLAGN from the Palomar survey (Filho, Barthel, and Ho, 2000; Filho, Barthel, and Ho, 2002; Filho, Barthel, and Ho, 2003; Filho, Barthel, and Ho, 2006; Nagar et al., 2000; Nagar et al., 2002; Ulvestad and Ho, 2001; Filho et al., 2004; Nagar, Falcke, and Wilson, 2005; Krips et al., 2007). These studies found almost similar incidence of radio cores in both Seyfert 2 and LINER galaxies (Ho, Filippenko, and Sargent, 2003), strengthening the bond between these two object classes.

Another specific feature of radio-AGN is the presence of the radio lobes and jets, that are emitted from the compact core, and can be detected on large distances from the galaxy's center, even reaching the size of the entire galaxy (Osterbrock and Ferland, 2006). Jetted AGN also appear to be radio-loud, while jetless AGN are mostly radio-quiet (Padovani, 2017). This feature is often linked to the LLAGN, and the modified structure of their accretion disks, therefore if such jets are detected in the spectrum of an object that doesn't reveal itself as AGN in the optical domain, we can claim with high accuracy that this is actually hidden LLAGN. Although only a small fraction ($10 - 20$%) of identified AGN are radio-loud (Croston et al., 2004; Mahatma et al., 2018), several studies (Hota and Saikia, 2006; Gallimore et al., 2006; Del Moro et al., 2013; Singh et al., 2016; Harrison et al., 2015) showed that jet-like structures are also detected in significant number of Seyfert galaxies and QSOs, that

are usually classified as radio-quiet AGN. Presence of jets in these AGN is still not well investigated, but it is certain that LLAGN, that are main focus of our work, have noticeable jet-like features in their radio images. Therefore, jet-signatures in radio images of the CALIFA objects can be used as a valid indicator of SMBH activity in the centres of these galaxies. These AGN detected in the radio domain are therefore very sensitive indicators for identifying AGN that are in radiativelly inefficient accretion regime (Narayan and Yi, 1994), where even BELs may be to weak to be detected. While conducting a uniform radio-survey that would detect AGN on all their scales is quite challenging, as more than one radio-band is required (Mingo et al., 2016), several surveys were shown to be very useful in this field, particularly NRAO VLA Sky survey (NVSS, Condon et al. (1998)) and FIRST (Becker, White, and Helfand, 1995; Helfand, White, and Becker, 2015). Previous studies on LLAGN detecte in radio wavelengths were conducted by Nagar et al. (2000) and Falcke et al. (2000), where they analyzed radio characteristics at 15 GHz of the sources from the Palomar survey (Ho, Filippenko, and Sargent, 1995), and found relatively high fraction of compact radio cores in these objects ($\sim 30 - 45$ %), mostly related to LINERs.

5.1.3 Extended AGN emission

Although AGN are located in the centers of galaxies, it is possible for their emission to do be detected up to 10 – 20 kpc from the nucleus (Husemann et al., 2012; Husemann et al., 2008; Husemann et al., 2014). These are, so-called, Extended Emission-Line Regions (EELRs) or Extended Narrow-Line Regions (ENLRs) of ionized gas, and are most likely produced by ionized radiation that escaped AGN along the axis of the dusty torus (Congiu et al., 2017). These EELRs are characterized by the line ratios ([NII]/Hα, [SII]/Hα, [OI]/Hα, [OIII]/Hβ) that correspond to Seyfert or LINER-like emission according to the standard emission-line ratio diagnostic diagrams. As such, this extended emission could be very useful in detection of the obscured AGN.

Development of the Integral Field Spectroscopy (IFS) plays a crucial role in detection of these objects, as it allows us to study galactic regions farther away from the center. IFS can provide us with the insightful information on the geometry of this "escaping" radiation, which often follows conical or bi-conical shapes, spreading away from the galactic core (Congiu et al., 2017). There are two most commonly proposed scenarios to explain this phenomenon: outflows and "light echos". Outflows in forms of radio jets, or even mergers may be responsible for such gas kinematics, where the ionizing AGN material is blown away from the center to the farther regions of the galaxy. In case of outflows, the ionization cones often align with the jet emission observed in the radio domain (Morganti, Oosterloo, and Tsvetanov, 1998; Stockton, Fu, and Canalizo, 2006; Morganti et al., 2007; Morganti et al., 2015).

The other possibility is that these EELRs represent the historical view of the past AGN activity, where AGN emission has recently turned off, and what we detect is the relic ionized material, so called the "light echos" that is spread over the large distances across the galaxy, corresponding to light travel time of the gass (Shapovalova et al., 2009; Dadina et al., 2010; McElroy et al., 2016). In some cases, the respective galaxies are no longer spectroscopically identified as AGN from their central spectra, since the nucleus activity has totally switched off. Such objects might serve as a good probe of AGN history, since they may reflect the past activity of the nucleus.

Also another possible explanation of extended AGN emission is that these objects are simply heavily obscured, and cannot be identified spectroscopically from the central spectra. Good confirmation of this scenario is the cross-correlation with

multiwavelength studies, especially in hard X-ray band, which is resistant to obscuration.

The nature and origin of ENLRs has been a subject of many studies for several decades (Heckman et al., 1981; McCarthy et al., 1987; Cracco et al., 2011; Keel et al., 2012; Keel et al., 2015; Obied et al., 2016; Belfiore et al., 2016; Wylezalek, 2017; Hviding et al., 2018), where the most detailed work was conducted by Belfiore et al. (2016) on a sample of $\sim$ 650 galaxies from the MaNGA survey. They created spatially resolved emission-line ratio diagnostic diagrams in order to classify the extended emission in MaNGA galaxies. We applied the similar approach on the binned CALIFA datacubes in our work, which will be the main discussion of the Section 5.4.

The extended LINER-like emission was the main drive for the newly proposed class of objects – LIERs, that show the presence of low ionization emission line regions across regions that are located 10 – 20 kpc from the nucleus (Sarzi et al., 2006; Sarzi et al., 2010; Singh et al., 2013), especially in the early-type galaxies. Multiple scenarios are proposed to expain the extended LINER-like emission, from Post Asymptotic Giant Branch (pAGB) stars (Binette et al., 1994; Stasińska et al., 2008; Fernandes et al., 2011) and hot evolved stars (Belfiore et al., 2016), over "starburst hypothesis" (Yuan, Kewley, and Sanders, 2010; Ho et al., 2014) where starburst generates the galactic winds and ionized outflows that may potentially lead to LINER-like emission line ratios, to "merger scenario" (Monreal-Ibero, Arribas, and Colina, 2006; Monreal-Ibero et al., 2010; Soto and Martin, 2012; Rich, Kewley, and Dopita, 2011) where tidally induced gas flows from galaxies' mergers produce shocks that ionize the extended gas.

In Chapter 2 of this thesis, by detecting the broad Hα line in nuclear spectra of LINER-like galaxies, we found what may be the lower limit of LINER-like emission that actually corresponds to AGN. Since non-AGN LINERs are out of the scope of this thesis, we will be focusing only on the extended Seyfert emission for the purpose of identifying the extend AGN (EAGN).

As we already partially showed in Chapter 2, AGN, and especially LLAGN, can hardly be precisely detected using only one method. Rather, different diagnostic techniques revel additional objects, and information about them. Therefore, in order to have a complete picture of AGN census, various detection methods should be used. Complete AGN census is the key to understanding the processes of coevolution of SMBHs and their host galaxies, and SMBH growth over cosmic history. By analyzing AGN in different wavelength bands, or detecting BELs in their nuclear spectra, as well as extended emission, we gain deeper insight into various stages of AGN activity and their duty cycles. Such approach will assure us that we are not missing the faintest sources, whose emission is either too weak or obscured to be detected in the optical domain.

For the purpose of this chapter, we used the result from Chapter 2, where we used BPT diagrams and BEL fitting method to detect type 2 (Seyfert 2) and type 1 LLAGN, respectively. The study was conducted on the sample of 542 local ($0.005 < z < 0.03$) galaxies from the Calar Alto Legacy Integral Field Area (CALIFA) curvey. We enriched the already classified AGN with additional objects by performing cross-correlations of the CALIFA galaxies with the X-ray *Swift* – BAT 105 month survey (Oh et al., 2018), and the radio NVSS catalogue, in order to detect possible additional AGN that were hidden in the optical domain. We also constructed spatially resolved BPT diagrams of the entire CALIFA galaxies in order to detect EAGN.

This chapter is organized as follows: In Section 5.2 we briefly describe the surveys that we used for the purpose of various AGN detection, in Section 5.3 we present our results from multiwavelength surveys, and spatially resolved CALIFA spectra. In Section 5.5 we discuss these additional objects and look for the cross-correlations and connections with previously classified AGN from the CALIFA survey, and in Section 5.6 we summarize our work and results.

5.2 Data surveys and spectral fitting

5.2.1 CALIFA survey

The main survey that we used for our AGN research is the CALIFA survey (Sánchez et al., 2012; Walcher et al., 2014), which provides integral-field spectroscopic data of 667 galaxies in the local Universe ($0.005 < z < 0.03$). We will only briefly describe the CALIFA survey in this chapter, as we already provided a detailed description in Chapter 1, as well as in previous chapters (2, 3 and 4). CALIFA observations were made with the Potsdam Multi Aperture Spectrograph (PMAS, Roth et al. (2005)), which is installed at 3.5m telescope at the Calar Alto Observatory. Being the integral field survey, it has a large hexagonal field of view of $74'' \times 64''$, with a sampling of $1'' \times 1''$ per spaxel, which is very convenient for studying both integrated and spatially resolved properties of galaxies, which we used both for the purpose of this chapter. CALIFA database sample consists of a mother sample that contains 939 target galaxies selected from the SDSS DR7 photometric catalogue (Abazajian et al., 2009), and has 3 data releases. For the purpose of this thesis, we used the Data Release 3 (DR3, Sánchez et al. (2016)), which contains 542 local galaxies. Data of each galaxy is stored within two datacubes, one for each spectral setup, a low resolution V500 ($3745 < \lambda < 7500$, R = 6 Å), and a medium resolution V1200 ($3650 < \lambda < 4840$, R = 2.3 Å) one. As we were interested in emission lines in the wavelength range $4800 - 6600$ Å, we used V500 spectral setup.

Spatial binning of the CALIFA datacubes

In order to trace potential extended AGN emission, we required spatially resolved information from CALIFA integral-field datacubes. As CALIFA datacubes are relatively large, gathering information from each pixel would be time consuming, and as we were interested in extended AGN emission that occupies a certain fraction of farther galactic regions, it is safe to perform a certain spatial binning of CALIFA galaxies, in order to increase time efficiency. For this purpose I designed a pipeline that performs spatial binning of the CALIFA datacubes, where the size of the binning factor was set to be 3×3 pixels. Depending on the entered binning factor (3 in our case), the pipeline creates square bins according to the central spaxel (spatial pixel) tuple, which is defined by the centre of a galaxy, obtained by the CALIFA collaboration. The binning is performed on the entire wavelength range of each datacube, and the final output is a binned datacube compressed by a factor of 9. This is significant for the next step of performing spectral fitting of each datacube, as the native resolution of PMAS and CALIFA is around $3''$, so each 3×3 bin is close to one resolution element. Also, time efficiency of the process is 9 times higher comparing to the spectral fitting of an original (unbinned) datacubes.

Spectral fitting of binned CALIFA datacubes

In order to obtain emission-line strengths for the purpose of designing both integraded and spatially resolved diagnostic diagrams, first we needed to eliminate stellar contamination from host galaxy spectra. As this process is described in detail in Chapter 2, here we offer only a brief summary of the spectral fitting process that we performed. For the purpose of obtaining pure emission-line spectra, we used pyPARADISE spectral fitting code (Huseman et al. (in prep.), Walcher et al. (2006) and Walcher et al. (2009) to model the stellar continuum and absorbtion generated by stars from the gaalxy. pyPARADISE performs both stellar kinematic and stellar population fitting in two iterative steps and produces a stellar component model spectrum and residual emission-line spectrum as an output. After subtracting this stellar continuum and absorbtion model from the original spectrum, we obtained the pure emission-line spectrum, which is then modeled Gausian distribution, where we assumed that each emission line can be represented by one Gausian. In case of central galactic regions, it is possible that emission lines, especially those from Balmer series of Hydrogen, Hα and Hβ are broadened by the gravitational effect of the central SMBH. Such spectra showed that these emission lines cannot be accurately represented by one Gausian, rather as a superposition of two separate Gausian functions – one describing the narrow component of the line, and another describing the broad component, caracteristical for type 1 AGN. We also assumed that all narrow emission lines have the same FWHM, while FWHMs of possible broad components were left as free parameters. Applying these criteria, we obtained emission line profiles of both narrow and broad (if present) Hydrogen lines, Hα and Hβ, and only narrow-line profiles of [NII] $\lambda\lambda 6548, 6583$, [OIII] $\lambda\lambda 4959, 5007$, [SII] $\lambda\lambda 6717, 6731$ and [OI] $\lambda 6300$. Detailed description of the emission-line fitting procedure is given in Chapter 2.2.

In Chapter 2 we applied these spectral fitting techniques to central 3×3 spaxels of each CALIFA datacube, in order to analyze emission arising from nuclei of CALIFA galaxies. As one of the main aspects of this chapter is the search for extended AGN emission, we applied the same spectral fitting procedure to the entire datacubes. The final output are the strengths and widths of emission lines, which we used for AGN diagnostics in later stage.

5.2.2 *Swift* – BAT 105 month catalogue

Hard X-ray surveys ($L_X > 10$ keV) provide significant information on obscured AGN, as hard X-rays can propagate through large columns of gas and dust without being absorbed, unlike X-rays from the soft band. One of the most common surveys used for this purposes is the cataloge obtained by *Swift* gamma-ray burst (GRB) observatory (Gehrels et al., 2004), with the Burst Alert Telecope (BAT). *Swift*-BAT survey is an all-sky survey at covering the hard X-ray band at $14 - 195$ keV. For the purpose of this Chapter we used the latest eddition of the survey *Swift*-BAT 105 month catalogue [1], in order to perform a cross-correlation with CALIFA DR3 galaxies. Detailed description of the *Swift*-BAT 105 month catalogue is given in Oh et al. (2018).

[1] https://swift.gsfc.nasa.gov/results/bs105mon/

5.2.3 NVSS

For the purpose of classifying radio AGN in CALIFA DR3 galaxy sample, we performed a cross-correlation with the NVSS catalogue. NVSS uses Very Large Array (VLA) radio telescope at wavelength 20 cm (1.4 G Hz^{-1}), and covers all areas north of J2000.0 $\delta = -40^{\circ}$, which accounts for $\sim$ 82% of the celestial sphere. Radio data collected by NVSS are packed in a set of 4 deg $\times$4 deg continuum cubes with planes containing Strokes I, Q and U images, and a catalogue of $\sim$2 $\times 10^6$ descrete sources brighter than 2.5 mJy (Condon et al., 1998). Although NVSS has a relatively small spatial resolution (45 arcsec), it is more than sufficient for the purpose of our research, as this Full Width at Half Maximum (FWHM) covers both host galaxy and possible AGN jet-like signature for the low redshifs of CALIFA.

5.3 Results

5.3.1 AGN detection from cross-correlation with multi-wavelength surveys

X-ray AGN in CALIFA

As we already mentioned, X-ray luminosities of galaxies may serve as valid identification method of AGN due to the fact that the most AGN are the strong X-ray emitters compared to the non-active galaxies, as X-rays emitted by AGN are typically 2 orders of magnitude brighter (Georgakakis et al., 2015). X-ray emission can be divided into two bands – soft X-ray emission, with energies 2 – 10 keV, and hard X-ray emission in 15 – 195 keV band. As soft X-rays may be undetectable due to obscuration, it is possible to miss heavily obscured AGN in this wavelength range.

When the X-ray luminosity in the soft (2 – 10 keV) band exceeds 10^{42} erg s^{-1} (Szokoly et al., 2004), or is larger than $10^{42.2}$ erg s^{-1} in the hard (15 – 195 keV) band (Walcher et al., 2014), a galaxy is probably hosting an AGN in its centre. The cross correlation of the CALIFA galaxy sample with the soft X-ray surveys – ROSAT all-sky survey catalogue and *Chandra* did not reveal any matches, most likely due to the fact that the soft X-rays are mostly absorbed in the obscured AGN. Unlike soft X-rays, cross correlation with the hard X-ray database *Swift*-BAT 105 month survey revealed 6 objects with $\log L_{(15-195)\ \mathrm{keV}} > 42.2$ that are also part of the CALIFA DR3 galaxy sample. Their X-ray luminosities $\log L_{(15-195)\ \mathrm{keV}}$ are in range ($10^{42.97} - 10^{44.15}$) erg s^{-1}. Three of them we already classified as galaxies with Seyfert 2 nuclei using emission-line ratio diagnostic diagrams (Chapter 2.3.1), while in two we detected broad Hα line in the central spectrum (Chapter 2.3.2), corresponding to the type 1 AGN, accordingly. One additional object have LINER-like nucleus, according to our classification using the standard emission-line ratio diagnostic diagrams, conducted in Chapter 2. The final outcome, therefore, revealed only one additional AGN that was hidden in the optical domain, and couldn't be detected with methods that are often applied in this wavelength regime. This is either heavily obscured AGN, or its emission is too weak, and is, as a result, masked by host galaxy's stellar emission, or both. As we already discussed in Chapter 2, galaxies that are classified according to BPT diagrams as intermediate, may be the mixing objects, indicating that there is more than one mechanism responsible for the ionization of the nucleus, and are therefore not strictly defined. This result, although statistically insignificant, amplifies the importance of using different wavelength bands in AGN detection, as

TABLE 5.1: X-ray AGN candidates properties

CALIFA ID	Object name	log $L_{(15-195)\ \mathrm{keV}}$	Hubble type	previous classification
111	MCG-02-08-014	43.20	Sa	Seyfert 2
114	NGC1142	44.15	Sd	Seyfert 2
154	UGC03973	43.68	Sb	type 1
314	UGC05498NED01	42.97	Sa	LINER-like
742	NGC5610	43.04	Sb	type 1
897	UGC12348	43.28	Sb	Seyfert 2

larger surveys may reveal more optically hidden AGN. In Table 5.1 we list the X-ray AGN as well as their X-ray luminosities $\log L_{(15-195)\ \mathrm{keV}}$, morphology types, and previous classification from Chapter 2.

5.3.2 Radio AGN in CALIFA

Strong radio activity is another indicator of AGN signature in galaxy's centre. Presence of radio jets that are emitted by compact radio core and are spread to the large distances across a galaxy are characteristical feature of LLAGN. These objects appear to be radio-loud and can therefore easily be distinguished from non-active galaxies by the strength of their radio luminosities.

Radio frequencies at 1.4 GHz are considered to be a valid indicator of presence of AGN in galaxy's centre. If the radio continuum luminosity satisfies the criterion $L_{1.4\ \mathrm{GHz}} > 10^{23}$ W Hz^{-1} (Best and Heckman, 2012) it is most likely hosting an AGN. Therefore, in order to search for additional AGN that we previously missed in optical and X-ray identification, we performed a cross-correlation of the CALIFA DR3 galaxy sample with NVSS catalogue at 1.4 GHz, from which we obtained radio continuum fluxes. We then calculated the radio continuum luminosity at 1.4 GHz using:

$$L_{1.4\ \mathrm{GHz}}\ [\mathrm{W\ Hz^{-1}}] = \frac{4\pi}{(1+z)^{1+\alpha}}\ F_{1.4\ \mathrm{GHz}}\ [\mathrm{Jy}]\ D_L\ [\mathrm{m^2}] \tag{5.1}$$

where $F_{1.4\ \mathrm{GHz}}$ is the radio flux obtained from the NVSS catalogue, $\alpha = -0.7$ is the spectral index and D_L is the luminosity distance. We found 12 objects that satisfy the criterion $L_{1.4\ \mathrm{GHz}} > 10^{23}$ W Hz^{-1}, whose $\log L_{1.4\ \mathrm{GHz}}$ are in range $10^{23.00} - 10^{24.79}$ W Hz^{-1}. These are considered to be strong radio emitters.

On the other hand, for galaxies with $L_{1.4\ \mathrm{GH}} < 10^{23}$ W Hz^{-1}, we need an additional criterion, such as the strength of the 4000 Å break ($D4000_n$, Best et al. (2005)), in order to accurately identify AGN. The $D4000_n$ serves as a stellar population age indicator. As the opacity in the stellar atmospheres raises with the decreasing stellar temperature, $D4000_n$ gets larger with older ages. Therefore, if star formation is currently happening, we would expect mostly young stars in the galaxy centre. In other words, we do not expect old stellar populations in the star-forming galaxies, so the objects hosting them are possible AGN candidates. Similar as described in Walcher et al. (2014), we measured the $D4000_n$, and assumed that, in order for galaxy to host an AGN, the 4000 Å break strength must satisfy the condition: $D4000_n > 1.7$. We calculated $D4000_n$ as the ratio of an average flux in the $3750 - 3950$ Å and $4050 - 4250$ Å wavelength range. This revealed 2 additional AGN candidates, with $\log L_{1.4\ \mathrm{GHz}} = 22.34$ and $\log L_{1.4\ \mathrm{GHz}} = 22.16$, in logarithmic units of

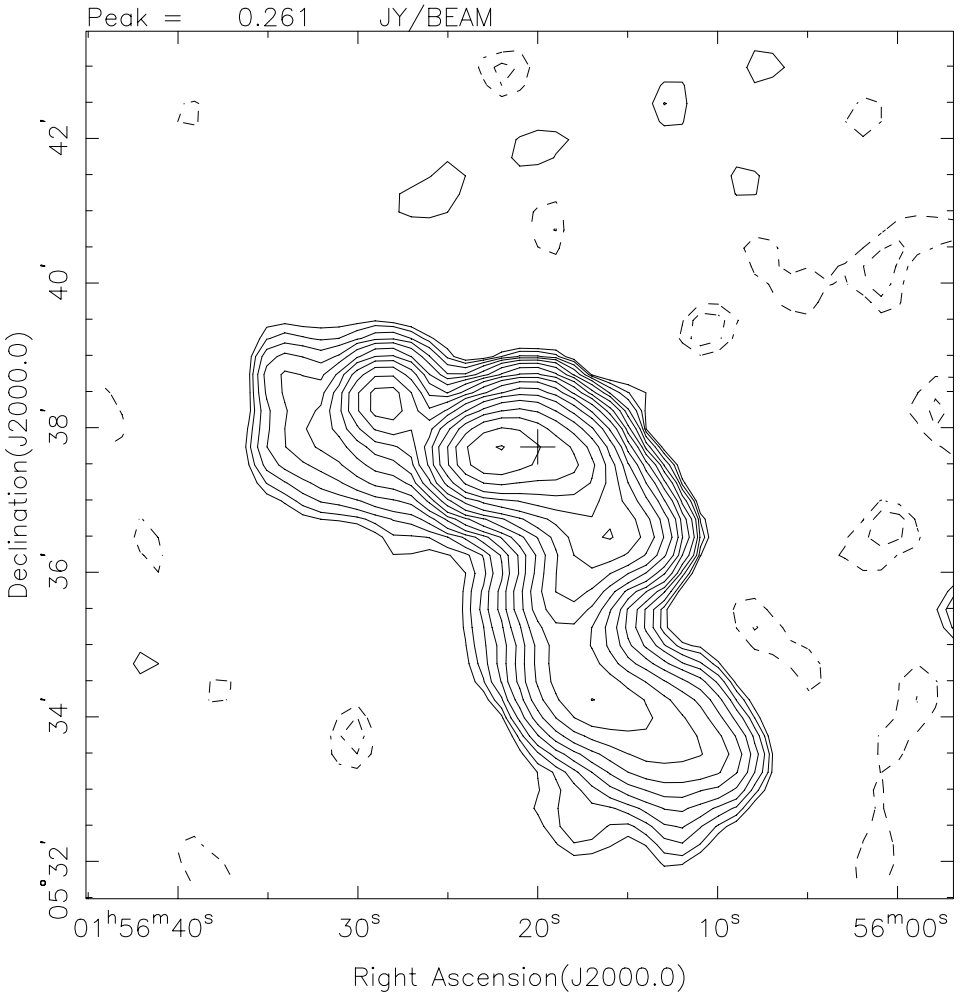

FIGURE 5.1: NVSS contour image in radio domain at 1.4 GHz. The object is NGC 0741 galaxy, with a cross symbol marking aproximate galactic centre. Contours represent spread of radio emission on a scale of $\sim 5''$, which is a clear signature of a radio jet coming from the central AGN.

W Hz^{-1}, originally classified as LINER and intermediate types from the diagnostic diagrams.

In order to increase the accuracy of radio-AGN identification, we checked NVSS radio images of the objects that we identified as radio-AGN candidates. If the radio images reveal a jet-like structure, we can claim with high confidence that these objects are in fact genuine AGN, and that their strong radio emission is not coming from stars. The total of 8 out of 14 objects showed a presence of the jet-like structure. On Figure 5.1 we show an example of NVSS contour images of NGC 0741, where we can clearly see the jet on the scale of $\sim 5''$. One object is in luminosity range of weak AGN, while the remaining 7 have $L_{1.4\,\mathrm{GH}} > 10^{23}$ W Hz^{-1}. For the remaining 6 objects that did not show a jet in the radio images, we can not claim with very high accuracy that their radio emission is coming from an AGN, although they are all very strong radio emitters.

The result of NVSS and CALIFA cross correlation revealed potential 14 AGN candidates, visible in radio domain, of which 5 of them correspond to our optically classified type 1 AGN, and 2 radio objects corresponding to X-ray AGN. Additional

7 objects that we identified as radio-AGN were previously classified as galaxies LINER-like (2) and intermediate (5) nucleus, with the standard diagnostic diagrams. Radio diagnostics revealed in total 7 new AGN that were previously not identified in the optical domain, while two objects correspond to both X-ray and radio AGN, and were previously identified as LINERs. This result, beside confirming some of the AGN candidates identified with BEL diagnostics, also implies on the potential AGN nature of some galaxies that are classified as LINERs or intermediate according to the optical emission-line ratio diagnostic diagrams. The overview of radio-AGN candidates is listed in Table 5.2.

5.4 Extended AGN in CALIFA

In order to detect extended AGN emission in CALIFA galaxy sample, we designed a pipeline that performs spatial binning of the CALIFA datacubes (Section 5.2.1), for the purpose of increasing time efficiency. We performed $3'' \times 3''$ spatial binnig of all 542 CALIFA DR3 datacubes, and take in each bin the mean over all valid pixels.

In order to create spatially resolved emission-line maps, we first performed stellar population and kinematics fitting of each bin for each galaxy, and later emission line fitting on the residual spectra. Thus we obtained emission line flux densities of [OIII], [NII] and [SII] lines, and narrow components Hα and Hβ lines, using the procedures described in Chapter 2.2.3. We required signal-to-noise ratio to be S/N > 2 for each line. First we used these emission line ratios to construct BPT diagrams of each galaxy, for the purpose of distinguishing between 4 different ionization mechanisms: star-formation, AGN, LINER-like, and intermediate, which most likely consist of combination of the previous 3 mechanisms. In order to preserve consistency, we adopted the classification scheme from Chapter 2, applied on the central bins only. First we analyzed the [OIII]/Hβ – [NII]/Hα diagnostic diagram in order to separate the regions that are ionized by star-formation processes in the galaxy. We used the (Kewley et al., 2001) "extreme starburst line" as a theoretical maximum above which the ionization by star-formation processes is no longer possible. Data points above this line are considered as AGN candidates, belonging to either Seyfert 2 or LINER-like types. Further, with (Kauffmann et al., 2003) empirical demarcation curve, we separated regions that are ionized purely by star-formation. The region between (Kauffmann et al., 2003) and (Kewley et al., 2001) we classified as "intermediate", according to Chapter 2. In order to divide Seyfert 2 from LINER-like regions, we used [SII]/Hα – [OIII]/Hβ diagnostic diagram, and the empirical line from (Kewley et al., 2006) as "AGN – LINER mixing line".

After applying the BPT diagnostics on each CALIFA DR3 datacube, we performed the visual inspection of each object. Since significant number of objects show presence of Seyfert emission-line ratios in the spatially resolved diagrams, we decided to discard objects where only single (3×3 binned) spaxels are AGN-like and surrounded by non-AGN spaxels (including LINER-like). Those cases we suspect to be due to noise. We demanded that significant regions must show AGN-like line ratios, in order to consider them as genuine extended AGN emission. This significantly reduced the number of objects that may be potential EAGN candidates. Similar to Belfiore et al. (2016), we estimated the number of Seyfert-like emission bins for each galaxy. We considered objects with Seyfert fraction larger f_{Sey} than 10% to be possible EAGN, while objects $f_{Sey} > 15\%$ have slightly higher probability, and finally for galaxies with $f_{Sey} > 20\%$ we can claim with high certainty that we detected the extended AGN emission. Out of 542 analyzed galaxies, this method narrowed

TABLE 5.2: Radio-AGN candidates properties

CALIFA ID	Object name	log $L_{1.4\ GHz}$	radio type	jet presence	Hubble type	previous classification
114	NGC1142	23.48	strong	0	Sd	X-ray
119	NGC1167	24.06	strong	1	S0	type 1
278	UGC05108	22.16	weak	0	Sb	intermediate
314	UGC05498NED01	22.34	weak	0	Sa	X-ray
341	UGC05771	23.28	strong	0	E6	type 1
592	NGC4874	23.44	strong	1	E0	intermediate
726	NGC5532	24.31	strong	1	E4	type 1
802	ARP220	23.39	strong	1	Sd	type 1
832	NGC6146	23.52	strong	1	E5	type 1
839	NGC6166NED01	24.79	strong	1	E4	LINER-like
851	NGC6338	23.00	radio-strong	0	E5	LINER-like
869	NGC6941	23.13	radio-strong	0	Sb	intermediate
888	UGC12127	23.81	radio-strong	0	E1	intermediate 939
NGC4676A	23.58	strong	1	E1	intermediate	

down the total of 8 potential EAGN candidates ($f_{Sey} > 10\%$), of which 3 of them also have a Seyfert nucleus. One of these three objects had later revealed to host broad Hα emission in its central bin, and is therefore classified as type 1 AGN according to its central spectrum. Out of the remaining 5 objects with detected extended AGN emission, 3 were also previously classified as type 1 AGN with LINER-like nuclear emission according to the BPT diagrams from Chapter 2, and one as radio AGN. The last remaining object is classified as LINER-like type from its central spectrum. Two out of eight objects have $f_{Sey} > 20\%$, for which AGN origin we are highly certain, as they were revealed as Seyferts from their nuclear spectra, and three of them have $f_{Sey} > 15\%$.

On Figure 5.2 we present the resulting distribution of our measured line ratios for four objects that have detectable extended AGN emission. From the left to the right panel of each sub-figure we have [NII] – [OIII] and [SII] – [OIII] diagnostic diagrams of the entire galaxy (left and middle panels respectively), while the right panels represent the spatially resolved emission-line ratio diagnostic maps, which show us how each of the classified regions is distributed on the scale of the entire galaxy. As some bins have undetectable [SII] emission which we used in the [SII] – [OIII] diagram to distinguish between Seyfert and LINER-like emission, we used the strength of [OIII]/Hβ line ratio as a separation point, where bins with $\log\frac{[OIII]}{H\beta} < 3.0$ we classified as contributors to LINER-like emission, while for those with $\log\frac{[OIII]}{H\beta} > 3.0$ we assumed that the emission is from AGN. Also, a certain number of data points in some objects were classified as star-forming in origin from the [SII] – [OIII], while they usually belonged to an intermediate type according to the [NII] – [OIII] diagram. These three types bins were represented as opened symbols on the Figure 5.2.

On the upper panel of Figure 5.2 we show an example of an object where we can claim with a high accuracy that we detected the extended AGN emission. This object is also classified as both Seyfert and type 1 AGN from its central spectrum. The second panel from top to bottom shows the only object that was not previously identified as AGN from BPT diagrams, BEL diagnostics or multiwavelength surveys. We can notice that majority of both Seyfert and LINER-like data points lie close to demarcation lines. In such objects we may assume that the LINER-like emission is a reflection of AGN, which is also confirmed by the detection of broad Hα emission line in the nuclear region of this object. We can also notice that LINER-like and Seyfert bins are always in the proximity of each other on the spatially resolved BPT diagram, implying the similar nature of the emission of these bins. In the third panel from top to bottom we have an example of a galaxy which is spectroscopically identified as LINER from its nuclear spectrum, while the further analysis revealed that this galaxy is both type 1 AGN and strong radio AGN. As we can see from the figure, we have a significant amount of extended AGN emission in the farther regions of the galaxy, while only the central bin has LINER-like emission. This may be due to uncertainty in emission-line fluxes estimation, as well as the uncertainty of the position of the galactic centre. Finally the bottom panel of Figure 5.2 shows an object for which we are not highly confident that we detected the extended AGN emission, but due to the relatively high fraction of Seyfert bins ($f_{Sey} \approx 15\%$) it is possible that this object is a valid EAGN candidate. Table 5.3 summarizes main properties of EAGN candidates, as well as their original classification.

While Belfiore et al. (2016) developed a method that measures the distance of each spaxel from the demarcation curves to account for each class, we took a different approach, and concluded that the contribution of each class may remain roughly

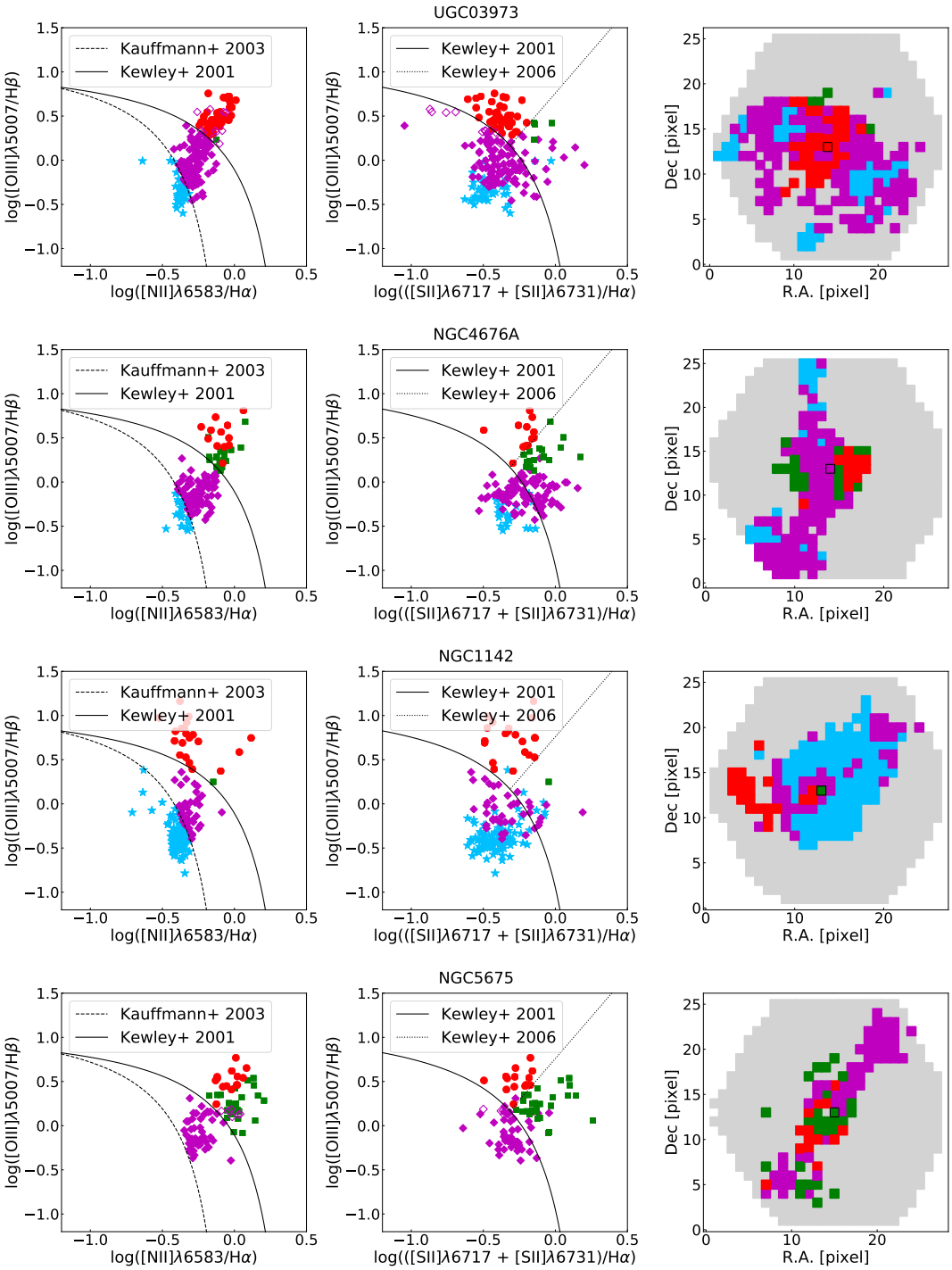

FIGURE 5.2: Spatially resolved diagnostic diagrams of EAGN. Left panel represents [OIII]/Hα over [NII]/Hβ emission line ratios of each $3'' \times 3''$ bin, while middle panel is [OIII]/Hα over [SII]/Hβ. Bins with star-forming emission-line ratios, below the empirical demarcation curve from KA03, are marked with light blue stars. Bins with line ratios typical for Seyfert emission are marked as red squares (closed symbols indicate that the classification is made using the [SII] – [OIII] diagram and the empirical KE06 line, while open symbols represent datapoints where [SII] could not be detected and the classification is made based on the strength of [OIII]/Hβ ratio). LINER-like emission is represented with open and closed green triangles. Additional "intermediate" type emission, with line ratios above the theoretical KE01 and below the empirical KA03 curves, is represented by purple diamonds. Small number of data points classified as star-forming in origin from [SII] – [OIII] only and not from [NII] – [OIII] diagram are marked with open magenta diamonds.

TABLE 5.3: Properties of extended AGN candidates

CALIFA ID	Object name	Hubble type	previous classification
114	NGC1142	Sd	type 1
154	UGC03973	Sb	type 1
186	IC2247	Sab	Seyfert 2
274	IC0540	Sab	LINER-like
577	NGC4676A	Sdm	radio
757	NGC5675	Sa	type 1
801	NGC5953	Sa	type 1
897	UGC12348	Sb	Seyfert 2

the same, as we will have effect of objects mixing from each side of the demarcation lines. To put it in a simple way, if we would loose some data points from Seyfert as they may actually belong to LINER-like emission, we will also gain some data-points from LINER-like emission on the other hand. The regions close to demarcation curves probably have high mixture of different classes, and it is hard to draw the clear line where one ends and the other begins.

We can conclude that, while we have identified only one new AGN with extended AGN emission diagnostics method, on the other hand we definitely did confirm that some of the objects with central LINER-like or intermediate emission are in fact genuine AGN, as they were classified as AGN with more than one method. This strengthens the assumption that definitely some (and probably high fraction) of LINERs or LIERs are actually a sub-class of LLAGN.

5.5 Discussion

5.5.1 AGN census in CALIFA

On Figure 5.3 we show [NII]/Hα – [OIII]/Hβ emission line ratio diagnostic diagram, previously established in Chapter 2.3.1. The diagrams show nuclear $3'' \times 3''$ spectra of the CALIFA DR3 emission-line galaxies that have detectable [NII] emission in their centers, consisting of 483 objects, originally divided into 4 categories based on the powering source of their nucleus: star-forming galaxies, Seyferts 2, LINER-like galaxies, and intermediate class. The classes are divided using the demarcation curves postulated by Kewley et al. (2001) ("extreme starburst line"), Kauffmann et al. (2003) (empirical separation between star-forming galaxies and AGN candidates including LINERs and intermediate mixed objects), and Kewley et al. (2006) (empirical "AGN – LINER mixing line). Detailed procedure on how the division is performed is described in previous section as well as in Chapter 2.3.1, where we performed a classification of all CALIFA emission-line galaxies. Beside emission line ratio diagnostic diagrams classification, we also performed broad Hα diagnostics (Chapter 2.2.3), where we performed emission line fit allowing Hα line to have an additional broad component. As the broad Hα lines are very weak in the CALIFA AGN sample, the final conclusion on whether or not the additional fit component has an actual physical meaning was made by comparison of the residuals after fitting the spectra with and without the additional broad component. This resulted in 89 galaxies that have broad Hα emission present in their spectra, subsequently classifying them as type 1 AGN. Majority of these objects (59 out of 89) are located on the LINER-like

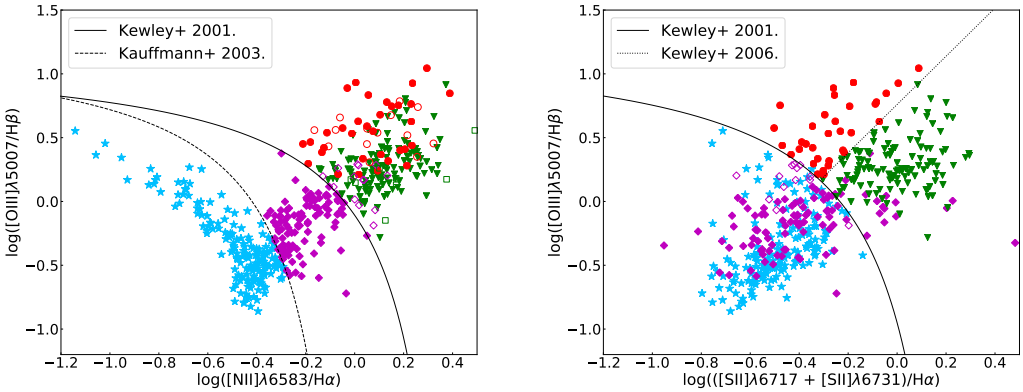

FIGURE 5.3: The central emission line ratios of the CALIFA galaxy sample represented on the [NII] – [OIII] (top) and [SII] – [OIII] (bottom) standard diagnostic diagrams. The galaxies with star-forming nuclei, determined using the empirical KA03 (dashed curve, top) line on the [NII] – [OIII] diagnostic diagram, are marked with blue stars. Seyfert 2 nuclei, located above the theoretical KE01 "maximum-starbust line" (solid line, bottom) and left from the KE06 "Seyfert-LINER classification line" (dotted line, top) on the [SII] – [OIII] diagram, are represented with red dots, while LINER-like nuclei (above the KE01 and right from the KE06 on the [SII] – [OIII] diagram) are marked with green triangles. The additional "intermediate nuclei" (located above the KA03 line on the [NII] – [OIII], and below the KE01 line on the [SII] – [OIII] diagram) are represented with purple diamonds.

part of the diagnostic diagrams, while the remaining 30 objects are originally classified as Seyferts (18) and galaxies with intermediate nucleus (12). Our classification and count from the Chapter 2 therefore consists of 89 type 1 AGN ($\sim$ 16% of the total sample of 542 objects), 29 Seyfert 2 galaxies ($\sim$ 5%), 76 LINER-like objects (14%), 110 intermediate ($\sim$ 23%), and 179 purely star-forming galaxies (33%). It is important to note that in Chapter 2 we analyzed only nuclear $3'' \times 3''$ apertures of CALIFA galaxies.

Within this chapter, we established 3 additional classes of AGN, using the multi-wavelength surveys in X-ray and radio domain, as well as spatially resolved emission-line diagnostic diagrams. Cross-correlation of the CALIFA DR3 sample with *Swift* – BAT 105 month catalogue revealed 6 AGN candidates with X-ray luminosities above $10^{42.2}$ erg s^{-1} in the hard 15 – 195 keV X-ray band. Out of these 6 objects, three have already been classified as Seyfert 2 nuclei using the nuclear emission-line rations and BPT diagrams, while two revealed the presence of the broad Hα emission line in its central spectrum, falling into category of type 1 AGN. The remaining one object is therefore identified as an additional X-ray AGN. Accordingly, cross-correlation between CALIFA and NVSS samples revealed 14 radio AGN, of which 9 of them have strong ($L_{1.4\,\mathrm{GHz}} > 10^{23}$ W Hz^{-1}) and 2 weak radio emission ($L_{1.4\,\mathrm{GHz}} < 10^{23}$ W Hz^{-1}). Eight of these radio AGN candidates showed the presence of a jet-like structure in their radio images. Some of these radio-AGN candidates were already previously identified type 1 (5 objects) or X-ray AGN (2 objects). This leaves 7 additional objects that that were spectroscopically identified as LINER-like or intermediate galaxies, according to their nuclear emission-line ratios.

We were also interested in the extended AGN emission, as some of the AGN candidates might be too obscured in the centers to be spectroscopically identified,

or their photioinized material was blown away by shocks and outflows into the farther regions of the galaxy. Another possible scenario that may explain the extended AGN emission is that we observe the light echos of the relic AGN emission that is spread over the galaxy, while the central engine is no longer in its active phase, and is therefore not identified as AGN. For the purpose of detecting these EAGN, we constructed spatially resolved emission-line ratio diagnostic diagrams, applying the same criteria as for the nuclear regions, on the binned data cubes of all CALIFA DR3 galaxies. This method introduced 8 potential EAGN candidates, of which 7 were previously already identified as either Seyfert, type 1, or radio AGN. The one additional object was previously classified as LINER-like type, and within this chapter we revealed that it actually contains extended AGN emission, and is therefore classified as EAGN.

According to the previously described emission-line ratio classification scheme, on Figure 5.4 we marked all our previously established AGN types (type 1 + Seyfert 2) with red pentagons, while black markers represent galaxies with star-forming, LINER-like, and intermediate nuclei, in order to avoid to many symbols and colors on one plot. Newly identified AGN candidates (6 X-ray, and 14 radio, and 8 EAGN) are represented with yellow Xs, purple triangles (with lighter color indicating weak radio emission, and darker – strong radio AGN), and light green squares, where we can also notice the overlapping between the respective AGN classes.

Beside overlapping between X-ray and radio AGN, cross-correlation of *Swift* – BAT and NVSS surveys with CALIFA also resulted in overlapping between each of AGN subclasses. Therefore our final classification has the following AGN count, with priority assigned by the following order:

- 89 type 1 AGN – 17% of all emission line galaxies from CALIFA
- 29 additional Seyfert 2 galaxies – 5.5%, out of 55 detected in total
- 1 additional X-ray AGN – 0.2%, out of 6 detected in hard X-ray band
- 7 radio AGN – 1.3%, out of total 14
- 1 EAGN 0.2%, out of 8

Inspecting the cross-correlation between the CALIFA and multiwavelength surveys in X and radio domain, as well as constructing spatially resolved emission-line ratio maps in order to detect extended AGN emission, did not reveal statistically significant number of new objects, but the important aspect of it is that it confirmed that certain objects can be classified as AGN with multiple methods. This emphasises the importance of using more than one method in AGN detection and classification, especially in case of LLAGN, whose nuclear emission can be extremely weak, therefore imposing significant challenges in the its detection and proper analysis.

With AGN diagnostic methods presented in this chapter as well as in Chapter 2 we can establish the complete AGN census in the CALIFA survey. We can conclude that the CALIFA sample consists of 125 AGN in total, or $\sim$ 23% of all sample galaxies that may be classified as active, which yields significantly high fraction. As we showed in Chapter 4, these AGN accrete at extremely low state, and have modified central engine. In order for these objects to be detected, sufficient spectral resolution as well as proper analysis, including precise stellar component subtraction and BEL fitting, have to be performed. Otherwise the abundance of these objects in the local Universe can be heavily underestimated, as they may either go undetected, or

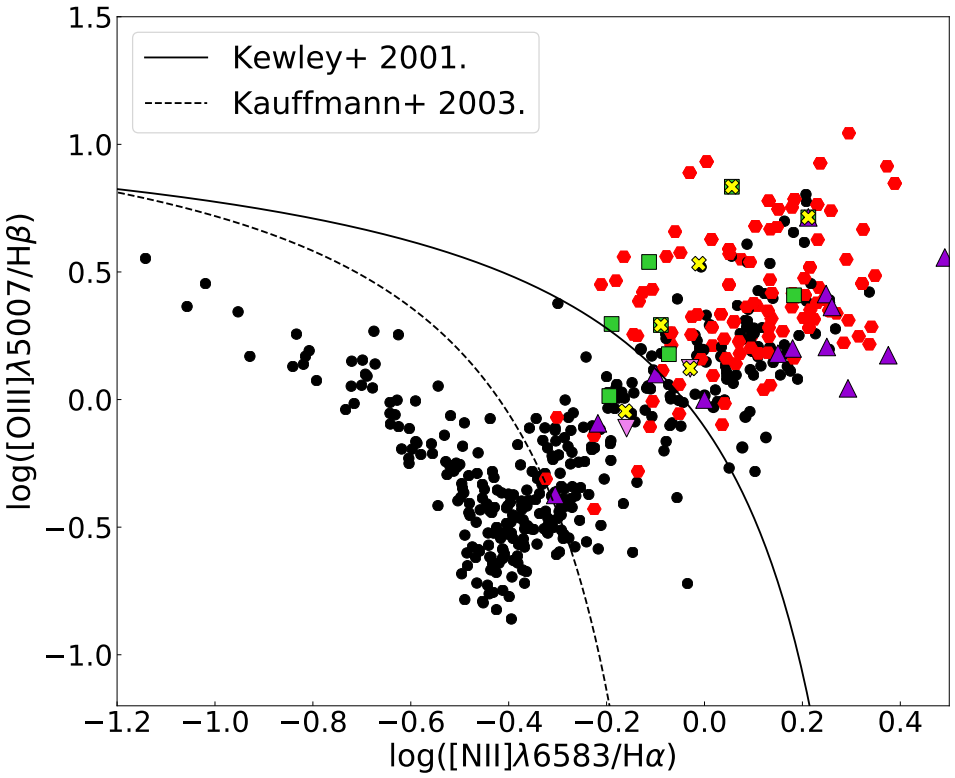

FIGURE 5.4: [NII]/Hα – [OIII]/Hβ emission-line ratio diagnostic diagram of the central CALIFA DR3 galaxies' regions. Red pentagons represent previously identified AGN types (type 1 AGN and Seyfert 2 galaxies, Chapter 2), while green squares represent EAGN candidates, yellow Xs – X-ray AGN, and purple inverted triangles – radio AGN, color-coded for the radio-strength, where lighter shade marks radio-weak, and darker – radio-strong AGN candidates. With black dots we marked all other types of objects from our classification (star-forming, LINER-like, and galaxies with intermediate nucleus). Overlapping between the respective AGN classes is only shown on the plot, and is avoided in final classification, given the priority of diagnostic methods.

classified as inactive. Different wavelength bands and different diagnostics methods can help us understand the full picture of AGN population, as it may provide us with different perspectives and types of active galaxies. This is important in realizing the selection effects of each survey and method and completing the AGN picture. Understanding the proper AGN census in the local Universe is essential in studies of these objects, and represent the zero-point in the study of the entire AGN population.

Throughout this thesis we assumed that LINER-like emission may be the result of the variety of mechanisms, of which one is certainly accretion of the gas onto the central SMBH. With our AGN census we imposed a lower limit of LINER-like emission that actually originates from AGN. It is important to be aware that processes such as shocks or emission from pAGB stars can also produce LINER-like emission-line ratios, and that observed LINER-like line ratios are not a reflection of the LLAGN in the center of a galaxy. It is therefore important to distinguish between AGN and non-AGN origin of these emission-line ratios, where multiwavelength

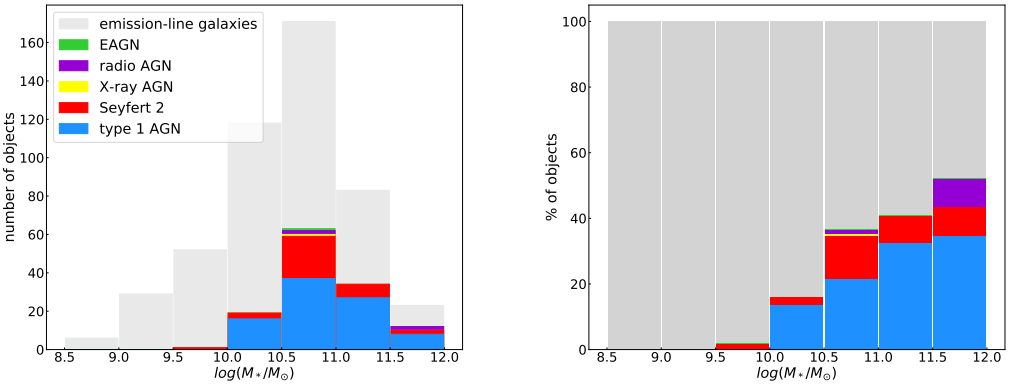

FIGURE 5.5: Left: Histogram showing total stellar masses M_* of AGN hosts in CALIFA, compared to the all emission-line galaxies in the sample. AGN hosts belong to the most massive galactic systems in the CALIFA sample, having M_* in range $10^{10} - 10^{12}$ $M_\odot$, with an average value of 10^{11} $M_\odot$. The plot is color-coded for different AGN types, as shown in the legend. Right: each AGN type given as a fraction of all emission-line galaxies in CALIFA, within each M_* bin. This clearly shows that the most massive M_* bins in the CALIFA sample contain large fraction of AGN.

surveys as well as BEL detection play a crucial role.

5.5.2 Properties of different types of AGN in CALIFA

As we already discussed in chapters 2 and 2, type 1 AGN were constituents of relatively massive galaxies ($M_* \approx 10^{11}$ $M_\odot$ on average), although their estimated black hole masses populate majorly the low-mass end (2.1×10^7 $M_\odot$). In this section we analyze the distribution of the different AGN sub-types respective to their total galaxies' stellar masses, as well as their respective Hubble types. Total stellar masses of the galaxies in the CALIFA sample were calculated by the CALIFA collaboration (Walcher et al., 2014) using Sloan Digital Sky Survey (SDSS) ugriz growth curve magnitudes. The M_* estimation method used the Bruzual and Charlot (2003) models with a Chabrier (2003) Initial Mass Function (IMF), where possible bursts and different amounts of dust extinction were accounted.

On Figure 5.5 we present the distribution of total galaxy stellar masses M_* color-coded for each AGN type. On the left we have a standard histogram of each AGN subtype, with previously established classification method priority as follows: type 1 AGN, galaxies with Seyfert 2 nucleus, X-ray AGN, radio-AGN, and finally EAGN. We can see similar distribution within sub-types, where the highest number of objects has M_* in range $10^{10} - 10^{11.5}$ $M_\odot$. On the right panel, we show the fraction of each AGN type within each bin, where full bin contains all emission line galaxies within that M_* range. It is interesting to note that AGN contribute to $\sim 50\%$ of the most massive bin in the sample ($10^{11.5} - 10^{12}$ $M_\odot$). This shows that large number of the most massive galaxies in CALIFA are in fact AGN hosts, where even though these LLAGN are significantly faint, they still prefer massive galactic systems. Also, majority of radio-AGN have the highest M_* in the sample, while type 1 and Seyfert 2 are more or less evenly distributed between 10^{10} $M_\odot$ and 10^{12} $M_\odot$.

On Figure 5.6 we show the link between total stellar masses and Hubble types, color-coded for each AGN subclass. We can see that radio AGN are mostly present

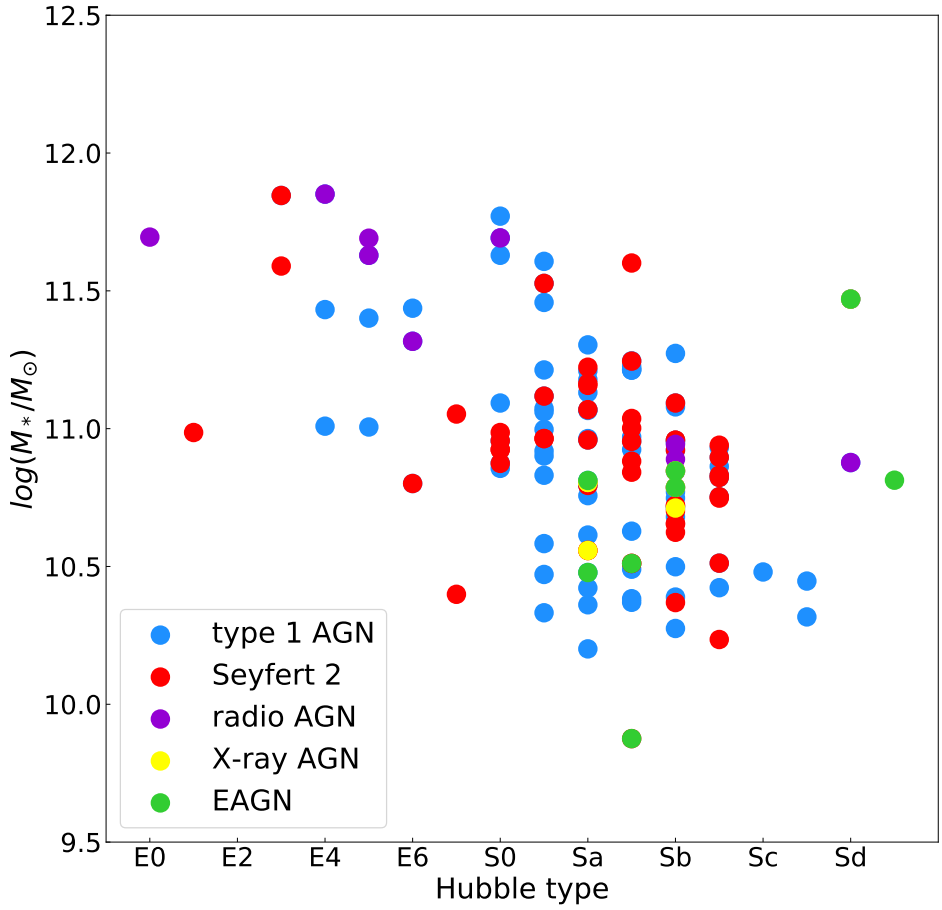

FIGURE 5.6: Relation between Hubble types and total stellar masses M_* of CALIFA AGN hosts, color-coded as in previous figure, for different AGN candidate type. As there is some overlapping between different AGN types, the final classification looks slightly different, containing larger number of type 1 AGN and Seyferts.

in massive elliptical galaxies, while Seyferts are majorly populating mid-mass spirals S0 – Sbc. Type 1 AGN, on the other side, are distributed over a wide range of morphological types and total stellar masses. Unlike the previous figure, where we tried to avoid overlapping of different AGN types, here we have some datapoints that may be represented by a color of one AGN type (for example radio or X-ray) while in general, we classified it as type 1 AGN. As type 1 AGN and Seyferts are most common AGN types in our study, their distribution of Hubble type —- total stellar mass is relatively wide, while other types might be more localized in specific areas of the plot. This was the main drive to give priority to less frequent AGN types in our study, for the purpose of this plot, in order to have a better representation of the distribution of different AGN types on the Hubble type — M* plane.

The final AGN classification is given in Table A.4 in Appendix where we document properties of each AGN type.

In this chapter we emphasised the importance of looking at different wavelength

bands and different methods of AGN identification, in order to gain better understanding of these objects. Different bands and methods give us different perspectives and reveal different types of AGN, pointing out that, with each AGN identification method, we need to be aware of potential selection effects. Obscured AGN can hardly be identified in the optical wavelengths, and a significant fraction of these objects can be lost if we would rely only on methods of optical AGN detection. X-ray AGN, and especially in hard X-ray band, on the other hand, are insensitive to obscuration and can reveal additional objects that we misclassified using the optical methods. In Chapter 2 we signified the importance of BEL detection for AGN identification, and as we confirmed in this chapter as well, this method remains very reliable for AGN diagnostics. Few additional objects that were revealed, either in multiwavelength bands, or in integrated spectra, were already previously classified as type 1 AGN, strengthening the validation of the method. Extended AGN emission, as we showed, is somewhat harder to be precisely defined, as majority of objects have emission-line ratios close to demarcation lines. For these objects we cannot claim with very high accuracy that we are certain they belong to AGN. On the other hand, this also points out to the similarity of AGN-like and LIER-like emission-line ratios, and extrapolated to a broader picture, that definitely some fraction of LINER-like emission is a reflection of central SMBH accretion. Of course, other processes, such as shocks or emission from stars with old stellar population can also produce LINER-, or LIER-like emission-line ratios, therefore it is important that we use other methods of AGN diagnostics, as emission-line ratio diagnostic diagrams are not sufficient to properly distinguish between LINER-like emission coming from AGN and other mechanisms. Detection of BELs, as well as radio-jets and/or strong X-ray emission, in these objects can definitely be a strong confirmation that we are in fact looking at LLAGN.

5.6 Conclusions

Using various AGN diagnostic methods finally brought us closer to a proper AGN census in CALIFA database, where we revealed that LLAGN are in fact, quite frequent in the local Universe. Previously, in Chapter 2, by applying standard emission-line ratio diagnostic diagrams on nuclear spectra of CALIFA galaxies, and BEL diagnostics of the central regions, we found that LLAGN in fact contribute to a significant fraction of all CALIFA DR3 emission-line galaxies. This classification consisted of type 1 AGN and galaxies with Seyfert 2 type of nucleus. While there were some overlapping between the two AGN types, we gave classification priority to type 1 AGN over Seyferts as BELs that we detected can only be produced by accretion onto the central SMBH, while emission-line ratios can are prone to larger uncertainty close to demarcation lines. In this chapter, we used multivawelength AGN diagnostics, combining X-ray (Swift-BAT 105 month catalogue) and radio (NVSS) surveys, and performing a cross-correlation with CALIFA DR3 galaxies, which revealed us few additional AGN in CALIFA, classified as X-ray and radio AGN, according to these respective surveys.

We found that 75% of our radio-AGN candidates reveal a presence of a jet-like structure, visible in their radio images from NVSS, which may serve as a great confirmation that this radio emission can only be attributed to LLAGN. The jet-like signature, beside being a clear evidence that a galaxy is hosting an AGN in its centre, is also very important for our understanding of SMBH – host coevolution, as jet-driven shocks may have an important impact on star formation history of AGN (Mingo et

al., 2016). The combination of X-ray and radio observations is important for investigating various areas of AGN physics, such as radio loudness, the origin of jets, and the structure of accretion disks, which are known to have a different structure in LLAGN.

Another method that we used in this chapter for AGN diagnostics is detection of extended AGN emission, that can be detected in further regions of galaxies. This method revealed few objects that might be potential EAGN candidates, of which all except one were previously identified as another type of AGN, mostly type 1 and Seyfert. Although not fully developed yet, this method provides a novel insight into AGN history and might be useful in the future for studying the coevolution between AGN and their host galaxies.

Our final research gave us five different types of AGN in the CALIFA survey, which constitute to a large fraction of all CALIFA galaxies. Overlapping of different AGN types required that we construct a hierarchy of the classification methods, according to how certain we are in the validity of the results. As we already mentioned, the top priority is given to type 1 AGN, followed by Seyferts, X-ray, radio, and finally, EAGN. This overlapping between different types only strengthened our claims and certainty of our classifications, but it also emphasises the importance of including different surveys and approaches, in order to maximally avoid selection biases in classification.

CHAPTER 6

Conclusions

6.1 Summary

The main goal of this thesis was to search for and investigate physical properties of Active Galactic Nuclei (AGN) in the local Universe, for which purpose we used the Calar Alto Legacy Integral Field Area (CALIFA) survey, which can be taken as representative for the local galaxy population.

AGN in the local Universe contribute to the extremely low-luminosity end of the population, and by understanding the physics behind these objects we may gain deeper understanding of the entire AGN phenomenon and their evolution across cosmic history.

Objects with extremely low luminosities such as local AGN are target of many observational challenges and they are still not properly studied and understood. So far it has been unanswered question whether these objects are genuine, but less active AGN, or a completely separate class of objects with different physical mechanism of the central engine. Yet, they are of great importance for understanding of black hole demographics, the coevolution of Super Massive Black Holes (SMBHs) and their host galaxies, and completing picture of the entire AGN phenomenon.

6.1.1 The quest for AGN in CALIFA

Emission line spectroscopy of the central galactic regions holds key information on the ionization mechanism of the central source. By analyzing the central $3'' \times 3''$ aperture spectra of all 542 CALIFA DR3 galaxies, we found that AGN constitute to a high fraction (23%) of the entire sample. We used standard emission-line ratio diagnostic diagrams which separate between different classes of objects based on their central ionization mechanism. According to this we were able to separate between star-forming galaxies, galaxies that have LINER-like emission, intermediate galaxies that are probably homogeneous class of objects, and galaxies with Seyfert 2 nucleus. We also searched for the signatures of broad Hα emission-line in the central spectra of these galaxies, as a definitive indicator of AGN activity in the nucleus.

We found that type 1 AGN that have broad Hα line present in their central spectrum are in fact quite common in our sample, consisting of 16% of all CALIFA galaxies. These Broad Emission Lines (BELs) are extremely weak ($L_{H\alpha} \sim 10^{39}$ erg s^{-1}), but with width comparable to those of "typical" high-luminosity high-z type 1 AGN ($1000 - 6000$ km s^{-1}).

An interesting finding is also that majority of these objects were acutally "masked" as LINER-like galaxies, where 66% of type 1 AGN are located in the LINER-region on the standard diagnostic diagrams. This resulet that almost half of LINER-like

galaxies (44%) are in fact genuine AGN, setting the lower limit on how many LINERs are actually powered by accretion onto the central SMBH. This is significantly higher than what is found in most recent work on this topic, conducted by Eun, Woo, and Bae (2017), where they found that only 3% of type 2 AGN from SDSS at $z < 0.1$ have broad Hα in their spectra. The differece may be due to two reasons: there are strong dilution effects in more distant galaxies when using a fixed 3″ SDSS aperture, and second is that they searched for broad lines in objects that were already classified as type 2 AGN, while here we definitelly confirmed that majority of type 1 AGN are hidden in LINER region.

An important result that serves as an evidence that these BELs are in fact generated by the accretion of the material onto the central SMBH, and are not a product of poor fitting procedure, or even some other excitation mechanism, is that all of them are located in the AGN (Seyfert 2 + LINER) region of the emission-line ratio diagnostic diagrams.

Our result shows that, although hard to detect, low-luminosity AGN (LLAGN) are widely present in the local Universe.

6.1.2 Ratio of type 1 : type 2 AGN in CALIFA

As we detected broad Hα line in almost 40% of the CALIFA galaxies located in Seyfert region of diagnostic diagrams, this significantly reduced the fraction of type 2 AGN in our sample (to only $\sim$ 5% of the entire sample). This high ratio of type 1/type 2 AGN is definitely something that should be investigated more in future works. One possible explanation is the modified structure of the dusty torus surrounding the central source. In "typical" luminous AGN, a clumpy dusty torus surrounds the Broad Line Region (BLR) from which we observe the BELs, blocking their emission on the line-of-sight. Narrow Line Region (NLR) on the other hand is not obscured by the dusty torus and this may be the main reason why we detect Narrow Emission Lines (NELs) more often than broad. According to the theoretical work of Elitzur and Shlosman (2006), dusty torus and the BLR disappear for bolometric AGN luminosities L_{bol} below 10^{42} erg s^{-1}. Clumpy optically thick torus collapses into a thin disk. This transition however most likely happens smoothly, and it is possible that for low bolometric luminosities of LLAGN the torus has mostly disappeared, while the BLR with extremely weak BELs still persists even below this limit, and is revealed by the disappearance of the torus.

There is no physical reason why type 2 AGN would be more common in the Universe than type 1 AGN, as this division depends only on the viewing angle. Type 1 AGN are masked as a different class of objects (LINERs, intermediate) according to their NEL ratios, but as the obscuration from the torus is out of the picture, these objects were revealed. Most likely luminous AGN are "hidden" in either LINERs or intermediate objects, where we are not able to detect BEL due to optically tick dusty torus.

6.1.3 On the black hole scaling relations in CALIFA

We estimated black hole masses and Eddington ratios of type 1 LLAGN from CALIFA using both $M_{BH} - \sigma_*$ correlation of Woo et al. (2013) and the virial method, and found significant discrepancy between the two results.

The $M_{BH} - \sigma_*$ correlation is considered to be one of the most reliable black hole mass estimators, as it is estimated for both quiescent and active galaxies in various luminosity and redshift ranges. On the other hand, the virial assumtion is often used

for estimation of black hole massses of local type 1 AGN and so far it yielded reliable results.

In order to understand which method can be applied for such faint AGN as we have in CALIFA, we analyzed the folowing scenarios:

- The BELs that we detected are not actually representing accretion onto the central SMBH
- $M_{BH} - \sigma_*$ correlation is not reliable black hole mass estimator for CALIFA type 1 AGN
- Virial scaling relations break down at these extremely low luminosity regimes

As we already mentioned in Section 6.1.1, we can claim with high accuracy that the BEL that we detected in nuclear spectra of CALIFA galaxies are in fact reflecting the accretion onto the central SMBH, as they are located exclusivelly in AGN-LINER region of the emision-line ratio diagnostic diagrams, and have widths comparable to those of "typical" luminous AGN.

We found that black hole masses estimated from $M_{BH} - \sigma_*$ fall right on the $M_{BH} - M_*$ correlation of Reines and Volonteri (2015). As $M_{BH} - \sigma_*$ correlation of Woo et al. (2013) and $M_{BH} - M_*$ correlation of Reines and Volonteri (2015) are estimated for totally independent data samples we have no reason to believe that black hole mass estimates from $M_{BH} - \sigma_*$ correlation of Woo et al. (2013) would be biased towards the $M_{BH} - M_*$ relation of Reines and Volonteri (2015).

Virial method requires a lot of assumtions that may result in high uncertainties when estimating black hole masses. Beside unknown virial factor that accounts for geometry and kinematics of the BLR which we have little to no information, scaling relationships are estimated in higher luminosity regime than what we probed in our work. Most likely these scaling relationships are no longer linear in this extreme low-luminosity regime and cannot be used in black hole mass estimations, while $M_{BH} - \sigma_*$ correlation still remainds a valid M_{BH} estimator.

As we cannot certainly claim that one of the last two scenarios is correct, this topic requires future work that would provide estimations of the scaling relationships in the luminosity regime where they were not established so far.

6.1.4 Structure of the central engine of LLAGN

Assuming that $M_{BH} - \sigma_*$ correlation still can be used as a valid black hole mass estimator of LLAGN in CALIFA, we estimated black hole masses for a sub-sample of 55 of our type 1 AGN that amounts on average 2.1×10^7 $M_\odot$, populating the mid- to low-mass end. We also estimated that these objects accrete at extremely low Eddington ratios ($4.1 \times 10^{-5} - 2.4 \times 10^{-3}$), which might be considered as inactive according to some previously established definitions (Nicastro, 2000).

At high accretion rates, the central engine consists of geometrically thin and optically thick accretion disk surrounding the central SMBH (Shakura and Sunyaev, 1973). At low Eddington rates, such we have in our type 1 AGN sample, the structure of the central engine is somewhat modified. According to (Nicastro, 2000), for Eddington ratios $\lambda < 10^{-3}$, the central engine is decomposed into 3-component structure. The optically thick and geometrically thin accretion disk truncates (Shakura and Sunyaev, 1976; Esin, McClintock, and Narayan, 1997; Ruan et al., 2019) and forms quasi-spherically radiativelly inefficient accretion flow (Quataert, 2003), while optically thick clumpy dusty torus collapses into outer thin disk. The

third component are the radio jets emitted by the central source that can reach the size of the entire galaxy, and serve as a great confirmation that we are in fact looking at AGN.

This model suggests that below these extremely low Eddingtion ratios, the BLR cannot be formed, and we could not possible detect the BELs as they would be so broad and faint that they would be merged with continuum. However, having a strong confirmation that we actutally detected BELs, although significantly weaker than those of luminous AGN, proves that such strict model may not be the proper explanation of the structure of LLAGN. As we already mentioned in Section 6.1.2, it is possbile that for bolometric luminosities $L_{bol} < 10^{42}$ erg s^{-1} the dusty torus shrinks to the size that the BLR becomes revealed. Accordingly, the transition from the "standard" AGN model with geometrically thin accretion disk and optically thick torus, to the radiativelly ineffective 3-component structure happens rather smoothly. It is possible in that case that for extremely low bolometric luminosities and Eddington ratios that we estimated in CALIFA type 1 AGN, that the BLR region still persists at very low level, and is revealed by the disappearance of the torus.

We conclude that LLAGN are still able to form the BLR that produces extremely weak, yet still detectable BELs. However, in order to fully understand the structure of the central engine of LLAGN, further studies on LLAGN are required.

Accretion rate shows us in which phase of activity a certain AGN is residing, providing us with information about the structure of the accretion disk and AGN itself.

6.1.5 Luminosity and distribution functions of type 1 AGN in CALIFA

In order to fully understand black hole growth across cosmic history, it is necessary to establish the AGN luminosity function (AGNLF) at different redshifts and luminosities. AGNLF of CALIFA type 1 AGN might serve as a great zero-point for further studies of AGNLF at higher redshifts.

We estimated emission-line luminosity function of broad Hα lines, as well as distribution functions of their central SMBH masses – the Black Hole Mass Function (BHMF) and Eddington ratios – Eddington Ratio Distribution Function (ERDF) for a sub-sample of 55 of type 1 AGN from CALIFA.

The shapes of BHMF and ERDF show indication of flattening towards low-mass and low-λ end, which is consistent with the flattening of the broad AGNLF. We also estimated the active fraction of SMBHs in our sample, which decreases with increasing black hole mass for $\log(M_{BH}) > 7.5$. These results agree with the well-known scenario of anti-hierarchical growth of black holes (Cowie et al., 2003; Ueda et al., 2003; Steffen et al., 2003; McLure and Dunlop, 2004; Merloni, 2004; Merloni and Heinz, 2008). According to this scenario, the most massive black holes were formed in luminous AGN in early cosmic times, while the local Universe is mostly populated by low-luminosity low-mass SMBHs.

Analyzing the flattening trend in BHMF and ERDF, we concluded that most likely both contribute to the shape of AGNLF, and AGN downsizing. This implies that the local Universe consists of high fraction of low-mass SMBH residing in extremely low accretion regimes. Our type 1 AGN from CALIFA reaches the upper limit of AGN duty cycle in local Universe, as we would not expect the active SMBH fraction to be significantly higher than what we estimated in our work.

6.1.6 Final census of CALIFA AGN

In order to obtain full AGN census in the CALIFA survey galaxy sample, more then one AGN diagnostic method is required, as each carry its own limitations and biases. As it is already mentioned in Chapter 6.1.1, we used both emission-line ratio and BEL detection diagnostics in order to identify type 2 and type 1 AGN, respectively. What we found out is that thes objects contribute a high fraction of CALIFA galaxies.

In the final chapter of this thesis, we performed cross-correlation between CALIFA and multiwavelength surveys – *Swift*-BAT 105 month catalogue in the X-ray, and NVSS in the radio domain. We also constructed spatially resolved emission-line ratio diagnostic diagrams in order to detect possible extended AGN emission, that may be a signature of the past AGN activity or the material blown away from the nucleus by jets or shocks.

Our final census consists of five different types of AGN types in the CALIFA survey, which contribute a large fraction (23%) of all CALIFA galaxies. Once again, we summarize our final classification, with given percentage of their contribute to the entire CALIFA DR3 galaxy sample (542 objects):

- 89 type 1 AGN – 16%
- 29 additional Seyfert 2 galaxies – 5%
- 1 additional X-ray AGN – 0.2%
- 7 radio AGN – 1.3%
- 1 extended AGN 0.2%

As some of the objects overlapped within different AGN types, we constructed a hierarchy in order listed above, based on our certainty on the classification methods used for diagnostics.

The combination of multiwavelenght observations is important for investigating various areas of AGN physics, such as radio loudness, the origin of jets, and the structure of accretion disks, while extended emission might reveal us information on the past AGN activity.

6.2 Future perspectives

Having a complete picture of AGN and SMBH demographics across cosmic history is essential for understanding the processes of formation and evolution of galaxies. While luminous AGN can easily be detected by their strong nuclear emission, they are very challenging for studying the coevolution of SMBHs and their hosts as their emission often outshines the entire galaxy. On the other hand, weak emission of LLAGN is very useful for studying the properties of central SMBHs and their hosts separately, as AGN emission doesn't dominate the spectrum. Hence, the proper detection of type 1 LLAGN is extremely important for establishing unbiased correlations between SMBHs and their hosts, and for determining the faint-end of AGNLF. Further studies of local LLAGN could bring new light on this topic, and may help construct the black hole scaling relationships that are valid in this extremely low luminosity regime. This, of course, requires high spectral resolution and proper techniques of stellar contamination subtraction.

That being said, as the emission coming from the LLAGN can be highly diluted by the host galaxy's starlight, it may be very challenging to detect them in the optical

domain. An important feature of AGN is that they emit a very broad spectrum, covering spectrum from X-ray to the radio wavelengths. So far not many studies were conducted on X-ray and radio properties of LLAGN, and as they are known to be very strong X-ray and radio emitters, this might help us uncover "hidden" LLAGN that we were not able to detect in the optical spectra due to their extremely weak emission.

Although we still lack the complete picture of the structure of the central engine of LLAGN, in this thesis we showed that the BLR can definitely still be detected at extremely low bolometric luminosities and Eddington ratios. But some questions still remain unanswered. Are these LLAGN in the stage when the torus has mostly disappeared but the BLR is still present? What is the structure of the central engine of the LLAGN? Mid-IR studies might hold an important information on the dust properties of these objects, and might help us understand how the dust is distributed in LLAGN.

Finally, the evolution of AGNLF across different refshift and luminosities, as well as BHMF and ERDF, provide key insight into SMBH and AGN demographics. Establishing these luminosity and distribution functions at low-end will not only show us how LLAGN fit into a bigger picture, but will also serve as a great zero-point for higher redshift AGN and QSO luminosity function studies. If AGNLF is well established for a wide range of luminosities at different redshifts, it can be used for studying of evolution of entire AGN population over cosmic time and better understanding of the AGN phenomenon.

Bibliography

Abazajian, K. N. et al. (2009). In: *ApJS* 182, pp. 543–558.

Aird, J. et al. (2010). In: *MNRAS* 401.4, pp. 2531–2551.

Aird, J. et al. (2015a). In: *MNRAS* 451.2, pp. 1892–1927.

Aird, J. et al. (2015b). In: *ApJ* 815.1, 66, p. 66.

Aller, M. C. and D. O. Richstone (2007). In: *ApJ* 665.1, pp. 120–156.

Alloin, D. et al. (1994). "The International AGN Watch: a Multiwavelength Monitoring Consortium". In: *Frontiers of Space and Ground-Based Astronomy*. Ed. by W. Wamsteker, Malcolm S. Longair, and Y. Kondo. Vol. 187. Astrophysics and Space Science Library, p. 325.

Almeida, C. Ramos et al. (2011). In: *The Astrophysical Journal* 731.2, p. 92.

Alonso-Herrero, A. et al. (2000). In: *ApJ* 530, pp. 688–703.

Asmus, D. et al. (2011). In: *A&A* 536, A36, A36.

Avni, Y. and J. N. Bahcall (1980). In: *ApJ* 235, pp. 694–716.

Baer, R. E., K. Schawinski, and A. Weigel (2016). "AGN from HeII: AGN host galaxy properties demographics". In: *American Astronomical Society Meeting Abstracts #227*. Vol. 227. American Astronomical Society Meeting Abstracts, p. 241.21.

Baldwin, J. A., M. M. Phillips, and R. Terlevich (1981). In: *PASP* 93, pp. 5–19.

Ballantyne, D. R. (2014). In: *MNRAS* 437.3, pp. 2845–2855.

Barger, A. J. et al. (2003). In: *ApJ* 584.2, pp. L61–L64.

Barger, A. J. et al. (2005). In: *AJ* 129.2, pp. 578–609.

Baron, Dalya et al. (2018). In: *MNRAS* 480.3, pp. 3993–4016.

Barth, A. J. and J. C. Shields (2000). In: *PASP* 112, pp. 753–767.

Barth, Aaron J., A. Pancoast, and LAMP2011 Collaboration (2012). "The Lick AGN Monitoring Project 2011: Reverberation Mapping of Markarian 50". In: *American Astronomical Society Meeting Abstracts #219*. Vol. 219. American Astronomical Society Meeting Abstracts, p. 209.04.

— (2013). "The Lick AGN Monitoring Project 2011: New Velocity-Resolved Reverberation-Mapping Results". In: *American Astronomical Society Meeting Abstracts #221*. Vol. 221. American Astronomical Society Meeting Abstracts, p. 309.07.

Barth, Aaron J. et al. (2001). In: *ApJ* 555.2, pp. 685–708.

Barth, Aaron J. et al. (2011). In: *ApJ* 743.1, L4, p. L4.

Becker, Robert H., Richard L. White, and David J. Helfand (1995). In: *ApJ* 450, p. 559.

Begelman, M. C. (1985). "Accretion disks in active galactic nuclei". In: *Astrophysics of Active Galaxies and Quasi-Stellar Objects*. Ed. by J. S. Miller, pp. 411–452.

Beifiori, A. et al. (2009). In: *ApJ* 692.1, pp. 856–868.

Belfiore, Francesco et al. (2016). In: *MNRAS* 461.3, pp. 3111–3134.

Bendo, G. J. et al. (2006). In: *ApJ* 652, pp. 283–305.

Bennert, N. et al. (2006). In: *Astronomy & Astrophysics* 456.3, pp. 953–966.

Bennert, Vardha N. et al. (2015). In: *ApJ* 809.1, 20, p. 20.

Bentz, M. C. et al. (2006). In: *ApJ* 644, pp. 133–142.

Bentz, M. C. et al. (2010). In: *ApJ* 716, pp. 993–1011.

Bentz, M. C. et al. (2013). In: *ApJ* 767, 149, p. 149.

Bentz, Misty C. et al. (2009). In: *ApJ* 705.1, pp. 199–217.

Berrier, Joel C. et al. (2013). In: *ApJ* 769.2, 132, p. 132.
Best, P. N. and T. M. Heckman (2012). In: *MNRAS* 421, pp. 1569–1582.
Best, P. N. et al. (2005). In: *MNRAS* 362.1, pp. 25–40.
Bhattacharyya, D. and A. Mangalam (2018). In: *Journal of Astrophysics and Astronomy* 39.1, 4, p. 4.
Binette, L. et al. (1994). In: *A&A* 292, pp. 13–19.
Binney, J. J., Roger L. Davies, and Garth D. Illingworth (1990). In: *ApJ* 361, p. 78.
Blandford, R. D. (1985). "Theoretical models of active galactic nuclei." In: *Active Galactic Nuclei*. Ed. by J. E. Dyson, pp. 281–299.
Blandford, R. D. and C. F. McKee (1982). In: *ApJ* 255, pp. 419–439.
Blandford, Roger D. and Mitchell C. Begelman (1999). In: *MNRAS* 303.1, pp. L1–L5.
Bongiorno, A. et al. (2007). In: *Astronomy & Astrophysics* 472.2, pp. 443–454.
Bongiorno, A. et al. (2014). In: *MNRAS* 443.3, pp. 2077–2091.
Bosch, R. C. E. van den et al. (2008). In: *MNRAS* 385.2, pp. 647–666.
Bosch, Remco C. E. van den and P. Tim de Zeeuw (2010). In: *Monthly Notices of the Royal Astronomical Society* 401.3, pp. 1770–1780.
Boyle, B. J., T. Shanks, and B. A. Peterson (1988). In: *Mon. Not. R. Astron. Soc.* 235.3, pp. 935–948.
Boyle, B. J. et al. (2000). In: *Monthly Notices of the Royal Astronomical Society* 317.4, pp. 1014–1022.
Braatz, J. A., A. S. Wilson, and C. Henkel (1996). In: *ApJS* 106, p. 51.
— (1997). In: *ApJS* 110.2, pp. 321–346.
Bremer, M. et al. (2013). In: *A&A* 558, A34, A34.
Brewer, Brendon J. et al. (2011). In: *ApJ* 733.2, L33, p. L33.
Brocklehurst, M. (1971). In: *MNRAS* 153, pp. 471–490.
Bruzual, G. and S. Charlot (2003). In: *MNRAS* 344, pp. 1000–1028.
Burbidge, G. R., E. M. Burbidge, and A. R. Sandage (1963). In: *Reviews of Modern Physics* 35.4, pp. 947–972.
Burkert, Andreas and Scott Tremaine (2010). In: *ApJ* 720.1, pp. 516–521.
Capetti, A. et al. (2005). In: *A&A* 431, pp. 465–475.
Cappellari, Michele (2008). In: *MNRAS* 390.1, pp. 71–86.
Cardelli, J. A., G. C. Clayton, and J. S. Mathis (1989). In: *ApJ* 345, pp. 245–256.
Chabrier, G. (2003). In: *PASP* 115, pp. 763–795.
Chen, K. and J. P. Halpern (1989). In: *ApJ* 344, pp. 115–124.
Cisternas, Mauricio et al. (2011). In: *ApJ* 726.2, 57, p. 57.
Civano, Francesca et al. (2019). In: *BAAS* 51.3, 429, p. 429.
Clavel, J. (1991). *International AGN Watch: Mapping the Broad-line Region in NGC 3783*. IUE Proposal.
Coccato, L. et al. (2006). In: *MNRAS* 366.3, pp. 1050–1066.
Collin, S. et al. (2006). In: *A&A* 456.1, pp. 75–90.
Condon, J. J. et al. (1998). In: *AJ* 115, pp. 1693–1716.
Congiu, E. et al. (2017). In: *A&A* 603, A32, A32.
Cowie, L. L. et al. (2003). In: *ApJ* 584.2, pp. L57–L60.
Cracco, V. et al. (2011). In: *MNRAS* 418.4, pp. 2630–2641.
Cristiani, S. et al. (2004). In: *ApJ* 600.2, pp. L119–L122.
Croom, S. M. et al. (2004). In: *MNRAS* 349.4, pp. 1397–1418.
Croom, Scott M. et al. (2009). In: *Monthly Notices of the Royal Astronomical Society* 399.4, pp. 1755–1772.
Croston, Judith H. et al. (2004). In: *Nuclear Physics B Proceedings Supplements* 132, pp. 165–168.
Croton, Darren J. et al. (2006). In: *MNRAS* 365.1, pp. 11–28.

Dadina, M. et al. (2010). In: *A&A* 516, A9, A9.
Dalla Bontà, E. et al. (2009). In: *ApJ* 690.1, pp. 537–559.
Davis, Benjamin L., Alister W. Graham, and Ewan Cameron (2018). In: *ApJ* 869.2, 113, p. 113.
Davis, Benjamin L., Alister W. Graham, and Marc S. Seigar (2017). In: *Monthly Notices of the Royal Astronomical Society* 471.2, pp. 2187–2203.
Del Moro, A. et al. (2013). In: *A&A* 549, A59, A59.
Devereux, Nick et al. (2003). In: *AJ* 125.3, pp. 1226–1235.
Dietrich, M. et al. (1993). In: *ApJ* 408, p. 416.
Dopita, M. A. and R. S. Sutherland (1995). In: *ApJ* 455, p. 468.
Dopita, Michael A. and Ralph S. Sutherland (1996). In: *ApJS* 102, p. 161.
Dressler, A. (1989). "Observational Evidence for Supermassive Black Holes". In: *Active Galactic Nuclei*. Ed. by Donald E. Osterbrock and Joseph S. Miller. Vol. 134. IAU Symposium, p. 217.
Dudik, R. P., S. Satyapal, and D. Marcu (2009). In: *ApJ* 691.2, pp. 1501–1524.
Ebrero, J. et al. (2009). In: *A&A* 493.1, pp. 55–69.
Elitzur, Moshe and Isaac Shlosman (2006). In: *ApJ* 648.2, pp. L101–L104.
Eracleous, Michael, Jason A. Hwang, and Helene M. L. G. Flohic (2010). In:
Esin, A. A., J. E. McClintock, and R. Narayan (1997). In: *ApJ* 489, pp. 865–889.
Eun, D.-i., J.-H. Woo, and H.-J. Bae (2017). In: *ApJ* 842, 5, p. 5.
Fabbiano, G. et al. (2004). In: *ApJ* 616.2, pp. 730–737.
Fabian, A. C. (2012). In: *ARA&A* 50, pp. 455–489.
Fabian, A. C. et al. (1986). In: *ApJ* 305, p. 9.
Falcke, Heino et al. (2000). In: *ApJ* 542.1, pp. 197–200.
Fan, X. et al. (2000). In: *Astron.J. 121 (2001) 54*.
Felten, J. E. (1976). In: *ApJ* 207, pp. 700–709.
Ferland, G. J. and H. Netzer (1983). In: *ApJ* 264, pp. 105–113.
Fernandes, R. Cid et al. (2011). In: *Monthly Notices of the Royal Astronomical Society* 413.3, pp. 1687–1699.
Ferrarese, L. and D. Merritt (2000). In: *ApJ* 539, pp. L9–L12.
Ferrarese, L. et al. (2001). In: *ApJ* 555, pp. L79–L82.
Ferrarese, Laura (2002). In: *ApJ* 578.1, pp. 90–97.
Ferrarese, Laura and Holland Ford (2005). In: *Space Sci. Rev.* 116.3-4, pp. 523–624.
Ferrarese, Laura, Holland C. Ford, and Walter Jaffe (1996). In: *ApJ* 470, p. 444.
Filho, M. E., P. D. Barthel, and L. C. Ho (2006). In: *A&A* 451.1, pp. 71–83.
Filho, M. E. et al. (2004). In: *A&A* 418, pp. 429–443.
Filho, Mercedes E., Peter D. Barthel, and Luis C. Ho (2000). In: *ApJS* 129.1, pp. 93–110.
— (2002). In: *ApJS* 142.2, pp. 223–238.
— (2003). In: *ApJS* 144.1, pp. 211–211.
Filippenko, A. V. (1989). "Low-Luminosity Active Galactic Nuclei". In: *Active Galactic Nuclei*. Ed. by D. E. Osterbrock and J. S. Miller. Vol. 134. IAU Symposium, p. 495.
Filippenko, A. V. and W. L. W. Sargent (1985). In: *ApJS* 57, pp. 503–522.
Filippenko, A. V. and R. Terlevich (1992). In: *ApJ* 397, pp. L79–L82.
Filippenko, Alexei V. (2003). In:
Fiore, F. et al. (2003). In: *A&A* 409, pp. 79–90.
Fiore, F. et al. (2012). In: *A&A* 537, A16, A16.
Fontanot, F., P. Monaco, and F. Shankar (2015). In: *MNRAS* 453, pp. 4112–4120.
Fosbury, R. A. E. et al. (1978). In: *MNRAS* 183, pp. 549–568.
Fotopoulou, S. et al. (2016). In: *A&A* 587, A142, A142.

Francesco, G. de, A. Capetti, and A. Marconi (2006). In: *A&A* 460.2, pp. 439–448.
— (2008). In: *A&A* 479.2, pp. 355–363.
Gadotti, Dimitri A. (2009). In: *MNRAS* 393.4, pp. 1531–1552.
Gallimore, Jack F. et al. (2006). In: *AJ* 132.2, pp. 546–569.
Gao, F. et al. (2016). In: *ApJ* 817.2, 128, p. 128.
Gao, F. et al. (2017). In: *ApJ* 834.1, 52, p. 52.
García-Benito, R. et al. (2015). In: *Astronomy & Astrophysics* 576, A135.
Gaskell, C. M. and A. J. Benker (2007). In: *ArXiv e-prints*.
Gaskell, C. M. and G. J. Ferland (1984). In: *PASP* 96, pp. 393–397.
Gebhardt, K. et al. (2000a). In: *ApJ* 539, pp. L13–L16.
Gebhardt, K. et al. (2000b). In: *ApJ* 543, pp. L5–L8.
Gebhardt, Karl and Jens Thomas (2009). In: *ApJ* 700.2, pp. 1690–1701.
Gebhardt, Karl et al. (2003). In: *ApJ* 583.1, pp. 92–115.
Gehrels, N. et al. (2004). In: *ApJ* 611.2, pp. 1005–1020.
Genzel, Reinhard, Frank Eisenhauer, and Stefan Gillessen (2010). In: *Reviews of Modern Physics* 82.4, pp. 3121–3195.
Georgakakis, A. et al. (2015). In: *MNRAS* 453.2, pp. 1946–1964.
Ghez, A. M. et al. (2004). In: *ApJ* 601.2, pp. L159–L162.
González-Martín, O. and S. Vaughan (2012). In: *A&A* 544, A80, A80.
González-Martín, O. et al. (2006). In: *Astronomy & Astrophysics* 460.1, pp. 45–57.
González-Martín, O. et al. (2009). In: *A&A* 506.3, pp. 1107–1121.
González-Martín, O. et al. (2014). In: *Astronomy & Astrophysics* 567, A92.
González-Martín, O. et al. (2015). In: *A&A* 578, A74, A74.
Graham, A. W. et al. (2007). In: *Monthly Notices of the Royal Astronomical Society* 378.1, pp. 198–210.
Graham, A. W. et al. (2011). In: *MNRAS* 412, pp. 2211–2228.
Graham, Alister W. et al. (2001). In: *ApJ* 563.1, pp. L11–L14.
Greene, J. E. and L. C. Ho (2005). In: *ApJ* 630, pp. 122–129.
— (2006). In: *ApJ* 641, pp. L21–L24.
— (2007). In: *ApJ* 670, pp. 92–104.
Greene, J. E. et al. (2016). In: *ApJ* 832.2, L26, p. L26.
Greene, Jenny E. and Luis C. Ho (2009). In: *The Astrophysical Journal* 704.2, pp. 1743–1747.
Greene, Jenny E. et al. (2010). In: *ApJ* 721.1, pp. 26–45.
Greenhill, L. J. et al. (1995). In: *ApJ* 440, p. 619.
Grier, C. J. et al. (2017). In: *ApJ* 851, 21, p. 21.
Gu, Q.-S. et al. (2007). In: *ApJ* 671, pp. L105–L108.
Gültekin, K. et al. (2009). In: *ApJ* 698, pp. 198–221.
Haardt, F. and L. Maraschi (1991). In: *ApJ* 380, p. L51.
Hagiwara, Yoshiaki et al. (2018). In: *PASJ* 70.3, 54, p. 54.
Halpern, J. P. and J. E. Steiner (1983). In: *ApJ* 269, pp. L37–L41.
Hao, L. et al. (2005a). In: *AJ* 129, pp. 1783–1794.
Hao, Lei et al. (2005b). In: *AJ* 129.4, pp. 1795–1808.
Hardcastle, M. J., D. A. Evans, and J. H. Croston (2007). In: *MNRAS* 376.4, pp. 1849–1856.
— (2009). In: *MNRAS* 396.4, pp. 1929–1952.
Häring, N. and H.-W. Rix (2004). In: *ApJ* 604, pp. L89–L92.
Harrison, C. M. et al. (2015). In: *ApJ* 800.1, 45, p. 45.
Hasinger, G., T. Miyaji, and M. Schmidt (2005). In: *A&A* 441.2, pp. 417–434.
Hawkins, M. R. S. and P. Veron (1995). In: *Monthly Notices of the Royal Astronomical Society* 275.4, pp. 1102–1116.

Heckman, T. M. (1980a). In: *A&A* 500, pp. 187–199.
Heckman, T. M. et al. (1981). In: *ApJ* 247, pp. 403–418.
Heckman, Timothy M. et al. (1989). In: *ApJ* 338, p. 48.
Heckman, Timothy M. et al. (2004). In: *The Astrophysical Journal* 613.1, pp. 109–118.
Heckman, T.M. (1980b). In: *Astronomy & Astrophysics* 87, pp. 142–151.
Hekatelyne, C. et al. (2018). In: *MNRAS* 474.4, pp. 5319–5329.
Helfand, David J., Richard L. White, and Robert H. Becker (2015). In: *ApJ* 801.1, 26, p. 26.
Henkel, C., J. E. Greene, and F. Kamali (2018). "Extragalactic maser surveys". In: *Astrophysical Masers: Unlocking the Mysteries of the Universe*. Ed. by A. Tarchi, M. J. Reid, and P. Castangia. Vol. 336. IAU Symposium, pp. 69–79.
Hernández-García, L. et al. (2013). In: *Astronomy & Astrophysics* 556, A47.
Hernández-García, L. et al. (2014). In: *Astronomy & Astrophysics* 569, A26.
Hewett, Paul C., Craig B. Foltz, and Frederic H. Chaffee (1993). In: *The Astrophysical Journal* 406, p. L43.
Hine, R. G. and M. S. Longair (1979). In: *MNRAS* 188, pp. 111–130.
Hirschmann, Michaela et al. (2012). In: *MNRAS* 426.1, pp. 237–257.
Ho, I. Ting et al. (2014). In: *MNRAS* 444.4, pp. 3894–3910.
Ho, L. C. (1996). "Optical Spectroscopy of LINERs and Low-Luminosity Seyfert Nuclei." In: *The Physics of Liners in View of Recent Observations*. Ed. by M. Eracleous et al. Vol. 103. Astronomical Society of the Pacific Conference Series, p. 103.
— (2003). "The Central Engines of Low-Luminosity AGNs". In: *Active Galactic Nuclei: From Central Engine to Host Galaxy*. Ed. by Suzy Collin, Francoise Combes, and Isaac Shlosman. Vol. 290. Astronomical Society of the Pacific Conference Series, p. 379.
Ho, L. C., A. V. Filippenko, and W. L. Sargent (1995). In: *ApJS* 98, p. 477.
Ho, L. C., A. V. Filippenko, and W. L. W. Sargent (1997a). In: *ApJS* 112, pp. 315–390.
— (1997b). In: *ApJ* 487, pp. 568–578.
Ho, L. C. and M. Kim (2016). In: *ApJ* 821, 48, p. 48.
Ho, L. C. et al. (1997). In: *ApJS* 112, pp. 391–414.
Ho, Luis C. (1999). In: *ApJ* 516.2, pp. 672–682.
— (2008). In: *Annual Review of Astronomy and Astrophysics* 46.1, pp. 475–539.
— (2009). In: *ApJ* 699.1, pp. 626–637.
Ho, Luis C., Alexei V. Filippenko, and Wallace L. W. Sargent (1993). In: *ApJ* 417, p. 63.
— (2003). In: *ApJ* 583.1, pp. 159–177.
Hota, Ananda and D. J. Saikia (2006). In: *MNRAS* 371.2, pp. 945–956.
Hu, Jian (2008). In: *Monthly Notices of the Royal Astronomical Society* 386.4, pp. 2242–2252.
Husemann, B. et al. (2008). In: *Astronomy & Astrophysics* 488.1, pp. 145–149.
— (2012). In: *Astronomy & Astrophysics* 549, A43.
Husemann, B. et al. (2013). In: *Astronomy & Astrophysics* 549, A87.
Husemann, B. et al. (2014). In: *MNRAS* 443.1, pp. 755–783.
Hviding, Raphael E. et al. (2018). In: *ApJ* 868.1, 16, p. 16.
Ichikawa, Kohei et al. (2019). In: *The Astrophysical Journal* 870.1, p. 31.
Ishibashi, W. and A. C. Fabian (2014). In: *MNRAS* 441.2, pp. 1474–1478.
Jahnke, Knud et al. (2009). In: *ApJ* 706.2, pp. L215–L220.
Jeter, Britton, Avery E. Broderick, and B. R. McNamara (2019). In: *The Astrophysical Journal* 882.2, p. 82.
Kaspi, S. et al. (2000). In: *ApJ* 533, pp. 631–649.
Kaspi, S. et al. (2005). In: *ApJ* 629, pp. 61–71.
Kauffmann, G. et al. (2003). In: *MNRAS* 346, pp. 1055–1077.

Kauffmann, Guinevere and Timothy M. Heckman (2009). In: *Monthly Notices of the Royal Astronomical Society* 397.1, pp. 135–147.
Keel, W. C. et al. (2012). In: *MNRAS* 420, pp. 878–900.
Keel, W. C. et al. (2015). In: *AJ* 149, 155, p. 155.
Kehrig, C. et al. (2012). In: *Astronomy & Astrophysics* 540, A11.
Kelly, Brandon C. and Andrea Merloni (2012). In: *Advances in Astronomy* 2012, 970858, p. 970858.
Kelly, Brandon C. and Yue Shen (2013). In: *ApJ* 764.1, 45, p. 45.
Kelz, A. et al. (2006). In: *PASP* 118, pp. 129–145.
Kewley, L. J. et al. (2001). In: *ApJ* 556, pp. 121–140.
Kewley, L. J. et al. (2006). In: *MNRAS* 372, pp. 961–976.
Koehler, T. et al. (1997). In:
Kollatschny, W. (2003). In: *Astronomy & Astrophysics* 407.2, pp. 461–472.
Kollatschny, W. et al. (2008). In: *A&A* 484.3, pp. 897–915.
Koratkar, A. P. and C. M. Gaskell (1991). In: *ApJS* 75, pp. 719–750.
Kormendy, J. (1993). "A critical review of stellar-dynamical evidence for black holes in galaxy nuclei". In: *The Nearest Active Galaxies*. Ed. by J. Beckman, L. Colina, and H. Netzer, pp. 197–218.
Kormendy, J. and L. C. Ho (2013). In: *ARA&A* 51, pp. 511–653.
Kormendy, John, R. Bender, and M. E. Cornell (2011). In: *Nature* 469.7330, pp. 374–376.
Kormendy, John and Karl Gebhardt (2001). "Supermassive black holes in galactic nuclei". In: *20th Texas Symposium on relativistic astrophysics*. Ed. by J. Craig Wheeler and Hugo Martel. Vol. 586. American Institute of Physics Conference Series, pp. 363–381.
Kormendy, John and Douglas Richstone (1995). In: *Annual Review of Astronomy and Astrophysics* 33.1, pp. 581–624.
Koski, A. T. and D. E. Osterbrock (1976). In: *ApJ* 203, p. L49.
Krips, M. et al. (2007). In: *A&A* 464.2, pp. 553–563.
Kuo, C. Y. et al. (2011). In: *ApJ* 727.1, 20, p. 20.
La Franca, F. et al. (2002). In: *ApJ* 570.1, pp. 100–113.
Labita, M. et al. (2009). In: *Monthly Notices of the Royal Astronomical Society* 396.3, pp. 1537–1544.
Lagos, Claudia Del P., Sofía A. Cora, and Nelson D. Padilla (2008). In: *MNRAS* 388.2, pp. 587–602.
Lamastra, A. et al. (2010). In: *MNRAS* 405, pp. 29–40.
Laor, A. (2003). In: *ApJ* 590, pp. 86–94.
Läsker, Ronald et al. (2014). In: *ApJ* 780.1, 70, p. 70.
Lauer, Tod R. et al. (2007). In: *The Astrophysical Journal* 670.1, pp. 249–260.
Lawrence, A. (2005). In: *MNRAS* 363, pp. 57–63.
Lawrence, A. et al. (1985). In: *ApJ* 291, pp. 117–127.
Leitherer, C., R. Gruenwald, and W. Schmutz (1992). "Models for starburst regions: how warm are warmers?" In: *Physics of Nearby Galaxies: Nature or Nurture?* Ed. by Trinh Xuan Thuan, Chantal Balkowski, and J. Tran Thanh Van, p. 257.
Li, Yan-Rong, Luis C. Ho, and Jian-Min Wang (2011). In: *The Astrophysical Journal* 742.1, p. 33.
Lípari, S. et al. (2004). In: *MNRAS* 355, pp. 641–681.
Loewenstein, Michael et al. (2001). In: *ApJ* 555.1, pp. L21–L24.
Macchetto, F. et al. (1997). In: *ApJ* 489.2, pp. 579–600.
Magorrian, J. et al. (1998). In: *AJ* 115, pp. 2285–2305.
Mahatma, V. H. et al. (2018). In: *MNRAS* 475.4, pp. 4557–4578.

Malkan, M. A. and W. L. W. Sargent (1982). In: *ApJ* 254, pp. 22–37.
Malmquist, K. G. (1922). In: *Meddelanden fran Lunds Astronomiska Observatorium Serie I* 100, pp. 1–52.
Maoz, D. et al. (1993). In: *ApJ* 404, p. 576.
Maoz, D. et al. (1998). In: *AJ* 116, pp. 55–67.
Maoz, Dan et al. (2005). In: *ApJ* 625.2, pp. 699–715.
Marconi, A. and L. K. Hunt (2003). In: *ApJ* 589, pp. L21–L24.
Marconi, A. et al. (2006). In: *A&A* 448.3, pp. 921–953.
Marconi, Alessandro et al. (2004). In: *Proceedings of the International Astronomical Union* 2004.IAUS222, pp. 49–52.
Marel, Roeland P. van der et al. (1998). In: *ApJ* 493.2, pp. 613–631.
Marshall, H. L. et al. (1983). In: *The Astrophysical Journal* 269, p. 35.
Marshall, Herman L. (1987). In: *AJ* 94, p. 628.
Mason, R. E. et al. (2012). In: *AJ* 144.1, 11, p. 11.
Matute, I. et al. (2006). In: *A&A* 451.2, pp. 443–456.
Mazzalay, X. et al. (2014). In: *MNRAS* 438.3, pp. 2036–2064.
McCarthy, Patrick J. et al. (1987). In: *ApJ* 319, p. L39.
McConnell, N. J. and C.-P. Ma (2013). In: *ApJ* 764, 184, p. 184.
McElroy, R. E. et al. (2016). In: *A&A* 593, L8, p. L8.
McLure, R. J. and J.S. Dunlop (2004). "The Cosmological Evolution of Quasar Black-Hole Masses". In: *Multiwavelength AGN Surveys*. WORLD SCIENTIFIC.
McNamara, B. R. and P. E. J. Nulsen (2012). In: *New Journal of Physics* 14.5, 055023, p. 055023.
Méndez-Abreu, J. et al. (2017). In: *Astronomy & Astrophysics* 598, A32.
Merloni, A. et al. (2010). In: *ApJ* 708.1, pp. 137–157.
Merloni, Andrea (2004). In: *Monthly Notices of the Royal Astronomical Society* 353.4, pp. 1035–1047.
Merloni, Andrea and Sebastian Heinz (2008). In: *Monthly Notices of the Royal Astronomical Society*, ???–???
Merritt, D. and L. Ferrarese (2001). In: *ApJ* 547, pp. 140–145.
Meyer, Eileen T. et al. (2013). In: *ApJ* 774.2, L21, p. L21.
Mingo, B. et al. (2014). In: *MNRAS* 440.1, pp. 269–297.
Mingo, B. et al. (2016). In: *MNRAS* 462.3, pp. 2631–2667.
Miyaji, T. et al. (2015). In: *ApJ* 804.2, 104, p. 104.
Miyaji, Takamitsu, Günther Hasinger, and Maarten Schmidt (2000). In: *A&A* 353, pp. 25–40.
Miyoshi, Makoto et al. (1995). In: *Nature* 373.6510, pp. 127–129.
Monreal-Ibero, A., S. Arribas, and L. Colina (2006). In: *ApJ* 637.1, pp. 138–146.
Monreal-Ibero, A. et al. (2010). In: *Astronomy and Astrophysics* 517, A28.
Morganti, R., T. Oosterloo, and Z. Tsvetanov (1998). In: *AJ* 115.3, pp. 915–927.
Morganti, R. et al. (2007). In: *A&A* 476.2, pp. 735–743.
Morganti, R. et al. (2015). "Radio Jets Clearing the Way Through a Galaxy: Watching Feedback in Action in the Seyfert Galaxy IC 5063". In: *Revolution in Astronomy with ALMA: The Third Year*. Ed. by D. Iono et al. Vol. 499. Astronomical Society of the Pacific Conference Series, p. 125.
Nagar, N. M. et al. (2002). In: *A&A* 392, pp. 53–82.
Nagar, Neil M., Heino Falcke, and Andrew S. Wilson (2005). In:
Nagar, Neil M. et al. (2000). In: *ApJ* 542.1, pp. 186–196.
Nandra, K., E. S. Laird, and C. C. Steidel (2005). In: *MNRAS* 360.1, pp. L39–L44.
Narayan, R. and I. Yi (1994). In: *ApJ* 428, pp. L13–L16.

Narayan, Ramesh, Igor V. Igumenshchev, and Marek A. Abramowicz (2000). In: *ApJ* 539.2, pp. 798–808.
Narayan, Ramesh and Jeffrey E. McClintock (2008). In: *New A Rev.* 51.10-12, pp. 733–751.
Nelson, C. H. et al. (2004). In: *ApJ* 615, pp. 652–661.
Netzer, Hagai et al. (2007). In: *ApJ* 671.2, pp. 1256–1263.
Netzer, Hagai et al. (2016). In: *ApJ* 819.2, 123, p. 123.
Neufeld, David A., Philip R. Maloney, and Sarah Conger (1994). In: *ApJ* 436, pp. L127–L130.
Neumayer, N. et al. (2007). In: *ApJ* 671.2, pp. 1329–1344.
Nicastro, F. (2000). In: *ApJ* 530, pp. L65–L68.
Nobuta, K. et al. (2012). In: *The Astrophysical Journal* 761.2, p. 143.
Novikov, I. D. and K. S. Thorne (1973). "Astrophysics of black holes." In: *Black Holes (Les Astres Occlus)*, pp. 343–450.
Obied, Georges et al. (2016). In: *MNRAS* 456.3, pp. 2861–2876.
Oh, Kyuseok et al. (2018). In: *The Astrophysical Journal Supplement Series* 235.1, p. 4.
Onken, C. A. et al. (2004). In: *ApJ* 615, pp. 645–651.
Onken, Christopher A. and Bradley M. Peterson (2002). In: *ApJ* 572.2, pp. 746–752.
Osterbrock, D. E. (1971). "Physical Conditions in the Active Nuclei of Galaxies and Quasi-Stellar Objects Deduced from Line Spectra". In: *Study Week on Nuclei of Galaxies*. Ed. by D. J. K. O'Connell, p. 151.
Osterbrock, D. E. and G. J. Ferland (2006). *Astrophysics of gaseous nebulae and active galactic nuclei*. Sausalito: University Science Books.
Osterbrock, D. E. and R. W. Pogge (1985). In: *ApJ* 297, pp. 166–176.
Padovani, Paolo (2017). In: *Nature Astronomy* 1, 0194, p. 0194.
Paggi, Alessandro et al. (2016). In: *ApJ* 823.2, 112, p. 112.
Palanque-Delabrouille, N. et al. (2013). In: *Astronomy & Astrophysics* 551, A29.
Pancoast, Anna et al. (2012). In: *ApJ* 754.1, 49, p. 49.
Pancoast, Anna et al. (2014). In: *MNRAS* 445.3, pp. 3073–3091.
Papaderos, P. et al. (2013). In: *Astronomy & Astrophysics* 555, p. L1.
Park, D. et al. (2012). In: *ApJS* 203, 6, p. 6.
Pastorini, G. et al. (2007). In: *A&A* 469.2, pp. 405–423.
Peebles, P. J. E. (1972). In: *ApJ* 178, pp. 371–376.
Pellegrini, Silvia, Luca Ciotti, and Jeremiah Ostriker (2008). "X-ray properties of elliptical galaxies as determined by feedback from their central black holes". In: *37th COSPAR Scientific Assembly*. Vol. 37, p. 2385.
Pesce, D. W. et al. (2018). In: *ApJ* 863.2, 149, p. 149.
Peterson, B. M. (1993). In: *PASP* 105, pp. 247–268.
Peterson, B. M. and A. Wandel (1999). In: *ApJ* 521, pp. L95–L98.
— (2000). In: *ApJ* 540, pp. L13–L16.
Peterson, B. M. et al. (1991). In: *ApJ* 368, p. 119.
Peterson, B. M. et al. (2004). In: *ApJ* 613, pp. 682–699.
Peterson, Bradley M. (2014). In: *Space Sci. Rev.* 183.1-4, pp. 253–275.
Pian, E. et al. (2010). In: *MNRAS* 401.1, pp. 677–686.
Pović, M. et al. (2013). In: *Astronomische Nachrichten* 334.3, p. 288.
Ptak, A. et al. (1998). In: *ApJ* 501.1, pp. L37–L40.
Ptak, A. et al. (2004). In: *ApJ* 606.1, pp. 173–184.
Quataert, E. (2003). In: *Astronomische Nachrichten Supplement* 324, pp. 435–443.
Ranalli, P. et al. (2016). In: *A&A* 590, A80, A80.
Reid, M. J. et al. (2009). In: *ApJ* 695.1, pp. 287–291.
Reines, A. E. and M. Volonteri (2015). In: *ApJ* 813, 82, p. 82.

Reines, Amy E. and Marta Volonteri (2019). In: *ApJ* 879.2, 133, p. 133.
Ricci, C. et al. (2013). In: *A&A* 553, A29, A29.
Rich, J. A., L. J. Kewley, and M. A. Dopita (2011). In: *ApJ* 734.2, 87, p. 87.
Richards, G. T. et al. (2006a). In: *ApJS* 166, pp. 470–497.
Richards, Gordon T. et al. (2006b). In: *The Astronomical Journal* 131.6, pp. 2766–2787.
Roth, M. M. et al. (2005). In: *PASP* 117, pp. 620–642.
Ruan, J. J. et al. (2019). "The Analogous Structure of Accretion Flows in Supermassive and Stellar Mass Black Holes". In: *AAS/High Energy Astrophysics Division*. Vol. 17. AAS/High Energy Astrophysics Division, p. 106.44.
Rusli, S. P. et al. (2013). In: *AJ* 146.3, 45, p. 45.
Sadler, Elaine M., C. R. Jenkins, and C. G. Kotanyi (1989). In: *MNRAS* 240, pp. 591–635.
Saglia, R. P. et al. (2016). In: *ApJ* 818.1, 47, p. 47.
Salucci, Paolo and Massimo Persic (1999). In: *MNRAS* 309.4, pp. 923–928.
Sánchez, S. F. et al. (2012). In: *Astronomy & Astrophysics* 538, A8.
Sánchez, S. F. et al. (2016). In: *Astronomy & Astrophysics* 594, A36.
Sanghvi, J. et al. (2014). In: *MNRAS* 445.2, pp. 1261–1268.
Sargent, W. L. W. et al. (1978). In: *ApJ* 221, pp. 731–744.
Sarzi, Marc et al. (2001). In: *ApJ* 550.1, pp. 65–74.
Sarzi, Marc et al. (2006). In: *MNRAS* 366.4, pp. 1151–1200.
Sarzi, Marc et al. (2010). In: *MNRAS* 402.4, pp. 2187–2210.
Savorgnan, G. et al. (2013). In: *MNRAS* 434.1, pp. 387–397.
Sazonov, S. Yu. and M. G. Revnivtsev (2004). In: *A&A* 423, pp. 469–480.
Schechter, P. (1976). In: *ApJ* 203, pp. 297–306.
Schmidt, M. and R. F. Green (1983). In: *ApJ* 269, pp. 352–374.
Schmidt, Maarten (1968). In: *ApJ* 151, p. 393.
Schmidt, Maarten, Donald P. Schneider, and James E. Gunn (1995). In: *The Astronomical Journal* 110, p. 68.
Schödel, R. et al. (2003). In: *ApJ* 596.2, pp. 1015–1034.
Schulze, A., L. Wisotzki, and B. Husemann (2009). In: *Astronomy & Astrophysics* 507.2, pp. 781–793.
Schulze, A. et al. (2015). In: *MNRAS* 447.3, pp. 2085–2111.
Schulze, Andreas and Karl Gebhardt (2011). In: *ApJ* 729.1, 21, p. 21.
Schulze, Andreas and Lutz Wisotzki (2010). In: *Proceedings of the International Astronomical Union* 5.S267, pp. 266–266.
Schwarzschild, M. (1979). In: *ApJ* 232, pp. 236–247.
Seigar, Marc S. et al. (2008). In: *ApJ* 678.2, p. L93.
Sexton, Remington O. et al. (2019). In: *ApJ* 878.2, 101, p. 101.
Shakura, N. I. and R. A. Sunyaev (1973). "Black Holes in Binary Systems: Observational Appearances". In: *X- and Gamma-Ray Astronomy*. Ed. by H. Bradt and R. Giacconi. Vol. 55. IAU Symposium, p. 155.
— (1976). In: *MNRAS* 175, pp. 613–632.
Shankar, F., D. H. Weinberg, and J. Miralda-Escudé (2013). In: *MNRAS* 428, pp. 421–446.
Shankar, F. et al. (2004). In: *MNRAS* 354.4, pp. 1020–1030.
Shankar, F. et al. (2016). In: *MNRAS* 460, pp. 3119–3142.
Shankar, Francesco, David H. Weinberg, and Jordi Miralda-Escudé (2009). In: *ApJ* 690.1, pp. 20–41.
Shankar, Francesco, David H. Weinberg, and Yue Shen (2010). In: *Monthly Notices of the Royal Astronomical Society*, no–no.
Shapiro, Kristen L. et al. (2006). In: *MNRAS* 370.2, pp. 559–579.

Shapovalova, A. I. et al. (2009). In: *Astronomy and Astrophysics* 509, A106.
Shen, Yue and Brandon C. Kelly (2012). In: *ApJ* 746.2, 169, p. 169.
Shen, Yue et al. (2008). In: *ApJ* 680.1, pp. 169–190.
Shields, G. A. (1978). In: *Nature* 272.5655, pp. 706–708.
Shields, J. C. (1992). In: *ApJ* 399, pp. L27–L30.
Silk, J. and M. J. Rees (1998). In: *Astronomy and Astrophysics* 1, p. 331.
Simpson, Chris (2005). In: *MNRAS* 360.2, pp. 565–572.
Singh, R. et al. (2013). In: *Astronomy & Astrophysics* 558, A43.
Singh, Veeresh et al. (2016). In: *The Astrophysical Journal* 826.2, p. 132.
Skielboe, Andreas et al. (2015). In: *MNRAS* 454.1, pp. 144–160.
Slater, R. et al. (2019). In: *A&A* 621, A83, A83.
Slee, O. B. et al. (1994). In: *MNRAS* 269, pp. 928–946.
Soltan, A. (1982). In: *MNRAS* 200, pp. 115–122.
Soto, Kurt T. and Crystal L. Martin (2012). In: *ApJS* 203.1, 3, p. 3.
Stalevski, Marko et al. (2016). In: *MNRAS* 458.3, pp. 2288–2302.
Stasińska, G. et al. (2008). In: *MNRAS* 391.1, pp. L29–L33.
Steffen, A. T. et al. (2003). In: *The Astrophysical Journal* 596.1, pp. L23–L26.
Stern, D. et al. (2012). In: *ApJ* 753, 30, p. 30.
Stockton, Alan, Hai Fu, and Gabriela Canalizo (2006). In: *New A Rev.* 50.9-10, pp. 694–700.
Szokoly, G. P. et al. (2004). In: *ApJS* 155, pp. 271–349.
Taniguchi, Y., Y. Shioya, and T. Murayama (2000). In: *AJ* 120, pp. 1265–1272.
Targett, Thomas A., James S. Dunlop, and Ross J. McLure (2012). In: *MNRAS* 420.4, pp. 3621–3631.
Terashima, Yuichi and Andrew S. Wilson (2003). In: *ApJ* 583.1, pp. 145–158.
Thater, S. et al. (2017). In: *A&A* 597, A18, A18.
Thater, Sabine et al. (2019). In: *A&A* 625, A62, A62.
Tran, H. D. et al. (2001). In: *AJ* 121.6, pp. 2928–2942.
Tremaine, S. et al. (2002). In: *ApJ* 574, pp. 740–753.
Trump, J. R. et al. (2011). In: *ApJ* 733, 60, p. 60.
Ueda, Yoshihiro et al. (2003). In: *The Astrophysical Journal* 598.2, pp. 886–908.
Ueda, Yoshihiro et al. (2011). In: *PASJ* 63, S937–S945.
Ueda, Yoshihiro et al. (2014). In: *ApJ* 786.2, 104, p. 104.
Ulvestad, James S. and Luis C. Ho (2001). In: *The Astrophysical Journal* 558.2, pp. 561–577.
Vanden Berk, Daniel E. et al. (2001). In: *AJ* 122.2, pp. 549–564.
Vazdekis, A. et al. (2012). In: *MNRAS* 424, pp. 157–171.
Veilleux, S. and D. E. Osterbrock (1987). In: *ApJS* 63, pp. 295–310.
Veilleux, Sylvain and David S. Rupke (2002). In: *ApJ* 565.1, pp. L63–L66.
Verheijen, M. A. W. et al. (2004). In: *Astronomische Nachrichten* 325, pp. 151–154.
Vestergaard, M. (2004). In: *ApJ* 601.2, pp. 676–691.
Vestergaard, M. and Patrick S. Osmer (2009). In: *The Astrophysical Journal* 699.1, pp. 800–816.
Vestergaard, M. et al. (2008). In: *The Astrophysical Journal* 674.1, pp. L1–L4.
Vestergaard, Marianne and Bradley M. Peterson (2006). In: *ApJ* 641.2, pp. 689–709.
Vika, Marina et al. (2009). In: *Monthly Notices of the Royal Astronomical Society* 400.3, pp. 1451–1460.
Vila-Vilaro, Baltasar (2000). In: *Publications of the Astronomical Society of Japan* 52.2, pp. 305–316.
Villar-Martín, M. et al. (2008). In: *MNRAS* 390, pp. 218–226.
Vito, F. et al. (2014). In: *MNRAS* 445.4, pp. 3557–3574.

Walcher, C. J. et al. (2006). In: *ApJ* 649, pp. 692–708.
Walcher, C. J. et al. (2009). In: *MNRAS* 398, pp. L44–L48.
Walcher, C. J. et al. (2014). In: *Astronomy & Astrophysics* 569, A1.
Walsh, Jonelle L., Aaron J. Barth, and Marc Sarzi (2010). In: *ApJ* 721.1, pp. 762–776.
Walsh, Jonelle L. et al. (2013). In: *The Astrophysical Journal* 770.2, p. 86.
Wandel, A., B. M. Peterson, and M. A. Malkan (1999). In: *ApJ* 526.2, pp. 579–591.
Weigel, Anna K. et al. (2017). In: *ApJ* 845.2, 134, p. 134.
Williams, Peter R. et al. (2018). In: *The Astrophysical Journal* 866.2, p. 75.
Willner, S. P. et al. (1985). In: *ApJ* 299, pp. 443–461.
Willner, S. P. et al. (2004). In: *ApJS* 154, pp. 222–228.
Wisotzki, Lutz (1999). In:
Wolf, C. et al. (2003). In: *A&A* 408, pp. 499–514.
Woo, J.-H. and C. M. Urry (2002). In: *ApJ* 579, pp. 530–544.
Woo, J.-H. et al. (2010). In: *ApJ* 716, pp. 269–280.
Woo, J.-H. et al. (2013). In: *ApJ* 772, 49, p. 49.
Woo, J.-H. et al. (2015). In: *ApJ* 801, 38, p. 38.
Wrobel, J. M. (1991). In: *AJ* 101, p. 127.
Wylezalek, Dominika (2017). "Observational Signatures Of Agn Feedback Across Cosmic Time". In: *Galaxy Evolution Across Time*, p. 57.
Xiao, T. et al. (2011). In: *ApJ* 739, 28, p. 28.
Yong, S. Y., R. L. Webster, and A. L. King (2016). In: *PASA* 33, e009, e009.
Younes, G. et al. (2010). In: *A&A* 517, A33, A33.
Younes, G. et al. (2011). In: *A&A* 530, A149, A149.
Younes, G. et al. (2012). In: *Astronomy & Astrophysics* 539, A104.
Younes, George et al. (2019). In: *The Astrophysical Journal* 870.2, p. 73.
Young, P. J. et al. (1978). In: *ApJ* 221, pp. 721–730.
Yu, Qingjuan, Youjun Lu, and Guinevere Kauffmann (2005). In: *ApJ* 634.2, pp. 901–909.
Yu, Qingjuan and Scott Tremaine (2002). In: *MNRAS* 335.4, pp. 965–976.
Yuan, Feng and Ramesh Narayan (2014). In: *ARA&A* 52, pp. 529–588.
Yuan, T. T., L. J. Kewley, and D. B. Sanders (2010). In: *ApJ* 709.2, pp. 884–911.
Zdziarski, Andrzej A. et al. (2001). In: *ApJ* 554.1, pp. L45–L48.
Zhang, X.-G., D. Dultzin-Hacyan, and T.-G. Wang (2007). In: *MNRAS* 374, pp. 691–696.
Zhao, W. et al. (2018). In: *ApJ* 854.2, 124, p. 124.
Zibetti, S., S. Charlot, and H.-W. Rix (2009). In: *MNRAS* 400, pp. 1181–1198.
Zubovas, K. and A. R. King (2012). In: *MNRAS* 426.4, pp. 2751–2757.

APPENDIX A

Tables

The following tables document results obtained for the purpose of this thesis. Table A focuses on the properties of type 89 1 AGN from CALIFA DR3 sample, identified using the broad-emission line detection. I present the measure broad Hα fluxes, widths, shifts, as well as calculated broad Hα, and total stellar masses M_* of the host galaxies, calculated by the CALIFA collaboration (Walcher et al., 2014).

Table A shows the classification of CALIFA objects based on the emission-line ratio of their nuclear spectra. These 483 objects are divided into four classes: galaxies with star-forming, Seyfert 2, LINER-like, and intermediate nucleus. The table contains their nuclear emission-line ratios of [NII], [SII], [OI], Hα, and Hβ , as well as redshifts and morphology types.

In Table A.3 I present properties of 55 type 1 AGN for which we have calculated black hole masses M_{BH} using the $M_{BH} - \sigma_*$ correlation. The table contains estimations of M_{BH}, bolometric luminosities L_{bol}, Eddington ratios λ_{Edd}, and bulge stellar velocity dispersion σ_*.

Finally, Table A.4 provides the final census of different types of AGN in CALIFA (127 objects): Seyfert 2, type 1, X-ray, radio, and extended AGN, estimated from standard emission-line ratio diagnostic diagrams, broad-emission line detection, multiwavelength surveys and spatial emission-line ratio diagnostic diagrams, respectively. Total stellar masses and Hubble types of the host galaxies are also given in the table.

TABLE A.1: Properties of 89 type 1 AGN from CALIFA DR3

CALIFA ID	Object name	$f_{\mathrm{H}\alpha,\ broad}$ [10^{-17} erg s^{-1} cm^{-2} Å^{-1}]	FWHM $_{\mathrm{H}\alpha,\ \mathrm{broad}}$ [km s^{-1}]	Shift $_{\mathrm{H}\alpha,\ \mathrm{broad}}$ [km s^{-1}]	$L_{\mathrm{H}\alpha,\ broad}$ [10^{39} erg s^{-1}]	$\log(\frac{M_\star}{M_\odot})$
2	UGC00005	16.24 ± 1.49	2289 ± 115	-257 ± 48	2.09 ± 0.83	$10.83^{+0.10}_{-0.10}$
6	NGC7824	48.69 ± 7.13	3527 ± 257	73 ± 29	4.45 ± 1.81	$11.25^{+0.09}_{-0.09}$
24	NGC0177	36.74 ± 7.20	2431 ± 248	-486 ± 104	1.31 ± 0.58	$10.37^{+0.12}_{-0.11}$
28	NGC0214	19.32 ± 3.15	2963 ± 129	0 ± 54	0.95 ± 0.45	$10.82^{+0.10}_{-0.11}$
36	NGC0429	31.19 ± 3.42	3452 ± 333	0 ± 21	2.33 ± 0.91	$10.79^{+0.08}_{-0.09}$
38	NGC0447	32.79 ± 3.31	2544 ± 140	-334 ± 54	2.48 ± 0.89	$11.13^{+0.09}_{-0.10}$
44	NGC0499	64.35 ± 5.96	6309 ± 394	276 ± 55	2.99 ± 0.81	$11.40^{+0.17}_{-0.16}$
49	UGC00987	188.22 ± 4.18	2460 ± 25	-386 ± 10	9.77 ± 3.41	$10.61^{+0.10}_{-0.10}$
54	NGC0570	14.52 ± 2.65	2300 ± 222	-347 ± 92	1.04 ± 0.61	$10.96^{+0.08}_{-0.08}$
75	NGC0787	26.59 ± 3.30	2260 ± 155	-307 ± 63	1.40 ± 0.67	$10.96^{+0.12}_{-0.11}$
77	NGC0825	31.05 ± 4.30	2790 ± 229	-362 ± 88	0.82 ± 0.28	$10.42^{+0.10}_{-0.11}$
85	NGC0924	48.51 ± 7.99	3382 ± 293	-842 ± 133	2.26 ± 0.85	$10.86^{+0.10}_{-0.11}$
91	NGC0955	44.20 ± 3.82	3032 ± 169	355 ± 81	0.23 ± 0.09	$10.20^{+0.09}_{-0.09}$
101	NGC1060	55.68 ± 8.69	4049 ± 352	-837 ± 139	3.58 ± 1.42	$11.85^{+0.18}_{-0.17}$
102	NGC1070	52.17 ± 4.02	2605 ± 107	-383 ± 42	2.00 ± 0.93	$10.95^{+0.13}_{-0.13}$
107	NGC1094	14.87 ± 3.71	2781 ± 414	391 ± 130	1.47 ± 0.58	$10.72^{+0.10}_{-0.11}$
108	NGC1093	19.90 ± 1.80	2065 ± 109	-398 ± 49	1.33 ± 0.51	$10.51^{+0.10}_{-0.13}$
114	NGC1142	118.26 ± 4.00	1543 ± 30	-312 ± 14	21.23 ± 8.14	$11.47^{+0.12}_{-0.12}$
118	UGC02465	31.06 ± 6.01	3399 ± 356	-337 ± 118	1.90 ± 0.67	$10.88^{+0.08}_{-0.09}$
119	NGC1167	233.81 ± 18.77	1676 ± 124	-149 ± 6	13.63 ± 5.52	$11.69^{+0.12}_{-0.12}$
134	NGC1645	40.02 ± 4.50	4544 ± 290	-4 ± 10	2.30 ± 0.91	$10.83^{+0.11}_{-0.11}$
135	UGC03151	47.56 ± 3.80	1676 ± 89	-396 ± 72	2.18 ± 0.89	$10.76^{+0.18}_{-0.17}$
139	NGC1666	44.86 ± 5.65	3763 ± 307	343 ± 138	0.81 ± 0.31	$10.47^{+0.09}_{-0.10}$
140	NGC1667	231.01 ± 3.76	2063 ± 16	-573 ± 8	11.52 ± 4.61	$10.86^{+0.11}_{-0.11}$
145	ARP180	10.19 ± 5.69	2985 ± 80	-371 ± 27	4.64 ± 2.01	$10.32^{+0.12}_{-0.13}$
155	UGC03995	94.38 ± 4.99	2157 ± 152	-173 ± 29	5.71 ± 2.31	$10.92^{+0.11}_{-0.10}$
160	NGC2476	58.27 ± 4.47	5154 ± 418	-203 ± 145	2.24 ± 0.88	$10.80^{+0.09}_{-0.10}$

164	NGC2487	19.44 ± 3.88	2990 ± 322	-352 ± 123	1.24 ± 0.60	$10.77^{+0.10}_{-0.10}$
167	UGC04145	105.76 ± 5.01	1445 ± 90	0 ± 15	6.17 ± 2.53	$10.96^{+0.09}_{-0.24}$
169	IC0485	38.68 ± 7.06	1426 ± 121	192 ± 67	7.10 ± 2.77	$10.92^{+0.10}_{-0.10}$
177	NGC2522	33.41 ± 6.90	4461 ± 290	-970 ± 100	2.02 ± 0.97	$11.23^{+0.10}_{-0.10}$
189	NGC2554	69.20 ± 6.06	2338 ± 96	0 ± 27	3.31 ± 1.11	$11.21^{+0.13}_{-0.13}$
191	NGC2558	35.03 ± 7.68	2576 ± 246	-809 ± 143	2.39 ± 0.91	$10.84^{+0.11}_{-0.11}$
213	NGC2623	46.70 ± 3.11	1321 ± 104	155 ± 56	3.93 ± 1.91	$10.45^{+0.11}_{-0.11}$
216	NGC2638	48.68 ± 3.08	3639 ± 311	-283 ± 31	2.02 ± 0.85	$10.75^{+0.09}_{-0.10}$
277	NGC2916	19.51 ± 2.01	3382 ± 289	292 ± 77	0.81 ± 0.38	$10.75^{+0.11}_{-0.11}$
311	NGC3106	48.85 ± 4.02	4198 ± 308	-181 ± 43	5.32 ± 2.23	$11.21^{+0.16}_{-0.16}$
319	NGC3160	19.44 ± 1.97	1791 ± 121	29 ± 10	2.61 ± 0.96	$10.95^{+0.10}_{-0.09}$
340	NGC3303	76.81 ± 5.11	1836 ± 70	-206 ± 32	8.75 ± 3.01	$11.06^{+0.13}_{-0.13}$
341	UGC05771	33.11 ± 4.72	2898 ± 201	61 ± 21	5.07 ± 2.29	$11.32^{+0.12}_{-0.10}$
391	NGC3619	60.71 ± 4.89	5538 ± 410	596 ± 31	0.60 ± 0.29	$10.58^{+0.15}_{-0.15}$
414	NGC3687	20.19 ± 2.95	2670 ± 261	157 ± 49	0.45 ± 0.22	$10.28^{+0.10}_{-0.11}$
476	NGC3994	129.02 ± 3.12	2051 ± 152	-320 ± 81	4.15 ± 1.71	$10.42^{+0.13}_{-0.13}$
479	NGC4003	20.73 ± 3.16	2711 ± 218	-361 ± 111	2.60 ± 1.05	$11.07^{+0.09}_{-0.09}$
593	UGC08107	39.12 ± 3.18	1570 ± 89	61 ± 12	7.60 ± 3.04	$11.07^{+0.11}_{-0.11}$
614	NGC5056	22.29 ± 3.02	1060 ± 99	0 ± 17	2.14 ± 0.94	$10.48^{+0.11}_{-0.11}$
684	NGC5406	35.50 ± 2.92	5325 ± 491	9 ± 9	2.96 ± 1.51	$11.27^{+0.13}_{-0.12}$
690	NGC5443	34.57 ± 4.51	4011 ± 361	-233 ± 67	0.47 ± 0.21	$10.49^{+0.09}_{-0.10}$
695	NGC5423	41.96 ± 4.21	4683 ± 214	293 ± 39	4.61 ± 1.89	$11.44^{+0.20}_{-0.18}$
705	NGC5475	42.31 ± 3.19	2830 ± 219	-256 ± 42	0.53 ± 0.29	$10.33^{+0.08}_{-0.09}$
723	NGC5525	27.62 ± 3.99	3463 ± 310	123 ± 28	2.68 ± 1.07	$11.30^{+0.12}_{-0.13}$
726	NGC5532	49.71 ± 5.07	4959 ± 379	45 ± 14	8.22 ± 3.28	$11.85^{+0.17}_{-0.16}$
724	NGC5533	31.22 ± 1.89	3689 ± 329	241 ± 57	1.54 ± 0.59	$11.22^{+0.08}_{-0.08}$
730	NGC5549	46.65 ± 3.84	3524 ± 312	-805 ± 122	8.31 ± 3.19	$11.63^{+0.13}_{-0.12}$
736	NGC5587	13.43 ± 2.10	2229 ± 218	-86 ± 47	0.27 ± 0.12	$10.36^{+0.09}_{-0.10}$
742	NGC5610	52.06 ± 4.33	1670 ± 47	-427 ± 108	4.25 ± 2.28	$10.71^{+0.10}_{-0.11}$
747	UGC09262	16.70 ± 3.01	1891 ± 61	0 ± 12	3.45 ± 2.99	$10.63^{+0.10}_{-0.10}$
750	NGC5635	41.83 ± 3.91	5958 ± 399	411 ± 111	2.53 ± 1.02	$11.18^{+0.11}_{-0.11}$

757	NGC5675	67.75 ± 5.63	1783 ± 52	-210 ± 38	3.52 ± 1.29	$10.81^{+0.12}_{-0.13}$
770	NGC5739	64.61 ± 5.02	3617 ± 278	-245 ± 26	5.73 ± 2.46	$11.46^{+0.26}_{-0.23}$
772	UGC09492	16.11 ± 2.56	2302 ± 198	0 ± 26	3.31 ± 1.97	$11.21^{+0.10}_{-0.09}$
777	NGC5772	44.07 ± 4.70	4470 ± 291	-19 ± 11	3.29 ± 1.51	$10.97^{+0.10}_{-0.10}$
787	NGC5876	42.51 ± 4,28	4984 ± 344	-222 ± 31	1.51 ± 0.62	$10.90^{+0.13}_{-0.11}$
801	NGC5953	311.34 ± 4.82	1653 ± 79	-468.77 ± 99	4.77 ± 1.61	$10.48^{+0.09}_{-0.10}$
802	ARP220	70.57 ± 4.82	2032 ± 175	-168 ± 26	6.52 ± 2.54	$10.88^{+0.12}_{-0.09}$
806	NGC5966	22.57 ± 2.17	3724 ± 351	140 ± 41	1.43 ± 0.65	$11.01^{+0.21}_{-0.20}$
809	NGC5987	39.09 ± 2.60	4195 ± 289	-444 ± 171	1.18 ± 0.59	$11.21^{+0.09}_{-0.09}$
816	NGC6021	43.20 ± 5.23	5141 ± 352	-470 ± 135	3.12 ± 0.81	$11.01^{+0.11}_{-0.11}$
822	UGC10205	15.53 ± 1.96	1758 ± 88	-558 ± 132	1.98 ± 0.66	$11.00^{+0.11}_{-0.11}$
826	NGC6081	90.64 ± 3.11	2410 ± 167	-265 ± 19	7.71 ± 2.93	$11.12^{+0.08}_{-0.09}$
832	NGC6146	46.01 ± 2.90	2446 ± 181	-87 ± 46	10.17 ± 3.56	$11.63^{+0.14}_{-0.15}$
844	NGC6278	64.75 ± 5.72	4554 ± 300	-174 ± 38	1.78 ± 0.58	$10.92^{+0.09}_{-0.10}$
857	NGC6394	24.57 ± 2.31	1904 ± 92	-39 ± 21	4.87 ± 2.42	$10.90^{+0.10}_{-0.10}$
858	UGC10905	36.83 ± 3.88	4578 ± 329	332 ± 84	6.52 ± 2.67	$11.61^{+0.21}_{-0.05}$
867	NGC6762	45.15 ± 3.88	2645 ± 206	-139 ± 41	1.20 ± 0.55	$10.38^{+0.08}_{-0.07}$
865	UGC11228	32.57 ± 2.18	3397 ± 299	37 ± 17	3.13 ± 1.67	$11.09^{+0.10}_{-0.09}$
868	MCG-02-51-004	23.66 ± 2.78	2557 ± 239	-209 ± 52	2.12 ± 0.95	$10.68^{+0.10}_{-0.10}$
873	UGC11680NED01	44.05 ± 5.01	1709 ± 57	-287 ± 39	7.01 ± 2.81	$11.09^{+0.12}_{-0.13}$
874	NGC7025	40.13 ± 4.12	5204 ± 299	-630 ± 61	2.67 ± 1.15	$11.53^{+0.18}_{-0.18}$
883	UGC11958	20.85 ± 3.19	2494 ± 227	-412 ± 147	3.32 ± 1.78	$11.77^{+0.28}_{-0.26}$
886	NGC7311	78.19 ± 4.96	4948 ± 189	-87 ± 7	4.11 ± 2.11	$11.07^{+0.09}_{-0.09}$
887	NGC7321	16.28 ± 2.00	1919 ± 107	0 ± 21	2.10 ± 0.86	$10.93^{+0.10}_{-0.11}$
900	NGC7550	45.58 ± 4.59	2567 ± 170	-447 ± 101	2.90 ± 1.28	$11.43^{+0.19}_{-0.17}$
915	NGC7653	26.95 ± 2.55	2808 ± 265	-232 ± 67	1.22 ± 0.60	$10.50^{+0.11}_{-0.11}$
916	NGC7671	56.82 ± 4.96	3627 ± 328	-926 ± 147	2.39 ± 1.03	$10.96^{+0.09}_{-0.09}$
924	NGC7716	23.42 ± 1.89	2594 ± 222	0 ± 18	0.39 ± 0.18	$10.39^{+0.13}_{-0.13}$
927	NGC7738	147.94 ± 4.72	1783 ± 86	-133 ± 17	16.55 ± 6.45	$11.08^{+0.10}_{-0.09}$

TABLE A.2: Table of properties of 483 emission-line galaxies from the CALIFA DR3 survey, divided into four classes, according to the primary ionization source of their nucleus

CALIFA ID	Object name	Nucleus type	Redshift	Hubble type	$\frac{[OIII]}{H\beta}$	$\frac{[NII]}{H\alpha}$	$\frac{[SII]}{H\alpha}$	$\frac{[OI]}{H\alpha}$
1	IC5376	Seyfert 2	0.0166	Sb	1.63	0.86	0.19	0.11
2	UGC00005	Type 1 AGN	0.0238	Sbc	4.24	1.03	0.24	0.09
3	NGC7819	Star-forming	0.0164	Sc	0.97	0.23	0.14	0.03
5	IC1528	Star-forming	0.0125	Sbc	0.17	0.36	0.10	0.03
6	NGC7824	Type 1 AGN	0.0201	Sab	1.65	2.17	0.71	0.34
7	UGC00036	Seyfert 2	0.0206	Sab	0.69	0.64	0.26	0.05
8	NGC0001	Star-forming	0.0150	Sbc	0.16	0.35	0.08	0.02
9	NGC0023	Intermediate	0.0150	Sb	0.34	0.56	0.13	0.04
10	NGC0036	LINER-like	0.0197	Sb	1.51	1.47	0.20	0.17
11	UGC00139	Star-forming	0.0130	Scd	0.61	0.28	0.17	0.04
12	UGC00148	Star-forming	0.0138	Sc	0.25	0.33	0.10	0.03
13	MCG-02-02-030	LINER-like	0.0115	Sb	2.64	0.75	0.19	0.04
14	UGC00312	Star-forming	0.0142	Sd	0.26	0.39	0.17	0.03
15	ESO539-G014	Star-forming	0.0233	Scd	0.38	0.37	0.25	0.08
16	MCG-02-02-040	Star-forming	0.0117	Scd	0.28	0.43	0.07	0.03
17	UGC00335NED02	Intermediate	0.0178	E4	1.93	1.22	0.13	0.12
19	ESO540-G003	Intermediate	0.0108	Sb	1.04	0.68	0.06	0.07
20	NGC0160	Intermediate	0.0172	Sa	1.03	0.85	...	0.23
21	NGC0165	Star-forming	0.0192	Sb	0.19	0.34	0.07	0.01
22	NGC0169	LINER-like	0.0151	Sab	2.34	1.17	0.44	0.17
23	NGC0171	Seyfert 2	0.0129	Sb	1.74	1.24	0.20	0.22
24	NGC0177	Type 1 AGN	0.0126	Sab	1.73	1.10	0.35	0.10
25	NGC0180	Star-forming	0.0172	Sb	1.41	0.19	0.15	0.03
26	NGC0192	Intermediate	0.0135	Sab	1.00	0.52	0.10	0.02
27	NGC0216	Star-forming	0.0051	Sd	0.21	0.38	0.08	0.02
28	NGC0214	Type 1 AGN	0.0148	Sbc	4.78	1.27	0.22	0.11
29	NGC0217	Intermediate	0.0130	Sa	1.60	1.36	0.00	0.22
30	NGC0237	Star-forming	0.0136	Sc	0.24	0.39	0.10	0.03

31	NGC0234	Star-forming	0.0145	Sc	0.24	0.39	0.10	0.03
32	MCG-02-03-015	LINER-like	0.0188	Sab	0.71	1.33	...	...
33	NGC0257	Star-forming	0.0171	Sc	0.49	0.37	0.18	0.06
34	NGC0309	Intermediate	0.0184	Scd	0.88	0.71	0.09	0.09
36	NGC0429	Type 1 AGN	0.0182	Sa	2.24	1.80	...	...
38	NGC0447	Type 1 AGN	0.0183	Sa	1.51	1.18	0.18	0.15
39	NGC0444	Star-forming	0.0158	Scd	0.26	0.34	0.06	0.01
40	UGC00809	Star-forming	0.0138	Scd	0.33	0.40	0.08	0.03
41	UGC00841	Star-forming	0.0182	Sbc	0.42	0.41	0.15	0.04
42	NGC0477	Star-forming	0.0193	Sbc	0.19	0.36	0.11	0.02
43	IC1683	Star-forming	0.0159	Sb	0.17	0.40	0.09	0.02
44	NGC0499	Type 1 AGN	0.0144	E5	2.39	1.70	0.29	0.14
45	NGC0496	Star-forming	0.0196	Scd	1.13	0.29	0.19	0.04
48	NGC0523	Intermediate	0.0155	Sd	1.06	0.72	0.17	0.11
49	UGC00987	Type 1 AGN	0.0152	Sa	4.64	2.11	0.65	0.37
50	NGC0528	LINER-like	0.0157	S0	2.75	1.71	0.13	0.20
51	NGC0529	LINER-like	0.0158	E4	1.35	1.48	...	...
52	NGC0551	Intermediate	0.0170	Sbc	1.01	0.67	0.15	0.04
53	UGC01057	Intermediate	0.0206	Sc	0.65	0.59	0.27	0.06
54	NGC0570	Type 1 AGN	0.0178	Sb	1.91	1.63	0.15	0.09
57	UGC01123	LINER-like	0.0159	Sab	3.45	1.22	0.35	0.14
58	IC0159	Star-forming	0.0126	Sdm	0.57	0.30	0.15	0.03
60	UGCA021	Star-forming	0.0064	Sdm	0.29	0.51	0.13	0.03
61	NGC0681	Intermediate	0.0057	Sa	1.47	0.57	0.26	0.10
62	UGC01274	LINER-like	0.0255	Sa	4.52	1.52	0.81	0.04
63	NGC0677	Intermediate	0.0165	E0	1.11	0.87	0.38	0.15
64	NGC0693	Star-forming	0.0051	E7	0.72	0.29	0.19	0.06
65	NGC0716	Star-forming	0.0147	Sb	0.30	0.48	0.11	0.03
66	UGC01368	Intermediate	0.0262	Sab	0.91	0.76	0.35	0.08
69	NGC0755	Star-forming	0.0053	Scd	0.47	0.32	0.19	0.06
70	IC1755	LINER-like	0.0257	Sb	1.36	1.30	0.62	0.08
71	NGC0768	LINER-like	0.0227	Sc	1.48	0.78	0.24	0.05
72	NGC0774	Seyfert 2	0.0149	S0	2.33	1.28	0.14	0.18

73	NGC0776	Intermediate	0.0159	S0	0.41	0.53	0.12	0.03
75	NGC0787	Type 1 AGN	0.0153	Sb	1.92	1.04	0.11	0.13
76	NGC0810	LINER-like	0.0248	Sa	3.42	1.36	0.62	0.21
77	NGC0825	Type 1 AGN	0.0109	E5	1.44	0.98	0.22	0.05
78	NGC0833	LINER-like	0.0125	Sa	2.60	1.33	0.39	0.30
80	NGC0842	LINER-like	0.0124	Sa	5.49	1.81	...	...
81	UGC01659	Intermediate	0.0267	S0	1.01	0.85	0.35	0.07
83	UGC01749	LINER-like	0.0261	Sc	1.91	1.26	0.63	0.10
84	NGC0873	Star-forming	0.0130	Sab	0.67	0.42	0.14	0.03
85	NGC0924	Type 1 AGN	0.0144	Scd	2.22	1.35	0.20	0.12
86	UGC01918	Star-forming	0.0165	S0	0.32	0.48	0.19	0.03
87	NGC0932	Seyfert 2	0.0132	Sb	2.52	1.53	0.21	0.27
88	UGC01938	Star-forming	0.0206	S0a	0.18	0.37	0.13	0.04
89	NGC0941	Star-forming	0.0052	Sbc	0.55	0.42	0.14	0.03
90	NGC0938	Seyfert 2	0.0133	Scd	2.03	1.15	...	...
91	NGC0955	Type 1 AGN	0.0048	E3	2.31	1.22	0.40	0.16
94	NGC0976	Intermediate	0.0139	Sa	0.79	0.85	0.13	0.06
95	NGC0991	Intermediate	0.0049	Sbc	0.69	0.83	0.38	0.13
96	UGC02099	Intermediate	0.0267	Scd	0.89	0.70	0.61	0.02
97	UGC02134	Star-forming	0.0149	S0a	0.25	0.35	0.15	0.05
99	NGC1041	Intermediate	0.0229	S0	0.62	0.54	0.99	...
100	NGC1056	Star-forming	0.0052	Sa	1.14	0.20	0.12	0.02
101	NGC1060	Type 1 AGN	0.0169	E3	3.30	1.64	...	...
102	NGC1070	Type 1 AGN	0.0131	Sb	3.06	2.23	0.46	0.38
104	UGC02229	Intermediate	0.0237	S0a	1.01	0.69	0.70	0.05
105	UGC02239	Star-forming	0.0157	Sab	0.38	0.29	0.16	0.03
107	NGC1094	Type 1 AGN	0.0209	Sb	0.98	0.78	0.78	0.05
108	NGC1093	Type 1 AGN	0.0172	Sbc	5.81	1.70	0.38	0.17
109	UGC02311	Star-forming	0.0230	Sbc	0.40	0.40	0.11	...
110	UGC02319	Star-forming	0.0228	Sbc	0.52	0.37	0.12	0.04
111	MCG-02-08-014	Seyfert 2	0.0162	Sa	3.41	0.97	0.23	0.07
112	NGC1132	Intermediate	0.0224	E6	0.47	0.73	0.74	0.10
113	UGC02367	LINER-like	0.0239	Sab	1.82	0.83	0.38	0.10

114	NGC1142	Type 1 AGN	0.0280	Sd	5.17	1.63	0.51	0.24
115	UGC02403	Intermediate	0.0133	Sb	0.29	0.53	0.11	0.03
116	UGC02405	Intermediate	0.0249	Sbc	0.65	0.53	0.28	0.07
117	UGC02443	Star-forming	0.0081	Scd	1.55	0.16	0.18	0.05
118	UGC02465	Type 1 AGN	0.0165	S0	1.80	0.72	0.26	0.14
119	NGC1167	Type 1 AGN	0.0161	S0	3.60	3.10	1.14	0.59
121	NGC1211	LINER-like	0.0103	S0a	1.57	1.80	0.47	0.27
122	MCG-01-09-006	Intermediate	0.0282	Sbc	0.46	0.54	0.10	0.01
123	IC0307	Intermediate	0.0252	Sab	0.92	0.66	0.27	0.06
124	UGC02628	Intermediate	0.0221	Sbc	0.36	0.50	0.19	0.05
125	UGC02690	Star-forming	0.0203	Scd	0.29	0.38	0.11	0.03
126	NGC1324	Intermediate	0.0183	Sb	1.10	0.78	...	...
127	NGC1349	LINER-like	0.0214	E6	1.20	1.11	0.76	0.11
128	NGC1361	Intermediate	0.0171	E5	0.99	0.89	0.12	...
129	MCG-01-10-015	Star-forming	0.0134	Sc	0.26	0.39	0.10	...
130	MCG-01-10-019	Star-forming	0.0170	Sbc	1.48	0.12	0.13	0.03
131	NGC1542	Star-forming	0.0121	Sab	1.13	0.19	0.10	0.02
132	UGC03038	Intermediate	0.0264	Sab	0.85	0.53	0.26	0.05
133	UGC03107	Star-forming	0.0273	Sb	0.41	0.35	0.18	0.04
134	NGC1645	Type 1 AGN	0.0160	S0a	1.67	1.92	0.30	0.27
135	UGC03151	Type 1 AGN	0.0143	Sa	1.15	0.89	0.32	0.08
137	NGC1659	Intermediate	0.0150	Sbc	0.28	0.57	0.08	0.03
139	NGC1666	Type 1 AGN	0.0090	S0a	2.47	1.75	0.23	0.40
140	NGC1667	Type 1 AGN	0.0149	Sbc	8.21	2.36	0.60	0.36
141	IC2095	Star-forming	0.0093	Sc	2.32	0.09	0.12	0.03
142	IC2098	Star-forming	0.0093	Sb	0.22	0.37	0.14	0.02
143	NGC1677	Star-forming	0.0090	Scd	0.25	0.50	...	...
144	IC2101	Intermediate	0.0148	Scd	0.69	0.47	0.15	0.06
145	ARP180	Type 1 AGN	0.0137	Scd	1.78	0.73	0.51	0.52
146	UGC03253	Intermediate	0.0145	Sb	0.38	0.51	0.12	0.04
148	UGC03539	Star-forming	0.0117	Sc	0.35	0.41	0.08	0.02
149	NGC2347	Seyfert 2	0.0153	Sbc	0.82	0.72	0.18	0.07
150	UGC03899	Star-forming	0.0135	Sd	0.55	0.30	0.19	0.04

151	NGC2410	Seyfert 2	0.0161	Sb	2.70	0.78	...	...
152	UGC03944	Star-forming	0.0136	Sbc	1.24	0.20	0.21	0.07
153	UGC03969	Intermediate	0.0275	Sb	0.69	0.50	0.15	0.04
154	UGC03973	Type 1 AGN	0.0226	Sbc	1.96	0.81	0.31	0.13
155	UGC03995	Type 1 AGN	0.0164	Sb	7.74	0.93	0.25	0.10
156	NGC2449	LINER-like	0.0169	Sab	1.20	1.55	0.23	0.12
157	UGC04029	Intermediate	0.0153	Sc	0.41	0.51	0.13	0.02
158	UGC04054	Star-forming	0.0078	Scd	0.34	0.50	0.12	0.02
159	IC0480	Star-forming	0.0158	Sc	0.50	0.33	0.19	0.07
160	NGC2476	Type 1 AGN	0.0131	E6	6.10	1.53	...	...
161	NGC2480	Star-forming	0.0086	Sdm	0.29	0.41	0.15	0.03
162	NGC2481	LINER-like	0.0085	S0	1.55	1.25	0.39	0.17
164	NGC2487	Type 1 AGN	0.0168	Sb	1.52	1.29	0.45	0.29
165	UGC04132	Star-forming	0.0180	Sbc	0.39	0.36	0.12	0.04
166	UGC04140	Star-forming	0.0163	Scd	0.31	0.44	0.11	0.02
167	UGC04145	Type 1 AGN	0.0161	Sa	7.03	2.45	0.41	0.16
168	UGC04136	LINER-like	0.0229	Sa	3.64	1.14	0.57	0.15
169	IC0485	Type 1 AGN	0.0283	Sab	2.15	0.97	0.23	0.06
170	NGC2507	Intermediate	0.0159	S0a	0.86	1.21	0.07	0.26
171	NGC2513	Star-forming	0.0162	E2	0.25	0.51	...	...
172	UGC04176	Star-forming	0.0111	Sd	0.96	0.19	0.21	0.07
173	UGC04190	Seyfert 2	0.0172	S0a	4.55	0.87	...	...
174	UGC04197	Intermediate	0.0159	Sab	1.58	0.74	0.15	0.03
175	UGC04210	Star-forming	0.0174	Scd	0.18	0.39	0.11	0.01
176	UGC04195	Star-forming	0.0170	Sb	0.47	0.47	0.14	0.03
177	NGC2522	Type 1 AGN	0.0164	Sab	1.85	1.44	0.29	0.09
179	NGC2530	Star-forming	0.0174	Sd	0.27	0.45	0.12	0.03
178	UGC04233	Star-forming	0.0306	Sbc	0.36	0.46	0.14	0.03
180	UGC04240	Intermediate	0.0291	Sb	1.15	0.66	0.25	0.07
181	UGC04245	Intermediate	0.0181	Sbc	0.93	0.63	0.15	0.04
182	UGC04258	Star-forming	0.0113	Sdm	0.25	0.39	0.11	0.03
183	NGC2540	Star-forming	0.0216	Sbc	0.56	0.32	...	...
184	NGC2543	Star-forming	0.0091	Sbc	0.31	0.51	0.10	0.03

185	UGC04280	Star-forming	0.0125	Sb	1.35	0.14	0.13	0.03
186	IC2247	Seyfert 2	0.0150	Sab	1.98	0.65	0.19	0.08
187	UGC04308	Star-forming	0.0127	Sc	0.99	0.26	0.16	0.04
189	NGC2554	Type 1 AGN	0.0146	S0a	3.54	1.95	0.64	0.43
190	UGC04262	LINER-like	0.0197	Sbc	1.49	0.96	...	...
191	NGC2558	Type 1 AGN	0.0174	Sb	1.77	2.07	0.62	0.19
192	NGC2565	Seyfert 2	0.0127	Sb	3.55	1.19	0.21	0.13
194	NGC2572	LINER-like	0.0272	Sa	1.25	1.26	0.57	0.12
195	NGC2577	Intermediate	0.0077	E7	0.25	0.71	...	...
196	UGC04375	Intermediate	0.0077	Sbc	0.39	0.68	...	...
197	IC2341	LINER-like	0.0179	E6	1.40	1.38	0.46	0.19
199	IC2361	Star-forming	0.0078	Sbc	0.37	0.42	0.15	0.03
201	NGC2592	Star-forming	0.0077	E4	0.40	0.42	...	...
203	NGC2596	Star-forming	0.0206	Sbc	0.30	0.36	0.12	0.02
204	NGC2595	Star-forming	0.0153	Sc	0.68	0.26	0.11	0.01
205	UGC04425	Star-forming	0.0204	Sc	0.59	0.25	0.21	0.07
208	UGC04461	Star-forming	0.0174	Sbc	3.57	0.07	0.08	0.05
209	NGC2604	Star-forming	0.0079	Sd	0.34	0.42	0.16	0.00
210	UGC04468	LINER-like	0.0259	E7	1.24	1.11	0.57	0.03
213	NGC2623	Type 1 AGN	0.0193	Scd	1.45	1.11	0.24	0.19
215	UGC04532	Star-forming	0.0163	S0a	0.64	0.25	0.19	0.04
216	NGC2638	Type 1 AGN	0.0136	Sb	1.59	1.24	0.42	0.25
218	UGC04550	Star-forming	0.0077	Sb	1.85	0.21	0.13	0.02
219	NGC2639	LINER-like	0.0121	Sa	2.64	2.17	0.47	0.24
220	UGC04546	Intermediate	0.0182	Sa	0.81	0.86	...	...
221	UGC04551	Seyfert 2	0.0069	S0	2.82	0.61	0.22	0.02
225	IC2407	Intermediate	0.0215	Sbc	0.46	0.51	0.15	0.04
226	UGC04659	Star-forming	0.0070	Sdm	0.38	0.43	0.10	0.04
231	UGC04722	Star-forming	0.0070	Sdm	0.41	0.32	0.16	0.03
232	NGC2730	Star-forming	0.0138	Scd	1.11	0.21	0.20	0.06
260	NGC2805	Star-forming	0.0069	Sc	0.41	0.45	0.21	0.06
273	IC2487	Star-forming	0.0156	Sc	0.27	0.42	0.10	0.04
274	IC0540	LINER-like	0.0078	Sab	3.46	0.77	0.26	0.06

275	NGC2906	LINER-like	0.0081	Sbc	1.28	1.11	0.23	0.09
277	NGC2916	Type 1 AGN	0.0136	Sbc	3.89	1.12	0.17	0.15
278	UGC05108	LINER-like	0.0280	Sb	0.77	0.69	0.17	0.05
279	NGC2918	LINER-like	0.0239	E6	2.25	1.23	0.47	0.18
280	UGC05111	Intermediate	0.0234	Sb	1.11	0.76	0.28	0.09
281	UGC05113	LINER-like	0.0235	S0a	0.90	1.24	0.60	0.15
297	UGC05244	Star-forming	0.0112	Sbc	0.30	0.37	0.11	0.04
306	UGC05358	Star-forming	0.0109	Sd	0.99	0.24	0.19	0.01
307	UGC05359	Intermediate	0.0295	Sb	0.65	0.60	0.11	...
309	UGC05396	Star-forming	0.0194	Sbc	0.51	0.34	0.14	0.08
311	NGC3106	Type 1 AGN	0.0219	Sab	1.45	1.52	0.72	0.26
312	NGC3057	Star-forming	0.0063	Sdm	0.21	0.32	0.09	0.01
314	UGC05498NED01	LINER-like	0.0221	Sa	1.32	0.93	0.38	0.10
318	NGC3158	Star-forming	0.0245	E3	0.86	0.30	...	...
319	NGC3160	Type 1 AGN	0.0243	Sab	8.45	1.72	0.46	0.21
320	UGC05520	Star-forming	0.0122	Scd	0.39	0.33	0.14	0.04
323	NGC3182	Seyfert 2	0.0082	E7	2.43	0.73	0.23	0.09
326	UGC05598	Star-forming	0.0202	Sb	0.34	0.48	0.19	0.01
340	NGC3303	Type 1 AGN	0.0224	S0a	1.09	1.32	0.59	0.35
341	UGC05771	Type 1 AGN	0.0259	E6	2.31	1.82	0.85	0.35
353	NGC3381	Star-forming	0.0070	Sd	0.23	0.41	0.09	0.02
355	NGC3395	Star-forming	0.0070	Scd	2.85	0.10	0.07	0.02
360	NGC3406NED01	Intermediate	0.02500	S0	3.03	1.30	0.74	0.43
361	UGC05990	Star-forming	0.0068	Sc	0.43	0.40	0.21	0.06
364	UGC06036	LINER-like	0.0231	Sa	1.25	1.16	0.77	0.13
381	IC0674	LINER-like	0.0264	Sab	2.67	1.29	0.60	0.19
383	UGC06256	Star-forming	0.0126	Sbc	1.26	0.20	0.17	0.05
386	UGC06312	LINER-like	0.0229	Sab	4.06	1.22	1.18	0.20
387	NGC3615	Intermediate	0.0239	E5	0.42	0.58	...	...
388	NGC3614	Intermediate	0.0093	Sbc	0.65	0.48	0.17	0.04
391	NGC3619	Type 1 AGN	0.0067	S0a	1.80	0.94	0.41	0.21
414	NGC3687	Type 1 AGN	0.0100	Sb	0.88	0.89	0.37	0.15
436	NGC3811	Star-forming	0.0119	Sbc	0.31	0.43	0.07	0.03

437	NGC3815	Intermediate	0.0141	Sbc	0.57	0.57	0.12	0.07
475	NGC3991	Star-forming	0.0124	Im	0.40	0.31	0.16	0.03
476	NGC3994	Type 1 AGN	0.0120	Sbc	0.72	0.59	0.26	0.12
479	NGC4003	Type 1 AGN	0.0235	Sbc	0.78	0.77	0.24	0.05
486	UGC07012	Star-forming	0.0120	S0a	0.54	0.31	0.16	0.04
489	NGC4047	Star-forming	0.0130	Scd	0.38	0.36	0.19	0.05
500	UGC07145	Star-forming	0.0238	Sbc	0.27	0.43	0.11	0.03
502	NGC4149	Intermediate	0.0117	Sbc	1.07	0.68	0.20	0.11
515	NGC4185	Intermediate	0.0148	Sa	1.47	1.09	0.18	0.05
518	NGC4210	Intermediate	0.0105	Sbc	0.65	1.19	0.26	0.13
520	NGC4211NED02	Intermediate	0.0238	Sb	0.42	0.55	0.21	0.03
528	IC0776	Star-forming	0.0098	S0a	1.80	0.15	0.10	0.02
548	NGC4470	Star-forming	0.0093	Sdm	0.32	0.49	0.19	0.04
562	IC3598	LINER-like	0.0274	Sc	6.37	1.61	0.67	0.24
569	NGC4644	Intermediate	0.0180	S0	1.07	0.64	0.11	0.06
577	NGC4676A	Intermediate	0.0239	Sb	1.03	0.64	0.21	0.08
580	NGC4711	Intermediate	0.0154	Sdm	0.49	0.62	0.11	0.02
581	UGC08004	Star-forming	0.0225	Sbc	2.21	0.11	0.13	0.03
589	NGC4841A	Intermediate	0.0245	Scd	0.77	0.44	...	...
592	NGC4874	Intermediate	0.0258	E3	0.81	0.61	0.06	0.23
593	UGC08107	Type 1 AGN	0.0291	E0	1.24	1.04	0.47	0.32
602	NGC4956	Seyfert 2	0.0177	Sa	5.66	1.51	0.10	0.14
603	NGC4961	Star-forming	0.0103	E1	0.45	0.32	0.13	0.03
606	UGC08231	Star-forming	0.0099	Scd	0.64	0.24	0.20	0.04
607	UGC08234	LINER-like	0.0282	Sd	0.54	1.12	0.29	...
608	NGC5000	Intermediate	0.0207	S0	0.26	0.54	0.09	0.03
609	UGC08250	Star-forming	0.0196	Sbc	0.81	0.32	0.27	0.09
610	UGC08267	Star-forming	0.0258	Sc	0.26	0.34	0.11	0.02
611	NGC5016	Seyfert 2	0.0106	Sb	0.77	0.47	0.11	0.04
613	UGC08322	Seyfert 2	0.0275	S0a	87.36	1.35	0.85	0.18
614	NGC5056	Type 1 AGN	0.0206	Sc	0.37	0.60	0.13	0.11
615	IC4215	LINER-like	0.0150	Sb	3.31	0.98	0.34	0.12
624	NGC5157	LINER-like	0.0263	Sab	2.03	1.22	0.55	0.21

630	NGC5205	Intermediate	0.0075	Sbc	1.14	0.84	0.26	0.12
631	NGC5198	LINER-like	0.0103	E1	1.61	1.08	0.22	0.14
633	NGC5216	LINER-like	0.0113	E0	1.73	0.83	0.42	0.32
634	NGC5218	Intermediate	0.0113	Sab	0.79	0.89	0.17	0.10
651	NGC5267	LINER-like	0.0216	Sab	1.29	1.50	0.18	0.22
652	UGC08662	Star-forming	0.0087	Scd	0.61	0.26	0.18	0.05
653	NGC5289	LINER-like	0.0103	Sab	1.82	1.18	0.45	0.24
657	UGC08733	Star-forming	0.0097	Sdm	1.19	0.16	0.16	0.07
659	NGC5320	Intermediate	0.0106	Sbc	0.58	0.64	0.17	0.02
663	IC0944	Intermediate	0.0255	Sab	1.11	0.66	0.16	0.08
664	UGC08778	Intermediate	0.0128	Sb	1.13	0.77	0.31	0.10
665	UGC08781	LINER-like	0.0274	Sb	4.13	1.60	0.54	0.20
672	NGC5376	Intermediate	0.0086	Sb	0.86	0.78	0.13	0.13
673	NGC5379	Star-forming	0.0071	Sab	0.33	0.34	0.17	0.04
676	NGC5378	LINER-like	0.0121	Sb	1.70	0.97	0.30	0.14
679	NGC5402	Star-forming	0.0117	Sc	0.37	0.35	0.09	0.05
685	NGC5425	Star-forming	0.0087	Scd	0.37	0.36	0.16	0.03
680	NGC5394	Intermediate	0.0134	Sbc	0.26	0.61	0.13	0.03
684	NGC5406	Type 1 AGN	0.0192	Sb	2.09	1.59	0.12	0.27
686	NGC5421NED02	Seyfert 2	0.0282	Sa	11.07	1.97	0.66	0.79
688	NGC5439	Star-forming	0.0082	Sb	0.15	0.38	0.10	0.01
690	NGC5443	Type 1 AGN	0.0078	Sab	2.61	1.51	0.65	0.33
695	NGC5423	Type 1 AGN	0.0220	E6	2.82	1.12	...	...
697	UGC08988	Star-forming	0.0086	Scd	0.43	0.39	0.18	0.07
699	NGC5434	Star-forming	0.0210	Sc	0.44	0.43	0.07	0.34
703	NGC5473	Star-forming	0.0085	S0	0.21	0.43	...	...
705	NGC5475	Type 1 AGN	0.0075	S0a	1.93	2.19	0.77	0.31
707	NGC5480	Star-forming	0.0080	Scd	0.21	0.43	0.12	0.02
708	NGC5485	LINER-like	0.0084	E5	1.05	0.96	0.43	0.13
711	UGC09071	Star-forming	0.0079	Scd	0.38	0.40	0.19	0.06
713	UGC09080	Star-forming	0.0119	Sc	0.32	0.43	0.13	0.02
714	UGC09067	Star-forming	0.0283	Sbc	0.32	0.38	0.15	0.03
715	NGC5520	Star-forming	0.0081	Sbc	0.23	0.38	0.09	0.02

717	UGC09110	Intermediate	0.0156	Sb	1.23	0.63	0.19	0.08
718	UGC09113	Star-forming	0.0126	Sb	0.84	0.36	0.23	0.04
719	NGC5519	Star-forming	0.0271	Sb	0.87	0.23	0.15	0.03
720	NGC5522	Intermediate	0.0174	Sb	0.67	0.64	0.17	0.07
723	NGC5525	Type 1 AGN	0.0207	Sa	0.52	0.73	...	...
724	NGC5533	Type 1 AGN	0.0148	Sab	1.77	1.35	0.42	0.17
725	IC0995	Star-forming	0.0120	Scd	0.77	0.25	0.19	0.08
726	NGC5532	Type 1 AGN	0.0269	E4	1.49	2.37	1.30	0.12
727	NGC5546	LINER-like	0.0267	E3	1.89	1.85	0.59	0.15
728	IC0994	LINER-like	0.0269	S0a	1.31	1.24	0.64	0.11
730	NGC5549	Type 1 AGN	0.0279	S0	2.39	1.26	0.96	0.08
731	UGC09165	Intermediate	0.0196	Sa	0.56	0.53	0.14	0.05
732	NGC5559	Intermediate	0.0193	Sb	0.64	0.59	0.08	0.04
733	UGC09182	Star-forming	0.0176	Scd	0.22	0.33	0.10	0.01
735	UGC09199	Intermediate	0.0280	Sb	0.78	0.57	0.17	0.02
736	NGC5587	Type 1 AGN	0.0095	Sa	1.52	1.35	0.38	0.18
737	NGC5602	LINER-like	0.0092	S0a	1.79	0.96	0.10	0.24
740	NGC5614	LINER-like	0.0149	Sa	2.46	1.80	0.40	0.32
741	NGC5616	Intermediate	0.0300	Sc	1.16	0.71	0.19	0.04
742	NGC5610	Type 1 AGN	0.0190	Sb	0.90	0.69	0.19	0.07
743	NGC5622	Intermediate	0.0147	Sbc	0.51	0.51	0.10	0.04
744	NGC5631	Intermediate	0.0083	S0	0.19	0.92	0.27	0.18
745	UGC09253	Star-forming	0.0151	Sc	0.30	0.40	0.10	0.04
746	NGC5623	LINER-like	0.0132	E7	1.80	1.25	0.35	0.17
747	UGC09262	Type 1 AGN	0.0300	Sab	0.80	1.09	0.41	0.11
748	NGC5633	Star-forming	0.0096	Sbc	0.26	0.43	0.12	0.02
749	NGC5630	Star-forming	0.0108	Sdm	0.30	0.48	0.13	0.03
750	NGC5635	Type 1 AGN	0.0164	Sa	1.69	1.18	0.46	0.32
751	UGC09291	Star-forming	0.0116	Scd	0.35	0.33	0.14	0.03
753	NGC5656	Seyfert 2	0.0125	Sb	0.79	0.59	0.09	0.04
754	NGC5657	Star-forming	0.0151	Sbc	0.88	0.23	0.17	0.04
755	NGC5659	Intermediate	0.0170	Sb	0.43	0.50	0.09	0.04
756	NGC5665	Star-forming	0.0091	Sc	0.24	0.41	0.13	0.01

757	NGC5675	Type 1 AGN	0.0152	Sa	2.56	1.52	0.68	0.57
758	NGC5682	Star-forming	0.0094	Scd	0.62	0.34	0.16	0.03
760	NGC5689	LINER-like	0.0090	E6	1.47	1.29	0.36	0.30
761	NGC5684	LINER-like	0.0156	E3	1.72	1.20	0.43	0.27
762	UGC09401	LINER-like	0.0209	Sa	1.52	1.48	...	...
763	NGC5714	Star-forming	0.0093	Sb	1.38	0.21	0.14	0.03
764	NGC5720	LINER-like	0.0275	Sbc	5.97	1.61	0.75	0.07
765	UGC09448	Star-forming	0.0092	Sb	0.34	0.48	0.14	0.04
766	NGC5730	Star-forming	0.0103	Scd	0.24	0.34	0.09	0.03
767	NGC5731	Star-forming	0.0103	Sd	0.30	0.40	0.09	0.03
768	NGC5732	Star-forming	0.0144	Sbc	0.44	0.38	0.18	...
769	UGC09476	Star-forming	0.0127	Sbc	0.31	0.47	0.10	...
770	NGC5739	Type 1 AGN	0.0198	S0a	2.18	1.86	0.50	0.31
771	NGC5735	Intermediate	0.0145	Sbc	1.31	0.79	0.20	0.12
772	UGC09492	Type 1 AGN	0.0299	Sab	1.14	1.36	0.45	0.13
774	UGC09537	LINER-like	0.0313	Sb	1.09	1.05	0.15	...
775	UGC09542	Star-forming	0.0200	Sc	0.24	0.36	0.12	0.03
777	NGC5772	Type 1 AGN	0.0182	Sab	2.30	1.51	0.34	0.17
778	NGC5784	LINER-like	0.0197	S0	2.43	1.62	0.27	0.17
779	UGC09598	Intermediate	0.0204	Sbc	0.45	0.56	0.01	0.02
783	UGC09665	Star-forming	0.0103	Sb	0.27	0.43	0.11	0.06
784	NGC5829	Star-forming	0.0209	Sc	0.39	0.42	0.12	0.02
785	UGC09711	LINER-like	0.0302	Sab	1.70	1.24	0.26	0.03
786	IC4534	Intermediate	0.0185	S0a	1.82	1.26	...	...
787	NGC5876	Type 1 AGN	0.0126	S0a	1.91	1.35	0.23	0.15
788	UGC09759	Intermediate	0.0131	Sab	0.84	0.45	0.22	0.03
789	NGC5888	LINER-like	0.0308	Sb	1.25	1.43	0.30	...
790	UGC09777	Star-forming	0.0178	Sbc	0.52	0.31	0.20	0.05
791	NGC5908	Seyfert 2	0.0127	Sa	3.76	0.89	0.13	0.07
792	UGC09842	Star-forming	0.0315	Sbc	0.78	0.24	0.15	0.07
795	NGC5930	Intermediate	0.0106	Sab	0.35	0.51	0.28	0.03
796	NGC5934	Intermediate	0.0208	Sb	0.97	0.90	0.13	0.08
797	UGC09873	Star-forming	0.0205	Sb	0.27	0.36	0.10	0.02

798	UGC09892	Star-forming	0.0207	Sbc	0.31	0.40	0.14	0.05
799	NGC5951	Star-forming	0.0077	Scd	0.16	0.32	0.09	0.02
800	UGC09901	Star-forming	0.0125	Sc	0.80	0.23	0.19	0.05
801	NGC5953	Type 1 AGN	0.0083	Sa	1.51	0.85	0.23	0.08
802	ARP220	Type 1 AGN	0.0202	Sd	2.59	1.77	0.33	0.26
803	NGC5957	LINER-like	0.0078	Sb	2.48	0.88	0.30	0.05
804	NGC5971	Intermediate	0.0159	Sb	2.38	0.50	0.31	0.28
805	UGC09919	Star-forming	0.0126	Sc	0.67	0.28	0.08	0.01
806	NGC5966	Type 1 AGN	0.0168	E4	2.01	1.15	0.39	0.23
807	IC4566	LINER-like	0.0210	Sb	1.78	1.56	0.22	0.19
808	UGC09937	Intermediate	0.0172	Sa	1.04	1.00	0.10	0.07
809	NGC5987	Type 1 AGN	0.0116	Sa	2.95	1.36	0.29	0.29
810	NGC5980	Intermediate	0.0157	Sbc	0.45	0.52	0.10	0.06
811	UGC10043	Intermediate	0.0091	Sab	0.76	0.50	0.21	0.09
812	UGC10042	Star-forming	0.0162	Sc	0.33	0.39	0.12	0.03
813	NGC6004	Intermediate	0.0148	Sbc	0.32	0.61	0.14	0.05
814	UGC10097	LINER-like	0.0215	E5	2.85	1.65	0.51	0.19
816	NGC6021	Type 1 AGN	0.0179	E5	2.62	1.37	0.53	0.19
817	IC1151	Star-forming	0.0091	Scd	0.47	0.35	0.18	0.04
818	UGC10123	Intermediate	0.0142	Sab	0.57	0.55	0.12	0.03
819	NGC6027	Intermediate	0.0169	Sa	0.60	0.49	0.11	0.03
820	NGC6032	Intermediate	0.0163	Sbc	0.38	0.54	0.15	0.03
821	NGC6060	Star-forming	0.0168	Sb	0.56	0.31	0.17	0.05
822	UGC10205	Type 1 AGN	0.0237	S0a	0.85	0.50	0.27	0.05
823	NGC6063	Intermediate	0.0114	Sbc	0.42	0.49	0.16	0.03
824	IC1199	Star-forming	0.0179	Sb	0.31	0.45	0.09	0.04
825	UGC10257	Star-forming	0.0146	Sbc	1.48	0.15	0.11	0.02
826	NGC6081	Type 1 AGN	0.0194	S0a	2.85	2.10	0.97	0.30
827	UGC10297	Star-forming	0.0095	Sc	0.34	0.43	0.04	...
828	UGC10331	Star-forming	0.0164	Sc	1.43	0.20	0.16	0.03
830	UGC10337	LINER-like	0.0313	Sb	2.04	1.21	0.34	0.00
831	NGC6132	Star-forming	0.0186	Sbc	0.19	0.43	0.10	0.02
832	NGC6146	Type 1 AGN	0.0310	E5	1.61	1.78	0.78	0.29

833	NGC6154	LINER-like	0.0216	Sab	1.64	1.46	0.39	0.25
834	UGC10380	Intermediate	0.0311	Sb	1.56	0.99	0.14	...
835	NGC6150	LINER-like	0.03070	E7	0.37	0.60	0.26	...
836	NGC6155	Star-forming	0.0098	Sc	0.36	0.37	0.14	0.03
837	UGC10384	Star-forming	0.0186	Sb	0.31	0.43	0.16	0.05
838	UGC10388	Seyfert 2	0.0175	Sa	3.62	0.68	...	...
840	NGC6173	Intermediate	0.0309	E6	0.41	0.88	0.10	...
841	NGC6168	Star-forming	0.0103	Sc	0.23	0.41	0.11	0.05
842	NGC6186	Star-forming	0.0117	Sb	0.49	0.46	...	...
843	UGC10650	Star-forming	0.0117	Scd	0.30	0.38	0.12	0.05
844	NGC6278	Type 1 AGN	0.0111	S0a	2.25	1.65	0.48	0.49
846	UGC10695	LINER-like	0.0292	E5	1.59	0.98	0.46	0.14
847	UGC10710	Star-forming	0.0294	Sb	0.43	0.32	0.19	0.04
848	NGC6310	LINER-like	0.0128	Sb	1.36	1.10	0.32	0.07
849	NGC6301	Intermediate	0.0293	Sbc	0.76	0.53	0.21	0.01
850	NGC6314	LINER-like	0.0239	Sab	0.98	1.06	0.57	...
851	NGC6338	LINER-like	0.0286	E5	1.11	1.96	0.42	0.09
852	UGC10796	Star-forming	0.0117	Scd	1.38	0.15	0.14	0.05
853	NGC6361	Intermediate	0.0141	Sab	0.77	0.50	0.08	0.06
854	UGC10811	LINER-like	0.0303	Sb	1.00	1.10	0.07	...
856	IC1256	Star-forming	0.0175	Sb	0.37	0.47	0.11	0.03
857	NGC6394	Type 1 AGN	0.0294	Sbc	6.00	1.35	0.36	0.14
858	UGC10905	Type 1 AGN	0.0278	S0a	4.65	1.36	0.81	0.15
861	UGC10972	LINER-like	0.0172	Sbc	1.52	0.82	0.23	0.12
862	NGC6478	Intermediate	0.0239	Sc	0.71	0.52	0.16	0.06
863	NGC6497	Seyfert 2	0.0217	Sab	2.08	1.37	0.20	0.06
864	NGC6515	LINER-like	0.0241	E3	1.16	1.14	0.46	0.17
866	UGC11262	Star-forming	0.0200	Sc	0.14	0.40	0.09	0.02
867	NGC6762	Type 1 AGN	0.0109	Sab	2.99	1.60	0.50	0.21
868	MCG-02-51-004	Type 1 AGN	0.0199	Sb	1.83	0.86	0.15	0.12
869	NGC6941	Intermediate	0.0216	Sb	0.42	0.50	0.22	0.03
871	NGC6978	LINER-like	0.0208	Sb	1.61	1.29	0.31	0.17
874	NGC7025	Type 1 AGN	0.0172	S0a	5.57	1.42	0.28	0.20

865	UGC11228	Type 1 AGN	0.0206	S0	2.05	1.97	0.57	0.31
872	UGC11649	LINER-like	0.0135	Sab	2.14	1.01	0.25	0.21
873	UGC11680NED01	Type 1 AGN	0.0264	Sb	8.55	1.01	0.33	0.13
876	NGC7047	Intermediate	0.0199	Sbc	1.48	1.08	0.13	0.17
877	UGC11717	Seyfert 2	0.0215	Sab	4.23	1.70	0.52	0.20
878	MCG-01-54-016	Star-forming	0.0104	Scd	0.38	0.39	0.15	0.04
879	UGC11740	Intermediate	0.0220	Sbc	0.61	0.50	0.33	0.02
880	UGC11792	Star-forming	0.0165	Sbc	0.91	0.18	0.23	0.09
883	UGC11958	Type 1 AGN	0.0264	S0	2.22	1.81	0.85	0.18
884	UGC11982	Star-forming	0.0163	Scd	0.52	0.44	0.15	0.05
885	UGC12054	Star-forming	0.0073	Sc	0.43	0.46	0.15	0.04
886	NGC7311	Type 1 AGN	0.0153	Sa	2.57	1.60	0.13	0.10
887	NGC7321	Type 1 AGN	0.0238	Sbc	2.11	0.94	0.24	0.13
888	UGC12127	. Intermediate	0.02750	E1	0.34	0.77	0.12	0.00
889	NGC7364	Intermediate	0.0163	Sab	0.58	0.49	0.05	0.05
890	UGC12185	LINER-like	0.0222	Sb	5.00	1.46	0.88	0.26
891	UGC12224	Star-forming	0.0119	Sc	0.36	0.33	0.14	0.03
893	NGC7436	LINER-like	0.0245	E2	0.52	1.27	0.59	0.26
892	VV488NED02	Intermediate	0.0169	Sb	0.59	0.49	0.11	0.06
894	UGC12274	LINER-like	0.0254	Sa	2.44	1.75	0.75	0.24
895	UGC12308	Star-forming	0.0077	Scd	0.56	0.25	0.20	0.07
896	NGC7466	Seyfert 2	0.0249	Sbc	2.92	0.66	0.19	0.06
897	UGC12348	Seyfert 2	0.0253	Sb	6.82	1.14	0.27	0.10
898	NGC7489	Star-forming	0.0207	Sbc	0.20	0.40	0.11	0.02
899	NGC7536	Star-forming	0.0156	Sc	0.32	0.43	0.12	0.05
900	NGC7550	Type 1 AGN	0.0168	E4	2.06	1.67	0.58	0.34
901	NGC7549	Intermediate	0.0158	Sbc	0.89	0.54	0.13	0.04
903	NGC7562	Intermediate	0.0121	E4	0.63	0.83	...	...
904	NGC7591	Intermediate	0.0164	Sbc	0.94	1.04	0.17	0.10
905	UGC12494	Seyfert 2	0.0140	Sd	3.64	0.84	...	...
906	IC5309	Star-forming	0.0140	Sc	0.24	0.37	0.11	0.03
907	NGC7608	Intermediate	0.0117	Sbc	0.38	0.52	0.22	0.06
909	UGC12519	Star-forming	0.0146	Sc	0.23	0.42	0.11	0.02

911	NGC7619	Star-forming	0.0126	E3	0.40	0.44	...	...
913	NGC7625	Star-forming	0.0058	Sa	1.79	0.24	0.17	0.07
914	NGC7631	Intermediate	0.0125	Sb	0.51	0.47	0.11	0.04
915	NGC7653	Type 1 AGN	0.0142	Sb	1.38	1.16	0.40	0.24
916	NGC7671	Type 1 AGN	0.0137	S0	2.16	1.08	0.15	0.45
917	NGC7683	LINER-like	0.0124	S0	2.49	1.38	0.24	0.27
918	UGC12633	Star-forming	0.0140	Sab	0.29	0.32	0.14	0.01
919	NGC7684	Seyfert 2	0.0170	S0	202.99	1.51	...	...
920	NGC7691	Star-forming	0.0134	Sbc	0.16	0.35	0.10	0.02
922	UGC12688	Star-forming	0.0173	Scd	0.44	0.36	0.17	0.05
923	NGC7711	Seyfert 2	0.0135	E7	3.46	1.24	...	...
924	NGC7716	Type 1 AGN	0.0087	Sb	0.96	1.10	0.33	0.30
925	NGC7722	Seyfert 2	0.0133	Sab	1.63	1.04	0.19	0.12
926	UGC12723	Star-forming	0.0180	Sc	0.51	0.30	0.11	0.02
927	NGC7738	Type 1 AGN	0.0222	Sb	1.30	0.82	0.16	0.06
928	UGC12767	LINER-like	0.0173	Sb	1.81	1.69	0.44	0.31
929	UGC12810	Star-forming	0.0266	Sbc	0.68	0.26	0.16	0.03
930	UGC12816	Star-forming	0.0175	Sc	0.47	0.47	0.18	0.05
931	NGC7782	LINER-like	0.0177	Sb	1.91	1.31	0.52	0.20
933	NGC7787	Star-forming	0.0219	Sab	0.23	0.37	0.11	0.03
934	UGC12857	Star-forming	0.0083	Sbc	0.30	0.52	0.13	0.03
935	UGC12864	Star-forming	0.0155	Sc	0.50	0.46	0.09	0.01
936	MCG-01-01-012	Intermediate	0.0189	Sab	1.96	1.03	0.06	0.13
937	NGC7800	Star-forming	0.0060	Ir	0.66	0.32	0.14	0.03
938	NGC5947	Type 1 AGN	0.0300	Sab	0.54	0.31	0.16	0.04
939	NGC4676A	Intermediate	0.0216	Sdm	0.76	0.61	0.53	0.21

TABLE A.3: Table of black hole properties and their respective stellar velocity dispersions for a sample of 55 type 1 AGN for which we have M_{BH} measurements estimated from the $M_{BH} - \sigma_*$ correlation

Califa ID	Object name	$\log(\frac{M^{\sigma}_{BH}}{M_{\odot}})$	L_{bol} [10^{42} erg s^{-1}]	$\log(\lambda^{\sigma}_{Edd})$	σ_* [km s^{-1}]
2	UGC00005	6.92 ± 0.27	0.27 ± 0.11	-3.51	153.85 ± 11.82
6	NGC7824	7.97 ± 0.31	0.58 ± 0.24	-3.24	311.21 ± 1.04
28	NGC0214	7.02 ± 0.27	0.12 ± 0.05	-3.85	164.45 ± 11.02
38	NGC0447	7.07 ± 0.21	0.32 ± 0.13	-3.44	169.99 ± 1.64
44	NGC0499	8.09 ± 0.32	0.39 ± 0.16	-3.42	337.08 ± 1.59
49	UGC00987	6.76 ± 0.18	1.27 ± 0.53	-2.83	138.97 ± 6.59
54	NGC0570	7.11 ± 0.21	0.13 ± 0.06	-3.82	175.28 ± 6.44
75	NGC0787	7.22 ± 0.24	0.18 ± 0.08	-3.70	187.81 ± 2.42
85	NGC0924	7.65 ± 0.27	0.29 ± 0.12	-3.52	251.34 ± 1.85
101	NGC1060	8.34 ± 0.36	0.47 ± 0.19	-3.35	396.98 ± 1.88
102	NGC1070	7.17 ± 0.21	0.26 ± 0.11	-3.54	182.38 ± 1.92
107	NGC1094	7.18 ± 0.26	0.19 ± 0.08	-3.67	183.85 ± 9.72
108	NGC1093	6.91 ± 0.29	0.17 ± 0.07	-3.70	153.60 ± 12.72
119	NGC1167	7.31 ± 0.16	1.77 ± 0.74	-2.72	199.76 ± 0.56
134	NGC1645	7.66 ± 0.28	0.30 ± 0.12	-3.51	251.71 ± 2.32
139	NGC1666	6.99 ± 0.18	0.11 ± 0.04	-3.92	161.73 ± 1.27
140	NGC1667	7.12 ± 0.21	1.50 ± 0.62	-2.78	175.93 ± 6.61
154	UGC03973	7.29 ± 0.21	39.42 ± 16.43	-1.37	197.70 ± 4.58
155	UGC03995	7.3 ± 0.18	0.74 ± 0.31	-3.09	198.65 ± 2.39
160	NGC2476	7.57 ± 0.26	0.29 ± 0.12	-3.52	237.27 ± 1.51
164	NGC2487	6.95 ± 0.28	0.16 ± 0.07	-3.74	157.04 ± 1.84
167	UGC04145	7.29 ± 0.18	0.80 ± 0.33	-3.06	197.64 ± 2.65
191	NGC2558	7.54 ± 0.34	0.31 ± 0.13	-3.49	233.49 ± 3.54
277	NGC2916	7.02 ± 0.26	0.11 ± 0.04	-3.92	164.78 ± 3.86
311	NGC3106	7.70 ± 0.32	0.69 ± 0.29	-3.15	258.87 ± 2.90
341	UGC05771	7.90 ± 0.33	0.66 ± 0.27	-3.18	297.14 ± 2.67
414	NGC3687	6.52 ± 0.18	0.06 ± 0.02	-4.15	118.28 ± 2.39
476	NGC3994	7.26 ± 0.21	0.54 ± 0.22	-3.23	193.32 ± 5.34
479	NGC4003	7.31 ± 0.16	0.34 ± 0.14	-3.43	199.46 ± 1.12
614	NGC5056	6.85 ± 0.27	0.28 ± 0.12	-3.49	146.83 ± 11.65
684	NGC5406	7.38 ± 0.25	0.38 ± 0.16	-3.38	209.97 ± 1.61
690	NGC5443	6.60 ± 0.19	0.06 ± 0.03	-4.14	124.65 ± 3.08
695	NGC5423	8.13 ± 0.33	0.60 ± 0.25	-3.23	344.80 ± 5.23
724	NGC5533	7.42 ± 0.23	0.20 ± 0.08	-3.67	215.18 ± 1.69
736	NGC5587	6.73 ± 0.15	0.04 ± 0.01	-4.38	136.16 ± 5.56
742	NGC5610	6.89 ± 0.26	0.55 ± 0.23	-3.20	151.53 ± 11.19
750	NGC5635	7.87 ± 0.29	0.33 ± 0.14	-3.48	289.37 ± 1.61
772	UGC09492	7.31 ± 0.16	0.43 ± 0.18	-3.33	199.56 ± 0.53
777	NGC5772	7.71 ± 0.27	0.43 ± 0.18	-3.36	261.28 ± 1.49
787	NGC5876	7.68 ± 0.27	0.20 ± 0.08	-3.69	256.36 ± 1.90
816	NGC6021	7.66 ± 0.27	0.41 ± 0.17	-3.38	252.67 ± 1.11
832	NGC6146	8.17 ± 0.36	1.32 ± 0.55	-2.89	354.40 ± 2.69
844	NGC6278	7.78 ± 0.27	0.23 ± 0.10	-3.63	273.14 ± 0.88
857	NGC6394	6.66 ± 0.31	0.63 ± 0.26	-3.12	129.76 ± 2.11
858	UGC10905	7.31 ± 0.15	0.85 ± 0.35	-3.04	199.81 ± 1.88

865	UGC11228	7.63 ± 0.26	0.41 ± 0.17	-3.37	247.81 ± 1.91
867	NGC6762	6.71 ± 0.17	0.16 ± 0.06	-3.74	134.44 ± 6.52
868	MCG-02-51-004	6.87 ± 0.26	0.28 ± 0.11	-3.50	148.97 ± 4.31
886	NGC7311	7.59 ± 0.24	0.53 ± 0.22	-3.25	241.64 ± 1.98
887	NGC7321	7.30 ± 0.17	0.27 ± 0.11	-3.53	198.68 ± 0.96
900	NGC7550	7.94 ± 0.31	0.38 ± 0.16	-3.42	303.59 ± 3.41
915	NGC7653	6.71 ± 0.22	0.16 ± 0.07	-3.73	134.12 ± 1.12
916	NGC7671	7.96 ± 0.32	0.31 ± 0.13	-3.51	308.71 ± 2.97
924	NGC7716	6.62 ± 0.16	0.05 ± 0.02	-4.21	126.61 ± 8.19
927	NGC7738	7.26 ± 0.22	2.15 ± 0.90	-2.63	193.64 ± 7.41

TABLE A.4: Table of properties of five different AGN types in CALIFA

CALIFA ID	Object name	AGN type(s)	Hubble type	$\log(\frac{M_\star}{M_\odot})$
1	IC5376	Seyfert 2	Sb	$10.65^{+0.10}_{-0.09}$
2	UGC00005	Type 1, Seyfert 2	Sbc	$10.83^{+0.10}_{-0.10}$
6	NGC7824	Type 1	Sab	$11.25^{+0.09}_{-0.09}$
7	UGC00036	Seyfert 2	Sab	$11.00^{+0.11}_{-0.10}$
23	NGC0171	Seyfert 2	Sb	$10.72^{+0.10}_{-0.10}$
24	NGC0177	Type 1	Sab	$10.37^{+0.12}_{-0.11}$
28	NGC0214	Type 1, Seyfert 2	Sbc	$10.82^{+0.10}_{-0.11}$
36	NGC0429	Type 1, Seyfert 2	Sa	$10.79^{+0.08}_{-0.09}$
38	NGC0447	Type 1	Sa	$11.13^{+0.09}_{-0.10}$
44	NGC0499	Type 1	E5	$11.40^{+0.17}_{-0.16}$
49	UGC00987	Type 1	Sa	$10.61^{+0.10}_{-0.10}$
54	NGC0570	Type 1, Seyfert 2	Sb	$10.96^{+0.08}_{-0.08}$
72	NGC0774	Seyfert 2	S0	$10.92^{+0.08}_{-0.09}$
75	NGC0787	Type 1	Sb	$10.96^{+0.12}_{-0.11}$
77	NGC0825	Type 1	E5	$10.42^{+0.10}_{-0.10}$
85	NGC0924	Type 1	Scd	$10.86^{+0.10}_{-0.10}$
87	NGC0932	Seyfert 2	Sb	$10.96^{+0.10}_{-0.11}$
90	NGC0938	Seyfert 2	Scd	$10.96^{+0.14}_{-0.14}$
91	NGC0955	Type 1	E3	$10.20^{+0.09}_{-0.09}$
101	NGC1060	Type 1, Seyfert 2	E3	$11.85^{+0.18}_{-0.17}$
102	NGC1070	Type 1	Sb	$10.95^{+0.13}_{-0.14}$
107	NGC1094	Type 1	Sb	$10.72^{+0.10}_{-0.11}$
108	NGC1093	Type 1, Seyfert 2	Sbc	$10.51^{+0.10}_{-0.13}$
111	MCG-02-08-014	Seyfert 2, X-ray	Sa	$10.56^{+0.10}_{-0.09}$
114	NGC1142	Type 1, X-ray, Radio, EAGN	Sd	$11.47^{+0.12}_{-0.12}$
118	UGC02465	Type 1	S0	$10.88^{+0.08}_{-0.09}$
119	NGC1167	Type 1, Radio	S0	$11.69^{+0.12}_{-0.12}$
134	NGC1645	Type 1	S0a	$10.83^{+0.10}_{-0.11}$
135	UGC03151	Type 1	Sa	$10.76^{+0.18}_{-0.17}$
139	NGC1666	Type 1	S0a	$10.47^{+0.09}_{-0.10}$
140	NGC1667	Type 1	Sbc	$10.86^{+0.11}_{-0.11}$
145	ARP180	Type 1	Scd	$10.32^{+0.12}_{-0.13}$
149	NGC2347	Seyfert 2	Sbc	$10.94^{+0.13}_{-0.12}$
151	NGC2410	Seyfert 2	Sb	$10.88^{+0.09}_{-0.10}$
154	UGC03973	Type 1, Seyfert 2, X-ray, EAGN	Sbc	$10.79^{+0.19}_{-0.18}$
155	UGC03995	Type 1, Seyfert 2	Sb	$10.92^{+0.11}_{-0.10}$

160	NGC2476	Type 1, Seyfert 2	E6	$10.80^{+0.09}_{-0.10}$
164	NGC2487	Type 1	Sb	$10.77^{+0.10}_{-0.10}$
167	UGC04145	Type 1, Seyfert 2	Sa	$10.96^{+0.09}_{-0.24}$
169	IC0485	Type 1	Sab	$10.92^{+0.10}_{-0.10}$
173	UGC04190	Seyfert 2	S0a	$10.84^{+0.12}_{-0.12}$
177	NGC2522	Type 1	Sab	$11.23^{+0.10}_{-0.10}$
186	IC2247	Seyfert 2, EAGN	Sab	$10.51^{+0.10}_{-0.09}$
189	NGC2554	Type 1	S0a	$11.21^{+0.13}_{-0.13}$
191	NGC2558	Type 1	Sb	$10.85^{+0.11}_{-0.11}$
192	NGC2565	Seyfert 2	Sb	$10.70^{+0.10}_{-0.10}$
213	NGC2623	Type 1	Scd	$10.45^{+0.11}_{-0.11}$
216	NGC2638	Type 1	Sb	$10.75^{+0.09}_{-0.10}$
221	UGC04551	Seyfert 2	S0	$10.34^{+0.10}_{-0.09}$
274	IC0540	EAGN	S0a	$9.8754^{+0.10}_{-0.09}$
277	NGC2916	Type 1, Seyfert 2	Sbc	$10.75^{+0.11}_{-0.11}$
278	UGC05108	Radio	Sb	$10.889^{+0.11}_{-0.11}$
311	NGC3106	Type 1	Sab	$11.21^{+0.16}_{-0.16}$
314	UGC05498NED01	X-ray, Radio	Sa	$10.805^{+0.10}_{-0.10}$
319	NGC3160	Type 1, Seyfert 2	Sab	$10.95^{+0.10}_{-0.09}$
323	NGC3182	Seyfert 2	E7	$10.40^{+0.14}_{-0.14}$
340	NGC3303	Type 1	S0a	$11.06^{+0.13}_{-0.13}$
341	UGC05771	Type 1, Radio	E6	$11.32^{+0.12}_{-0.10}$
391	NGC3619	Type 1	S0a	$10.58^{+0.15}_{-0.15}$
414	NGC3687	Type 1	Sb	$10.28^{+0.10}_{-0.10}$
476	NGC3994	Type 1	Sbc	$10.42^{+0.13}_{-0.13}$
479	NGC4003	Type 1	Sbc	$11.07^{+0.09}_{-0.09}$
577	NGC4676A	Radio, EAGN	Sdm	$10.813^{+0.10}_{-0.13}$
592	NGC4874	Radio	E0	$11.695^{+0.27}_{-0.26}$
593	UGC08107	Type 1	E0	$11.07^{+0.11}_{-0.11}$
602	NGC4956	Seyfert 2	Sa	$10.99^{+0.11}_{-0.10}$
611	NGC5016	Seyfert 2	Sb	$10.23^{+0.11}_{-0.10}$
613	UGC08322	Seyfert 2	S0a	$11.16^{+0.10}_{-0.09}$
614	NGC5056	Type 1	Sc	$10.48^{+0.11}_{-0.11}$
684	NGC5406	Type 1	Sb	$11.27^{+0.13}_{-0.12}$
686	NGC5421NED02	Seyfert 2	Sa	$11.16^{+0.10}_{-0.10}$
690	NGC5443	Type 1	Sab	$10.49^{+0.09}_{-0.10}$
695	NGC5423	Type 1	E6	$11.44^{+0.20}_{-0.18}$
705	NGC5475	Type 1	S0a	$10.33^{+0.09}_{-0.09}$
723	NGC5525	Type 1	Sa	$11.30^{+0.12}_{-0.13}$
724	NGC5533	Type 1	Sab	$11.22^{+0.08}_{-0.08}$
726	NGC5532	Type 1, Radio	E4	$11.85^{+0.17}_{-0.16}$
730	NGC5549	Type 1	S0	$11.63^{+0.13}_{-0.12}$
736	NGC5587	Type 1	Sa	$10.36^{+0.09}_{-0.10}$
742	NGC5610	Type 1, X-ray	Sb	$10.71^{+0.10}_{-0.11}$
747	UGC09262	Type 1	Sab	$10.63^{+0.10}_{-0.10}$
750	NGC5635	Type 1	Sa	$11.18^{+0.11}_{-0.11}$
753	NGC5656	Seyfert 2	Sb	$10.62^{+0.10}_{-0.10}$
757	NGC5675	Type 1, EAGN	Sa	$10.81^{+0.12}_{-0.13}$
770	NGC5739	Type 1	S0a	$11.46^{+0.26}_{-0.23}$
772	UGC09492	Type 1	Sab	$11.21^{+0.10}_{-0.09}$
777	NGC5772	Type 1	Sab	$10.97^{+0.10}_{-0.10}$

787	NGC5876	Type 1	S0a	$10.90^{+0.13}_{-0.11}$
791	NGC5908	Seyfert 2	Sa	$11.22^{+0.10}_{-0.10}$
801	NGC5953	Type 1, EAGN	Sa	$10.48^{+0.09}_{-0.10}$
802	ARP220	Type 1, Radio	Sd	$10.88^{+0.12}_{-0.09}$
806	NGC5966	Type 1	E4	$11.01^{+0.21}_{-0.20}$
809	NGC5987	Type 1	Sa	$11.21^{+0.09}_{-0.09}$
816	NGC6021	Type 1	E5	$11.01^{+0.11}_{-0.11}$
822	UGC10205	Type 1	S0a	$11.00^{+0.11}_{-0.11}$
826	NGC6081	Type 1, Seyfert 2	S0a	$11.12^{+0.08}_{-0.09}$
832	NGC6146	Type 1, Radio	E5	$11.63^{+0.14}_{-0.15}$
838	UGC10388	Seyfert 2	Sa	$10.82^{+0.12}_{-0.12}$
839	NGC6166NED01	Radio	E4	$11.950^{+0.22}_{-0.21}$
844	NGC6278	Type 1	S0a	$10.92^{+0.09}_{-0.10}$
851	NGC6338	Radio	E5	$11.691^{+0.14}_{-0.13}$
857	NGC6394	Type 1, Seyfert 2	Sbc	$10.90^{+0.10}_{-0.10}$
858	UGC10905	Type 1	S0a	$11.61^{+0.21}_{-0.06}$
863	NGC6497	Seyfert 2	Sab	$11.04^{+0.11}_{-0.11}$
867	NGC6762	Type 1	Sab	$10.38^{+0.08}_{-0.07}$
868	MCG-02-51-004	Type 1	Sb	$10.68^{+0.10}_{-0.10}$
869	NGC6941	Radio	Sb	$10.943^{+0.11}_{-0.10}$
874	NGC7025	Type 1, Seyfert 2	S0a	$11.53^{+0.18}_{-0.18}$
865	UGC11228	Type 1	S0	$11.09^{+0.10}_{-0.09}$
873	UGC11680NED01	Type 1	Sb	$11.09^{+0.12}_{-0.13}$
877	UGC11717	Seyfert 2	Sab	$10.84^{+0.11}_{-0.11}$
883	UGC11958	Type 1	S0	$11.77^{+0.28}_{-0.26}$
886	NGC7311	Type 1, Seyfert 2	Sa	$11.07^{+0.09}_{-0.09}$
887	NGC7321	Type 1	Sbc	$10.93^{+0.10}_{-0.11}$
888	UGC12127	Radio	E1	$11.369^{+0.26}_{-0.26}$
896	NGC7466	Seyfert 2	Sbc	$10.75^{+0.11}_{-0.10}$
897	UGC12348	Seyfert 2, X-ray, EAGN	Sb	$10.85^{+0.10}_{-0.11}$
900	NGC7550	Type 1	E4	$11.43^{+0.19}_{-0.17}$
905	UGC12494	Seyfert 2	Sd	$9.44^{+0.12}_{-0.10}$
915	NGC7653	Type 1	Sb	$10.50^{+0.11}_{-0.11}$
916	NGC7671	Type 1, Seyfert 2	S0	$10.96^{+0.09}_{-0.09}$
919	NGC7684	Seyfert 2	S0	$10.99^{+0.06}_{-0.09}$
923	NGC7711	Seyfert 2	E7	$11.05^{+0.09}_{-0.09}$
924	NGC7716	Type 1	Sb	$10.39^{+0.13}_{-0.14}$
925	NGC7722	Seyfert 2	Sab	$11.24^{+0.16}_{-0.16}$
927	NGC7738	Type 1	Sb	$11.08^{+0.10}_{-0.09}$
938	NGC5947	Type 1	Sab	

APPENDIX B

Type 1 AGN emission-line fits

Examples of the emission line fits of type 1 AGN from the CALIFA DR3 that have broad Hα present in their central spectra. The fits are showing the region around the Hα + [NII] emission-line complex, with majority of spectra also showing the presence of [SII] doublet. The faintest objects lack [SII] lines. The black dots represent the data points of the spectra after subtraction of the stellar component. Each emission line is fitted by a Gaussian distribution, where narrow emission lines of [NIII], [SII] and Hα all have the same widths, while the broad component of Hα have flux, width and shift left as free parameters durning fitting. The red lines show the best-fit models, while blue lines are representing the individual fit components. The smaller panels below each main panel show the fit residuals. Additional two objects (UGC03973 and MCG-02-51-004) are previously shown on Figure 2.2 in Chapter 2.

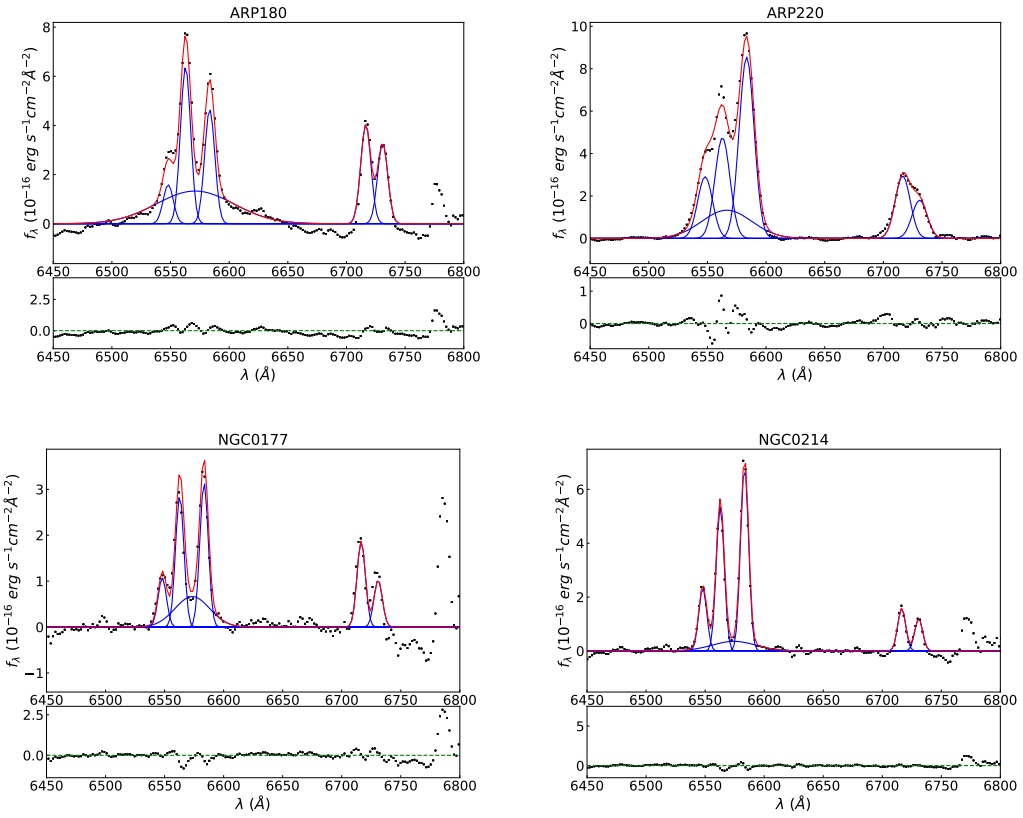

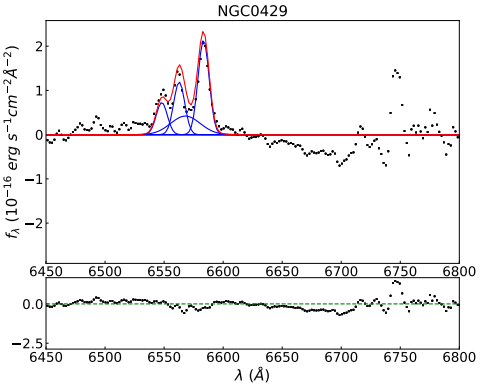
NGC0429
f_λ (10^{-16} erg s^{-1}cm^{-2}Å^{-2})
λ (Å)

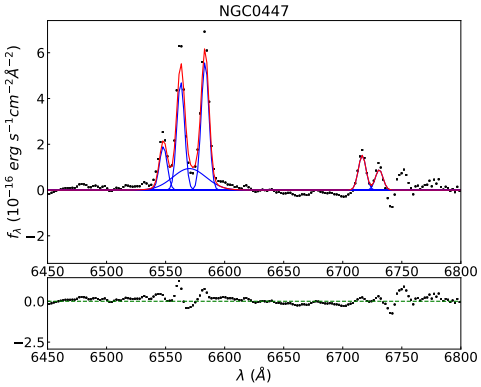
NGC0447
f_λ (10^{-16} erg s^{-1}cm^{-2}Å^{-2})
λ (Å)

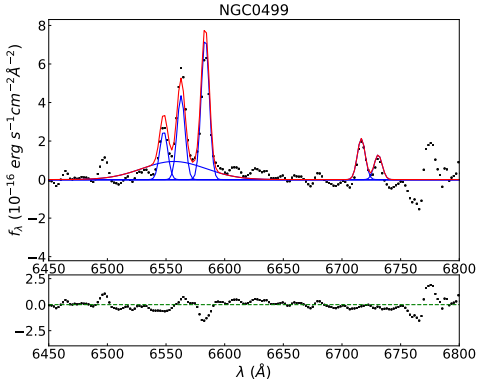
NGC0499
f_λ (10^{-16} erg s^{-1}cm^{-2}Å^{-2})
λ (Å)

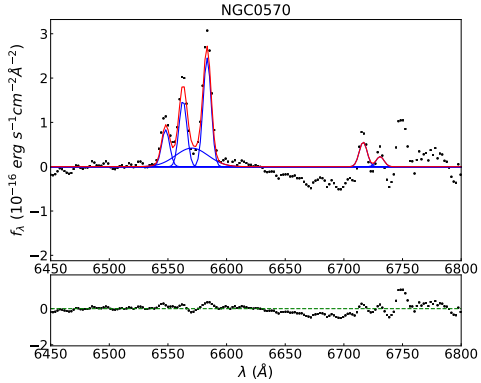
NGC0570
f_λ (10^{-16} erg s^{-1}cm^{-2}Å^{-2})
λ (Å)

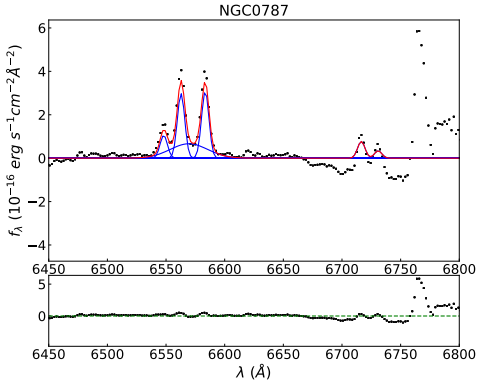
NGC0787
f_λ (10^{-16} erg s^{-1}cm^{-2}Å^{-2})
λ (Å)

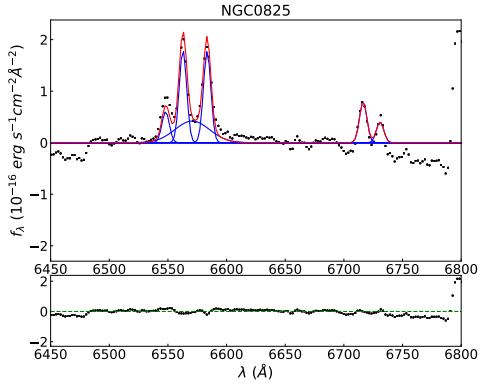
NGC0825
f_λ (10^{-16} erg s^{-1}cm^{-2}Å^{-2})
λ (Å)

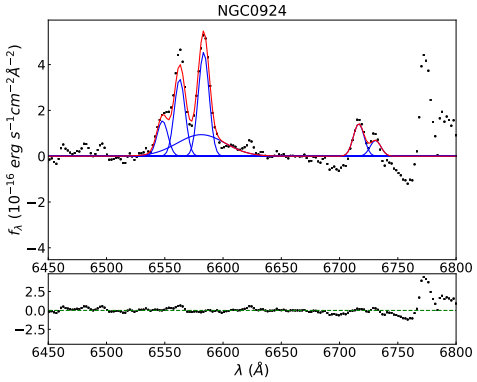
NGC0924
f_λ (10^{-16} erg s^{-1}cm^{-2}Å^{-2})
λ (Å)

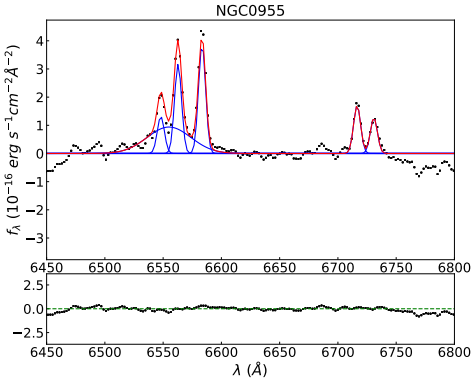
NGC0955
f_λ (10^{-16} erg s^{-1}cm^{-2}Å^{-2})
λ (Å)

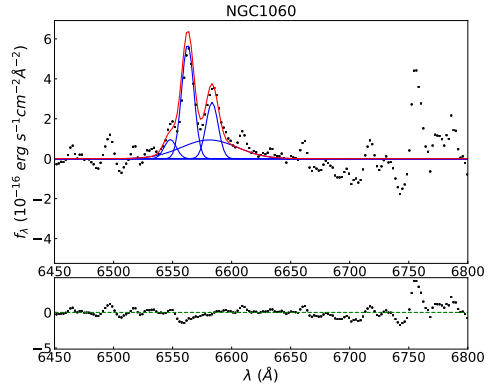
NGC1060
f_λ (10^{-16} erg s^{-1}cm^{-2}Å^{-2})
λ (Å)

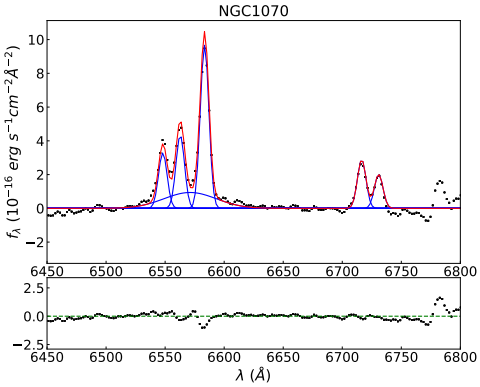
NGC1070
f_λ (10^{-16} erg s^{-1}cm^{-2}Å^{-2})
λ (Å)

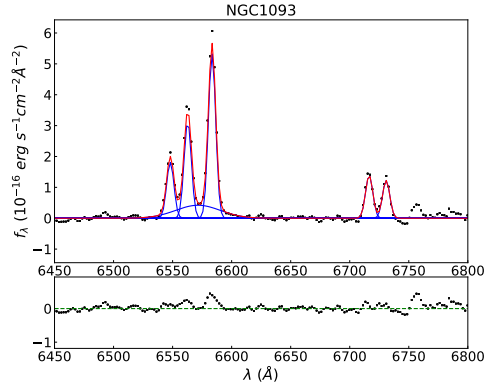
NGC1093
f_λ (10^{-16} erg s^{-1}cm^{-2}Å^{-2})
λ (Å)

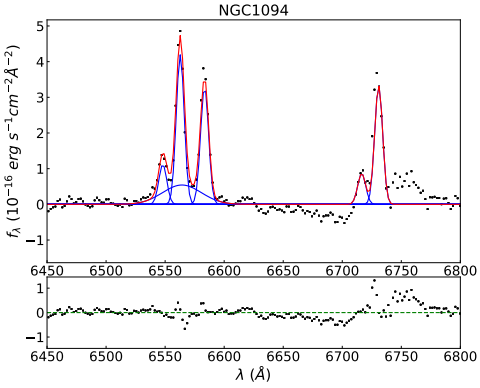
NGC1094
f_λ (10^{-16} erg s^{-1}cm^{-2}Å^{-2})
λ (Å)

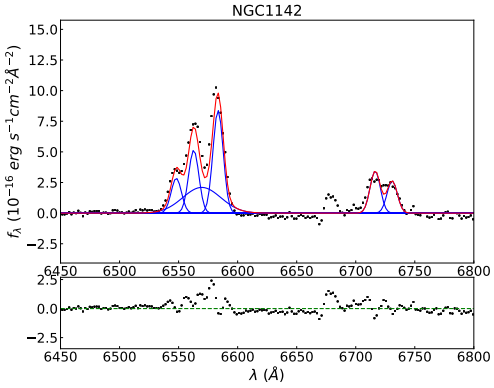
NGC1142
f_λ (10^{-16} erg s^{-1}cm^{-2}Å^{-2})
λ (Å)

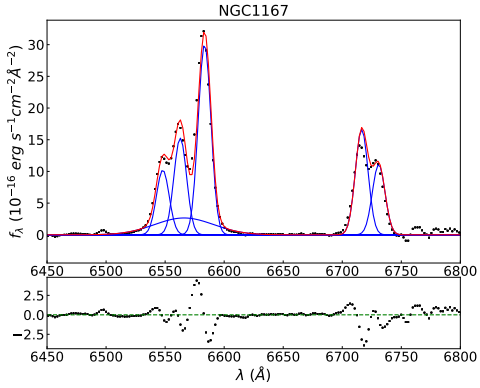
NGC1167
f_λ (10^{-16} erg s^{-1}cm^{-2}Å^{-2})
λ (Å)

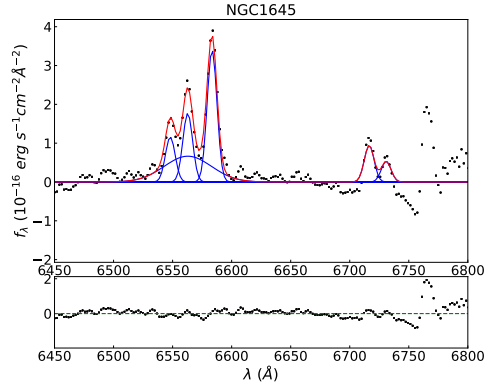
NGC1645
f_λ (10^{-16} erg s^{-1}cm^{-2}Å^{-2})
λ (Å)

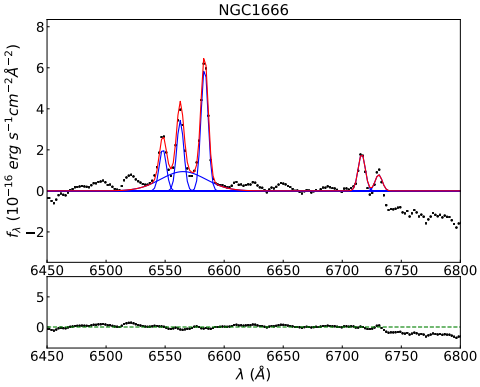
NGC1666
f_λ (10^{-16} erg s^{-1}cm^{-2}Å^{-2})
λ (Å)

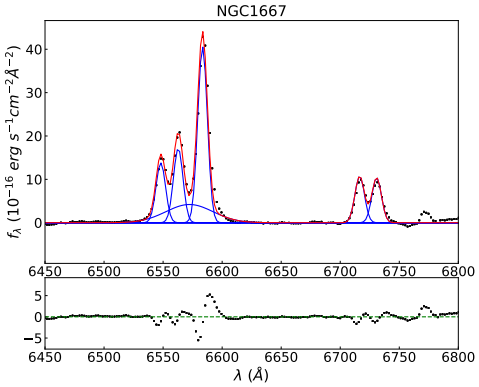
NGC1667
f_λ (10^{-16} erg s^{-1}cm^{-2}Å^{-2})
λ (Å)

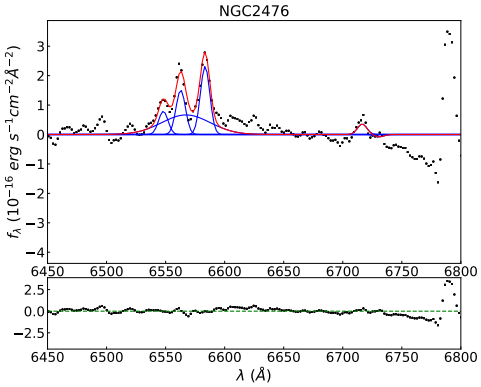
NGC2476
f_λ (10^{-16} erg s^{-1}cm^{-2}Å^{-2})
λ (Å)

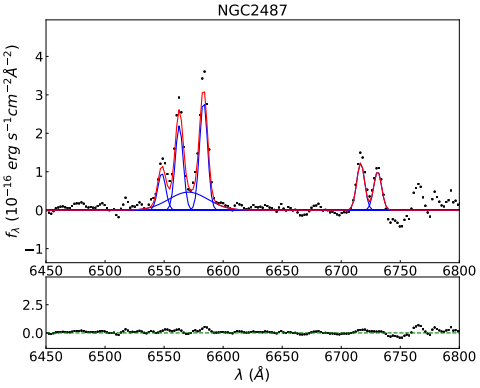
NGC2487
f_λ (10^{-16} erg s^{-1}cm^{-2}Å^{-2})
λ (Å)

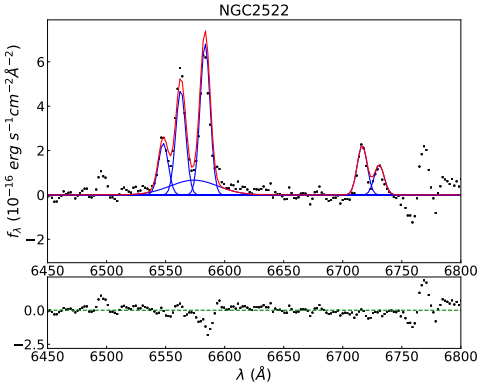
NGC2522
f_λ (10^{-16} erg s^{-1}cm^{-2}Å^{-2})
λ (Å)

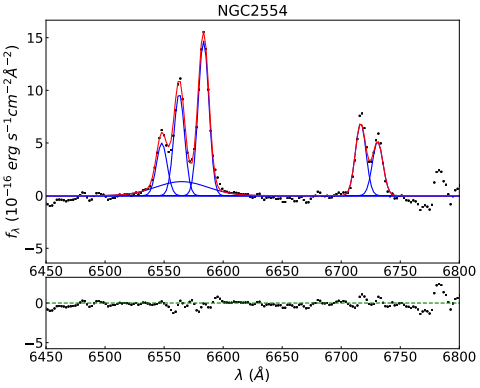
NGC2554
f_λ (10^{-16} erg s^{-1}cm^{-2}Å^{-2})
λ (Å)

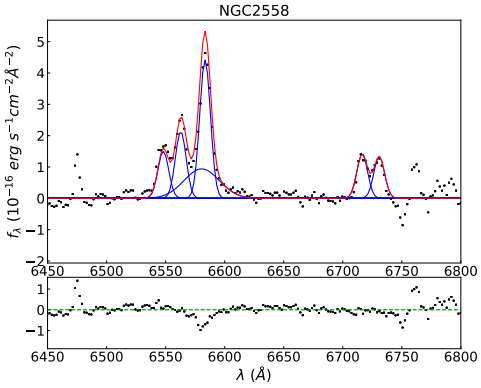
NGC2558
f_λ (10^{-16} erg s^{-1}cm^{-2}Å^{-2})
λ (Å)

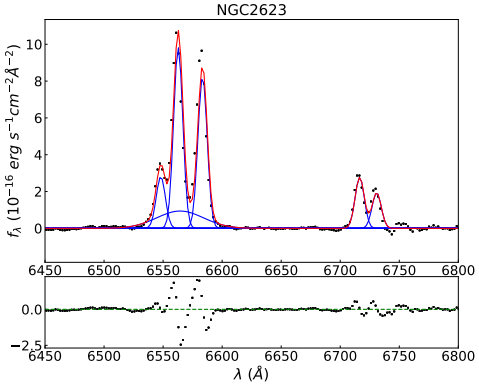
NGC2623
f_λ (10^{-16} erg s^{-1}cm^{-2}Å^{-2})
λ (Å)

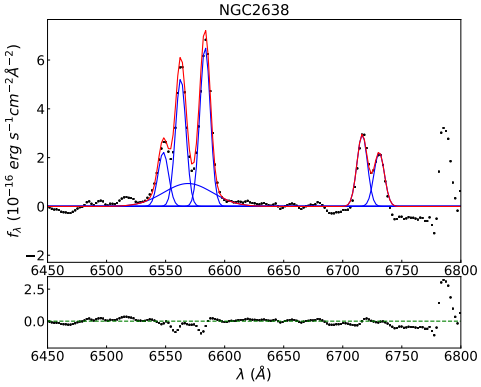
NGC2638
f_λ (10^{-16} erg s^{-1}cm^{-2}Å^{-2})
λ (Å)

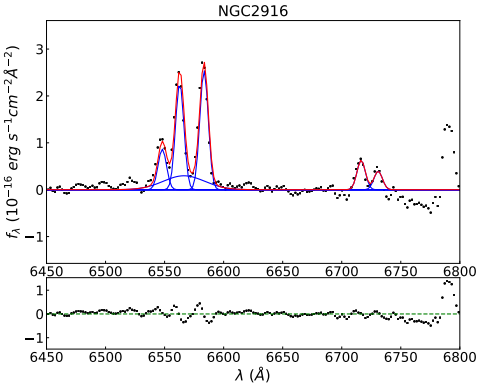
NGC2916
f_λ (10^{-16} erg s^{-1}cm^{-2}Å^{-2})
λ (Å)

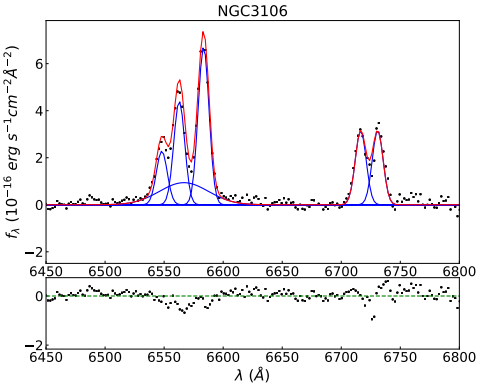
NGC3106
f_λ (10^{-16} erg s^{-1}cm^{-2}Å^{-2})
λ (Å)

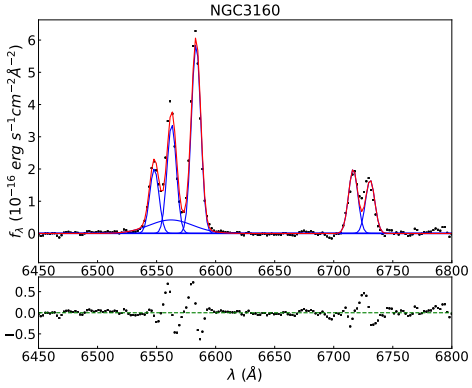
NGC3160
f_λ (10^{-16} erg s^{-1}cm^{-2}Å^{-2})
λ (Å)

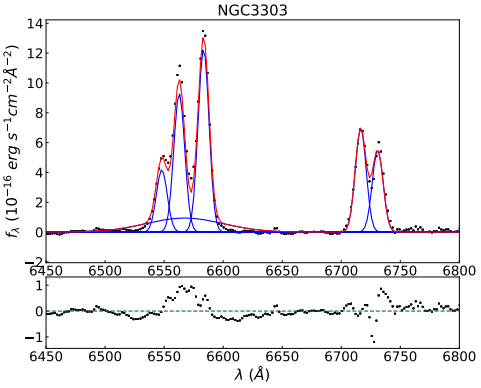
NGC3303
f_λ (10^{-16} erg s^{-1}cm^{-2}Å^{-2})
λ (Å)

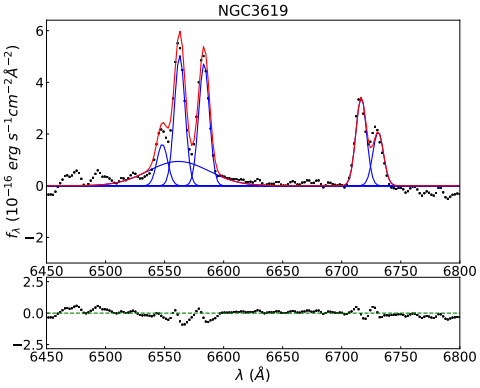
NGC3619
f_λ (10^{-16} erg s^{-1}cm^{-2}Å^{-2})
λ (Å)

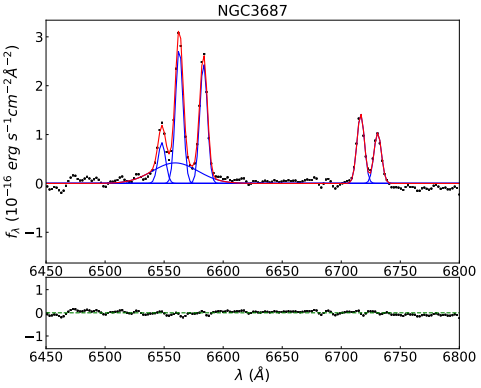
NGC3687
f_λ (10^{-16} erg s^{-1}cm^{-2}Å^{-2})
λ (Å)

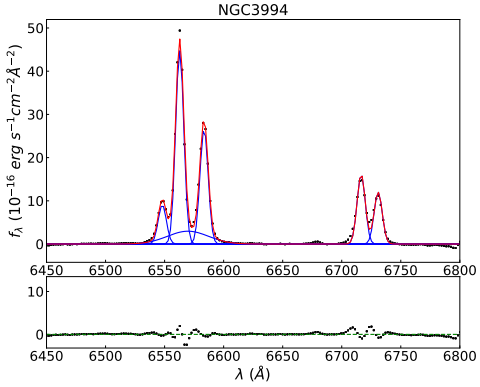
NGC3994
f_λ (10^{-16} erg s^{-1}cm^{-2}Å^{-2})
λ (Å)

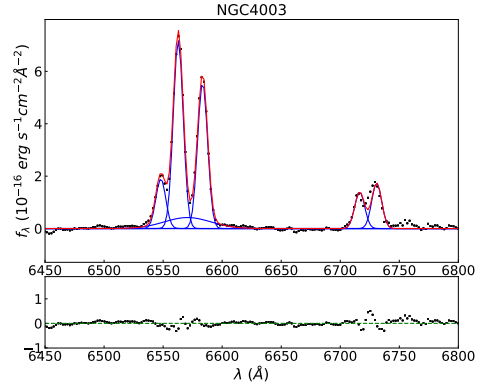
NGC4003
f_λ (10^{-16} erg s^{-1}cm^{-2}Å^{-2})
λ (Å)

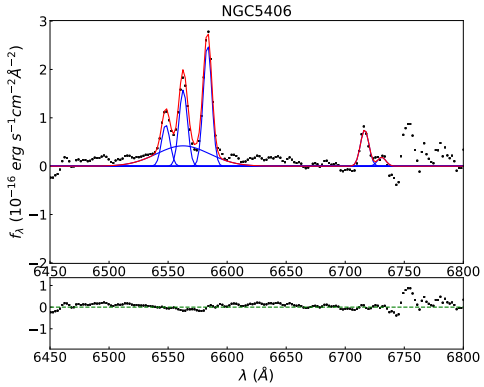
NGC5406
f_λ (10^{-16} erg s^{-1}cm^{-2}Å^{-2})
λ (Å)

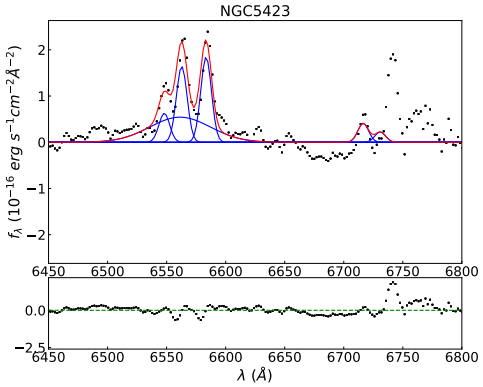
NGC5423
f_λ (10^{-16} erg s^{-1}cm^{-2}Å^{-2})
λ (Å)

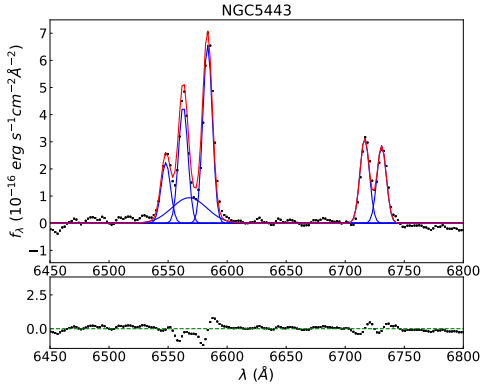
NGC5443
f_λ (10^{-16} erg s^{-1}cm^{-2}Å^{-2})
λ (Å)

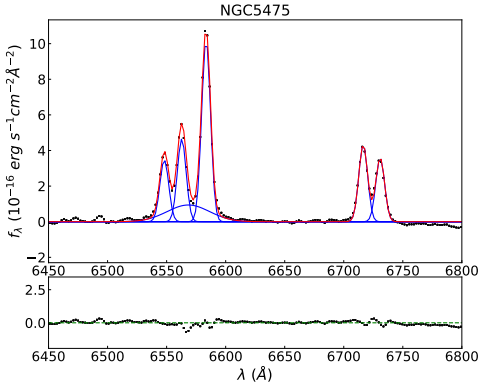
NGC5475
f_λ (10^{-16} erg s^{-1}cm^{-2}Å^{-2})
λ (Å)

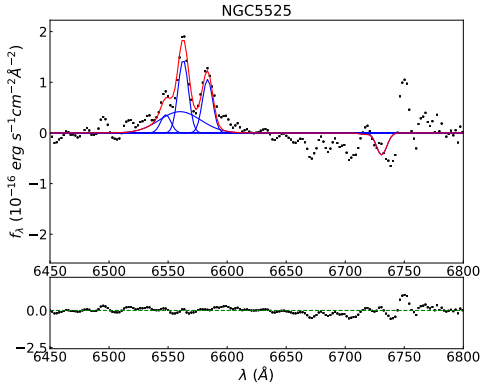
NGC5525
f_λ (10^{-16} erg s^{-1}cm^{-2}Å^{-2})
λ (Å)

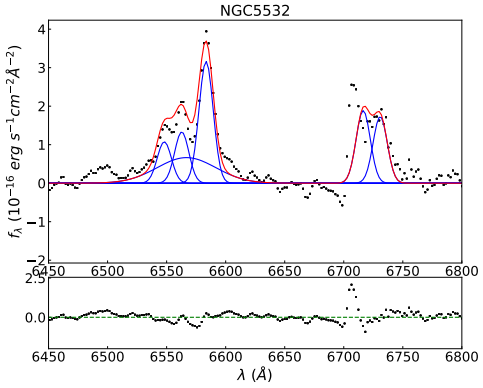
NGC5532
f_λ (10^{-16} erg s^{-1}cm^{-2}Å^{-2})
λ (Å)

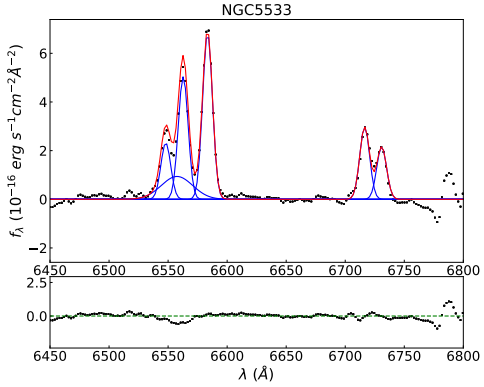
NGC5533
f_λ (10^{-16} erg s^{-1}cm^{-2}Å^{-2})
λ (Å)

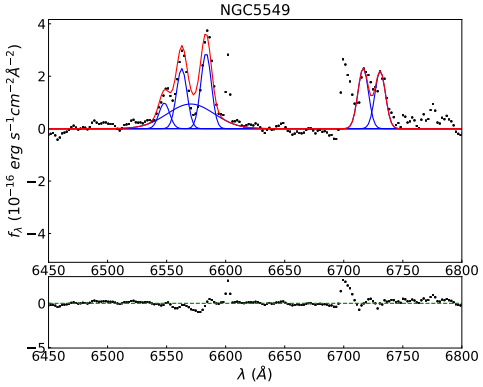
NGC5549
f_λ (10^{-16} erg s^{-1}cm^{-2}Å^{-2})
λ (Å)

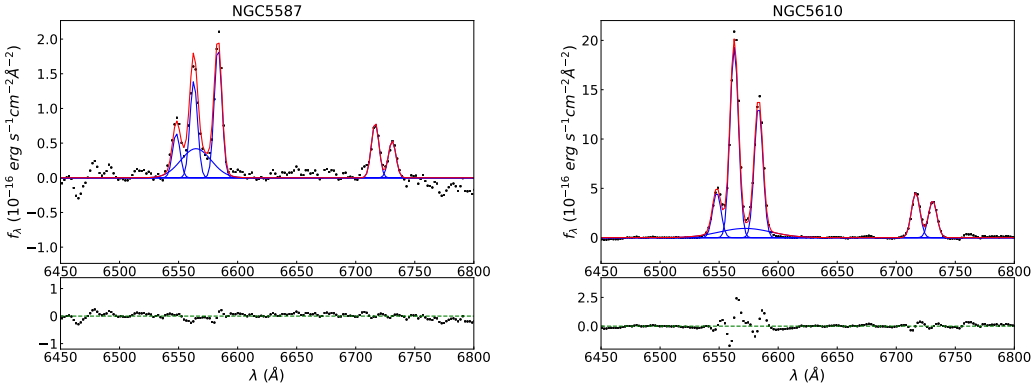
NGC5587
NGC5610
f_λ (10^{-16} erg s^{-1}cm^{-2}Å^{-2})
λ (Å)

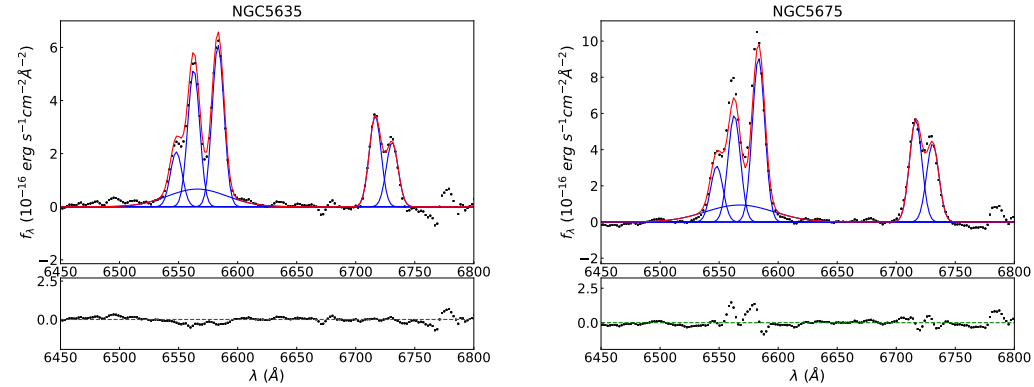
NGC5635
NGC5675
f_λ (10^{-16} erg s^{-1}cm^{-2}Å^{-2})
λ (Å)

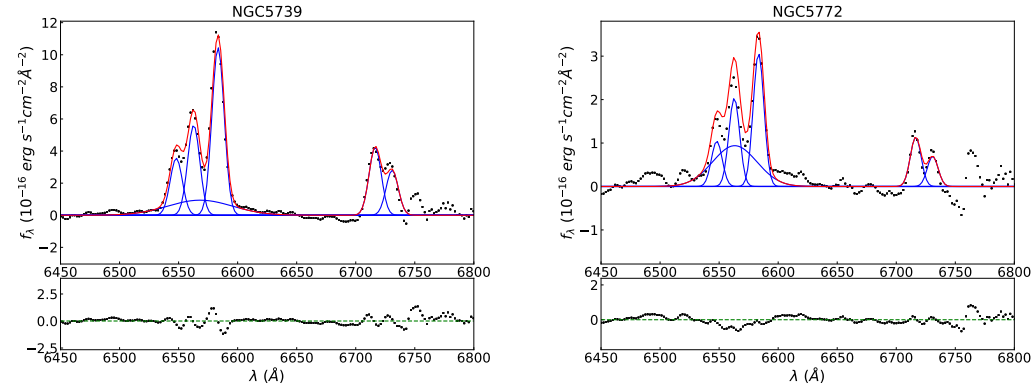
NGC5739
NGC5772
f_λ (10^{-16} erg s^{-1}cm^{-2}Å^{-2})
λ (Å)

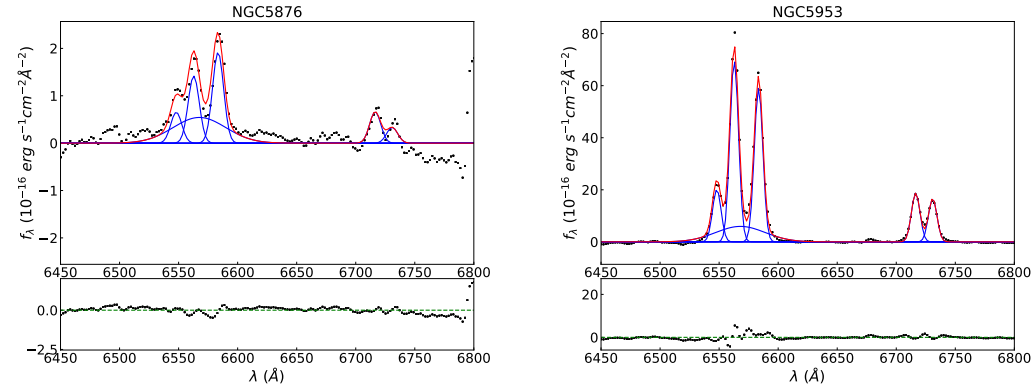
NGC5876
NGC5953
f_λ (10^{-16} erg s^{-1}cm^{-2}Å^{-2})
λ (Å)

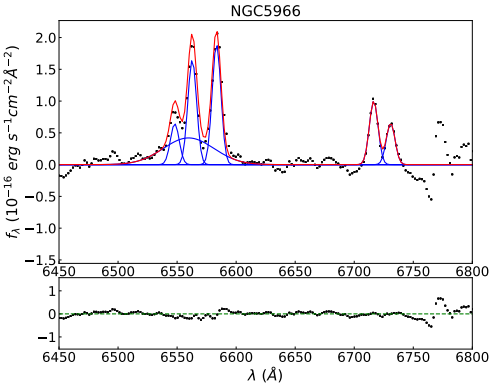
NGC5966
f_λ (10^{-16} erg s^{-1}cm^{-2}Å^{-2})
λ (Å)

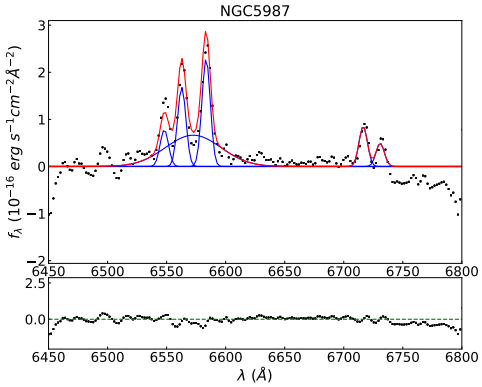
NGC5987
f_λ (10^{-16} erg s^{-1}cm^{-2}Å^{-2})
λ (Å)

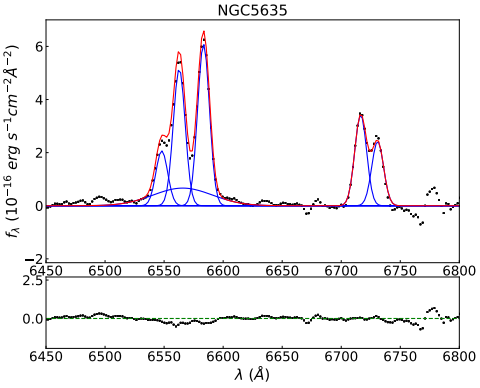
NGC5635
f_λ (10^{-16} erg s^{-1}cm^{-2}Å^{-2})
λ (Å)

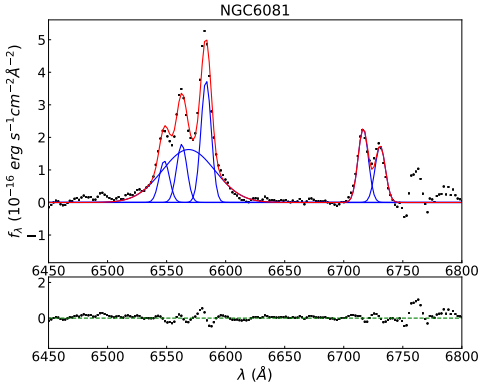
NGC6081
f_λ (10^{-16} erg s^{-1}cm^{-2}Å^{-2})
λ (Å)

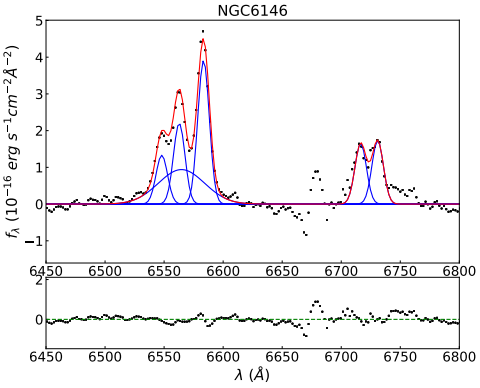
NGC6146
f_λ (10^{-16} erg s^{-1}cm^{-2}Å^{-2})
λ (Å)

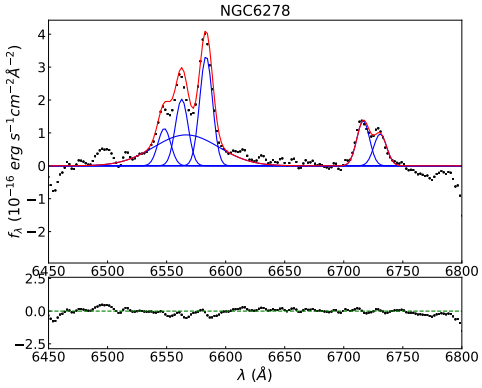
NGC6278
f_λ (10^{-16} erg s^{-1}cm^{-2}Å^{-2})
λ (Å)

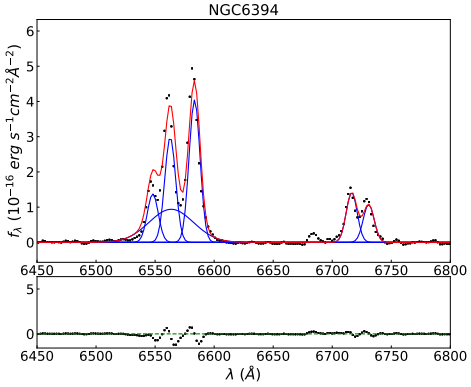
NGC6394
f_λ (10^{-16} erg s^{-1}cm^{-2}Å^{-2})
λ (Å)

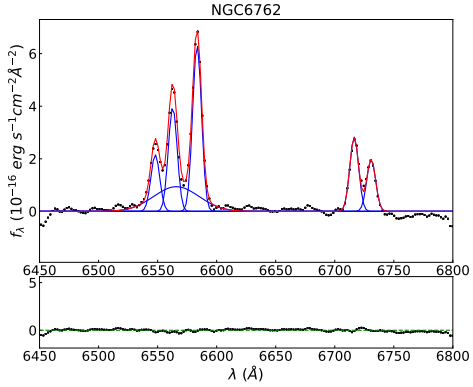
NGC6762
f_λ (10^{-16} erg s^{-1}cm^{-2}Å^{-2})
λ (Å)

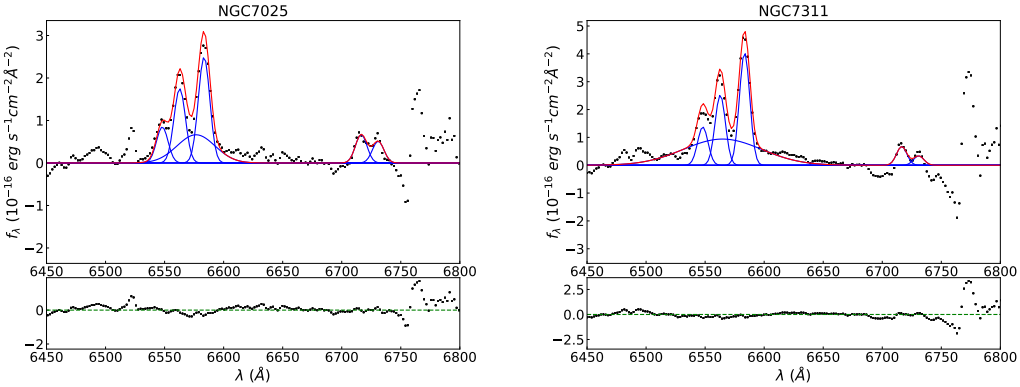
NGC7025
NGC7311
f_λ (10^{-16} erg s^{-1}cm^{-2}Å^{-2})
λ (Å)

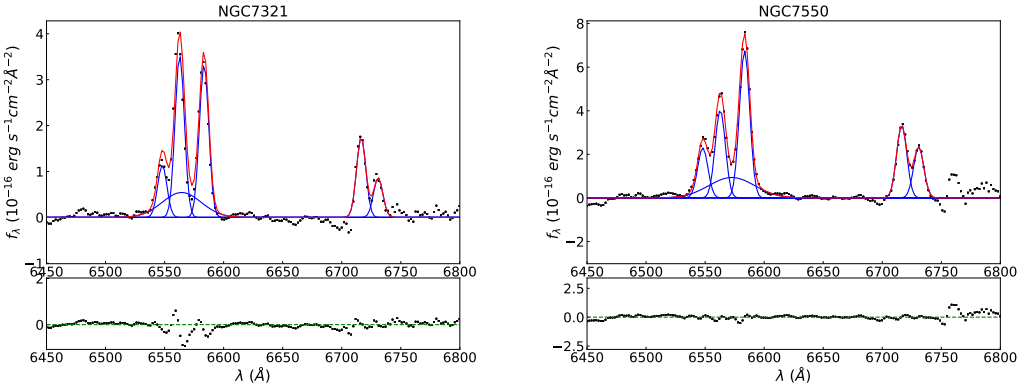
NGC7321
NGC7550
f_λ (10^{-16} erg s^{-1}cm^{-2}Å^{-2})
λ (Å)

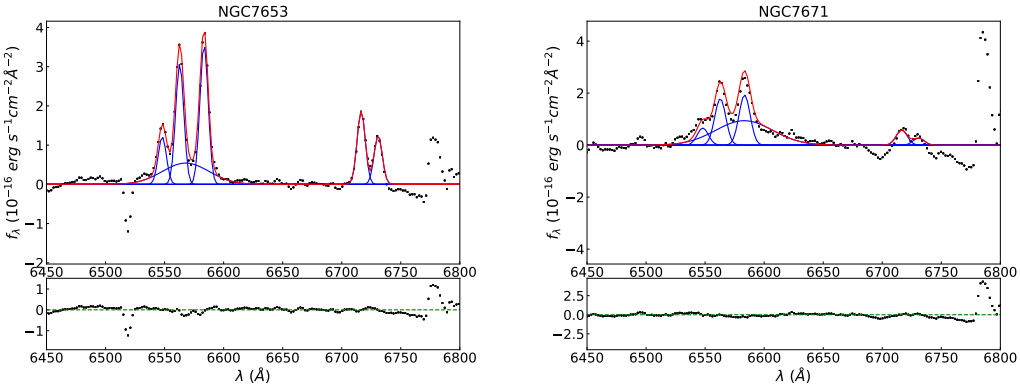
NGC7653
NGC7671
f_λ (10^{-16} erg s^{-1}cm^{-2}Å^{-2})
λ (Å)

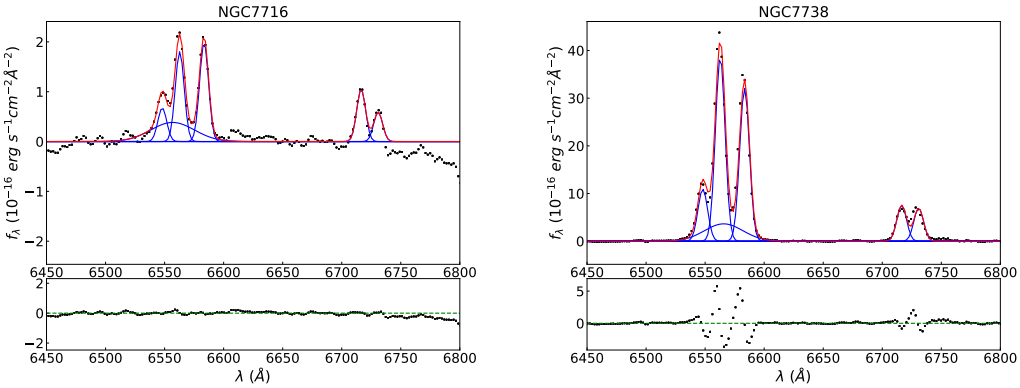
NGC7716
NGC7738
f_λ (10^{-16} erg s^{-1}cm^{-2}Å^{-2})
λ (Å)

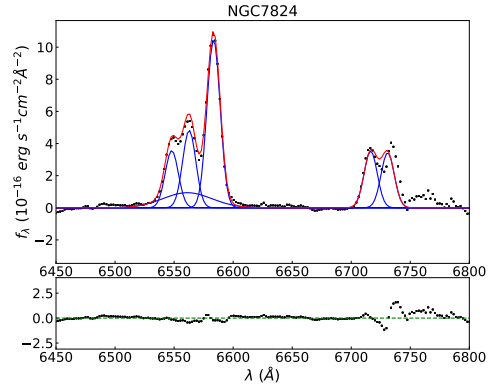
NGC7824
f_λ (10^{-16} erg s^{-1}cm^{-2}Å^{-2})
λ (Å)

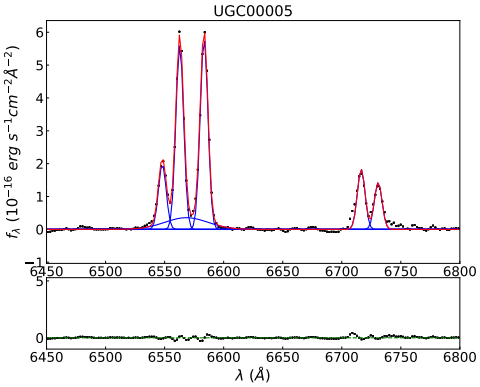
UGC00005
f_λ (10^{-16} erg s^{-1}cm^{-2}Å^{-2})
λ (Å)

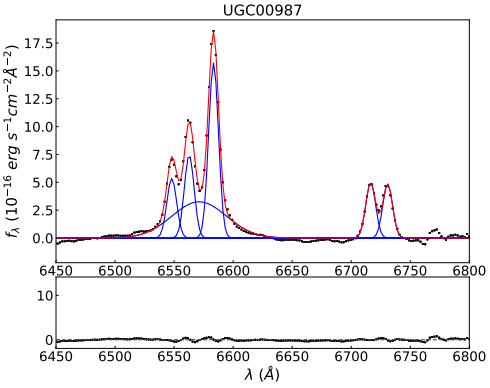
UGC00987
f_λ (10^{-16} erg s^{-1}cm^{-2}Å^{-2})
λ (Å)

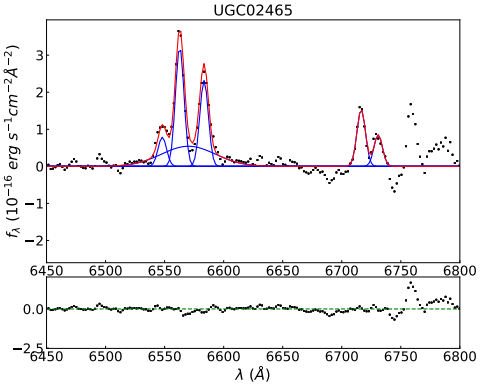
UGC02465
f_λ (10^{-16} erg s^{-1}cm^{-2}Å^{-2})
λ (Å)

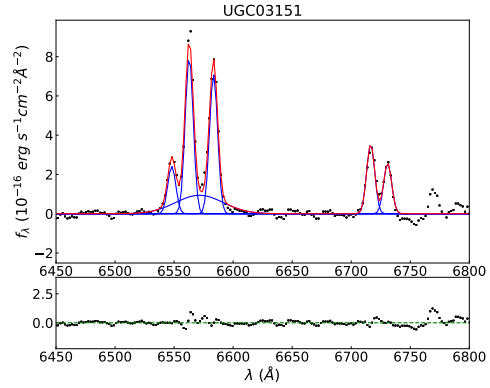
UGC03151
f_λ (10^{-16} erg s^{-1}cm^{-2}Å^{-2})
λ (Å)

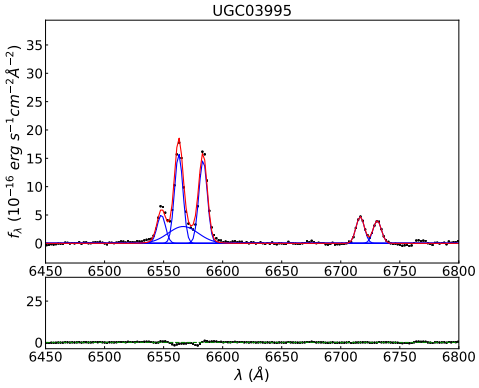
UGC03995
f_λ (10^{-16} erg s^{-1}cm^{-2}Å^{-2})
λ (Å)

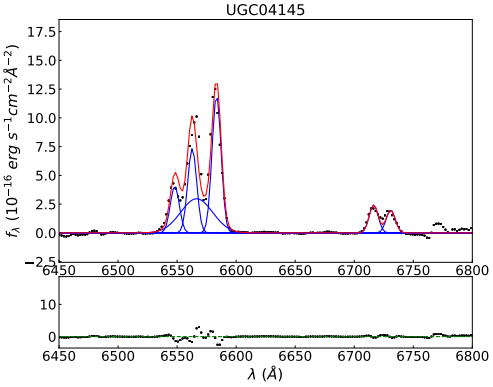
UGC04145
f_λ (10^{-16} erg s^{-1}cm^{-2}Å^{-2})
λ (Å)

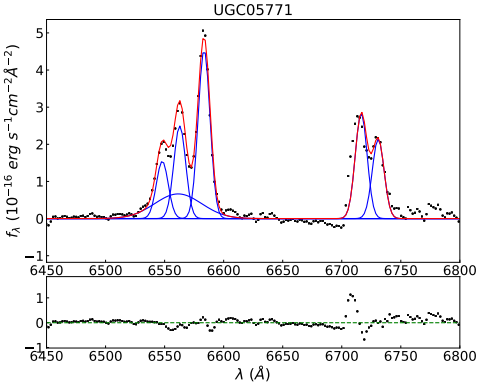
UGC05771
f_λ (10^{-16} erg s^{-1}cm^{-2}Å^{-2})
λ (Å)

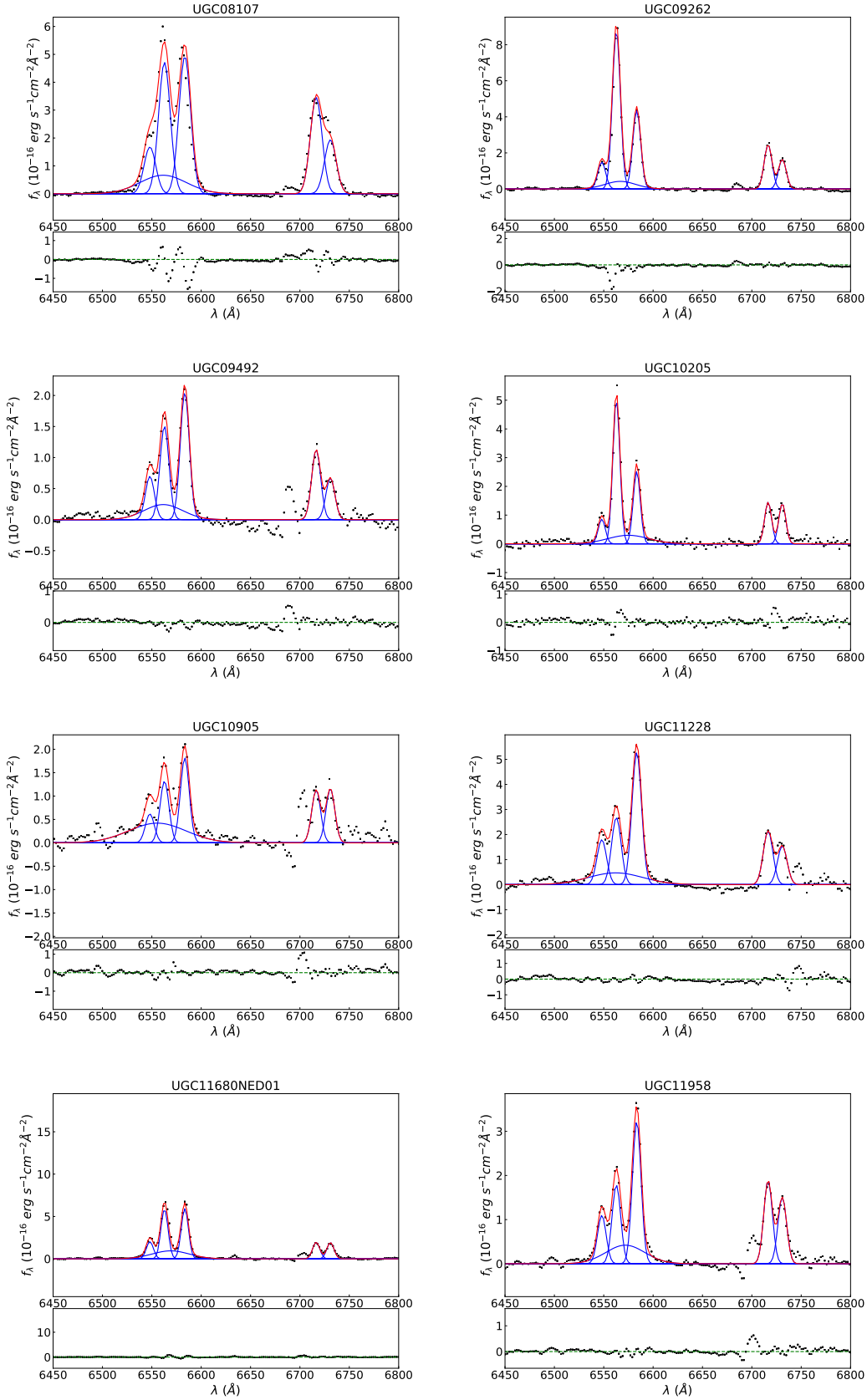
UGC08107
UGC09262
UGC09492
UGC10205
UGC10905
UGC11228
UGC11680NED01
UGC11958
f_λ (10^{-16} erg s^{-1}cm^{-2}Å^{-2})
λ (Å)

List of Abbreviations

AGN	**A**citve **G**alactic **N**uclei
AGNLF	**A**ctive **G**alactic **N**uclei **L**uminosity **F**unction
BEL	**B**road **E**mission **L**ine
BHMF	**B**lack **H**ole **M**ass **F**unction
BLR	**B**road **L**ine **R**egion
CALIFA	**C**alar **A**lto **L**egacy **I**ntegral **F**ield **A**rea
EELR	Extended **E**mission **L**ine **Region**
ENLR	Extended **N**arrow **L**ine **R**egion
ERDF	**E**ddington **R**atio **D**istribution **F**unction
FWHM	**F**ull **W**idth (at) **H**alf **M**aximum
IFS	**I**ntegral **F**ield **S**pectropscopy
IMF	**I**nitial **M**ass **F**unction
LIER	**L**ow **I**onization **E**mission **R**egion
LINER	**L**ow **I**onization **N**uclear **E**mission **R**egion
LLAGN	**L**ow **L**uminosity **A**ctive **G**alactic **N**uclei
NEL	**N**arrow **E**mission **L**ine
NLR	**N**arrow **L**ine **R**egion
pAGB	**p**ost **A**symptotic **G**iant **B**ranch
QSO	**Q**uasi **S**tellar **O**bject
SED	**S**pectral **E**nergy **D**istribution
SMBH	**S**uper **M**assive **B**lack **H**ole
spaxel	**spa**tial pi**xel**
ULIRG	**U**ltra **L**uminous **I**nfra **R**ed **G**alaxy

Acknowledgements

First I would like to thank my mentor and supervisor, Lutz Wisotzki, for guidance, ideas, patience when I made mistakes, and encouragement to finish the thesis even after I stopped working at the AIP. During the past five years I learned a lot about AGN and black holes, and I cannot thank you enough, Lutz, for giving me the opportunity to work on this project and finally put all of that work into this thesis.

I would also like to thank the reviewers, Philipp Richter and Amy Reines, for taking time to read this thesis.

This all wouldn't have been possible without DAAD scholarship that I was granted for the first three years of my thesis. I would like to thank the entire organization for giving me such opportunity.

I would also like to thank to the entire Galaxies and Quasars group at the AIP, as well as PhD students I spent majority of these years with.

Last but not least, I would like to thank my friends and family for supporting and tolerating me especially in the final months of my thesis, as well as my current team at Adjust for having patience and understanding when my brain is not fully functional due to lack of sleep over the thesis. And my cat for simply existing.

This has been hard but wonderful journey that heavily impacted my life in the best possible way.